Search for supersymmetry in events containing light leptons, jets and missing transverse momentum in $\sqrt{s} = 8\,\mathrm{TeV}$ pp collisions with the ATLAS detector

Dissertation zur Erlangung des
naturwissenschaftlichen Doktorgrades
der Julius-Maximilians-Universität Würzburg

vorgelegt von

Manuel Schreyer
aus Amberg

Würzburg 2015

Eingereicht am 25.06.2015
bei der Fakultät für Physik und Astronomie

1. Gutachter: Prof. Dr. Raimund Ströhmer
2. Gutachter: Prof. Dr. Werner Porod
der Dissertation

Vorsitzender: Prof. Dr. Randolf Hanke
1. Prüfer: Prof. Dr. Raimund Ströhmer
2. Prüfer: Prof. Dr. Werner Porod
3. Prüfer: Prof. Dr. Matthias Kadler
im Promotionskolloquium

Tag des Promotionskolloquiums: 25.09.2015

Doktorurkunde ausgehändigt am: ______________

Abstract

The results of two analyses searching for supersymmetry (SUSY) in data of the ATLAS experiment are presented in this thesis. The data were recorded in proton-proton collisions at the Large Hadron Collider in 2012 at a centre of mass energy of $\sqrt{s} = 8\,\mathrm{TeV}$ and correspond to an integrated luminosity of $\int \mathcal{L}\,dt = 20.3\,\mathrm{fb}^{-1}$.

The first search is performed in signatures containing an opposite-sign electron or muon pair, which is compatible with originating from a Z boson decay, in addition to jets and large missing transverse momentum. The analysis targets the production of squarks and gluinos in R-parity-conserving (RPC) models with SUSY breaking via General Gauge Mediation (GGM). The main Standard Model (SM) backgrounds are $t\bar{t}$, WW, $W+t$ and $Z \to \tau\tau$ processes which are entirely estimated from data using different-flavour events. Besides that, the SM production of Z bosons in association with jets and large fake missing momentum from mismeasurements plays a role and is predicted with the data-driven jet smearing method. Backgrounds from events with fake leptons are estimated with the data-driven matrix method. WZ/ZZ production as well as smaller background contributions are determined from Monte-Carlo simulations. The search observes an excess of data over the SM prediction with a local significance of $3.0\,\sigma$ in the electron channel, $1.7\,\sigma$ in the muon channel and $3.0\,\sigma$ when the two channels are added together. The results are used to constrain the parameters of the GGM model.

The second analysis uses the already published results of an ATLAS search for SUSY in events with one isolated electron or muon, jets and missing transverse momentum to reinterpret them in the context of squark and gluino production in SUSY models with R-parity-violating (RPV) $LQ\bar{D}$ operators. In contrast to RPC models, the lightest SUSY particle (LSP) is not stable but decays into SM particles. “Standard” analyses often do not consider SUSY models with RPV although they are in principle sensitive to them. The exclusion limits on the squark and gluino mass obtained from the reinterpretation extend up to 1200 GeV. These are the first results by any ATLAS SUSY search which systematically cover a wide range of RPV couplings in the case of prompt LSP decays. However, the analysis is not sensitive to the full parameter space of the $LQ\bar{D}$ model and reveals gaps in the ATLAS SUSY program which have to be closed by dedicated search strategies in the future.

Zusammenfassung

In dieser Arbeit werden die Ergebnisse von zwei Suchen nach Supersymmetrie (SUSY) in Daten des ATLAS-Experiments präsentiert. Die Messdaten wurden im Jahr 2012 in Proton-Proton-Kollisionen am Large Hadron Collider bei einer Schwerpunktsenergie von $\sqrt{s} = 8\,\mathrm{TeV}$ gewonnen und entsprechen einer integrierten Luminosität von $\int \mathcal{L}\, dt = 20.3\,\mathrm{fb}^{-1}$.
Die erste Suche verwendet Signaturen mit Jets, großem fehlenden Transversalimpuls sowie einem Elektron- oder Myonpaar mit entgegengesetzter Ladung, dessen Eigenschaften mit einem Leptonpaar aus dem Zerfall eines Z-Bosons vereinbar sind. Die Analyse zielt auf die Untersuchung von Squark- und Gluinoproduktion im Rahmen R-paritätserhaltender (RPC) Modelle mit SUSY-Brechung durch General Gauge Mediation (GGM) ab. Die Hauptuntergründe des Standardmodells (SM) sind $t\bar{t}$, WW, $W + t$ und $Z \to \tau\tau$ Prozesse. Diese werden komplett aus den Daten selbst unter Verwendung von Ereignissen mit Leptonpaaren unterschiedlichen Flavours abgeschätzt. Daneben spielt der Untergrund aus der SM-Produktion von Z-Bosonen in Verbindung mit Jets und großem fehlenden Impuls, der durch Fehlmessungen fälschlicherweise rekonstruiert wird, ein Rolle. Dieser wird mit der datengestützten Jet-Smearing-Methode abgeschätzt. Der Hintergrundbeitrag von Ereignissen mit fehlidentifizierten Leptonen wird mit der datengestützten Matrix-Methode bestimmt, während die Produktion von WZ/ZZ-Paaren sowie kleinere Untergrundprozesse mit Hilfe von Monte-Carlo-Simulationen abgeschätzt werden. Die Suche beobachtet einen Überschuss an Daten über der SM-Vorhersage mit einer lokalen Signifikanz von $3{,}0\,\sigma$ im Elektronkanal, $1{,}7\,\sigma$ im Myonkanal und $3{,}0\,\sigma$, wenn beide Kanäle zusammengezählt werden. Mit den Ergebnissen lassen sich die Parameter des GGM-Modells einschränken.
Die zweite Analyse interpretiert die bereits veröffentlichten Ergebnisse einer ATLAS SUSY-Suche in Ereignissen mit einem isolierten Elektron oder Myon, Jets und fehlendem Transversalimpuls im Rahmen von Squark- und Gluinoproduktion in SUSY-Modellen, in denen die R-Parität durch $LQ\bar{D}$-Operatoren verletzt wird. Im Gegensatz zu RPC-Modellen ist das leichteste SUSY-Teilchen (LSP) dort nicht stabil, sondern zerfällt in SM-Teilchen. R-paritätsverletzende (RPV) SUSY-Modelle werden von „Standardanalysen" oft vernachlässigt, obwohl diese prinzipiell sensitiv auf RPV SUSY sind. Die Ausschlussgrenzen auf die Squark- und Gluinomasse, die sich aus der Reinterpretation ergeben, reichen bis zu 1200 GeV. Dies sind die ersten derartigen Ergebnisse einer ATLAS SUSY-Suche, die einen großen Bereich möglicher RPV-Kopplungen für den Fall prompter LSP-Zerfälle auf systematische Art und Weise abdecken. Allerdings ist die Analyse nicht im gesamten Parameterraum des $LQ\bar{D}$-Modells sensitiv und deckt somit Lücken im ATLAS SUSY-Programm auf. Diese sollten in Zukunft durch speziell optimierte Suchstrategien geschlossen werden.

Contents

1 Introduction **11**

2 The Standard Model and beyond **13**
2.1 The Standard Model of particle physics . . . 13
2.1.1 Quarks, leptons and their interactions . . . 13
2.1.2 The Higgs mechanism and electro-weak symmetry breaking . . . 16
2.1.3 Shortcomings of the Standard Model . . . 17
2.2 Supersymmetry . . . 20
2.2.1 Squarks, sleptons and gauginos . . . 20
2.2.2 R-parity . . . 21
2.2.3 Phenomenology . . . 23
2.2.4 Experimental constraints . . . 26

3 Experimental setup **29**
3.1 The Large Hadron Collider . . . 29
3.2 The ATLAS detector . . . 31
3.2.1 ATLAS coordinate system . . . 31
3.2.2 Tracking system . . . 32
3.2.3 Calorimeters . . . 33
3.2.4 Muon spectrometer . . . 35
3.2.5 Trigger system . . . 36
3.2.6 Simulated collision events . . . 36

4 Analysis basis **39**
4.1 General analysis strategy . . . 39
4.2 Data and Monte-Carlo samples . . . 42
4.2.1 Data samples . . . 42
4.2.2 Background samples . . . 42
4.3 Physics object identification and selection . . . 45
4.3.1 Primary vertex . . . 45
4.3.2 Jets and b-tagging . . . 45
4.3.3 Muons . . . 46
4.3.4 Electrons . . . 47
4.3.5 Missing transverse energy $E_{\mathrm{T}}^{\mathrm{miss}}$ . . . 49
4.4 Trigger strategy . . . 50
4.5 Event cleaning and preselection . . . 50

5 Z+jets+E_T^{miss} analysis 53
5.1 Motivation . . . 53
5.2 Analysis optimization . . . 55
5.3 Background estimation . . . 63
5.3.1 $Z+$jets background . . . 63
5.3.2 Flavour symmetric backgrounds . . . 76
5.3.3 Fake lepton backgrounds . . . 79
5.3.4 WZ/ZZ and rare top backgrounds . . . 82
5.3.5 Validation of the background estimate . . . 84
5.4 Systematic uncertainties . . . 86
5.4.1 Uncertainties of data-driven methods . . . 86
5.4.2 Experimental uncertainties . . . 88
5.4.3 Theoretical uncertainties . . . 89
5.5 Results of the Z+jets+E_T^{miss} analysis . . . 90
5.6 Validation of the results . . . 97
5.6.1 Events in the Z signal region . . . 98
5.6.2 Background prediction . . . 106
5.6.3 Physics objects . . . 115
5.7 Interpretation and conclusion . . . 126

6 $LQ\bar{D}$ reinterpretation of the 1-lepton+jets+E_T^{miss} analysis 129
6.1 The $LQ\bar{D}$ model . . . 129
6.2 Analysis overview . . . 133
6.3 Validation of the analysis assumptions . . . 135
6.3.1 Signal contamination of control regions . . . 137
6.3.2 Theoretical signal uncertainties . . . 138
6.4 Constraints on the $LQ\bar{D}$ model . . . 139
6.4.1 Results . . . 139
6.4.2 Combinations with other analyses . . . 142
6.5 Sensitivity of the signal selection to bRPV models . . . 146

7 Summary and Outlook 149

Bibliography 166

A Overview over the Monte-Carlo datasets 169

B Details about the GGM model 175

C Further plots on the $Z+$jets background 179

D Details about the events in the Z signal region 183

E Further cross-checks on the $E_{\mathrm{T}}^{\text{miss}}$ calibration 189

F Further results of the $LQ\bar{D}$ reinterpretation 195

1 Introduction

The Standard Model (SM) of particle physics describes the elementary constituents of matter and how they interact with each other. Its predictions have been tested in experiments with enormous precision. The most recent breakthrough was the discovery of the Higgs boson with a mass of $\sim$125 GeV by ATLAS [1] and CMS [2] in July 2012 in proton-proton (pp) collisions at CERN's Large Hadron Collider (LHC). The boson had been predicted by Peter Higgs and other theorists in the 1960s [3–8] as a consequence of the mechanism of spontaneous symmetry breaking, which explains how elementary particles acquire their mass. The Higgs boson was the last missing piece to complete the Standard Model and its observation was truly a milestone of modern physics.

However, there are good reasons why the completion of the SM is not the end of particle physics. A lot of fine tuning is needed to explain why the Higgs boson is relatively light although the loop corrections to its mass can become many orders of magnitude larger than the electro-weak scale. The unification of the three gauge interactions is not possible within the SM nor does it incorporate a quantum theory of gravity. It is known from astrophysical observations that about 95 % of the universe's energy content is not contained in ordinary matter but in dark matter and dark energy. The SM does not include an explanation for either of the two. New physics models are needed to solve the shortcomings of the SM.

One of the most promising and popular extensions of the SM is the framework of supersymmetry (SUSY) developed in the early 1970s [9–17]. It introduces a symmetry between fermions and bosons. Each SM particle gets a supersymmetric partner whose spin differs by a value of $\frac{1}{2}$. SUSY particles can cancel the loop contributions to the Higgs mass. Furthermore, SUSY can give guidance to the unification of forces. In many models, the lightest SUSY particle (LSP) is stable and only weakly interacting and therefore a candidate for the dark matter. If SUSY was an exact symmetry of nature the supersymmetric particles would have the same masses as their SM counterparts. No SUSY particles have been observed in any experiment so far which indicates that SUSY must be a broken symmetry. As little is known about the breaking mechanism and the mass spectrum of the new particles, the possible signatures of SUSY are very diverse.

This drives a plethora of searches for new physics at the LHC experiments. Besides the discovery of the Higgs boson, these are one of the main purposes why the LHC was built. With its unprecedented centre of mass energy, $\sqrt{s}$, and luminosity, $\mathcal{L}$, it offers excellent conditions to extend searches for new particles of masses up to the TeV scale and discover also very rare production processes. The ATLAS experiment whose data is used in this thesis is one of the general purpose detectors at the LHC. It is designed to cover a wide range of physics questions within and beyond the SM.

In this thesis, two analyses searching for signs of supersymmetric particles in the ATLAS dataset from 2012 are presented. Both focus on signatures of strongly interacting SUSY particles (squarks and gluinos) which involve electrons or muons in their decay chains. This offers the advantage that background from QCD processes is suppressed effectively by the lepton requirement and that leptons can be used to trigger possible signal events.

The first search targets models with SUSY breaking via General Gauge Mediation (GGM) with an higgsino-like lightest neutralino. This can decay into a Z boson and a gravitino with large branching fraction. The gravitino escapes the detector unobserved leading to an imbalance in the transverse momentum. In association with the leptonic decay modes of the Z boson and with highly energetic jets originating from squark or gluino decays, this provides a distinctive signal in the detector with intrinsically low background from SM processes. An existing ATLAS analysis has constrained the parameter space of the model already using a subset of 2012 data [18]. These results are extended to the full integrated luminosity of $\int \mathcal{L}\, dt = 20.3\,\text{fb}^{-1}$ recorded in pp collisions at $\sqrt{s} = 8\,\text{TeV}$ which means more than a tripling of the statistics available before.

The second analysis focuses on SUSY models with lepton-number-violating interactions via $LQ\bar{D}$ operators. Most searches for new physics are optimized for models where R-parity is conserved. Thus, the bounds on models with R-parity violation (RPV) can be significantly weaker or these models can be missed completely by the ATLAS SUSY search program. However, RPV interactions are well motivated in SUSY and experimental constraints can easily be fulfilled if only individual RPV couplings are set to zero. The already published results of a SUSY search in events with one isolated lepton, jets and missing transverse momentum [19] are used to constrain the parameter space of $LQ\bar{D}$ couplings in a systematic way. Two simplified models with squark and gluino production, respectively, are considered. There, coloured particles decay directly into the lightest neutralino which decays into a pair of jets and one lepton via the R-parity-violating interactions. These are the first limits on the $LQ\bar{D}$ model in case of prompt LSP decays from any ATLAS analysis.

2 The Standard Model and beyond

Many particle physicists regard the Standard Model as an effective theory for energies around the electro-weak scale at the order of 100 GeV. At higher energies, the effects of new physics beyond the Standard Model should become visible. This happens at the latest at the Planck scale $m_P \approx 10^{19}$ GeV where quantum effects of gravity start to play a role. There are many phenomena which could be explained by new physics at much lower scales of the order of $\sim$1 TeV and are thus in the reach of the LHC. One of the most popular theories beyond the Standard Model is the framework of supersymmetry which offers possible explanations for many of the shortcomings of the SM.

2.1 The Standard Model of particle physics

The Standard Model of particle physics describes the fundamental constituents of matter and how these elementary particles interact. It is implemented as a quantum field theory with three main ingredients [20]:

- Particle content, namely quarks and leptons.
- Interactions between these particles described by gauge theories and mediated by vector bosons.
- Electro-weak symmetry breaking via the Higgs mechanism which leads to non-vanishing particle masses.

2.1.1 Quarks, leptons and their interactions

The Standard Model contains twelve elementary fermions with spin $\frac{1}{2}$: Six quarks and six leptons [21]. The quarks carry fractional electric charge and can be grouped into three generations (or families) which will be motivated below. Up (u) and down (d) quarks belong to the first generation, charm (c) and strange (s) quarks form the second and top (t) and bottom (b) are quarks of the third generation. The quarks of each generation which are named first have an electric charge Q of $\frac{2}{3}$ (referred to as up-type quarks) while the other quarks have $Q = -\frac{1}{3}$ (down-type quarks). A baryon number of $\frac{1}{3}$ is assigned to each quark and a flavour quantum number is introduced to distinguish the different kind (=flavours) of quarks. For

	Q	I	I_3	c	s	t	b	mass [MeV]
up u	$+\frac{2}{3}$	$\frac{1}{2}$	$+\frac{1}{2}$	0	0	0	0	2.3
down d	$-\frac{1}{3}$	$\frac{1}{2}$	$-\frac{1}{2}$	0	0	0	0	4.8
charm c	$+\frac{2}{3}$	0	0	1	0	0	0	$1.3 \cdot 10^3$
strange s	$-\frac{1}{3}$	0	0	0	-1	0	0	95
top t	$+\frac{2}{3}$	0	0	0	0	1	0	$173.2 \cdot 10^3$
bottom b	$-\frac{1}{3}$	0	0	0	0	0	-1	$4.2 \cdot 10^3$

Table 2.1: Overview over the properties of all quarks in the Standard Model [22]. Q denotes the electric charge, while the flavour quantum numbers are given in the other columns and explained in more detail in the text.

the second and third generation, the flavour is labelled as the corresponding quark symbol, while up and down quarks are distinguished by their strong isospin I for historical reasons. They both have $I = \frac{1}{2}$ with the third component I_3 being positive for u quarks and negative for d.

Also the leptons can be divided into three generations with one charged and one neutral lepton each: The electron (e) and electron neutrino (ν_e), the muon (μ) and muon neutrino (ν_μ) and the τ lepton and τ neutrino (ν_τ). Electrons, muons and τ leptons have an electric charge of -1 while the three neutrinos are uncharged. A lepton flavour is assigned to each lepton generation, denoted as L_e, L_μ and L_τ, respectively. Each lepton has $L_i = 1$ for the lepton number of the corresponding family and 0 for the two other. An antiparticle exists for each fermion of the Standard Model which has the same properties as the particle but opposite charges and opposite baryon or lepton number.

There are three interactions between fermions in the SM: The strong, the electromagnetic and the weak force. Each interaction is introduced by requiring that the SM Lagrangian is invariant under local gauge transformations. This is only possible through the introduction of gauge bosons which have a spin of 1 and mediate the forces. A charge is connected with each gauge symmetry which governs how strongly the different fermions are affected by the corresponding interaction.

The theory describing the strong interaction is called quantum chromodynamcis (QCD) and is based on the symmetry group $SU(3)$. Only quarks interact via the strong force and carry the connected charge which is denoted as colour and can have three values (called red, green and blue). Antiquarks have an anticolour which has the value antired, antigreen or antiblue. The strength of the interaction is the same for all three charges and is governed by the strong coupling constant α_S.

The mediator of the strong interaction is the gluon which carries both colour and anticolour. This has two important implications. The first is colour confinement which describes the fact that α_S becomes large at low energy scales. As a consequence, quarks and gluons cannot exist as free particles at low energies but are always bound together to colourless states, the hadrons. This can happen in two ways. A quark and an antiquark with opposite colour charge can be bound to a meson or three (anti-)quarks with three different (anti-)colours can

	Q	L_e	L_μ	L_τ	mass [MeV]
electron e	-1	1	0	0	0.511
electron neutrino ν_e	0	1	0	0	≈ 0
muon μ	-1	0	1	0	106
muon neutrino ν_μ	0	0	1	0	≈ 0
τ lepton	-1	0	0	1	1777
τ neutrino ν_τ	0	0	0	1	≈ 0

Table 2.2: Overview over the properties of all leptons in the Standard Model [22]. Q denotes the electric charge, while the lepton flavour quantum numbers are given in the other columns and explained in more detail in the text. The masses of the neutrinos are much smaller than the masses of the other SM fermions. An upper bound on the sum of all three neutrino masses can be obtained from astrophysical experiments and is $\sum_{i=1}^{3} m_{\nu_i} < 0.66\,\text{eV}$.

form a (anti-)baryon. Due to colour confinement, no free quarks or gluons can be detected experimentally. Instead, they hadronise into colourless objects shortly after their production. The only exception is the top quark which decays before hadronisation due to its large mass. In high energy experiments, the hadrons form a collimated beam of particles boosted in the direction of the original quark or gluon. This typical signature of strongly interacting particles is called jet.

The second important effect of QCD is the asymptotic freedom. The coupling constant α_S is small for large scales and quarks and gluons can be treated as free particles at high energies. The value of α_S is of the order of 0.1 for interactions at a scale around 100 GeV to 1 TeV [22] while it is of the order of 1 for scales below ~1 GeV [23] where processes of the strong interaction cannot be calculated perturbatively anymore. Quarks and gluons are commonly referred to as partons.

The electromagnetic and weak forces can be described by the unified $U(1) \times SU(2)_L$ gauge group and are collectively referred to as the electro-weak interaction. The invariance of the SM Lagrangian under these gauge transformations is ensured by the introduction of four gauge fields: B_μ for the $U(1)$ group and W_μ^i $(i = 1, 2, 3)$ for $SU(2)_L$. The hypercharge Y and the weak isospin T, respectively, are the quantum numbers connected to the two gauge groups. As indicated by the subscript “L”, the electro-weak interaction is a chiral symmetry. Only the left-handed component of the fermion fields is influenced by the interaction with the three gauge fields W_μ^i, while the right-handed component is not affected. The left- and right-handed components, Ψ_L and Ψ_R, are obtained from the Dirac spinor Ψ of the fermion fields by applying the projection operators P_L and P_R to them:

$$P_L\,\Psi = \frac{1-\gamma^5}{2}\,\Psi = \Psi_L\,, \qquad\qquad P_R\,\Psi = \frac{1+\gamma^5}{2}\,\Psi = \Psi_R\,, \tag{2.1}$$

where γ^5 is the product of the four Dirac matrices multiplied by an imaginary unit. The left-handed components of the two fermion fields of the i-th generation are comprised in $SU(2)$

doublets

$$\begin{pmatrix} \nu_i \\ \ell_i \end{pmatrix} , \begin{pmatrix} u_i \\ d'_i \end{pmatrix} , \tag{2.2}$$

where ν (ℓ) refers to the neutral (charged) leptons and u_i (d_i) denotes the up-(down-)type quarks. The two particles of a generation can be regarded as up and down states of the weak isospin with values of $\pm\frac{1}{2}$ for its third component T_3. The $SU(2)_L$ "flips" the weak isospin and converts the particles within one generation into each other. As indicated by the d'_i in the lower component of the quark doublets, the eigenstates of the electro-weak interactions are not identical to the quark mass eigenstates with a characteristic flavour. The electro-weak eigenstates d'_i are a superposition of the mass eigenstates and the mixing is given by the CKM matrix.

As already indicated at the beginning of the Sec. 2.1, the electro-weak symmetry is broken spontaneously by the Higgs mechanism to the electromagnetic and the weak interaction. The Higgs mechanism will be explained in more detail in the next section. The electromagnetic force acts only on charged particles while the weak force affects all fermions. After symmetry breaking, only the electric charge Q is a conserved quantum number. It is related to the charges of the unbroken symmetries through the Gell-Mann-Nishijima equation [21]:

$$Q = T_3 + \frac{Y}{2} \, . \tag{2.3}$$

Besides the charges, there are other conserved quantum numbers in the Standard Model. The total baryon and lepton numbers, B and L, are constant in all processes as well as the lepton numbers for the individual generations. The quark flavour, on the other hand, is only conserved in processes of the strong and electromagnetic interaction while the weak interaction can change it as discussed above. The properties of all SM quarks and leptons are summarised in Tab. 2.1 and 2.2, respectively.

2.1.2 The Higgs mechanism and electro-weak symmetry breaking

Explicit mass terms in the Lagrangian of the Standard Model are forbidden for two reasons [24]. First, the mass terms for the gauge bosons would break the gauge symmetry. Second, the mass terms for the fermions would mix right-handed and left-handed components and thus violate the chiral symmetry of the electro-weak interaction. Therefore, all fermions and bosons must be massless a priori. This entirely contradicts the experimental observations as most of the SM particles have masses different from 0 (compare Tab. 2.1, 2.2 and 2.3). The conflict can be solved by the Higgs mechanism. Its basic idea is to generate particle masses via spontaneous symmetry breaking. The Lagrangian fulfils all symmetries of the theory but the vacuum (i.e. the state of lowest energy) is not symmetric. This can be achieved by adding a $SU(2)$ doublet Φ (referred to as the Higgs doublet) with two scalar complex fields Φ^+ and Φ^0 as components to the Lagrangian. Spontaneous symmetry in its simplest form occurs if the potential V for Φ has the structure [25]:

$$V(\Phi) = \mu^2 \, \Phi^\dagger \Phi + \lambda \, (\Phi^\dagger \Phi)^2 \, . \tag{2.4}$$

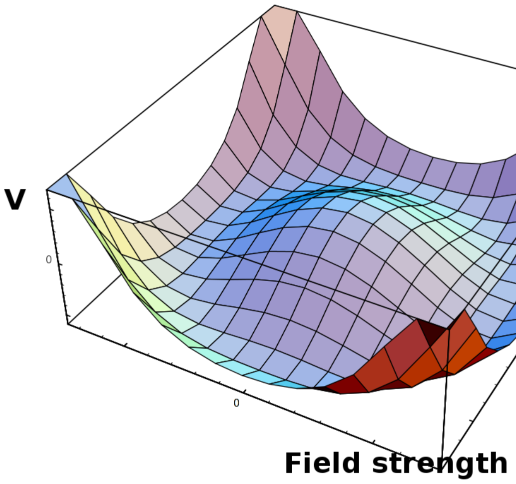

Figure 2.1: Illustration of the Higgs potential V from Eq. (2.4) [24].

For $\mu^2 < 0$, the potential itself is symmetric while the vacuum state is not at $\Phi = 0$ and therefore not symmetric. Instead, the potential has its minimum at a non-vanishing vacuum expectation value (VEV), $\langle\Phi\rangle$, for the Higgs field. A three-dimensional illustration of the Higgs potential is shown in Fig. 2.1. V is symmetric under rotations around the z-axis in this sketch, but has its minimum at values where the field strength is not 0. The particle masses are generated via interactions of the fermion/boson fields with the Higgs field and the coupling between them is proportional to the mass of the particle.
The four gauge fields of the electro-weak interaction B_μ and W^i_μ $(i = 1, 2, 3)$ mix and form four gauge bosons. The superposition of the charged W_1 and W_2 fields leads to the $W^\pm$ bosons, while the superposition of the two neutral B and W_3 fields gives two neutral bosons, W^0 and B^0. After electro-weak symmetry breaking, the $W^\pm$ and the W^0 acquire mass and can be recognized as the massive $W^\pm$ and Z bosons observed in the experiment. The B^0 remains massless and can be identified as the photon. The gluon is not affected by the symmetry breaking and remains massless. The two complex components of the Higgs doublet have four degrees of freedom. Three of them are absorbed in the longitudinal polarisation modes of the three massive gauge bosons. The fourth degree of freedom manifests itself as a new massive particle with spin 0, the Higgs boson. It acquires its mass via the λ term of the potential in Eq. (2.4) which is called the Higgs self-coupling. The properties of the SM bosons are summarised in Tab. 2.3.

2.1.3 Shortcomings of the Standard Model

The Standard Model has been tested with enormous precision and almost all experimental results are compatible with the theoretical predictions. Still, the SM has experimental and theoretical shortcomings and new theories beyond the SM are necessary to resolve them.
The mass of the Higgs bosons M_H was measured to be $125.09 \pm 0.21(\text{stat.}) \pm 0.11(\text{syst.})$ GeV [26] by the ATLAS and CMS experiments at the LHC. This value has important implica-

Gauge bosons				
	Q	S	Γ [GeV]	mass [GeV]
$W^{\pm}$ boson	± 1	1	2.1	80.4
Z boson	0	1	2.5	91.2
photon γ	0	1	0	0
gluon g	0	1	0	0
Higgs bosons				
Higgs H	0	0	unknown	125.7

Table 2.3: Overview over the properties of all bosons in the Standard Model [22]. Q denotes the electric charge of the particle, S its spin and Γ the decay width.

tions for the mechanism of spontaneous symmetry breaking as M_H is connected to the other parameters of the electro-weak sector (e.g. the masses of the W and Z bosons). For theoretical reasons, the Higgs boson mass can be neither too large nor too small to ensure the validity of the theory [25]. This can be seen in Fig. 2.2. There, the upper and lower bound on M_H is shown depending on the energy scale Λ where new physics effects start to play a role. The upper bound comes from the requirement that the Higgs self-coupling parameter λ in Eq. (2.4) should remain finite when loop corrections are taken into account. The lower bound is connected to the fact that λ has to be positive to ensure that the Higgs potential has a minimum and thus a stable vacuum. It can be seen that the allowed range for M_H is only between ~160 GeV and ~180 GeV if the Standard Model shall be valid up to the Planck scale. The experimental value of M_H is in the uncertainty band of the lower bound and it remains unclear if new physics is needed to ensure the consistency of the theory.

Another weakness of the Standard Model is called the hierarchy problem and is due to the fact that the mass of a scalar particle obtains divergent corrections from loop diagrams as shown in Fig. 2.3. The corrections to the mass squared depend quadratically on the cut-off scale Λ. As the Higgs mass is rather low, this scale must either be close to M_H itself or the corrections must be cancelled by a new symmetry.

In the SM, the electromagnetic and weak interaction can successfully be united in the electroweak theory. The question naturally arises if this is also possible for the strong force. A grand unified theory (GUT) beyond the SM might explain all three interactions by one superior gauge group [20]. This could also guide the way to the integration of the gravitational force into the framework of gauge theories. It possibly also leads to an explanation of the apparent symmetry between the quarks and leptons of the Standard Model.

There are also experimental results which cannot be explained by the Standard Model. It is known from different astrophysical observations that only about 5 % of the universe's energy content is comprised in the known matter while dark matter and dark energy contribute about 27 % and 68 %, respectively (compare e.g. [27]). Dark matter constituents have not been detected directly but can only be seen indirectly via their gravitational interaction. The Standard Model does not contain a particle candidate for the dark matter nor an explanation

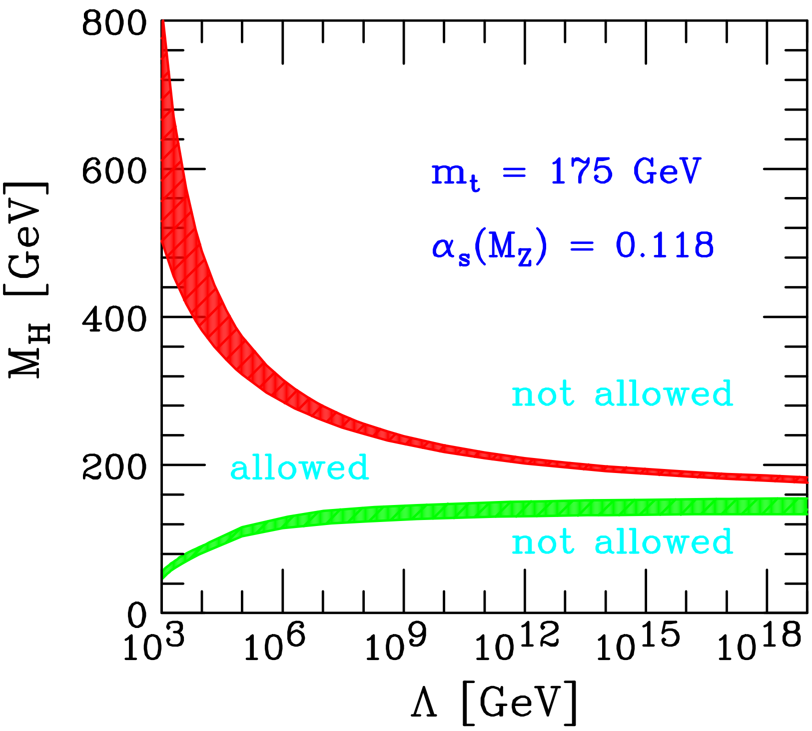

Figure 2.2: Upper and lower bound on the Higgs mass M_H as a function of the new physics scale Λ [25]. The top mass m_t was set to 175 GeV and α_S at the mass of the Z boson to 0.118 ± 0.002. The widths of the shaded bands indicate the impact of theoretical uncertainties on the bounds.

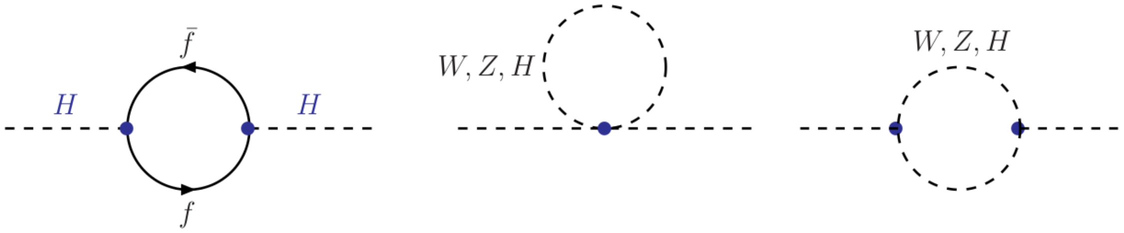

Figure 2.3: Loop corrections to the Higgs mass from the coupling between fermions and the Higgs (left) as well as from the interaction of the Higgs field with the W and Z boson or from the Higgs self-coupling (middle and right) [25].

for the dark energy.

Another experimental weakness of the Standard Model is that neutrinos are treated as massless although it is known from neutrino oscillation data that at least two of the three neutrino generations must have a small but non-zero mass [28]. The sum of the masses of all three neutrinos $\sum_{i=1}^{3} m_i$ is bound to be smaller than 0.66 eV [22]. This is not a real problem of the SM, of course, as neutrino masses can be generated via the introduction of right-handed neutrinos and the Higgs mechanism as for the other fermions. The question which remains open is why the neutrinos are so much lighter than the other particles. Neutrinos are the only known neutral elementary fermions and can in principle be Majorana particles which means that they are their own antiparticles. As a result, Majorana mass terms are allowed for them in the Lagrangian. These can arise through the seesaw mechanism [29] which introduces new heavy right-handed neutrinos and leads to a natural explanation for the smallness of the masses of the three known neutrinos.

2.2 Supersymmetry

Supersymmetry is one of the most popular and promising extensions of the Standard Model and can address many of the open questions discussed in Sec. 2.1.3. It provides a rich phenomenology which can be tested at the LHC experiments. SUSY introduces a new symmetry between fermions and bosons and predicts supersymmetric partners for all SM particles whose spin differs by a value of $\frac{1}{2}$ [30]. The interactions and couplings of the SUSY particles are identical to their SM partners. Therefore, loops with supersymmetric particles cancel the divergences in the corrections to the Higgs mass and can solve the hierarchy problem [31–36].

The minimum supersymmetric extension of the Standard Model (MSSM), which is the SUSY model with the minimum number of new particles necessary for a consistent theory, predicts that the coupling strengths of the three gauge groups approach the same value at energy scales around 10^{16} GeV, where the unification of forces is expected to happen. This is not the case in the Standard Model as it can be seen from Fig. 2.4. Hence, SUSY might give guidance about how to unify the three interactions in a GUT and even how to include gravity as well (compare Sec. 2.2.3). Furthermore, the lightest SUSY particle is stable and only weakly interacting in many models and thus a dark matter candidate [37,38].

2.2.1 Squarks, sleptons and gauginos

SUSY introduces scalar partners for the quarks and leptons which are called squarks and sleptons, respectively. The gauge bosons get fermionic counterparts, the gauginos with spin $\frac{1}{2}$. SUSY particles and their SM partners are contained in the same multiplet of the symmetry group (referred to as supermultiplets).

In supersymmetric model at least two Higgs doublets are needed: One which couples to up-type quarks (components H_u^0 and H_u^+) and one which couples to down-type quarks (components H_d^0 and H_d^+). The ratio of their VEVs is denoted as $\tan\beta$. All Higgs fields get supersymmetric partners which are called higgsinos.

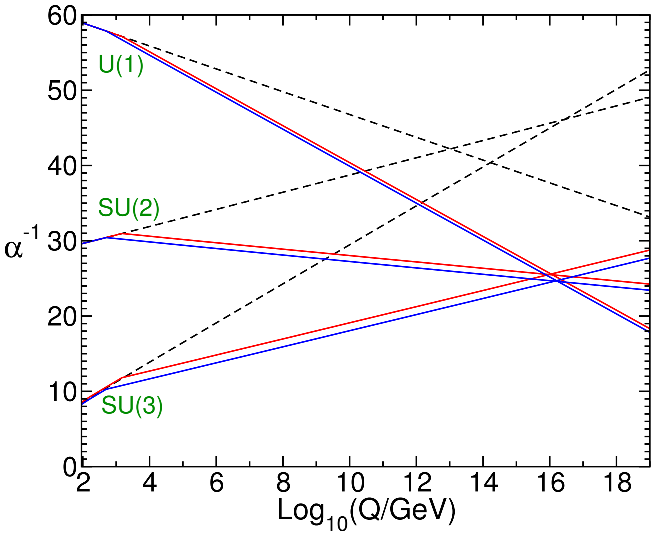

Figure 2.4: Dependency of the couplings of the three gauge groups on the process scale Q in the SM (black dashed lines) and the MSSM (coloured solid lines) [30]. Red and blue correspond to two different hypothetical mass spectra.

No supersymmetric particles have been observed so far, so SUSY must be a broken symmetry and the SUSY particles must be heavier than their SM partners. The physical particles (i.e. the mass eigenstates) are superpositions of all gauge eigenstates which are not distinguishable by any observable quantum number. The mixing is assumed to be negligible for the left- and right-handed components of the squarks and sleptons of the first and second generation. The mass eigenstates of the sbottom and stop quarks are denoted $\tilde{b}_1$, $\tilde{b}_2$ and $\tilde{t}_1$, $\tilde{t}_2$, respectively. The five degrees of freedom of the two Higgs doublets, which are not transferred into the longitudinal polarisation modes of the massive gauge bosons, lead to three neutral and two charged massive Higgs particles, called h^0, H^0, A^0 and $H^{\pm}$. The charged components of the SUSY Higgs fields mix with the superpartners of the $W^{\pm}$ fields to the four charginos $\tilde{\chi}_1^{\pm}$ and $\tilde{\chi}_2^{\pm}$ where the lighter states gets the index "1". The mixing of the neutral supersymmetric Higgs fields and the SUSY partners of the B^0 and W^0 fields gives the four neutralinos $\tilde{\chi}_1^0$, $\tilde{\chi}_2^0$, $\tilde{\chi}_3^0$ and $\tilde{\chi}_4^0$ (ordered according to increasing mass). Depending on which of the components makes the dominant contribution to a specific neutralino, they are referred to as higgsino-like, bino-like or wino-like. The SUSY partners of the gluons are the gluinos. An overview over all SUSY particles is given in Tab. 2.4. The symbols for them are the same as for the SM particles but with a "$\sim$" above.

2.2.2 R-parity

In the Standard Model, no baryon and lepton number violating interactions occur in the Lagrangian and baryon or lepton number violating processes have never been observed experimentally. However, B and L conservation seem to be "accidental" conservation laws of nature as they are not caused by some underlying symmetry. In the superpotential W, which

	S	Gauge eigenstates	Mass eigenstates
Higgs bosons	0	H_u^0, H_u^+, H_d^0, H_d^+	h^0, H^0, A^0, $H^\pm$
Squarks	0	$\tilde{u}_L$, $\tilde{u}_R$, $\tilde{d}_L$, $\tilde{d}_R$	same
	0	$\tilde{c}_L$, $\tilde{c}_R$, $\tilde{s}_L$, $\tilde{s}_R$	same
	0	$\tilde{t}_L$, $\tilde{t}_R$, $\tilde{b}_L$, $\tilde{b}_R$	$\tilde{b}_1$, $\tilde{b}_2$, $\tilde{t}_1$, $\tilde{t}_2$
Sleptons	0	$\tilde{e}_\mathrm{L}$, $\tilde{e}_\mathrm{R}$, $\tilde{\nu}_e$	same
	0	$\tilde{\mu}_\mathrm{L}$, $\tilde{\mu}_\mathrm{R}$, $\tilde{\nu}_\mu$	same
	0	$\tilde{\tau}_\mathrm{L}$, $\tilde{\tau}_\mathrm{R}$, $\tilde{\nu}_\tau$	$\tilde{\tau}_1$, $\tilde{\tau}_2$, $\tilde{\nu}_\tau$
Neutralinos	$\frac{1}{2}$	$\tilde{B}^0$, $\tilde{W}^0$, $\tilde{H}_u^0$, $\tilde{H}_d^0$	$\tilde{\chi}_1^0$, $\tilde{\chi}_2^0$, $\tilde{\chi}_3^0$, $\tilde{\chi}_4^0$
Charginos	$\frac{1}{2}$	$\tilde{W}^\pm$, $\tilde{H}_u^+$, $\tilde{H}_d^+$	$\tilde{\chi}_1^\pm$, $\tilde{\chi}_2^\pm$
Gluinos	$\frac{1}{2}$	$\tilde{g}$	same

Table 2.4: Overview over the particles which are new in supersymmetric models with respect to the Standard Model [30]. The indices L and R refer to the left-handed and right-handed components of the fields. Neutrinos are treated as massless in the SM and thus do not have right-handed components. Therefore the index is omitted for them. S denotes the spin of a particle.

describes the particle interactions in SUSY models, B and L number violating terms are in principle allowed. In its most general form, four different operators can be added to W which violate either B or L (labelled as $\not{B}$ and $\not{L}$, respectively):

$$W_{\not{B}} = \frac{1}{2}\lambda''_{ijk}\bar{U}_i\bar{D}_j\bar{D}_k\,, \tag{2.5}$$

$$W_{\not{L}} = \frac{1}{2}\lambda_{ijk}L_iL_j\bar{E}_k + \frac{1}{2}\lambda'_{ijk}L_iQ_j\bar{D}_k + \epsilon_iL_iH_u\,, \tag{2.6}$$

where $\bar{U}$, $\bar{D}$ and $\bar{E}$ denote the right-handed supermultiplets for up-type quarks, down-type quarks and leptons, respectively. L and Q indicate the left-handed supermultiplets for leptons and quarks. The parameters λ_{ijk}, λ'_{ijk}, λ''_{ijk} and ϵ_i are new coupling constants governing the strength of the baryon or lepton number violation. The indices i, j, k refer to the lepton and quark flavour and can thus have the values $1, 2, 3$.

B and L number violating processes are allowed by the new operators in Eq. (2.5) and (2.6) but highly constrained by experimental results. Processes like the proton decay are possible via diagrams as shown in Fig. 2.5. To fulfil experimental bounds (e.g. on the proton lifetime of $\tau_p > 10^{31}$ to 10^{33} years [22]), the B and L violating couplings are forbidden in many SUSY models by the requirement of R-parity conservation (RPC). The R-parity is defined as

$$R = (-1)^{3B+L+2S}\,, \tag{2.7}$$

where S is the spin. The R-parity is +1 for all SM particles and -1 for SUSY particles. In case of RPC, SUSY particles cannot decay into final states with SM particles only and thus

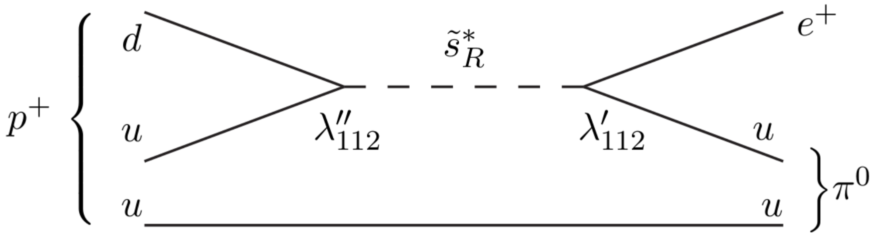

Figure 2.5: Decay of the proton into a positron and a neutral pion via the two R-parity-violating couplings λ''_{112} and λ'_{112} mediated by a virtual strange squark [30].

the lightest SUSY particle is stable.

In models with R-parity violation, experimental limits can be satisfied when only some of the L and B violating operators are forbidden or suppressed, while the other λ_{ijk}, λ'_{ijk}, λ''_{ijk} or ϵ_i couplings get a value different from zero. The LSP is not stable anymore in RPV models but decays into Standard Model particles. This has important implications for the expected phenomenology (see next section) [39–43].

The $\bar{U}\bar{D}\bar{D}$ operator from Eq. (2.5) as well as the $LL\bar{E}$ and $LQ\bar{D}$ terms from Eq. (2.6) are referred to as trilinear R-parity violation. Typical experimental constraints on the trilinear RPV parameters are of the order of $[\lambda_{ijk}, \lambda'_{ijk}, \lambda''_{ijk}] < [\mathcal{O}(10^{-1}) - \mathcal{O}(10^{-2})] \times \frac{\bar{m}}{100\,\mathrm{GeV}}$ (with $\bar{m}$ being the average mass scale of the new particles) when it is assumed that a single coupling dominates [44]. Concrete limits on individual couplings or on combinations of different terms are model-dependent.

The last term in Eq. (2.6) is called bilinear R-parity violation (bRPV). In bRPV models, the neutrinos can acquire a mass via neutrino-neutralino mixing [45–47]. These models provide a connection between RPV SUSY and the experimental results from neutrino oscillation measurements. Therefore, the ϵ_i couplings can be constrained by current neutrino data, which will be discussed further in Sec. 6.5.

2.2.3 Phenomenology

SUSY models provide a rich phenomenology as little is known about the exact properties of the new particles. Depending on the SUSY mass spectrum and whether R-parity is conserved or violated, the possible signatures of SUSY at the LHC can be very diverse. If strongly interacting SUSY particles (i.e. squarks and gluinos) are accessible at the LHC, the cross-sections for their production can be of the order of 10 pb and approach cross-sections of comparable SM processes like $t\bar{t}$ production with a cross-section of 260 pb [48]. This can be seen in Fig. 2.6.

If SUSY offered a solution of the hierarchy problem discussed in Sec. 2.1.3, at least the masses of the third generation squarks should not be larger than ~1 TeV. The top quarks make the biggest contribution to the loop corrections of the Higgs mass as the couplings of the top quark to the Higgs field is the strongest in the SM due to the large top quark mass. Therefore, the stops cannot be much heavier than their SM partners to cancel the contributions to the Higgs mass without much fine tuning. Models which are motivated by a solution of

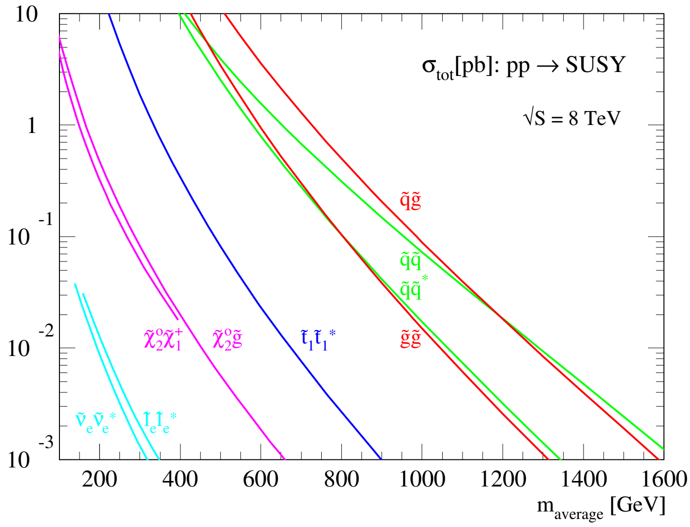

Figure 2.6: SUSY cross-sections for different production modes depending on the average mass of the involved particles calculated with PROSPINO [49]. The values are for proton-proton collisions at $\sqrt{s} = 8$ TeV [50].

the hierarchy problem often contain light stop and/or sbottom quarks [51, 52]. Models with light third generation squarks are referred to as natural SUSY. If only these two squarks can be produced at the LHC, the cross-section for the production of SUSY particles will be an order of magnitude smaller compared to the gluino or first/second generation squark production at the same mass scale. This can also be seen in Fig. 2.6. If all strongly interacting SUSY particles are too heavy to be produced, weakly interacting supersymmetric particles like neutralinos, charginos and sleptons can still be within the LHC reach. In this case, the production cross-section would decrease further as shown in the same figure for comparison. This thesis mainly focuses on the strong production of SUSY particles as a wide gluino and squark mass range can be investigated with the dataset collected in the 2012 run of the LHC. The squarks and gluinos decay into other real or virtual SUSY particles under the emission of quarks and gluons. These SUSY particles then decay further until the decay chain reaches the LSP which is only weakly interacting in many models (e.g. the lightest neutralino $\tilde{\chi}_1^0$). This is motivated by the fact that it is thus a possible dark matter candidate. In RPC models, the LSP is stable and escapes detection leading to a large momentum imbalance (denoted as missing energy). In contrast, the LSP can decay inside the ATLAS volume which leads to reduced missing energy and a higher lepton and/or jet multiplicity in the final state if the R-parity is violated.

Final states with many jets are typical signatures of new strongly interacting particles. Leptons can arise from the decays of W bosons, Z bosons or intermediate sleptons in the SUSY decay chains. The analyses presented in this thesis search for SUSY in signatures involving electrons or muons. These offer the advantage that the QCD multijet background can be suppressed efficiently and the leptons can be used to trigger possible signal events. Two typical signatures of SUSY processes targeted by the analyses in this thesis are shown in Fig. 2.7.

The expected signatures at the LHC can be predicted if a specific model of SUSY breaking is adopted. This can be implemented in two principle ways: Full phenomenological models

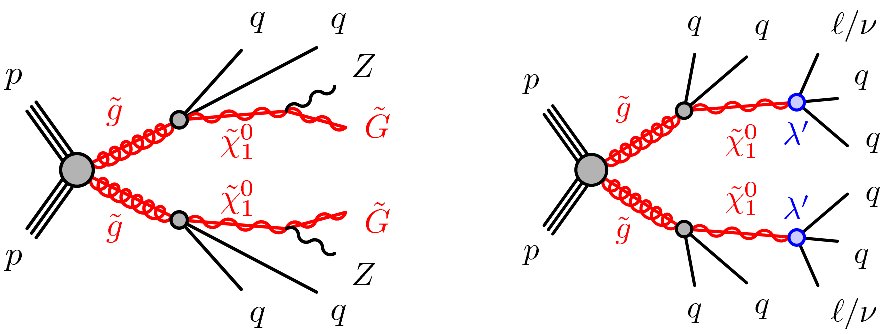

Figure 2.7: Examples for the production of SUSY particles (gluinos in this case) and their subsequent decays into the LSP. The diagram on the left shows a RPC model where the LSP is a stable $\tilde{G}$ which escapes undetected [53]. A RPV model where the $\tilde{\chi}_1^0$ LSP decays into SM particles is shown on the right side [54].

assume that the large amount of new free parameters in the MSSM at the electro-weak scale (124 new masses and mixing angles in total [20]) can be derived from a small set of unified parameters at a much higher scale. In contrast, the masses of the SUSY particles are fixed "by hand" in simplified models [55, 56], usually assuming that only a few new particles can be produced at the LHC and setting the mass of the others so high that they are effectively decoupled. Both approaches to implement a specific SUSY model are used in this thesis and the models are explained here briefly.

General Gauge Mediation

General Gauge Mediation [57, 58] is a full phenomenological model and assumes that SUSY breaking occurs in a hidden sector decoupled from the SM interactions. The effects of SUSY breaking are transferred from the hidden sector to the visible sector by messenger particles. GGM incorporates also gravity and contains therefore a graviton as the mediator of the gravitational force as well as its superpartner, the gravitino $\tilde{G}$ with spin $\frac{3}{2}$ [20].
In GGM, the messenger of SUSY breaking is a heavy particle with a mass so high that it could not be discovered in any experiment so far. It carries the charges of the Standard Model gauge groups and interacts with the visible sector via normal gauge interactions. In addition, it must have a new coupling to interact also with the hidden sector. A light gravitino is typically the LSP in GGM models. The next-to-lightest SUSY particle (NLSP) governs the phenomenology. It is a higgsino-like $\tilde{\chi}_1^0$ in the implementation of GGM used in this thesis. More specific details can be found in Sec. 5.1.

Constrained MSSM

The other full SUSY model considered here is the constrained MSSM (cMSSM) [59–64]. In the cMSSM, SUSY breaking is mediated from the hidden to the visible sector via gravity. The $\tilde{\chi}_1^0$

is typically the LSP. Both in GGM models as well as in the cMSSM, the gluinos and squarks of the first and second generation are typically considerably heavier than the charginos and neutralinos. This leads to decay chains with several intermediate steps.

Simplified models

Also simplified models try to reduce the number of free parameters of the MSSM to a manageable amount and are used in many ATLAS and CMS searches as benchmark models (e.g. [19]). They usually assume that only one production mode is accessible at the LHC and all other SUSY particles are so heavy that their effects on the expected signatures can be neglected. Also only one decay mode is normally open for the SUSY particles. The advantage is that the model remains simple. The results can be easily compared to other experiments and mass limits can be applied to other SUSY models involving the production and decay modes of the simplified model. In contrast to GGM and the cMSSM, simplified models do not contain any assumptions on the underlying theory of the SUSY breaking mechanism.

In this thesis, two simplified models are considered, one with squark and one with gluino production. In both models, the strongly interacting particles decay directly into the $\tilde{\chi}_1^0$ LSP which decays into SM particles via R-parity-violating couplings. More details about the implementation of the simplified models are presented in Sec. 6.1.

Phenomenological MSSM

Simplified models do not provide any insight into the mechanism of SUSY breaking while the parameter space of full phenomenological models, like GGM and the cMSSM, might be already too constrained by current experimental results (see next section). The phenomenological MSSM (pMSSM) [65, 66] serves as a compromise between the two approaches. Experimental bounds are used to reduce the number of free parameters from 124 in the MSSM to 19 in the pMSSM. In this thesis, pMSSM models with a natural mass spectrum are used which means that the stop quarks are light. Details about the precise implementation are given in Sec. 6.5.

2.2.4 Experimental constraints

The variety of possible SUSY models and mass spectra becomes apparent from the vast search program of ATLAS and CMS as well as from the different analysis approaches presented in this thesis. The searches for SUSY at the LHC have constrained the allowed mass range for new particles significantly. Current results of some ATLAS analyses are summarised in Fig. 2.8. It can be seen that gluino masses up to ∼1.3 TeV are excluded in general. Limits on stops and sbottoms extend up to masses of ∼600 GeV. The mass limits on direct chargino, neutralino and slepton production are usually of the order of ∼500 GeV.

However, it has to be noted that the exclusion limits depend on the specific SUSY model

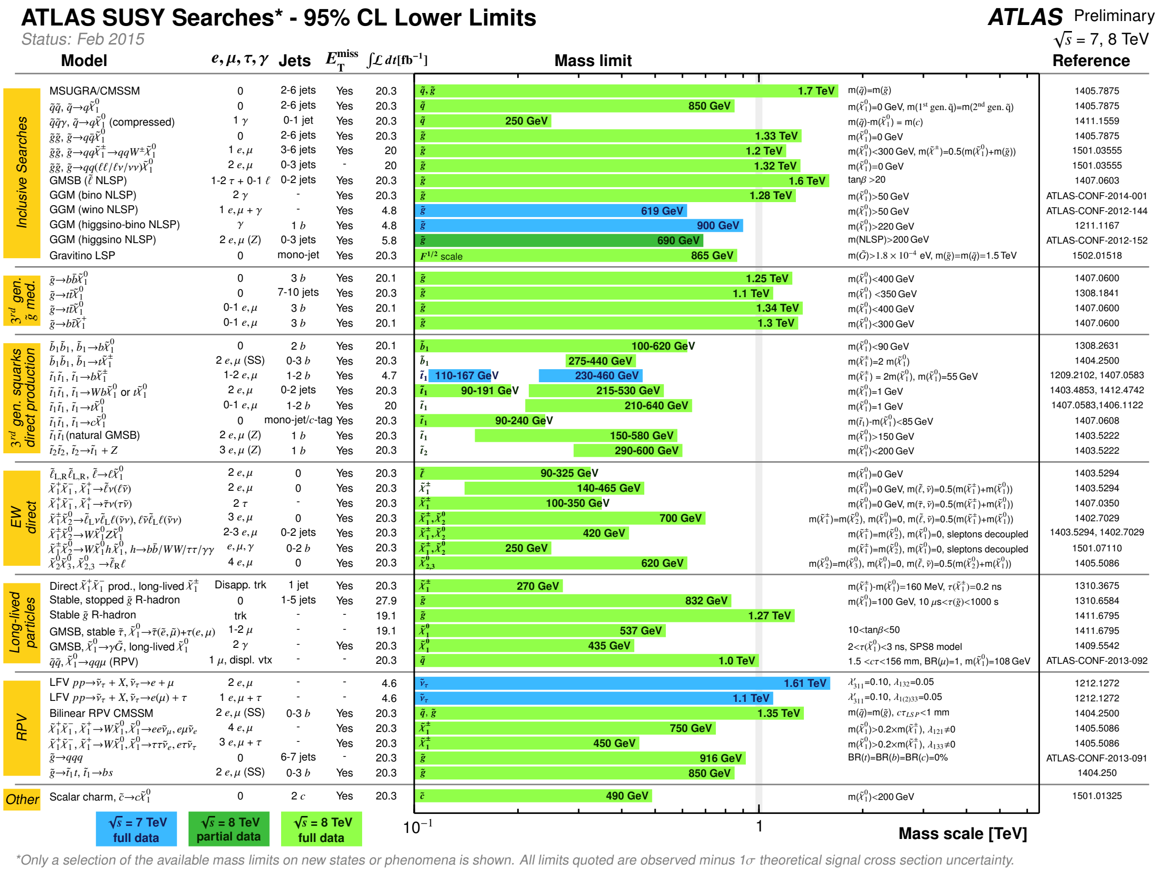

Figure 2.8: Overview of the mass limits for different SUSY particles obtained from various ATLAS SUSY searches [67]. The exclusion bounds depend on the specific SUSY model under study. Previous gluino mass limits in case of the GGM model with a higgsino-like $\tilde{\chi}_1^0$ as NLSP, which is the main target model of the analysis discussed in Sec. 5, are of the order of 690 GeV and shown in dark green.

considered in the interpretation of the results. For the GGM model, which the main analysis presented in this thesis is targeting, gluino masses below 690 GeV were already excluded by a search using about one third of the 2012 ATLAS dataset with an integrated luminosity of 5.8 fb^{-1} [18] (see also Fig. 2.8). The analysis discussed in Sec. 5 extends the results by including the full integrated luminosity of 20.3 fb collected by ATLAS in 2012.

Some SUSY models with very distinctive signatures might be only accessible with dedicated analyses or might even be missed completely by the ATLAS SUSY search program. This can be due to long-lived particles with displaced decay vertices or due to R-parity-violating couplings leading to signatures with reduced missing energy. An example for the latter case is discussed in Sec. 6.

SUSY is not only constrained by the results from direct searches for new particles. Indirect bounds can be derived from the results of flavour physics. Quarks can change their flavour via the electro-weak interaction (compare Sec. 2.1.1). Some of these processes are highly suppressed in the SM and could be enhanced in SUSY models. One example is the decay of the B_s^0 meson which consists of s and d quarks. Its decay into $\mu^+\mu^-$ is only allowed via a loop process and has a very small branching fraction in the SM. It can be enhanced if new particles additionally contribute to the loop. The LHCb and CMS experiments have measured the branching fraction of the $B_s^0 \to \mu^+\mu^-$ decay to be $2.9^{+1.1}_{-1.0} \cdot 10^{-9}$ [68] and $3.0^{+1.0}_{-0.9} \cdot 10^{-9}$ [69], respectively, which is in agreement with the SM prediction. Therefore, the contribution of SUSY particles to flavour changing processes like the B_s^0 decay must be small.

Other constraints on SUSY can be derived from dark matter experiments as summarised in [22]. These can exclude cross-sections above $\sim 10^{-6}$ fb for the interaction of dark matter particles with the nuclei of ordinary matter for masses of the dark matter candidate above ~ 10 GeV.

3 Experimental setup

The analyses presented in this thesis use data recorded by the ATLAS experiment in proton-proton collisions at the LHC. The dataset was collected during the 2012 data taking period at a centre of mass energy of $\sqrt{s} = 8\,\text{TeV}$ and corresponds to an integrated luminosity of $\int \mathcal{L}\,dt = 20.3\,\text{fb}^{-1}$.

3.1 The Large Hadron Collider

CERN's Large Hadron Collider is a circular collider with a circumference of 26.7 km located in the area of Geneva, Switzerland [70]. Two particle beams orbit in the clockwise and anti-clockwise direction, respectively, and collide in four dedicated interaction points. Protons as well as lead ions can be filled into the LHC. The centre of mass energy for *pp* collisions was $\sqrt{s} = 7$ TeV at the beginning of LHC's run-I in 2010 and 2011 and was raised to 8 TeV in 2012. The beam energy is increased to 13 – 14 TeV in run-II of the LHC which has started in spring 2015. The beams are kept on their orbits by 1232 superconducting dipole magnets with a field of more than 8 T. Additional dipole as well as quadrupole and sextupole magnets are necessary to guide and focus the beams.
Before the protons are filled into the LHC at a injection energy of 450 GeV, they are pre-accelerated by a linear accelerator (LINAC) and by different smaller synchrotrons (Booster, PS and SPS). CERN's complete accelerator complex can be seen in Fig. 3.1 where also some accelerators not involved in the LHC operation are shown. The protons circulated in the LHC in 1374 bunches of $1.6 - 1.7 \cdot 10^{11}$ particles each during 2012 run conditions [72]. The distance between two proton bunches was 50 ns time-wise. This resulted in a peak instantaneous luminosity of $7.7 \cdot 10^{33}\,\text{cm}^{-2}\text{s}^{-1}$ and was close to LHC's design luminosity of $10^{34}\,\text{cm}^{-2}\text{s}^{-1}$.
The products of the particle collisions are detected by four major experiments built around the interaction points of the LHC and also shown in Fig. 3.1. They are accompanied by three smaller experiments which make use of the collision data at one of the four interaction points. The seven LHC experiments are:

- ATLAS [73] is one of the multi-purpose detectors of the LHC and was designed to perform a plethora of physics analyses ranging from the search for the Higgs boson, over Standard Model measurements to the hunt for new physics. This thesis is carried out with ATLAS data and the design of the detector is described in detail in Sec. 3.2.

- CMS [74] is the other multi-purpose detector and targets the same physical questions like ATLAS but differs slightly in design.

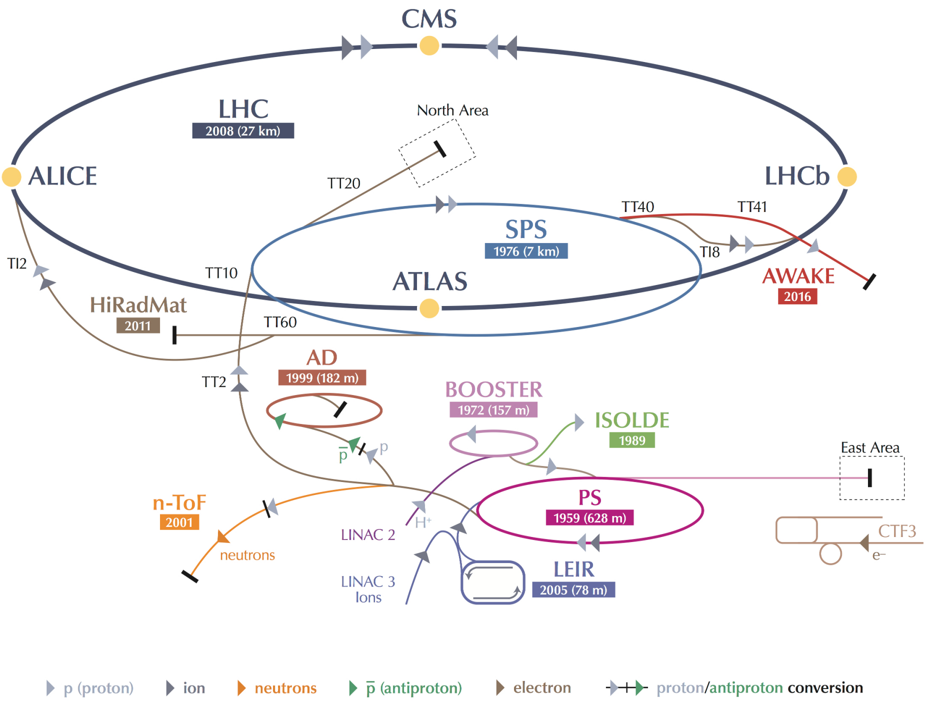

Figure 3.1: The accelerator infrastructure at CERN as well as the four main LHC experiments [71].

- ALICE [75] is designed to study lead-lead collisions and the properties of the quark-gluon plasma which emerges from these collision.

- LHCb [76] focuses on flavour physics and was optimized for high particle identification capabilities in order to distinguish between the various decay modes of mesons containing a bottom or charm quark.

- TOTEM [77] consists of detectors built at a distance of ±147 m and ±220 m from the CMS interaction point very close to the beam pipe. It measures the total proton-proton cross-section.

- LHCf [78] aims at the measurement of neutral particles emitted in the very forward direction which improves the hadron interaction models necessary to study highly energetic cosmic rays. It is composed of calorimeters located on each side of the ATLAS and CMS interaction points at a distance of 140 m.

- MoEDAL [79] is a passive detector built around the LHCb interaction point. It searches for magnetic monopoles and other highly ionizing particles

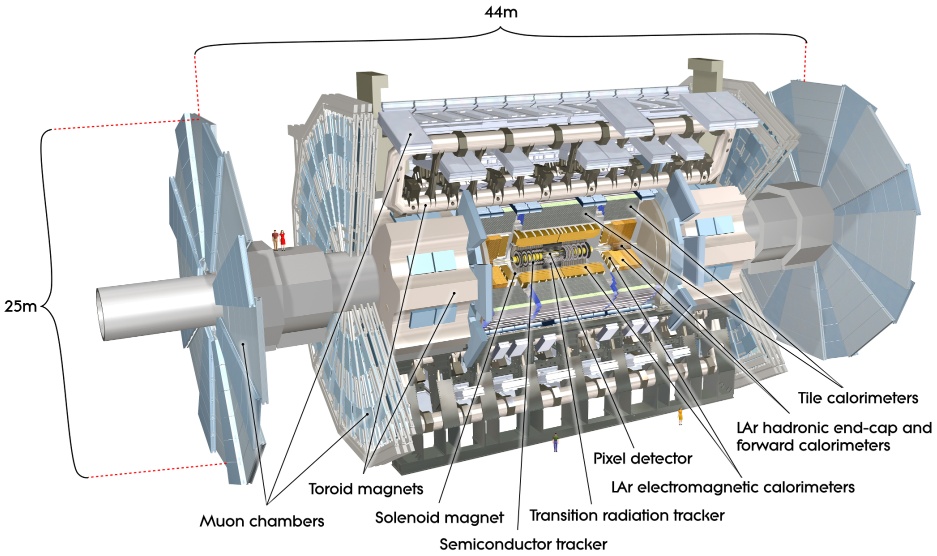

Figure 3.2: The ATLAS detector with all its subsystems and magnets [80].

3.2 The ATLAS detector

ATLAS is a multi-purpose detector aiming at a wide range of physics questions. One of its main goals was the discovery of the Higgs boson already mentioned in Sec. 1. Besides, it has a vast new physics search program and carries out precision measurements of SM processes and particle properties. ATLAS is designed to determine the momentum and energy of jets, leptons and photons with good resolution over a wide momentum range.
To achieve a high accuracy, ATLAS consists of various subdetectors which are built in different layers around the interaction point. They cover almost the complete solid angle to measure as many of the products of the particle collisions as possible. This is necessary to reconstruct particles which interact only weakly (such as neutrinos) and can only be measured indirectly via the imbalance in the total transverse momentum (denoted as $E_{\mathrm{T}}^{\mathrm{miss}}$). An illustration of the ATLAS detector is shown in Fig. 3.2.

3.2.1 ATLAS coordinate system

ATLAS uses a right-handed coordinate system with the origin at the nominal interaction point. The x-axis points towards the centre of the LHC ring, the y-axis points upwards and the z-axis is aligned with the beam direction. However, spherical coordinates are used in most cases instead of Cartesian coordinates due to the symmetry of the particle collisions. The azimuthal angle ϕ is measured with respect to the x-axis and ranges from $-\pi$ to $+\pi$. The pseudo-rapidity η is normally used instead of the polar angle θ which is measured towards the positive z-direction. The two quantities are connected via:

$$\eta = -\ln \tan \left(\frac{\theta}{2} \right) . \tag{3.1}$$

This has the advantage that the pseudo-rapidity difference $\Delta\eta$ between two highly energetic objects, for which the masses can be neglected, is invariant under Lorentz boosts into the z-direction. The angular distance ΔR is defined as:

$$\Delta R = \sqrt{(\Delta\eta)^2 + (\Delta\phi)^2} , \tag{3.2}$$

where $\Delta\phi$ is the difference in the azimuthal angle between two objects. For the momentum vector, the transverse component $p_{\mathrm{T}} = \sqrt{p_x^2 + p_y^2}$ is often stated together with its ϕ and η value instead of the absolute magnitude p and the components p_x, p_y, p_z.
Due to its cylindrical shape, ATLAS can be subdivided into the barrel region and the two endcaps. The position of individual detector components can be specified best in cylindrical coordinates via the distance to the beam pipe, r, together with the ϕ angle and z coordinate as defined above.

3.2.2 Tracking system

The innermost layer of the ATLAS detector comprises the tracking system where the tracks of charged particles are measured. It is also referred to as the inner detector (ID) and consists of three different components. Pixel detectors are mounted at the closest distance to the beam pipe in three cylindrical layers in the barrel (a fourth layer was installed after run-I of the LHC) and in three disks in the endcaps. They can cope with the high rates in this region. The accuracy of the pixel detectors is $10\,\mu$m in the $r - \phi$ $(z - \phi)$ plane and $140\,\mu$m in the z-direction (r-direction) in the barrel (endcaps). They are followed by four layers (barrel) and nine disks (endcaps) of semiconductor trackers (SCT) with readout strips. The SCT reaches an accuracy of $17\,\mu$m in $r - \phi$ $(z - \phi)$ and $580\,\mu$m in z (r) in the barrel (endcaps).
Pixel and SCT detectors are surrounded by the transition radiation tracker (TRT) which consists of straw drift tubes with a diameter of 4 mm. They are aligned parallel to the beam axis in the barrel and in the radial direction in the endcaps. Their intrinsic accuracy is $130\ \mu$m per straw in $r - \phi$. The transition radiation can be measured in the xenon-based gas mixture of the TRT and is used to distinguish electrons from charged hadrons. The layout of the complete inner detector can be seen in Fig. 3.3.
Tracks of charged particles are reconstructed from the hits in the different detector layers along the particle trajectory. The inner detector is immersed in a solenoid magnetic field with a strength B of 2 T. This allows for a p_{T} measurement from the bending of the track in the transverse plane. The momentum resolution is limited by the intrinsic spatial resolution, $\sigma(x)$, of the detector components and multiple scattering of the particles in the detector material. The uncertainty on the momentum measurement, $\sigma(p_{\mathrm{T}})$, generally gets larger with

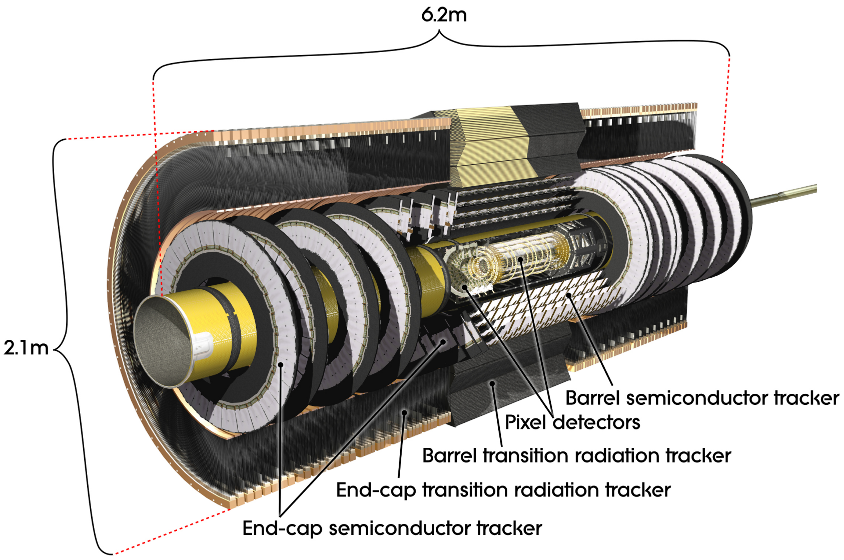

Figure 3.3: The inner detector of ATLAS with all its subsystems [81].

increasing p_T and shows the following approximate behaviour [82]:

$$\frac{\sigma(p_\mathrm{T})}{p_\mathrm{T}} = \left.\frac{\sigma(p_\mathrm{T})}{p_\mathrm{T}}\right|^{\mathrm{det}} \oplus \left.\frac{\sigma(p_\mathrm{T})}{p_\mathrm{T}}\right|^{\mathrm{ms}}, \tag{3.3}$$

$$\left.\frac{\sigma(p_\mathrm{T})}{p_\mathrm{T}}\right|^{\mathrm{det}} = \frac{\sigma(x)\ [\mathrm{m}]}{0.3\,B\ [\mathrm{T}]\ (L\ [\mathrm{m}])^2}\sqrt{\frac{720}{N+4}} \cdot p_\mathrm{T}\ [\mathrm{GeV}]\,, \tag{3.4}$$

$$\left.\frac{\sigma(p_\mathrm{T})}{p_\mathrm{T}}\right|^{\mathrm{ms}} = \frac{13.6\ \sqrt{L/X_0}\ \mathrm{MeV}}{e\ B\ L}\,, \tag{3.5}$$

where “$\oplus$” indicates that the uncertainty due to detector resolution (det) and due to multiple scattering (ms) are summed in quadrature. L is the path length of the particles in the magnetic field which is assumed to be homogeneous along the path. N is the number of detector layers along the trajectory and X_0 is the average radiation length of the material inside the tracking volume. The uncertainty due to the detector resolution is proportional to p and dominates for highly energetic particles while the multiple scattering contribution is approximately constant and dominates for tracks with low momenta. L/X_0 is of the order of 1 for the ATLAS inner detector. The relative resolution of the p_T measurement is about 4 % for a muon with 100 GeV [83].

3.2.3 Calorimeters

The ATLAS sampling calorimeters cover the range $|\eta| < 4.9$. They consist of several layers and have a high readout granularity both in ϕ- as well as in η-direction to achieve a precise

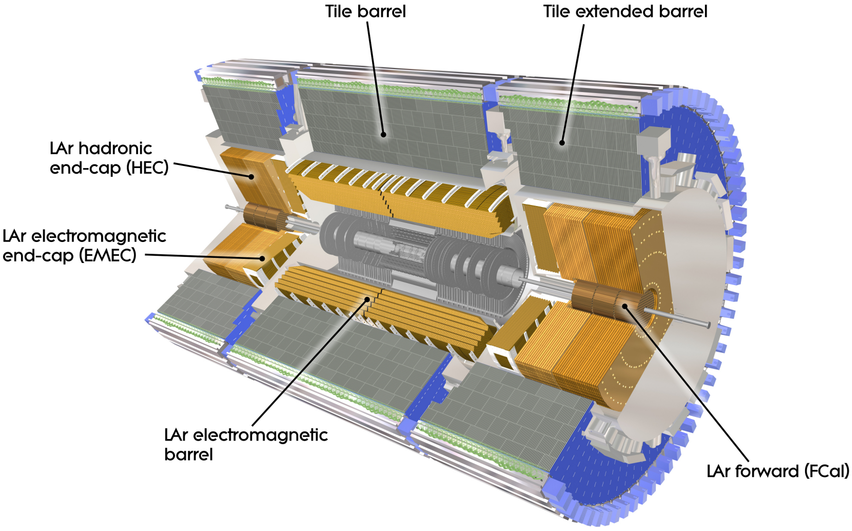

Figure 3.4: The different components of the ATLAS electromagnetic and hadronic calorimeters [84].

energy measurement for electrons, photons and jets. The innermost part of the calorimeter is referred to as the electromagnetic calorimeter which has the highest granularity needed for electrons and photons. The granularity of the outer part, which is called the hadronic calorimeter, is coarser and sufficient to measure the jet energy with good resolution as well as to achieve a good missing energy reconstruction. The thickness of the electromagnetic calorimeter expressed in numbers of X_0 is above 20 which ensures that nearly all electrons and photons are stopped in the inner layers. The approximate thickness of the hadronic calorimeter in numbers of interaction lengths is 10. This limits punch-through of jets into the muon system surrounding the calorimeters (see Sec. 3.2.4).

A liquid argon (LAr) calorimeter is used for the electromagnetic calorimeter. It consists of accordion-shaped kapton electrodes and lead or copper absorbers and is filled with liquid argon as active material. LAr components are also used in the endcaps and forward region of the hadronic calorimeter. Copper and tungsten serve as absorber materials there. The barrel region of the hadronic calorimeter is covered by a tile calorimeter built up from steel as absorber and scintillating tiles as active material. An overview over the different components of the ATLAS calorimeters can be found in Fig. 3.4.

Electrons and photons lose their energy in the calorimeter material via bremsstrahlung and pair production, respectively, leading to an electromagnetic shower in the inner part of the calorimeter. The hadrons contained in the jets lose their energy via interactions with the nuclei of the detector material. This leads to a hadronic shower which penetrates the outer part of the calorimeter. The energy can be estimated from the total length of all particle paths in the showers. The relative uncertainty on the energy measurement $\frac{\sigma(E)}{E}$ decreases in general with increasing energy like $\frac{1}{\sqrt{E}}$ [82] in contrast to the resolution of tracking detectors (compare Sec. 3.2.2). This behaviour is due to stochastic effects in the shower formation. The ATLAS calorimeters were designed to achieve a resolution of $\frac{\sigma(E)}{E} = \frac{10\%}{\sqrt{E}} \oplus 0.7\%$ for the electromagnetic part and $\frac{50\%}{\sqrt{E}} \oplus 3\%$ ($\frac{100\%}{\sqrt{E}} \oplus 10\%$) in the barrel and endcaps (forward region)

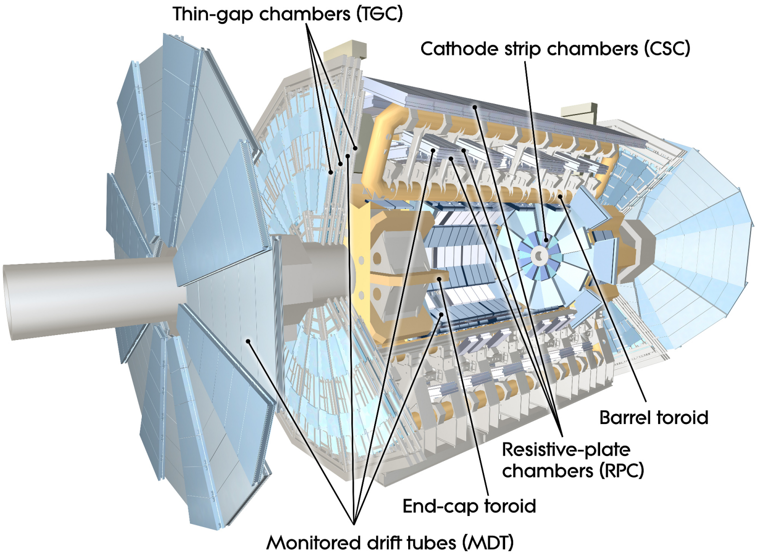

Figure 3.5: The precision and trigger detectors of the ATLAS muon spectrometer [85].

of the hadronic calorimeters. The additional constant contribution to the energy resolution originates from the calibration uncertainty.

3.2.4 Muon spectrometer

The outermost part of ATLAS is the muon spectrometer as the only collision products which reach it are muons (and neutrinos which do not interact with any detector system, however). It contains precision detectors which are used to reconstruct the muon track and measure the momentum. Monitored drift tubes (MDTs) filled with an argon-CO_2 gas mixture are used for this in the major part of the muon system. The MDTs are built into chambers of usually two multilayers with three or four tube layers each. The two multilayers have a distance of the order of 10 cm. The chambers are positioned in three cylindrical layers around the beam pipe (barrel) and in three wheels (endcaps). In the region closest to the beam pipe of the inner endcap wheel, cathode strip chambers (CSCs) are used as precision detectors instead of MDTs as the CSCs can cope better with the high particle rates in this region. The MDTs and CSCs are accompanied by fast trigger chambers with reduced spatial resolution. Resistive plate chambers (RPCs) and thin gap chambers (TGCs) are used for this in the barrel and endcaps, respectively. The layout of the ATLAS muon spectrometer can be seen in Fig. 3.5.
The muon system is immersed in the field of three air-core toroids with a strength of $\sim$0.5 T ($\sim$1 T) in the barrel (endcaps). The intrinsic accuracy of a single MDT is 80 μm in the bending plane while no measurement of the second coordinate can be provided. This can be obtained from the trigger detectors with an accuracy of 10 mm (RPCs) and 3–7 mm (TGCs). The CSCs provide a coordinate measurement with an precision of 40 μm in the bending plane and 5 mm in the perpendicular direction. A momentum resolution of $\frac{\sigma(p_\mathrm{T})}{p_\mathrm{T}} \approx 10\,\%$ for a muon with $p_\mathrm{T} = 1$ TeV can be achieved with the ATLAS muon detectors.

3.2.5 Trigger system

ATLAS has a trigger system with three levels. This is necessary to reduce the rate of *pp* collisions from about 1 GHz at the design luminosity of the LHC to a recordable amount of the order of a few 100 Hz. The first trigger level (L1) uses information from the muon trigger chambers to find patterns of muons, as well as from all calorimeters, but with reduced granularity, to trigger events with electrons, photons, hadronically decaying τ leptons, jets, missing energy or large total energy. It is based on fast hardware which provides a trigger decision within $2.5\,\mu$s and has a output rate of about 30 kHz [86]. The L1 trigger also defines the region of interest, i.e. the η and ϕ coordinates of the objects which have caused the trigger to fire.

The region of interest is transferred to the second trigger level (L2) together with coarse information about the object itself. The software-based L2 trigger uses the information from all detectors in the region of interest at full granularity and accuracy, which is about 2 % of the total data in the event. It reduces the rate to $\sim$4 kHz and passes its decision on to the final trigger level, the event filter (EF). The full event is reconstructed using the complete detector information for the decision of the EF. It selects events which are recorded for offline physics analyses based on different requirements on the objects and their properties (momenta, energy, etc.) with a rate of $\sim$450 Hz. L2 and EF are collectively referred to as the high level trigger (HLT).

3.2.6 Simulated collision events

Computer simulations of *pp* collisions are widely used in ATLAS for several purposes. They help to understand the detector behaviour, are utilized to model backgrounds and signals in searches for new physics or serve as template for measurements of particle properties. Simulated events are generated with Monte-Carlo (MC) methods. Several programs are available to perform such simulations and are used in this thesis (compare Sec. 4.2.2, 5.1 and 6.1). A sketch of the different simulation steps is shown in Fig. 3.6.

Quarks and gluons that take part in the hard scattering process can be regarded as free particles due to the asymptotic freedom (compare Sec. 2.1.1). The hard subprocess itself can be treated with the methods of perturbation theory at a fixed order. Before, the partons have to be resolved from the proton bound state. This cannot be calculated perturbatively but is encoded in parton density functions $f(Q^2, x)$ (PDF). These functions indicate the probability that a certain parton is resolved from the proton at a scale Q^2 and with a fraction x of the total proton momentum.

The parton shower step follows the hard scattering and takes into account higher orders effects by allowing for the emission of additional partons. This results in a shower of partons. Showering of inital state partons is usually also considered but not shown in the figure for simplicity. The hadronization step, which incorporates how the quarks and gluons form colourless objects, can also not be calculated perturbatively but is treated with phenomeological models. Eventually, the decay of unstable hadrons or leptons is simulated.

The underlying event is added to the simulation of the hard scattering process. This includes the treatment of the two proton remnants as well as of other proton-proton interactions in

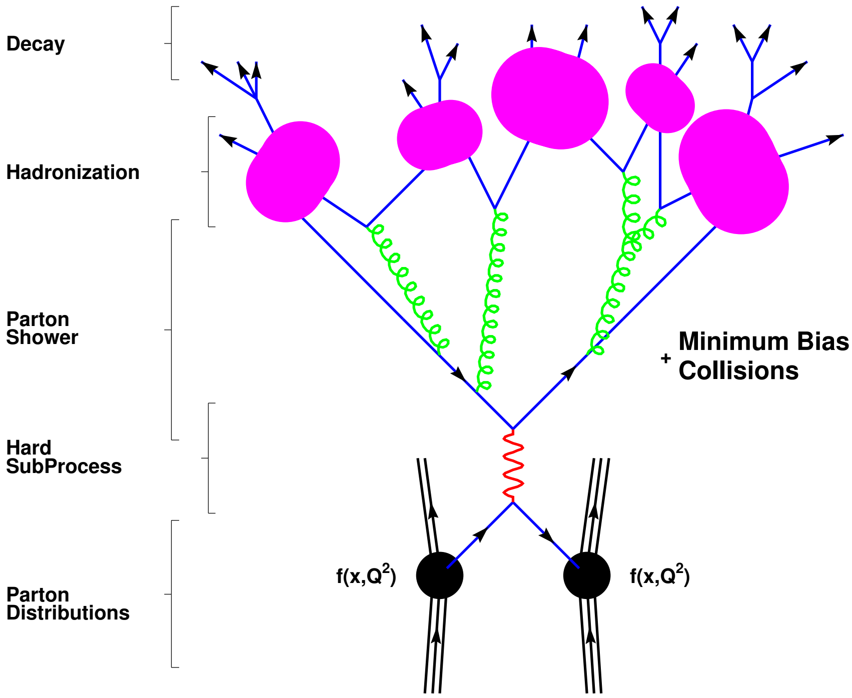

Figure 3.6: Sketch of the different steps of a Monte-Carlo simulation [23].

the same bunch crossing, referred to as pile-up and denoted as minimum bias collisions in the sketch. The different simulation steps can be implemented in a single MC generator or different programs can be used for the individual steps.

4 Analysis basis

As described in Sec. 2.2.3, searches for squarks and gluinos with charged leptons in their decays are well motivated and have the advantage of being less affected by backgrounds from QCD processes. In this thesis, “leptons” refers only to light leptons (electrons and muons) as τ leptons are more difficult to reconstruct. They usually suffer from larger fake rates and bigger uncertainties and are thus not considered here.

The two analyses presented here both make use of leptonic signatures but target different models: While the 2-lepton search [53] (referred to as Z+jets+E_T^{miss}) aims for leptonically decaying Z bosons from the SUSY cascade predicted by GGM models, the 1-lepton analysis [19] (referred to as 1L+jets+E_T^{miss}) is used for a reinterpretation [54] in the context of models with RPV. Both analyses use a similar strategy and the same datasets, object definitions and event preselection. The parts specific to each analysis are described later in Sec. 5 and 6, respectively.

4.1 General analysis strategy

Most of the searches for supersymmetric particles in ATLAS use a similar approach and usually proceed in the following steps:

Optimization of the search regions: As the predicted cross-sections for the production of supersymmetric particles are relatively low compared to typical Standard Model processes, areas in the phase space have to be found where the signal to background ratio is enhanced. The new particles must be heavier than most of the known particles and their decays include highly energetic objects, such as jets and leptons, in most cases. The LSP is predicted to be stable and only weakly interacting in many SUSY models, so it would not be detected with ATLAS. Therefore, it would only show up as an imbalance of the total transverse momentum (see 4.3.5).

Various variables can be used to distinguish between background-like and signal-like events and to define a signal region (SR). Signatures with high-p_{T} objects and large $E_{\mathrm{T}}^{\text{miss}}$ serve as a very generic starting point to find a region of phase space where signals of SUSY particles would appear above the background. Other variables used in the following analyses are H_{T} and the effective mass m_{eff}:

$$H_{\mathrm{T}} = \sum_{\text{jets}} p_{\mathrm{T}} + \sum_{\text{leptons}} p_{\mathrm{T}}\,, \tag{4.1}$$

$$m_{\text{eff}} = H_{\mathrm{T}} + E_{\mathrm{T}}^{\text{miss}}\,, \tag{4.2}$$

where the p_{T}-sum in the H_{T} definition runs over all jets and leptons selected in the event. Both variables provide an estimate for the total activity in an event and are hence related to the mass scale of the particles involved in the hard scattering process. Therefore, H_{T} and m_{eff} are expected to be on average higher for SUSY events compared to SM events.
Another useful variable for decays with one visible and one invisible massless decay product (e.g. $W \to \ell\nu$) is the transverse mass m_{T}

$$m_{\mathrm{T}} = \sqrt{2\, p_T^{\mathrm{visible}}\, E_{\mathrm{T}}^{\mathrm{miss}}\, (1 - \cos{(\Delta\phi)})}\,. \tag{4.3}$$

Here p_T^{visible} is the transverse momentum of the visible particle and $\Delta\phi$ is the angle in the transverse plane between the visible particle and $E_{\mathrm{T}}^{\mathrm{miss}}$. The missing transverse energy should point in the direction of the invisible particle in case all detectable particles are measured correctly. The upper bound on m_{T} is the mass of the decaying particle (e.g. the W boson) in case detector resolution effects are neglected.
One usually defines some benchmark SUSY models to optimize a signal region with good sensitivity. Then different event selections are explored by applying varying upper or lower bounds (cuts) to the variables used for the optimization. The selection providing the best expected exclusion or discovery power for a given benchmark point is chosen as signal region.
Analyses in high energy physics are usually performed in a blinded way in order to avoid subjective biases. This means the signal region optimization is based on computer simulations of the expected signal and does not use any experimental data. The data are only unblinded as soon as the background is understood and validated properly.

Background estimation: The background from SM processes in the signal region has to be evaluated carefully to allow for a proper interpretation of the observed data. For this, dedicated methods for the individual background components are used. They can be based on computer simulations with Monte-Carlo methods or derived from the experimental data directly (data-driven).
For large background components, a control region (CR) is typically defined in which the corresponding process is dominating. This way the background prediction can be constrained and extrapolated to the signal region. Therefore, the control regions should be close to the signal region to keep the uncertainty due to the extrapolation small. On the other hand, they must be separated enough in order not to suffer from a significant contamination of the expected signal.

Validation: The background prediction is usually scrutinised in validation regions (VR) which are positioned between signal and control regions and where little signal is expected. In these regions, the agreement between the predicted background and the measured data can be cross-checked before unblinding the signal region.

Interpretation of the results: Statistical methods are used to interpret the observed result in the signal region with respect to the predicted number of background events and the expected signal. Two different questions can be asked:

- How likely is the observed number of events caused by background only? The answer can be quantified by the p-value which represents the probability that the predicted

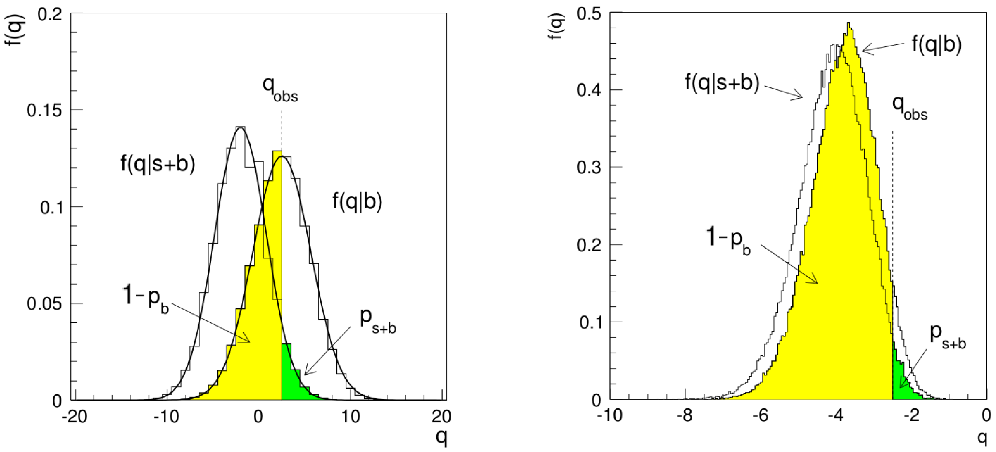

Figure 4.1: Distributions f of the test statistic q for the background only (b) and signal+background hypothesis ($s+b$) in case the two distributions being well separated (left) and having a large overlap (right) [87].

background gives a result equally or less probable than the observed one. The p-value is not depending on any specific signal model. It is often expressed by the number, Z, of Gaussian standard deviations σ such that a Gaussian distributed variable would have the same probablity p to be found as many or more standard deviations above its mean value [88]:

$$Z = \Phi^{-1}(1-p)\,, \tag{4.4}$$

where Φ^{-1} is the quantile of the standard normal distribution.

- Is a specific SUSY model allowed by the data? In ATLAS the CL_s method [89] is used to perform hypothesis tests between the background only hypothesis (b) on the one hand and the signal+background hypothesis ($s+b$) on the other hand. A test statistic q (to be defined later in Sec. 5.7) has to be constructed which allows distinguishing between the two hypotheses. Simple examples for the distributions of q under the background only hypotheses, $f(q|b)$, and the signal+background hypothesis, $f(q|s+b)$, are shown in the left sketch of Fig. 4.1. The $s+b$ hypothesis is rejected and regarded as being excluded if the probability p_{s+b} that $f(q|s+b)$ would yield a result equally or less probable than the observed value q_{obs} is smaller than 5 %. The green shaded area indicates the value of p_{s+b} in the figure.
  The quantity $1 - p_{s+b}$ is called the confidence level CL_{s+b}. A feature of CL_{s+b} is that models can be excluded even if the analysis is not sensitive to them. This happens when $f(q|s+b)$ and $f(q|b)$ are not well separated, as depicted in the right plot of Fig. 4.1, and there are less events observed in data than expected from the background only. To prevent such cases, a modified confidence level CL_s is used in ATLAS:

$$CL_s = 1 - \frac{p_{s+b}}{p_b}\,, \tag{4.5}$$

where p_b is the probability that the b hypothesis yields a result equally or less probable than the observed value q_{obs}. The value of $1 - p_b$ is illustrated as the yellow area in

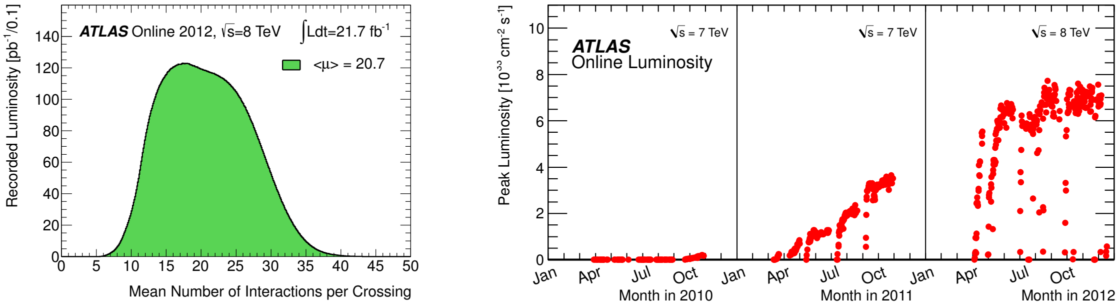

Figure 4.2: Mean number of pp interactions per bunch crossing (left) and peak instantaneous luminosity of the LHC in the years 2010 – 2012 (left) [91].

Fig. 4.1. The definition of CL_s implies that p_{s+b} gets a large penalty in case there is a large overlap between the two hypothesis. From the definition, it can be seen that CL_s is always smaller than CL_{s+b} and leads to conservative exclusion limits.

For all statistical interpretations, uncertainties on the number of predicted background and signal events have to be taken into account which will be discussed in Sec. 5.4 in more detail.

4.2 Data and Monte-Carlo samples

4.2.1 Data samples

The searches presented in this thesis analyse the dataset which was recorded by the ATLAS experiment in pp collision at a centre of mass energy of $\sqrt{s} = 8\,\text{TeV}$ between 5th April and 6th December 2012. It corresponds to an integrated luminosity of $\int \mathcal{L}\,dt = 20.3\,\text{fb}^{-1}$ where the uncertainty on the luminosity measurement is estimated to be 2.8 % following the same methods as described in [90].
The running conditions of the LHC changed throughout the year going to higher instantaneous luminosities which resulted in an increase in the average number of pp interaction per bunch crossing, μ. The value of $\langle\mu\rangle$ averaged over the full data taking period was 20.7 as displayed in the left plot of Fig. 4.2. The peak instantaneous luminosity reached in 2012 was $\sim 7.7 \cdot 10^{33}\,\text{cm}^{-2}\,\text{s}^{-1}$ (compare right plot).

4.2.2 Background samples

Simulated events of different background processes are used in the analyses for various reasons. On the one hand, some of the smaller backgrounds are estimated from MC simulations directly. On the other hand, they serve as a starting point for data-driven techniques and are

Physics process	Generator	Parton Shower	Cross-section	Tune	PDF set
$t\bar{t}$	Powheg-Box r2129	Pythia 6.426	NNLO+NNLL	Perugia2011C	NLO CT10
$Z/\gamma^* + \text{jets}$, $W + \text{jets}$	sherpa 1.4.1	sherpa 1.4.1	NNLO	sherpa default	NLO CT10
WW, WZ, ZZ (≥ 2 leptons)	Powheg-Box r1508	Pythia 8.163	NLO	AUET2	NLO CT10
WW, WZ, ZZ (1 lepton)	sherpa 1.4.1	sherpa 1.4.1	NLO	sherpa default	NLO CT10
$W\gamma$, $Z\gamma$	sherpa 1.4.1	sherpa 1.4.1	LO	sherpa default	NLO CT10
$t + Z$	MadGraph5 1.3.28	Pythia 6.426	LO	AUET2	CTEQ6L1
$t\bar{t} + W$, $t\bar{t} + Z$	MadGraph5 1.3.28	Pythia 6.426	NLO	AUET2	CTEQ6L1
$t\bar{t} + WW$	MadGraph5 1.3.28	Pythia 8.165	LO	AUET2	CTEQ6L1
Single top ($W + t$, s-channel)	Powheg-Box r1556	Pythia 6.426	Approx. NNLO	Perugia2011C	NLO CT10
Single top (t-channel)	AcerMC 3.8	Pythia 6.426	NNLO+NNLL	Perugia2011C	CTEQ6L1
Dijet	Pythia 8.160	Pythia 8.160	LO	AU2	NLO CT10

Table 4.1: Overview over the MC generators used to simulate various background processes. The version number, the parton shower model, the accuracy of the cross-section calculation, the underlying event tune and the PDF set are also indicated.

utilized for cross-checks.

All MC samples are taken from the official MC12a ATLAS production and are commonly used in many ATLAS analyses. The simulated events are overlaid with minimum bias events generated with Pythia 8 [92] with μ values between 0 and 40. They are reweighted such that the final μ distribution matches the one observed in the 2012 data (compare right plot of Fig. 4.2). The total cross-section for inelastic pp interactions is not known with infinite precision, therefore the distribution of the number of vertices N_{vtx} in data is not reproduced perfectly by this procedure. As N_{vtx} is the physical quantity of greater importance for the analysis, μ of the simulation is multiplied by a factor of $\frac{1}{1.11}$ before reweighting to improve the agreement in N_{vtx} [93].

The MC generators for the individual samples as well as the order in α_{S} of the cross-section calculation, the PDF set and the underlying event tune are summarised in Tab. 4.1. The MC generator version which was used for the productions is indicated, too. Detailed information about the exact ATLAS datasets as well as values of the cross-sections and generator efficiencies can be found in App. A.

$t\bar{t}$ processes are generated with powheg [94–96] interfaced with Pythia [97] for the parton shower. The Perugia2011C tune [98] for the underlying event and the NLO CT10 PDF set [99] are used. The cross-section to which the sample is normalised is calculated at next-to-next-to-leading order in α_{S} (NNLO) with the resummation of soft gluon emission at next-to-next-to-leading-logarithmic accuracy (NNLL) being included [100, 101].

Drell-Yan (8 GeV<$m_{\ell\ell}$ <40 GeV), $\boldsymbol{Z+}$ **jets** ($m_{\ell\ell}$ >40 GeV) and $\boldsymbol{W+}$ **jets** events are simulated with SHERPA [102] using SHERPA's own underlying event tune and parton shower model. The cross-section is calculated at NNLO accuracy [103, 104]. The samples were generated in different bins of the p_T of the Z/W boson to have a sufficient number of events also for boosted gauge bosons. All decay modes involving charged leptons are considered for the Z/W in the MC samples (this is also true for the other samples discussed below). For the analysis focusing on two leptons compatible with coming from a Z boson decay (see Sec. 5) the statistics of the $Z+$jets MC in corners of the phase space was further increased by applying a generator filter on $H_\mathrm{T} > 400$ GeV defined in Eq. (4.1) and calculated with the p_T at particle level.

Diboson backgrounds in the 1-lepton channels are estimated with SHERPA using the same settings as for the $Z/\gamma^* +$jets and $W+$jets samples described above. WW, WZ, WZ, $W\gamma$ and $Z\gamma$ processes are included in the simulation.
For the analysis with at least two leptons, only the first three processes are taken into account and POWHEG is used for the event generation while the showering is done with PYTHIA. The simulation uses the AUET2 tune [105] for the underlying event and the NLO CT10 PDF set. For WW, WZ, WZ cross-sections are available at NLO accuracy [106, 107], while LO calculations are used for $W\gamma$, $Z\gamma$.

$\boldsymbol{t\bar{t}+W/Z}$**,** $\boldsymbol{t\bar{t}+WW}$ and $\boldsymbol{t+Z}$ background is simulated with MADGRAPH5 [108] and showered with PYTHIA using the AUET2 tune and the CTEQ6L1 PDF set [109]. Cross-sections are calculated at NLO accuracy for $t\bar{t}+W/Z$ [110, 111] and at LO for $t\bar{t}+WW$ and $t+Z$.

Single top ($\boldsymbol{W+t}$ **and** $\boldsymbol{s}$**-channel)** events are generated with POWHEG and PYTHIA using the PERUGIA2011C tune for the underlying event and NLO CT10 PDFs. Cross-sections are calculated at NNLO+NNLL [112, 113].

Single top ($\boldsymbol{t}$**-channel)** processes are simulated with the ACERMC event generator [114]. PYTHIA is used for the parton shower, the PERUGIA2011C tune for the underlying event and CTEQ6L1 as PDF set. This background is normalised to the NNLO+NNLL cross-section [115].

Dijet simulated events are not used for background estimation in any of the analyses, but they serve as a starting point to evaluate the detector response to jets. This is needed for the jet smearing method which will be explained in Sec. 5.3.1. Dijet processes are simulated with PYTHIA using the NLO CT10 PDF set and the AU2 generator tune [116].

All MC samples are passed through a simulation of the ATLAS detector and can afterwards be treated with the same reconstruction algorithms as real data [117]. For most of the simulated events a full detector simulation with GEANT4 [118] is performed, while for a few samples a fast detector simulation is used [119]. The main difference between the two approaches is that the latter uses a parametrization for the calorimeter response instead of a step-by-step simulation as in GEANT4. For other detector parts also the fast simulation relies on GEANT4. Details about which detector simulation is applied for the individual samples can be found in App. A.

4.3 Physics object identification and selection

The physics objects, such as jets, leptons and the missing transverse energy, are reconstructed from the signals in the detector with dedicated algorithms. Additional identification criteria are applied to the output of the algorithms to enhance the purity and to avoid misidentification as much as possible. The analyses in this thesis rely on light leptons (muons and electrons), large missing transverse energy and jets, which can be additionally tagged as containing mesons with a b quark. As τ leptons and photons are not used in any of the analysis parts, their description is omitted here. The definitions of all objects follow the recommendations of the ATLAS performance groups [120].

4.3.1 Primary vertex

Vertices are reconstructed using all particle tracks with a transverse momentum $p_{\mathrm{T}} > 400\,\mathrm{MeV}$ [19]. The one with the highest $\sum p_{\mathrm{T}}^2$ of the associated tracks is called the primary vertex where the hard interaction process is assumed to have taken place. Its position has to be consistent with the beam-spot envelope.

4.3.2 Jets and b-tagging

Topological calorimeter clusters serve as input for the jet reconstruction algorithm [121]. Neighbouring (i.e. topologically connected) calorimeter cells with sufficient signal over noise threshold are merged into clusters. This suppresses the influence of individual cells with high noise, which could lead to jet mismeasurements. The clusters are calibrated using local cell signal weighting (LCW). This means it is evaluated for each cluster if the energy deposit is more likely to originate from a particle in an electromagnetic or hadronic shower. Information about the measured energy density and the longitudinal shower depth is used for this. Depending on the classification, energy corrections derived from simulations are applied to the cluster, which improves the jet energy resolution.

Jets are reconstructed with the anti-k_t algorithm [122] with a radius parameter of 0.4 using the Lorentz vectors of the calibrated topological clusters as input, where the cluster mass is assumed to be zero. The jets are corrected for pile-up effects and adjusted so that their direction points to the primary vertex instead of the nominal centre of the ATLAS detector. They are further calibrated based on MC studies comparing the momentum at particle level to the one of the reconstructed jet. Eventually, an additional correction accounts for small differences between data and simulation.

For the analyses described here, two kind of jets are defined: Baseline and signal jets. For the first ones, the transverse momentum has to be greater than $20\,\mathrm{GeV}$ and they have to fulfil “Looser” quality criteria defined in [123, 124]. These requirements make use of information about the signals in individual cells and the distribution of the energy in the different calorimeter parts to suppress fake jets from detector noise or non-collision and cosmic backgrounds.

Requirement	Cut/description
	Baseline jet
Algorithm	anti-k_t using topological calorimeter clusters with LCW
Acceptance	$p_{\mathrm{T}} > 20$ GeV
Quality	`Looser`
	Signal jet
Acceptance	$p_{\mathrm{T}} > 35$ GeV , $\lvert\eta\rvert < 2.5$
Pile-up suppression	$\lvert\mathrm{JVF}\rvert > 0.25$ for jets with $p_{\mathrm{T}} < 50$ GeV and $\lvert\eta\rvert < 2.4$
	b-jet
b-tagging algorithm	MV1
b-tag efficiency	60%

Table 4.2: Summary of the jet and b-jet definitions (details are given in the text).

For signal jets, $p_{\mathrm{T}} > 35$ GeV and $|\eta| < 2.5$ is required in addition. Furthermore, the absolute value of the jet vertex fraction (JVF) has to be greater than 0.25 for jets with $p_{\mathrm{T}} < 50$ GeV and $|\eta| < 2.4$ in order to eliminate jets from pile-up as much as possible. JVF is defined as the p_{T} weighted fraction of tracks associated with the jet, that originate from the primary vertex (jets without any track have JVF $= -1$).
The relatively long life time of about 1 ps for mesons containing a bottom quark allows it to distinguish between jets containing a b quark (b-jets) and jets from light quarks ($= u$, d, s), charm quarks and gluons, on the other hand. The impact parameters of the associated tracks and the reconstructed decay vertices of the mesons with a b quark are used to tag jets which are likely to contain a b quark. The analyses described here use the b-tagging algorithm MV1 [125] which is based on an artificial neural network. The efficiency of MV1 for the identification of b-jets, as it is applied here, is 60 %, while the rejection rate for light and gluon jets is about 600 (i.e. every 600th jet is misidentified as a b-jet) and about 8 for charm jets. The definitions for jets and b-jets are summarised in Tab. 4.2.

4.3.3 Muons

Information from the inner detector and the muon spectrometer is combined to reconstruct muons [126]. Track seeds are built from the hits in the pixel and SCT systems and then extended into the TRT, where suitable drift circles are matched to the track candidate. Subsequently the whole track is refitted with the data from all three systems to get the best track measurement.
The track finding procedure in the muon system is similar: the drift circles in the MDTs or the charge clusters in the CSCs or trigger chambers are used as possible starting points for segments which are tracks in an individual chamber. The segments in the outer and middle layer of the muon system are extrapolated into the inner layer taking into account the cur-

vature of the trajectory in the magnetic field. Track candidates are formed from segments which match reasonably well and could therefore come from the passage of the same charged particle. Then the whole track is refitted using all segments assigned to it.
For the SUSY searches presented here, muon candidates are then formed in two ways:

- **Combined muons** are reconstructed from tracks in the muon system that have a matching counterpart in the inner detector. The statistical combination of both tracks gives the best measurement for the muon p_{T}.

- **Segment-tagged muons** are built from a track in the inner detector that matches one of the segments in the MDT or CSC chambers, when extrapolated into the muon system. These muon candidates are used to recover inefficiencies in regions where the muon spectrometer is not fully equipped with chambers and to reconstruct low p_{T} muons. These do not reach the outer layers of the muon system due to the bending of their track in the magnetic field.

Additional quality requirements are applied to the muon candidates to select only well measured muons with high purity and suppress muons from hadron decays [127]. The track in the inner detectors is required to have at least one hit in the pixel detector and six hits in the SCT system, where broken sensors along the track are also counted as hits in both cases. One hit has to be in the innermost layer of pixel sensors if they are expected to be operational in the region of the particle passage. A maximum number of two missing hits (holes) in the pixel and SCT sensors traversed by the track is allowed.
For muons with $|\eta| < 1.9$, at least six hits in the TRT tubes are required and at most 90 % of these hits are allowed to be marked as outliers. When one extrapolates the track from the pixel and SCT system into the TRT, two sorts of hits are counted as outliers: signals that are assigned to a different track than the one under consideration and signals in the TRT tubes which fail to form a smooth trajectory with the pixel and SCT hits. The latter case is typical for a decay in flight of a long-lived hadron. The outlier criterion is also applied to muons with $|\eta| > 1.9$ if they have at least six TRT hits.
Baseline muons are further required to have a transverse momentum greater than 10 GeV and $|\eta| < 2.4$. Signal muons which are used for the final selection of possible SUSY events have to be isolated from other particles in addition. For muons with $p_{\mathrm{T}} > 25\,\mathrm{GeV}$, the p_{T} sum of all tracks in a cone of $\Delta R < 0.2$ around the muon (excluding the muon track itself) has to be smaller than 1.8 GeV. For muons with $p_{\mathrm{T}} < 25\,\mathrm{GeV}$, the p_{T} sum in a cone of $\Delta R < 0.3$ has to be less than 12 % of the muon momentum. In addition, these low p_{T} muons have to fulfil $|z_0 \sin(\theta)| < 1\,\mathrm{mm}$ and $|d_0/\sigma_{d_0}| < 3$, where d_0 (z_0) is the track impact parameter in the transverse plane (along the z-axis) and σ_{d_0} is the uncertainty on the d_0 measurement. The complete muon selection can be found in Tab. 4.3.

4.3.4 Electrons

The electron reconstruction relies on the measurement of the energy deposition in the electromagnetic calorimeter in combination with a track found in the inner detector [128]. All

Requirement	Cut/description
	Baseline muon
Algorithm	combined or segment-tagged muon
Acceptance	$p_\mathrm{T} > 10$ GeV, $\lvert\eta\rvert < 2.4$
Track quality	Number of pixel hits + number of crossed dead pixel sensors ≥ 1 Number of SCT hits + number of crossed dead SCT sensors ≥ 6 ≥ 1 inner pixel layer hit when it can be expected Pixel holes + SCT holes ≤ 2 If $\lvert\eta\rvert < 1.9$: $n_\mathrm{TRT} \geq 6$ and $n_\mathrm{TRT}^\mathrm{outliers} < 0.9\, n_\mathrm{TRT}$ If $\lvert\eta\rvert \geq 1.9$ and $n_\mathrm{TRT} \geq 6$: $n_\mathrm{TRT}^\mathrm{outliers} < 0.9\, n_\mathrm{TRT}$
	Signal muon
Isolation and impact parameters	$p_\mathrm{T} < 25\,\mathrm{GeV}$: $p_\mathrm{T}^{\mathrm{cone}<0.3}/p_\mathrm{T} < 0.12$ $\lvert z_0 \sin\theta\rvert < 1$ mm $\lvert d_0/\sigma_{d_0}\rvert < 3$ $p_\mathrm{T} \geq 25\,\mathrm{GeV}$: $p_\mathrm{T}^{\mathrm{cone}<0.2} < 1.8\,\mathrm{GeV}$

Table 4.3: Summary of the muon definition. The number of hits in the TRT is denoted as n_TRT, while $n_\mathrm{TRT}^\mathrm{outliers}$ is the number of outliers in the TRT system which is defined in the text.

reconstructed tracks are extrapolated from the ID to the middle layer of the electromagnetic calorimeter and it is checked if there exists a matching energy cluster at this position. After that, the cluster size is adjusted to include as much of the total electron energy as possible. The measurement is corrected for effects due to losses in the material in front of the calorimeter, the sampling structure of the calorimeter and energy leakage out of the reconstructed cluster.

Further identification requirements are applied to the electron candidates to enhance the purity. These make use of information about the shower shape inside the electromagnetic calorimeter, the track quality (similar to the requirements for muons described in Sec. 4.3.3), the track impact parameter d_0 and the amount of transition radiation in the TRT.

In this thesis, baseline electrons have to fulfil criteria similar to the “medium” definition from [128], but tuned to cope better with the data taking conditions in 2012. They must have $p_\mathrm{T} > 10\,\mathrm{GeV}$ and lie inside $\lvert\eta\rvert < 2.47$.

Signal electrons, which are used for the selection of the search region, are defined by applying the stricter “tight” identification criteria (also adjusted to the 2012 run conditions). Furthermore, they have to be isolated from other objects in the event. For electrons with $p_\mathrm{T} < 25\,\mathrm{GeV}$, the sum of all momenta in a cone of $\Delta R < 0.3$ around the electron track (not including the electron track itself) has to be less than 16 % of the electron p_T. The absolute value of z_0 weighted with $\sin\theta$ has to be smaller than 0.4 mm and the absolute value of d_0 must not deviate from zero by more than five standard deviations of the d_0 measurement. Electrons with $p_\mathrm{T} > 25$ GeV must have less than 10 % of p_T relative to their transverse momentum in a cone of $\Delta R < 0.2$ around their direction. The absolute values of their transverse and longitudinal impact parameter, d_0 and z_0, must be less than 1 mm and 2 mm, respectively. An overview over the electron definition is shown in Tab. 4.4.

The isolation requirement introduces an intrinsic difference between the electron and muon

Requirement	Cut/description	
	Baseline electron	
Acceptance	$p_\mathrm{T} > 10$ GeV, $\lvert\eta\rvert < 2.47$	
Quality	Medium++	
	Signal electron	
Quality	Tight++	
Isolation and impact parameters	$p_\mathrm{T} < 25\,\mathrm{GeV}$:	$p_\mathrm{T}^{\mathrm{cone}<0.3}/p_\mathrm{T} < 0.16$ $\lvert z_0 \sin(\theta)\rvert < 0.4$ mm $\lvert d_0/\sigma_{d_0}\rvert < 5$
	$p_\mathrm{T} \geq 25\,\mathrm{GeV}$:	$p_\mathrm{T}^{\mathrm{cone}<0.2}/p_\mathrm{T} < 0.10$ $\lvert z_0\rvert < 2$ mm $\lvert d_0\rvert < 1$ mm

Table 4.4: Summary of the electron definition

definition in the analyses in this thesis. Muons with with $p_\mathrm{T} > 25\,\mathrm{GeV}$ use an absolute isolation criterion (compare Tab. 4.3) while a p_T-dependent isolation requirements is applied for electrons.

4.3.5 Missing transverse energy $E_\mathrm{T}^\mathrm{miss}$

A momentum imbalance $\vec{p}_T^{\,\mathrm{miss}}$ observed in the plane transverse to the beam axis is a sign for invisible particles which have escaped detection inside the ATLAS volume, such as neutrinos. It is calculated from all calorimeter clusters as the negative of the sum over all E_T vectors [129]. Hereby, each cluster is calibrated according to the object it is matched to (photons, signal electrons or baseline jets). The momentum of muons which is not measured in the calorimeters is added from their p_T measurement. Calorimeter clusters not associated to any object are calibrated using LCW and taken into account for the momentum imbalance calculation. This contribution to the missing energy is called the soft term $E_T^{\mathrm{miss,soft}}$ as it is mainly caused by low energetic objects and pile-up activity.
The magnitude of the imbalance vector is referred to as the missing transverse energy, $E_\mathrm{T}^\mathrm{miss}$, and its ϕ angle is used to characterise the direction. The $E_\mathrm{T}^\mathrm{miss}$ calculation can be summarised as follows:

$$\vec{p}_T^{\,\mathrm{miss}} = -\left(\sum_{\text{electrons}} \vec{E}_T + \sum_{\text{photons}} \vec{E}_T + \sum_{\text{jets}} \vec{E}_T + \sum_{\text{soft}} \vec{E}_T + \sum_{\text{muons}} \vec{p}_T\right), \tag{4.6}$$

$$E_\mathrm{T}^\mathrm{miss} = \left|\vec{p}_T^{\,\mathrm{miss}}\right| . \tag{4.7}$$

The photons used in this equation are required to have $p_\mathrm{T} > 10\,\mathrm{GeV}$ and to satisfy the tight identification requirements defined in [130].

4.4 Trigger strategy

For the signatures discussed in this thesis, possible signal events can be triggered by the leptons. Single lepton triggers with an additional requirement on $E_{\mathrm{T}}^{\mathrm{miss}}$ and possibly jets are used in channels with exactly one lepton [19, 93, 131] and summarised in Tab. 4.5. The additional $E_{\mathrm{T}}^{\mathrm{miss}}$ cut is necessary as single lepton triggers without it require the leptons to be isolated to achieve the same p_{T} threshold. However, also non-isolated baseline leptons are used in the analyses (compare Sec. 4.3.3 and 4.3.4) and so these triggers are not suitable.

The electron trigger is seeded at L1 by a cluster in the electromagnetic calorimeter for which the shower shape is consistent with an electron. The HLT requires a reconstructed electron with $p_{\mathrm{T}} > 24\,\mathrm{GeV}$ and $E_{\mathrm{T}}^{\mathrm{miss}} > 35\,\mathrm{GeV}$. The trigger is fully ($\sim$100 %) efficient for events which have $E_{\mathrm{T}}^{\mathrm{miss}} > 80\,\mathrm{GeV}$ in the offline reconstruction and an electron with $p_{\mathrm{T}} > 30\,\mathrm{GeV}$. For offline electrons with $p_{\mathrm{T}} \approx 24\,\mathrm{GeV}$, the efficiency decreases to $\sim$70 %.

Muon events are recorded by requiring a muon and a jet candidate at L1. The HLT bases its decision on a reconstructed muon with $p_{\mathrm{T}} > 24\,\mathrm{GeV}$, a jet with $p_{\mathrm{T}} > 65\,\mathrm{GeV}$ and $E_{\mathrm{T}}^{\mathrm{miss}} > 40\,\mathrm{GeV}$. The efficiency for this trigger is $\sim$70 % for events with a muon in the barrel region of the ATLAS detector with $p_{\mathrm{T}} > 25\,\mathrm{GeV}$, a fully calibrated jet with $p_{\mathrm{T}} > 80\,\mathrm{GeV}$ and $E_{\mathrm{T}}^{\mathrm{miss}} > 100\,\mathrm{GeV}$. For events with muons in the endcaps the efficiency is $\sim$90 %.

In the analysis targeting signatures with two leptons, a logical `OR` between different dilepton triggers is used [53,132]. Depending on the p_{T} of the two leptons, the trigger combination with the best efficiency is chosen. Additionally, single lepton triggers with high p_{T} thresholds are used to recover inefficiencies for high-energy leptons. This trigger strategy offers the advantage that no lepton isolation requirements or cuts on $E_{\mathrm{T}}^{\mathrm{miss}}$ and jets are necessary in the trigger decision while relatively low p_{T} thresholds for the leptons can be kept. The different triggers are explained in more detail in Tab. 4.5. The efficiency is about 96 %, 88 % and 80 % for ee, eμ and $\mu\mu$ events with both leptons in the barrel region and 91 %, 92 % and 82 % when both leptons are in the ATLAS endcaps.

For all triggers, it is required that the leptons causing the trigger to fire can be matched to the leptons used to select the event offline.

4.5 Event cleaning and preselection

Only collision events with the full detector operational and good data quality are used for the physics analyses presented here. Furthermore, events containing objects which possibly originate from non-collision backgrounds (e.g. cosmic muons) are vetoed. This event cleaning procedure follows standard ATLAS recommendations common to most physics analyses [93]:

- Use of a good runs list: All data taking periods with good detector and data quality conditions are gathered in this list and only events from these periods are considered.

- Selection of events according to the trigger strategy described in Sec. 4.4.

Region	Lepton p_{T}	Trigger
	single e channel	
A	$p_{\mathrm{T}}(e) > 25\,\mathrm{GeV}$	`EF_e24vh_medium1_EFxe35_tclcw`
	single μ channel	
A	$p_{\mathrm{T}}(\mu) > 25\,\mathrm{GeV}$	`EF_mu24_j65_a4tchad_EFxe40_tclcw`
	$e\mu$ channel	

A	$p_{\mathrm{T}}(e_1) > 14\,\mathrm{GeV}$, $p_{\mathrm{T}}(\mu_1) > 10\,\mathrm{GeV}$	`EF_e12Tvh_medium1_mu8`
		or
		`EF_e60_medium1`

B	$14 > p_{\mathrm{T}}(e_1) > 10\,\mathrm{GeV}$, $p_{\mathrm{T}}(\mu_1) > 18\,\mathrm{GeV}$	`EF_mu18_tight_e7_medium1`
		or
		`EF_mu40_tight`

	ee channel	

A	$p_{\mathrm{T}}(e_1) > 14\,\mathrm{GeV}$, $p_{\mathrm{T}}(e_2) > 14\,\mathrm{GeV}$	`EF_2e12Tvh_loose1`
		or
		`EF_e60_medium1`

B	$p_{\mathrm{T}}(e_1) > 25\,\mathrm{GeV}$, $14 > p_{\mathrm{T}}(e_2) > 10\,\mathrm{GeV}$	`EF_e24vh_medium1_e7_medium1`
		or
		`EF_e60_medium1`

	$\mu\mu$ channel	

A	$p_{\mathrm{T}}(\mu_1) > 18\,\mathrm{GeV}$, $p_{\mathrm{T}}(\mu_2) > 18\,\mathrm{GeV}$	`EF_mu18_tight_mu8_EFFS`
		or
		`EF_mu40_tight`

B	$p_{\mathrm{T}}(\mu_1) > 18\,\mathrm{GeV}$, $18 > p_{\mathrm{T}}(\mu_2) > 14\,\mathrm{GeV}$	`EF_mu18_tight_mu8_EFFS`
		or
		`EF_2mu13`
		or
		`EF_mu40_tight`

C	$p_{\mathrm{T}}(\mu_1) > 18\,\mathrm{GeV}$, $14 > p_{\mathrm{T}}(\mu_2) > 10\,\mathrm{GeV}$	`EF_mu18_tight_mu8_EFFS`
		or
		`EF_mu40_tight`

D	$18 > p_{\mathrm{T}}(\mu_1) > 14\,\mathrm{GeV}$, $p_{\mathrm{T}}(\mu_2) > 14\,\mathrm{GeV}$	`EF_2mu13`
		or
		`EF_mu40_tight`

Table 4.5: Overview over the different triggers used in 1-lepton and 2-lepton channels. Depending on the p_{T}, the trigger combination with the highest efficiency is chosen. The index 1 (2) refers to the lepton with the highest (second highest) p_{T} in the event. In the trigger name starting with “EF” (event filter), the number behind “e” or “mu” gives the p_{T} threshold of the trigger for this lepton. A “j” in the name denotes the jet p_{T} threshold and “xe” the missing energy cut. The additional notations behind the number (e.g. “medium1”) indicate different identification requirements for the objects at trigger level.

- Veto on events with either the LAr or the tile calorimeter being flagged as problematic.
- Veto on incomplete events due to a reset in the trigger timing.
- Veto on events for which the standard procedure to recover non-operational calorimeter cells has failed.
- Veto on events with a baseline jet that failed the quality requirements ("bad jets") as described in Sec. 4.3.2. These jets arise either from hardware problems or non-collision backgrounds, like cosmic ray showers or beam halo events, and could lead to the reconstruction of large fake $E_{\mathrm{T}}^{\mathrm{miss}}$. Therefore, the affected event is rejected completely.
- Veto on events containing a badly reconstructed muon with $\sigma(q/p)/\left|(q/p)\right| > 0.2$, where q/p is the charge over momentum measured from the bending of the track inside the magnetic field and $\sigma(q/p)$ is the uncertainty of the measurement.
- Requirement on the primary vertex to have at least 5 tracks.
- Veto on events containing muons with $|z_0| > 1\,\mathrm{mm}$ and $|d_0| > 0.2\,\mathrm{mm}$ to suppress backgrounds from cosmic muons.
- Veto on events with electrons in the transition region between the endcaps and the barrel at $1.37 < |\eta| < 1.52$ ("crack veto").

In addition, a overlap removal procedure is necessary [53] as it can happen that the same baseline object is reconstructed twice as two different objects (e.g. electrons are mostly also reconstructed as jets as they are measured in the calorimeter, too):

- Two electrons overlapping with each other within $\Delta R < 0.05$: Remove the electron with lower E_{T}.
- A jet overlapping with an electron within $\Delta R < 0.2$: Remove the jet.
- A electron or muon overlapping with any of the remaining jets within $\Delta R < 0.4$: Remove the lepton.
- A electron overlapping with a muon within $\Delta R < 0.01$: Remove the electron as it possibly originates from muon bremsstrahlung.

The remaining objects are used for the final event selection of the signal, control and validation regions which is specified in Sec. 5 for the Z+jets+E_T^{miss} analysis and in Sec. 6 for the 1L+jets+E_T^{miss} analysis.

5 Search for supersymmetry in events with a Z boson, jets and large missing transverse momentum

A same-flavour opposite-sign dilepton pair from the decay of a Z boson leads to a very distinctive signal in the detector. This signature has the advantage that it suffers only very little from irreducible Standard Model backgrounds as the characteristic peak in the dilepton mass distribution around the Z mass at $\sim$91 GeV is not present e.g. in $t\bar{t}$ events.
The Z mass window is often vetoed by dilepton analyses to suppress the $Z+$jets background (compare e.g. [19]). However, various models predict the extended production of Z bosons in the decay chains of supersymmetric particles. The SUSY search in events with a leptonically decaying Z boson, jets and large missing energy targets the production of strongly interacting sparticles within these models and completes the ATLAS search program. The basic object and event selection has already been described in Sec. 4.

5.1 Motivation

The search for supersymmetry in events with a Z boson, jets and large missing transverse energy [53] mainly targets the production of gluinos in GGM models which were described in Sec. 2.2.3. An example Feynman diagram for such a signal process can be found on the left side of Fig. 5.1. In the models considered here, the gravitino $\tilde{G}$ is always the LSP, which leaves the detector unobserved leading to missing energy. The remaining phenomenology depends on the next-to-lightest SUSY particle. For this search, the GGM parameters were chosen such that a higgsino-like $\tilde{\chi}_1^0$ is the NLSP. This can have high a branching ratio (BR) for the decay $\tilde{\chi}_1^0 \rightarrow Z + \tilde{G}$.
Two signal grids are considered. In the first one, the ratio of the vacuum expectation values of the two Higgs doublets, $\tan\beta$, is set to 1.5 which results in $BR(\tilde{\chi}_1^0 \rightarrow Z + \tilde{G}) \approx 100$ % in a vast area of the parameter space. The other one has $\tan\beta = 30$ and a decreased $BR(\tilde{\chi}_1^0 \rightarrow Z + \tilde{G})$ of $\sim$60 %, while the decay $\tilde{\chi}_1^0 \rightarrow h^0 + \tilde{G}$ starts to play a role ($BR \approx 40$ %). Here, h^0 is the lightest Higgs boson with properties equivalent to the Standard Model Higgs and a mass set to 126 GeV. The dependency of these branching ratios on the model parameters can be found in Fig. 5.2.
The gluino mass $m(\tilde{g})$ and higgsino mass parameter μ are treated as free parameters in these models. Signal samples are considered in the range 600 GeV $< m(\tilde{g}) <$ 1200 GeV and 400 GeV $< m(\tilde{g}) <$ 1200 GeV for the $\tan\beta = 1.5$ and $\tan\beta = 30$ signal grid, respectively.

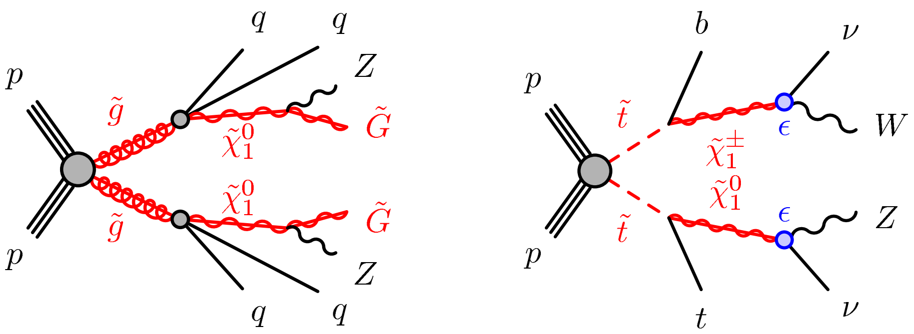

Figure 5.1: Example processes for the production of strongly interacting SUSY particles in the GGM (left) and the bRPV model (right) with subsequent decays to a Z boson, jets and missing energy [53, 133].

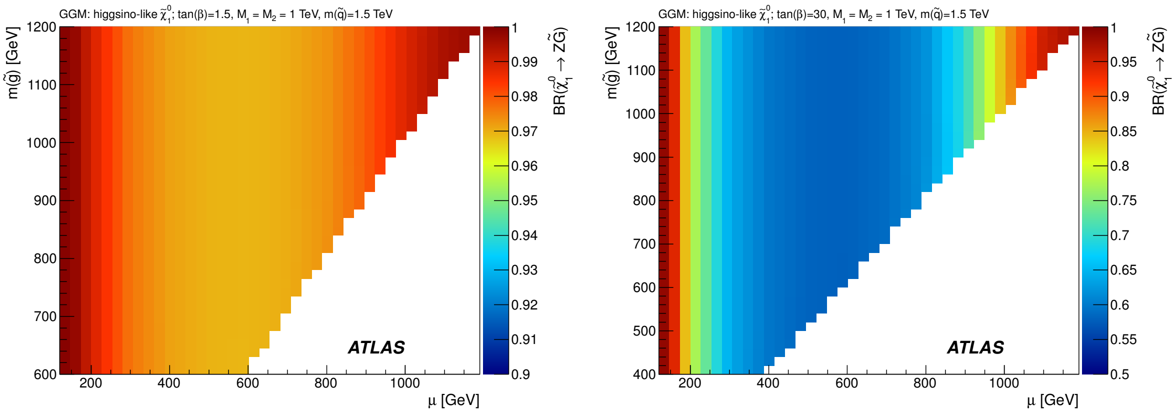

Figure 5.2: Branching fractions for the decay $\tilde{\chi}_1^0 \rightarrow Z + \tilde{G}$ in the plane of the gluino mass $m(\tilde{g})$ versus the higgsino mass parameter μ for the GGM model with $\tan\beta = 1.5$ (left) and $\tan\beta = 30$ (right) [134]. In the remaining cases, the neutralino decays via $\tilde{\chi}_1^0 \rightarrow h^0 + \tilde{G}$.

The value of μ was varied between 120 GeV and ($m(\tilde{g})-10$ GeV). As μ is positive, the neutralino dominantly decays into a Z boson and a gravitino.
The masses of all other squarks and sleptons are set to ~1.5 TeV, while the $U(1)$ and $SU(2)$ gaugino mass parameters M_1 and M_2 are fixed to 1 TeV. The mass of the gravitino is chosen to be small enough so that the $\tilde{\chi}_1^0$ decay is prompt, as signatures with displaced decay vertices require dedicated analysis strategies and are not the goal of this search. The neutralino life time, $c\tau_{\text{NLSP}}$, can go up to 2 mm for $\mu = 120$ GeV, while it is well below 0.1 mm for $\mu \geq 150$ GeV, where this analysis is most sensitive.
For the optimization and interpretation of the Z+jets+E_T^{miss} analysis, simulated events of GGM signal processes are generated. SUSPECT 2.41 [135] and SDECAY 1.3 [136] are used to calculate mass spectra and decay properties of the SUSY particles. An MC simulation of multiple GGM parameter points is carried out with PYTHIA 6.423 and the MRST 2007 LO* PDF set [137] and the AUET2 tune for the underlying event. The generated signal events are passed through a fast simulation of the ATLAS detector (compare Sec. 4.2.2). Signal cross-sections are calculated at NLO+NLL [138–142] accuracy. The nominal cross-section

and its uncertainties are retrieved as recommended by the ATLAS SUSY group [143, 144]. The calculations are performed with two different PDF sets (MSTW and CTEQ). For each PDF, the maximum and minimum cross-section is calculated for the cases when the PDF is varied within its uncertainties, when the renormalisation and factorisation scales are changed and when α_S is varied. The total uncertainty for the MSTW and the CTEQ calculation is estimated from the quadratic sum of all variations. The largest upward and downward error from the two is taken for the uncertainty of the cross-section and the value midway between them is used as the nominal cross-section. Details about the signal cross-section and its experimental uncertainty can be found in App. B.

Due to the choice of parameters, the strong production of gluinos is the dominant production mode. Electro-weak production of the lightest gaugino pairs is also included in the MC simulation. However, the analysis is little sensitive to the latter processes, as the number of high-energy jets in the final state is strongly reduced there and other searches, like [145], show better results.

In principle, the bRPV model described in Sec. 2.2.2 also predicts signatures with a Z boson, jets and missing energy. A possible signal process is shown in the diagram on the right-hand side of Fig. 5.1. However, it became apparent that this analysis has only limited sensitivity to the bRPV model as it is a full phenomenological model including diverse production and decay modes. Therefore, more inclusive search strategies as in [19, 146] give better results.

5.2 Analysis optimization

The event selection for the signal regions of the Z+jets+E_T^{miss} analysis is optimized following the procedure described in Sec. 4.1. To determine the expected sensitivity of the analysis, an approximation for the expected discovery significance, Z, is used [88]:

$$Z = \sqrt{2\left((s+b)\ln\left(1+\frac{s}{b}\right)-s\right)}, \tag{5.1}$$

where s (b) is the expected number of signal (background) events. This definition is preferred to a simple $s/\sqrt{b}$ ratio as it approximates the sensitivity more correctly in regions where s and b are of the same order of magnitude. It gives a rough estimate which significance (expressed in numbers of Gaussian standard deviations) the signal would have relative to the background when the systematic uncertainty on b is small.

For the optimization procedure, events with a same-flavour opposite-sign electron or muon pair with an invariant mass, $m_{\ell\ell}$, between 81 GeV and 101 GeV are preselected as this signature is expected from the decay of the Z boson targeted by this analysis. If there are more than two leptons in the event, the charge, flavour and $m_{\ell\ell}$ requirements are applied to the two leptons with the highest p_{T}. There is no veto on additional electrons or muons.

The lepton with the highest p_{T} (referred to as leading lepton) must have $p_{\mathrm{T}} > 25$ GeV and the subleading lepton $p_{\mathrm{T}} > 10$ GeV. This is necessary to be in a phase space where the combination of different lepton triggers (compare Sec. 4.4) has reached its maximum efficiency.

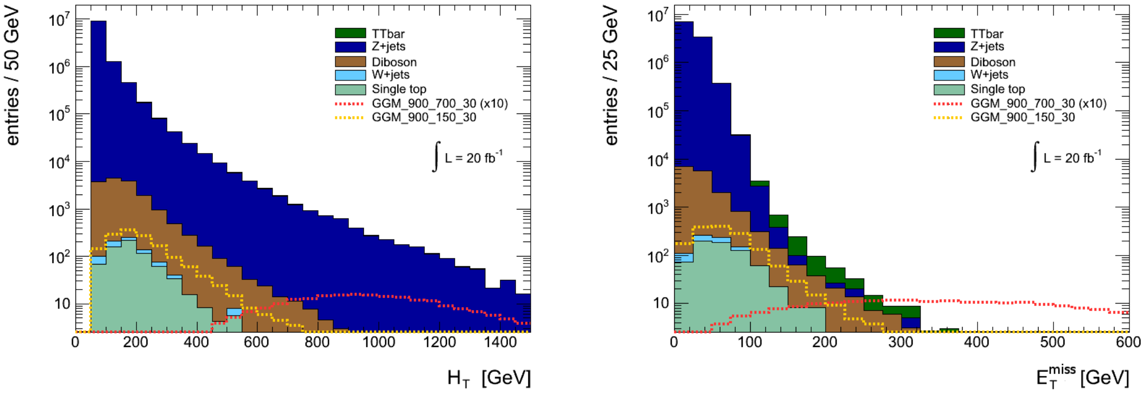

Figure 5.3: Distributions of H_{T} (left) and $E_{\mathrm{T}}^{\mathrm{miss}}$ (right) for the dominant background processes estimated from MC. Two GGM signal models with $m(\tilde{g}) = 900\,\mathrm{GeV}$ and $\tan\beta = 30$ are overlaid for comparison. The dashed red line shows the signal for $\mu = 700\,\mathrm{GeV}$ (scaled by a factor of 10 for better visibility) and the yellow line corresponds to $\mu = 120\,\mathrm{GeV}$.

The signal region optimization is performed assuming the integrated luminosity of the 2012 ATLAS dataset of $20.3\,\mathrm{fb}^{-1}$ and the following variables are altered:

- Minimum number of signal jets: 0, 1, …, 5
- Minimum $E_{\mathrm{T}}^{\mathrm{miss}}$ cut: 50 GeV, 75 GeV, …, 400 GeV
- Minimum H_{T} cut: 200 GeV, 300 GeV, …, 1200 GeV

The definition of H_{T} used here includes the p_{T} of all signal jets and the two leading leptons (compare Eq. (4.1)). All these quantities are suitable to distinguish between signal and background processes as it can be seen for H_{T} and $E_{\mathrm{T}}^{\mathrm{miss}}$ from Fig. 5.3. There, the expected background is shown together with two signal points. For high values of the higgsino mass parameter μ, the signal peaks at higher H_{T} and $E_{\mathrm{T}}^{\mathrm{miss}}$ values than the background. However, the shape of the background and the signal distribution becomes much more similar for low μ values, where the lightest charginos and neutralinos have smaller masses. This is due to two effects: First, the direct production of charginos and neutralinos becomes the dominant production process there, which leads to the reduction of the hadronic activity in the event. Second, the Z boson and the $\tilde{G}$ from the neutralino decay are less boosted and hence the missing energy and the momenta of the leptons are lower compared to models with a higher μ value.
The estimated significance Z from Eq. (5.1) is calculated for each combination of cuts on the number of jets, H_{T} and $E_{\mathrm{T}}^{\mathrm{miss}}$. The prediction of the background b is based on MC simulations only. For the expected signal s, simulated events of a few benchmark points from the GGM model, which lie close to the exclusion limit of the previous analysis [18], were chosen. It is sufficient to use points from the model with $\tan\beta = 30$ as the branching ratio for the decay $\tilde{\chi}_1^0 \to Z + \tilde{G}$ is increasing for decreasing $\tan\beta$. So the expected sensitivity for the signal model with $\tan\beta = 1.5$ will be even higher.

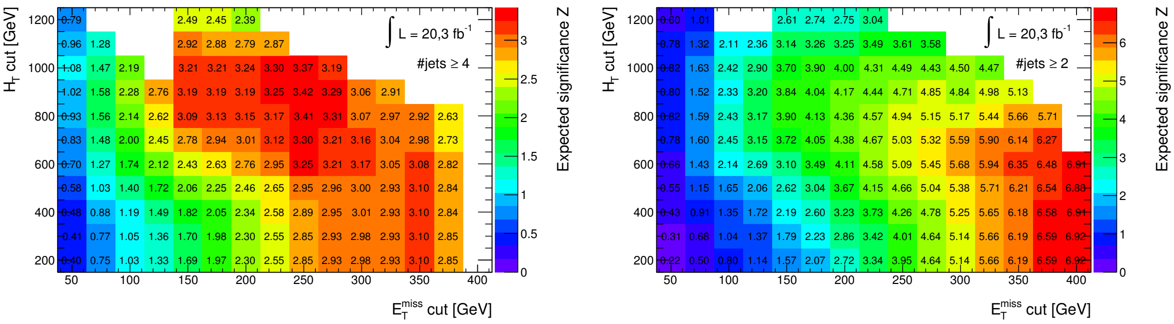

Figure 5.4: Expected significances Z for varying cuts on H_T and $E_\mathrm{T}^\mathrm{miss}$. The results for the signal point with $m(\tilde{g}) = 900\,\mathrm{GeV}$, $\mu = 500\,\mathrm{GeV}$ and $\tan\beta = 30$ for events with at least four jets are shown on the left, while the right plot uses the $m(\tilde{g}) = 900\,\mathrm{GeV}$, $\mu = 800\,\mathrm{GeV}$, $\tan\beta = 30$ signal point and events with at least two jets. In white bins, the signal prediction is zero or the uncertainty on the background estimation due to the limited number of MC events is greater than 30 %. In the area where the maximum of the expected significance appears, at least two background events are predicted in all cases.

The Z values for two example signal points with $m(\tilde{g}) = 900\,\mathrm{GeV}$ and $\mu = 500\,\mathrm{GeV}$ or $800\,\mathrm{GeV}$, respectively, are shown in Fig. 5.4. It can be seen that the expected sensitivity increases when the cuts on H_T and $E_\mathrm{T}^\mathrm{miss}$ are tightened as the number of background events decreases faster than the number of signal events. At some point, also most of the signal is rejected by the cuts and the significance decreases again. A similar behaviour is also observed when the cut on the number of jets is tightened. For a given gluino mass, the optimal H_T cut decreases the larger μ is, while the optimal $E_\mathrm{T}^\mathrm{miss}$ requirement increases.

There is a correlation between H_T, $E_\mathrm{T}^\mathrm{miss}$ and the number of jets as all variables are influenced by the kinematics of the SUSY decays. Thus, similar sensitivities can be achieved by tightening one cut while loosening another cut at the same time. Due to these correlations, adding more variables to optimization procedure, like the momenta of the jets, does not improve the results.

In the end, three signal regions are optimized such that they cover a wide range of models and different areas of the parameter space. Also, the reliability of the background prediction is taken into account and only cut combinations with a relative statistical uncertainty on b of less than 30 % are used in the optimization process. The definitions of the regions (called SR-Z, SR-2 and SR-3) are given in Tab. 5.1. SR-Z targets GGM models with high μ values, while SR-2 is designed for GGM models with low and intermediate μ parameters. SR-3 is optimized for a cMSSM model with additional bRPV terms in the superpotential (compare Sec. 2.2.2 and 2.2.3).

For the final analysis, only the results from SR-Z are used as it became apparent that other analyses exceed the sensitivity for the models SR-2 and SR-3 were aiming at. As discussed above, the sensitivity of the Z+jets+$E_\mathrm{T}^\mathrm{miss}$ analysis for GGM models with very low μ values is limited and analyses without explicit jet requirements, like [145], perform better in this area of the parameter space. In the intermediate μ range SR-Z and SR-2 have similar sensitivity. A search for SUSY in events with two same-sign or three leptons [146] shows better results for bRPV models.

Furthermore, a discrepancy between data and simulation in the $E_\mathrm{T}^\mathrm{miss}$ reconstruction is ob-

Region	$E_{\mathrm{T}}^{\text{miss}}$ [GeV]	H_{T} [GeV]	n_{jets}
SR-Z	> 225	> 600	≥ 2
SR-2	> 150	> 900	≥ 4
SR-3	> 100	> 900	≥ 5

Table 5.1: Overview of the signal regions SR-Z, SR-2 and SR-3. All regions require an opposite-sign same-flavour lepton pair (e^+e^- or $\mu^+\mu^-$) with an invariant dilepton mass 81 GeV $< m_{\ell\ell} <$ 101 GeV. The leading lepton must have $p_{\mathrm{T}} > 25\,\text{GeV}$ and the subleading $p_{\mathrm{T}} > 10\,\text{GeV}$. The results from SR-2 and SR-3 are omitted from the further discussion for the reasons mentioned in the text.

served in the phase space at high H_{T} and high jet multiplicity, where SR-2 and SR-3 are located. The $E_{\mathrm{T}}^{\text{miss}}$ distributions of the muon channel show a dip in the MC-to-data comparison in the region between ~50 GeV and ~100 GeV in validation regions identical to SR-2 and SR-3 but with the $E_{\mathrm{T}}^{\text{miss}}$ cut inverted (denoted as VRZ 2 and VRZ 3). This dip is not visible in the electron channel as shown in Fig. 5.5.

As VRZ 2 and VRZ 3 have a large overlap, the observed discrepancies have the same origin. The significance of the deviations is more than 2σ in several consecutive bins so it is unlikely that they are caused by statistical fluctuations. The discrepancies arise only for very high requirements on H_{T} and on the number of jets as it can be seen from Fig. 5.7 and 5.6 where the same $E_{\mathrm{T}}^{\text{miss}}$ distributions are shown but in different bins of H_{T} and for different jet multiplicities, respectively. The origin of the $E_{\mathrm{T}}^{\text{miss}}$ mismodelling in simulations could not be completely understood on the timescale of this analysis. Hence, SR-2 and SR-3 are omitted for the results presented in Sec. 5.3 to 5.7.

A set of control and validation regions is defined close to SR-Z by loosening one or several of the cuts on H_{T}, $E_{\mathrm{T}}^{\text{miss}}$ or $m_{\ell\ell}$. The event selection of all regions is summarised in Tab. 5.2. A sketch of their position in phase space relative to each other is shown in Fig. 5.8. All regions require at least two opposite-sign leptons and the leading (subleading) lepton must fulfil $p_{\mathrm{T}} > 25\,\text{GeV}$ ($p_{\mathrm{T}} > 10\,\text{GeV}$). A minimum cut of $m_{\ell\ell} > 15\,\text{GeV}$ is applied to suppress backgrounds from the decays of low-mass resonances (e.g. J/ψ) and Drell-Yan processes. The naming convention for the VRs and CRs is the following: regions with a “T” in their name target background from $t\bar{t}$ production, while regions with a “Z” are enriched with $Z+\text{jets}$ background. There are also regions with a mixed background composition, denoted as “TZ”. It has to be noted that a cut on the azimuthal angle between the two jets with the highest energy and $E_{\mathrm{T}}^{\text{miss}}$ of $\Delta\phi(\text{jet}_{1,2}, E_{\mathrm{T}}^{\text{miss}}) > 0.4$ has been added to SR-Z after optimization as well as to all VRs and CRs besides regions enriched with $Z+\text{jets}$ background. This cut suppresses background events with high fake $E_{\mathrm{T}}^{\text{miss}}$ in the case the energy of a single highly energetic jet is underestimated. The effect will be discussed further in Sec. 5.3. The case that the energy of a highly energetic jet is measured too high is less likely. Backgrounds with fake $E_{\mathrm{T}}^{\text{miss}}$ due to the overestimation of the jet energy could be suppressed by a cut on $\Delta\phi(\text{jet}, E_{\mathrm{T}}^{\text{miss}}) < (\pi - 0.4)$. However, such a cut would also remove a significant part of the expected signal and is thus not applied (compare Sec. 5.5).

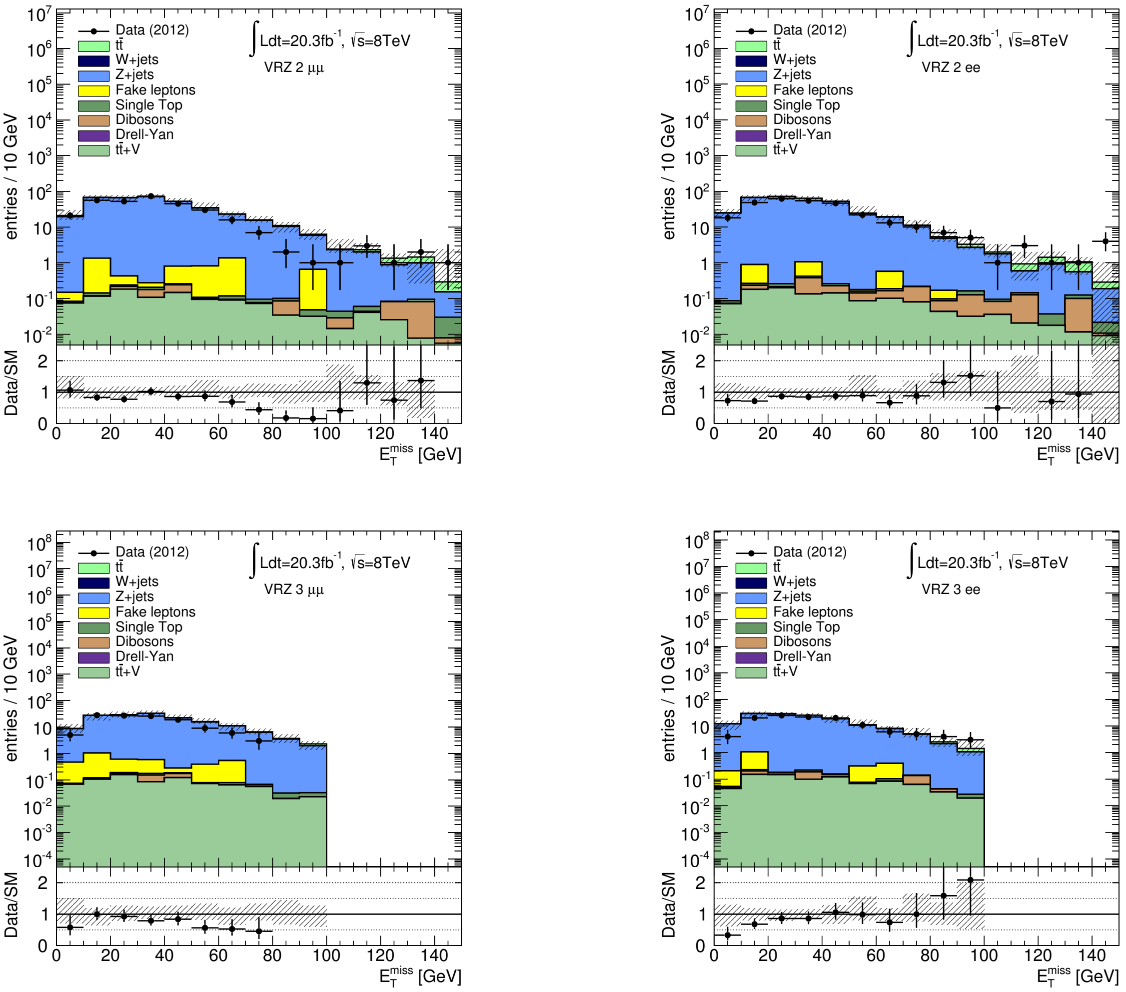

Figure 5.5: MC-to-data comparison for the $E_{\mathrm{T}}^{\mathrm{miss}}$ distribution in the validation regions VRZ 2 (top) and VRZ 3 (bottom) for the muon (left) and the electron channel (right). A dip in the data to MC agreement between $\sim$50 GeV and $\sim$100 GeV is observed in $\mu\mu$ events only. All detector related systematic uncertainties described in Sec. 5.4 as well as the uncertainties due to limited MC statistics are included in the hatched error band.

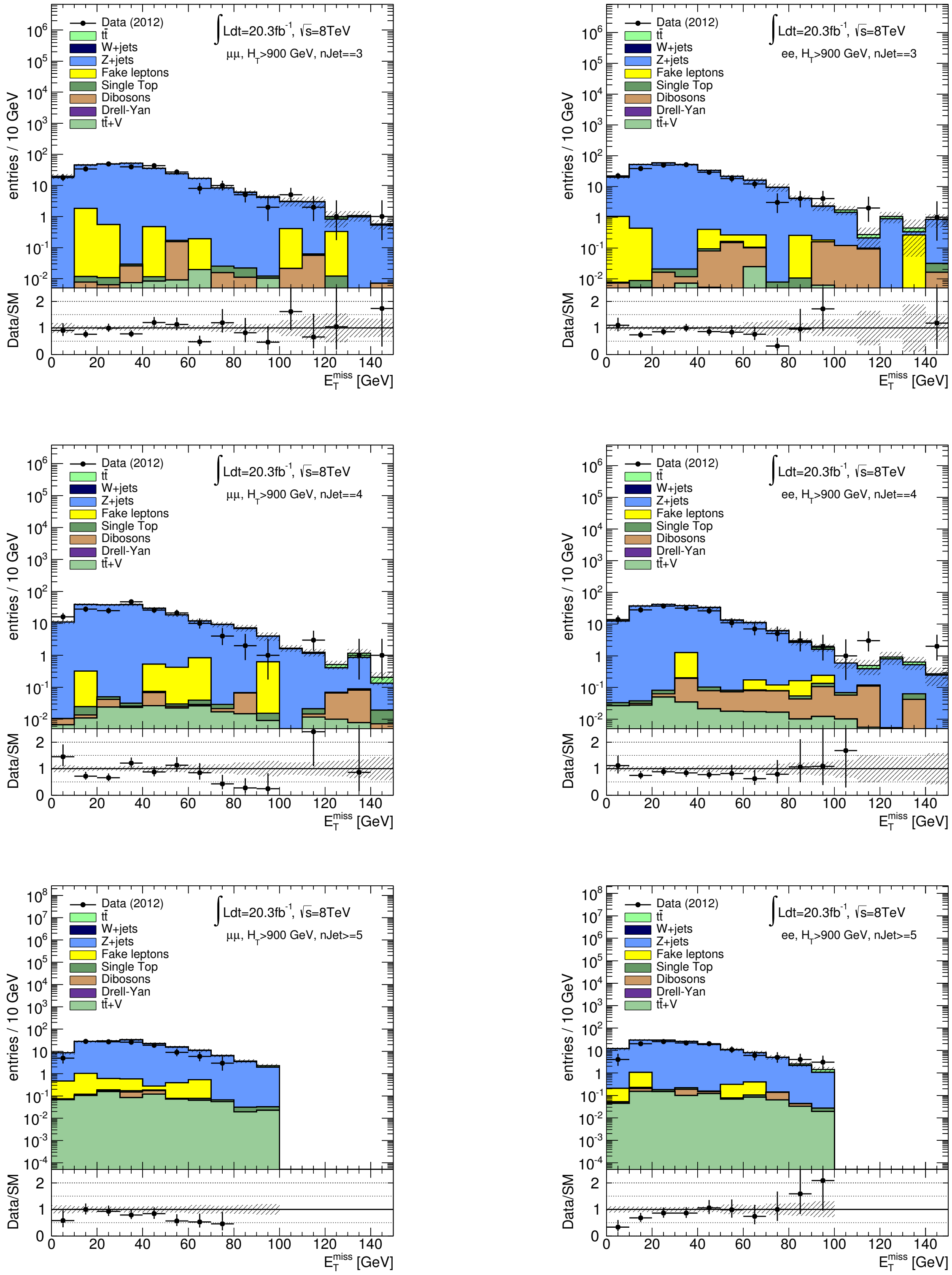

Figure 5.6: MC-to-data comparison for the $E_{\mathrm{T}}^{\mathrm{miss}}$ distribution in the muon (left) and the electron channel (right) for $H_T > 900\,\mathrm{GeV}$ and different jet multiplicities: #jets=3 (top), #jets=4 (middle) and #jets≥5 (bottom). The dip between ∼50 GeV and ∼100 GeV is only observed in the $\mu\mu$ channel for events with high jet multiplicity. Only statistical uncertainties are included in the error band.

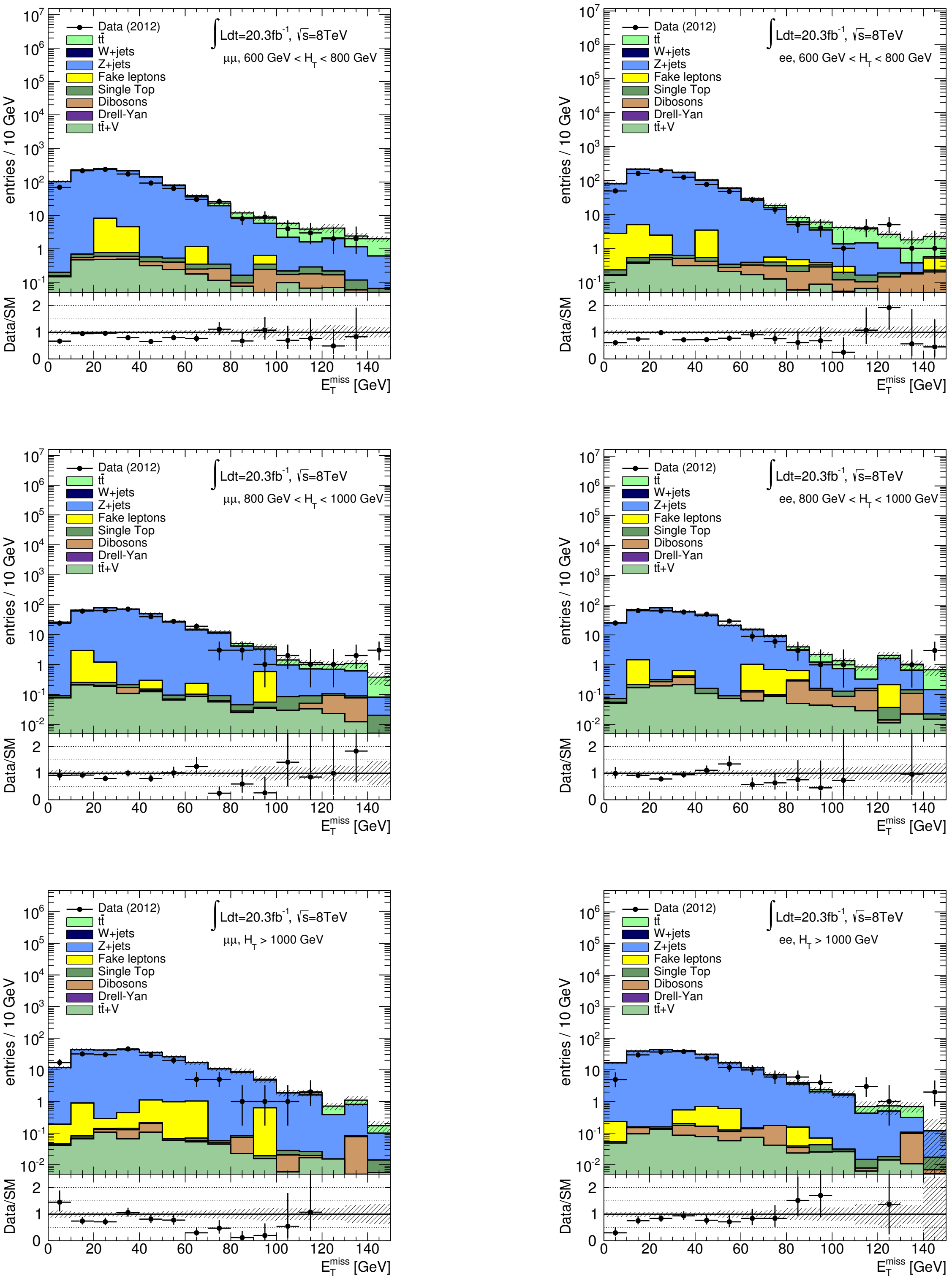

Figure 5.7: MC-to-data comparison for the $E_{\mathrm{T}}^{\mathrm{miss}}$ distribution in the muon (left) and the electron channel (right) for #jets≥4 and different H_T bins: $600\,\mathrm{GeV} < H_T < 800\,\mathrm{GeV}$ (top), $800\,\mathrm{GeV} < H_T < 1000\,\mathrm{GeV}$ (middle) and $H_T > 1000\,\mathrm{GeV}$ (bottom). The dip between ~50 GeV and ~100 GeV is only observed in the $\mu\mu$ channel for events with $H_T > 800\,\mathrm{GeV}$. Only statistical uncertainties are included in the error band.

Region	$E_{\text{T}}^{\text{miss}}$ [GeV]	H_{T} [GeV]	n_{jets}	$m_{\ell\ell}$ [GeV]	SF/DF	$\Delta\phi(\text{jet}_{1,2}, E_T^{\text{miss}})$
Signal regions						
SR-Z	> 225	> 600	≥ 2	$81 < m_{\ell\ell} < 101$	SF	> 0.4
Control regions						
CReμ	> 225	> 600	≥ 2	$81 < m_{\ell\ell} < 101$	DF	> 0.4
CRT	> 225	> 600	≥ 2	$m_{\ell\ell} \notin [81, 101]$	SF	> 0.4
Validation regions						
VRZ	< 150	> 600	≥ 2	$81 < m_{\ell\ell} < 101$	SF	-
VRT	$150 < E_{\text{T}}^{\text{miss}} < 225$	> 500	≥ 2	$m_{\ell\ell} \notin [81, 101]$	SF	> 0.4
VRTZ	$150 < E_{\text{T}}^{\text{miss}} < 225$	> 500	≥ 2	$81 < m_{\ell\ell} < 101$	SF	> 0.4
VRT_highHT	$150 < E_{\text{T}}^{\text{miss}} < 225$	> 600	≥ 2	$m_{\ell\ell} \notin [81, 101]$	SF	> 0.4
VRTZ_highHT	$150 < E_{\text{T}}^{\text{miss}} < 225$	> 600	≥ 2	$81 < m_{\ell\ell} < 101$	SF	> 0.4
VRT_highMET	> 225	$400 < H_{\text{T}} < 600$	≥ 2	$m_{\ell\ell} \notin [81, 101]$	SF	> 0.4
VRTZ_highMET	> 225	$400 < H_{\text{T}} < 600$	≥ 2	$81 < m_{\ell\ell} < 101$	SF	> 0.4

Table 5.2: Overview of all signal, control and validation regions used in the Z+jets+E_T^{miss} analysis. The flavour combination of the dilepton pair is denoted as "SF" for same-flavour or "DF" for different-flavour. The preselection for all regions is: At least two opposite-sign leptons, leading lepton $p_{\text{T}} > 25\,\text{GeV}$, subleading lepton $p_{\text{T}} > 10\,\text{GeV}$, $m_{\ell\ell} > 15\,\text{GeV}$. Regions with a "T" in their name are enriched with $t\bar{t}$ background, regions with a "Z" target Z + jets processes, while regions with "TZ" have a mixed background composition.

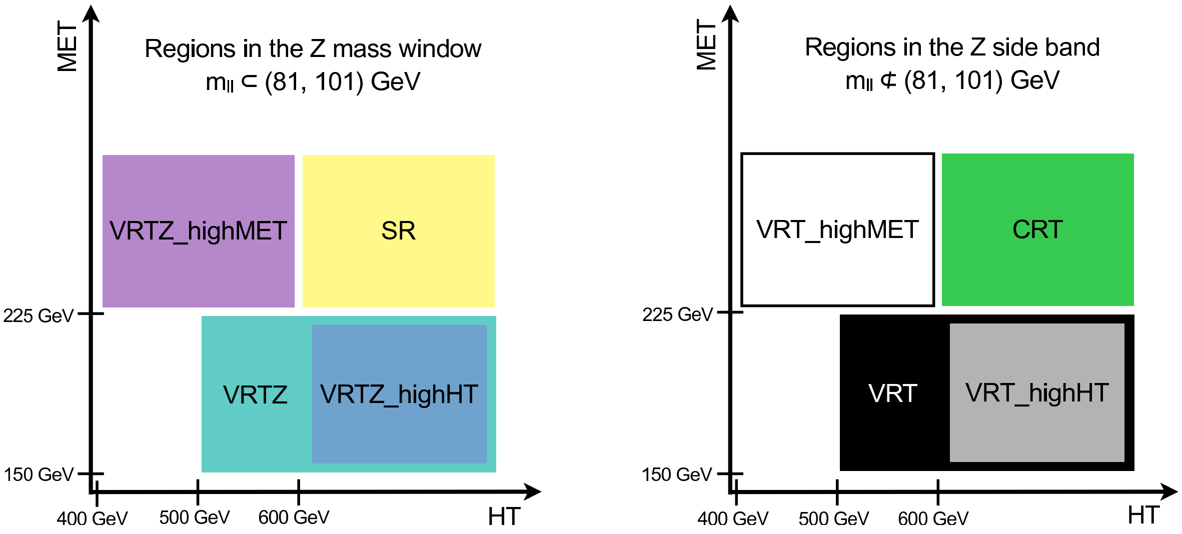

Figure 5.8: Sketch with the relative position of the signal, control and validation region of the Z+jets+E_T^{miss} analysis in the plane H_{T} vs. $E_{\text{T}}^{\text{miss}}$ (denoted as "MET" here). The regions in the Z mass window are shown on the left side, while the Z mass sidebands are summarised on the right [132].

5.3 Background estimation

The main backgrounds for the Z+jets+E_T^{miss} analysis are Z+jets, $t\bar{t}$, fake lepton and WZ/ZZ events. The first three of them are estimated in a data driven way, while MC simulations are used for the latter.

Standard Model processes with leptonically decaying Z bosons in association with jets can mimic the signal signature under study as they show the same peak in the invariant dilepton mass. Although no genuine missing energy is expected there, large $E_{\mathrm{T}}^{\text{miss}}$ can be reconstructed by mistake if the energy of one or more of the jets is mismeasured by a large amount. To account for this background the jet smearing method is used. For this, the detector response to jets is modelled with a set of dedicated functions which are used to smear well measured jets in data events. The method is favoured over the MC prediction as detector effects are usually difficult to model in computer simulations. Furthermore, it is difficult to generate sufficient MC statistics to estimate the rare cases of dramatically wrong jet energy measurements. The details about the jet smearing method are presented in Sec. 5.3.1.

Dileptonic final states from $t\bar{t}$ as well as WW, $W+t$ and $Z \rightarrow \tau\tau$ production are flavour symmetric where the number of e^+e^-, $\mu^+\mu^-$ and $e^\pm\mu^\mp$ events fulfils the relation 1:1:2. The contribution from the GGM model is expected to be negligible in the $e^\pm\mu^\mp$ channel. So different-flavour events are not used in the signal region and a statistically independent control region CReμ can be constructed (compare Tab. 5.2). The flavour symmetric background can be estimated from the data in CReμ in a data-driven way. This will be described in Sec. 5.3.2 in more detail.

Other backgrounds arise from events with fake leptons. In most of these cases, there is one real prompt lepton in the event (e.g. from the decay of a W boson) and additionally another electron or muon is reconstructed by mistake. This can be caused by the misidentification of jets, non-prompt leptons from heavy flavour decays, which pass the isolation requirements for signal leptons specified in Sec. 4.3.4 and 4.3.3, or the conversion of photons. All these effects are denoted as fake leptons and are estimated with the matrix method which will be described in Sec. 5.3.3.

Backgrounds from WZ and ZZ processes as well as the production of top quarks in association with additional vector bosons are predicted using MC simulations (see Sec. 5.3.4). Rare backgrounds from triboson and $Z+\gamma$ processes as well as from Higgs bosons decaying into WW or ZZ are neglected as they have been found to contribute less than 0.1 %.

The complete background estimate is summarised at the end of the section in Tab. 5.9.

5.3.1 $Z+$jets background

In background events with a leptonically decaying Z boson in association with jets, there is no real missing energy expected. If, however, one or more of the objects in the corresponding event are mismeasured, fake missing energy can occur and events like this can enter the signal regions. As such detector effects are usually difficult to model in computer simulations, this background is estimated with the data-driven jet smearing method [132, 147] which proceeds in the following steps:

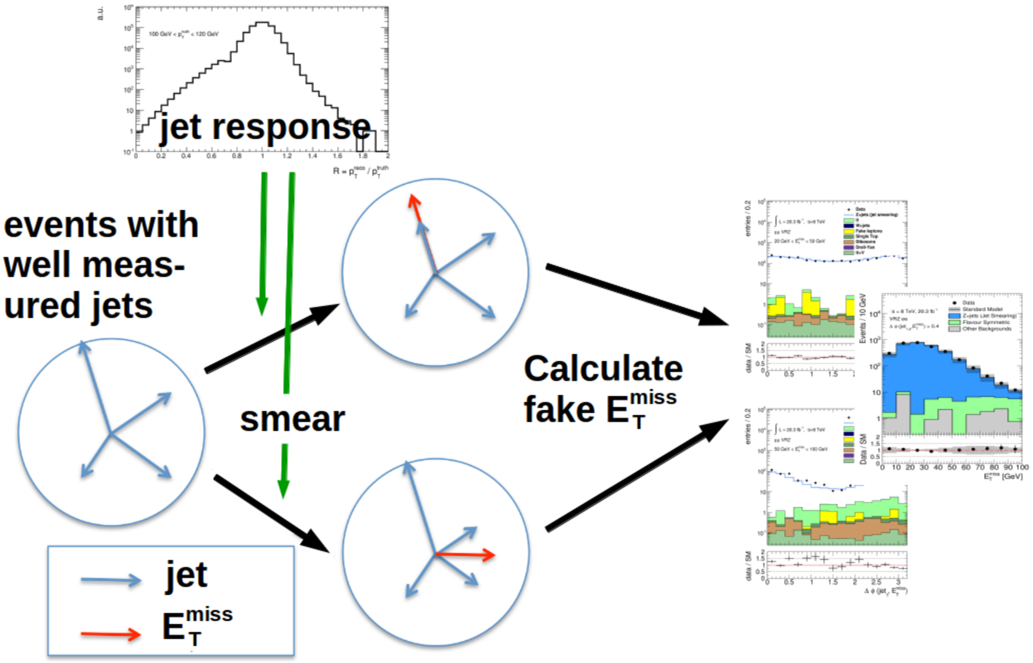

Figure 5.9: Sketch of the jet smearing method. Data events with well measured jets are smeared using functions modelling the detector response to jets. The missing energy is recalculated from the smeared jets to estimate the distribution of fake $E_\mathrm{T}^\mathrm{miss}$ from mismeasured jets.

- Definition of a seed region in data where Z + jets events with well measured jets are selected.

- Smearing of the momentum and direction of the jets in the seed events with a function modelling the detector response to jets. These smeared data events are referred to as pseudo data.

- Recalculation of $E_\mathrm{T}^\mathrm{miss}$ using the smeared p_T and ϕ values of the jets to get the distribution of the fake missing energy.

- Normalisation of pseudo data to data in the low missing energy region with $10\,\mathrm{GeV} < E_\mathrm{T}^\mathrm{miss} < 50\,\mathrm{GeV}$ where the impact of large jet mismeasurements is small.

These steps are illustrated in the sketch in Fig. 5.9. The application of this method to the Z + jets background relies on the assumption that the lepton energy and momentum measurements are better than those for jets and mismeasured jets are thus the dominant source of fake $E_\mathrm{T}^\mathrm{miss}$. This is especially true for this analysis as the signal region selection requires the two leptons to be compatible with coming from a Z boson. Events with badly measured leptons would fail the cut on the invariant dilepton mass of $81\,\mathrm{GeV} < m_{\ell\ell} < 101\,\mathrm{GeV}$ and would not be selected. Furthermore, the lepton energy resolution has been studied as shown in Sec. 5.6.3 and has been found to have a negligible impact on the background estimation in the signal region.

Response functions and smearing procedure

For the method, functions which model the detector response to jets are needed. The response R is defined as the ratio of the reconstructed jet momentum, $p_{\mathrm{T}}^{\mathrm{reco}}$, to the true momentum, $p_{\mathrm{T}}^{\mathrm{true}}$:

$$R = \frac{p_{\mathrm{T}}^{\mathrm{reco}}}{p_{\mathrm{T}}^{\mathrm{true}}} \, . \tag{5.2}$$

The true jet p_{T} refers to the momentum which the jet originating from the hard scattering process really has, while $p_{\mathrm{T}}^{\mathrm{reco}}$ is the momentum which was reconstructed from the signals in the detector. As the value of $p_{\mathrm{T}}^{\mathrm{true}}$ is unknown for jets measured in data, the jet response is first estimated from simulated dijet events generated with Pythia where the true jet p_{T} can be calculated at particle level. Different response functions are derived in bins of the true jet p_{T}. Separate response functions are used for b-tagged and non-b-tagged jets to account also for neutrinos from heavy flavour decays.

The MC response functions are then tuned to data in two dedicated analyses. First, the Gaussian core of the response is fitted in a dijet balance analysis. For this, events with two back-to-back jets with momenta $p_{\mathrm{T}}^{\mathrm{jet1}}$ and $p_{\mathrm{T}}^{\mathrm{jet2}}$ are selected, in which $E_{\mathrm{T}}^{\mathrm{miss}}$ is less than 10 % of the average p_{T} of the two jets. The distribution of the asymmetry A

$$A = \frac{p_{\mathrm{T}}^{\mathrm{jet1}} - p_{\mathrm{T}}^{\mathrm{jet2}}}{p_{\mathrm{T}}^{\mathrm{jet1}} + p_{\mathrm{T}}^{\mathrm{jet2}}} \tag{5.3}$$

can be fitted with a Gaussian function where the width gives an estimate of the jet energy resolution. The widths of the cores of the MC response functions are subsequently adjusted to match the widths observed in data.

After that, the non-Gaussian tails of the detector response are tuned to data by using events with three jets where the missing energy can be associated with one of the jets unambiguously. This means that $E_{\mathrm{T}}^{\mathrm{miss}}$ points in the direction of one of the jets or in the opposite direction. The true jet p_{T} for this jet can be approximated with $p_{\mathrm{T}}^{\mathrm{true}} = E_{\mathrm{T}}^{\mathrm{miss}} + p_{\mathrm{T}}^{\mathrm{reco}}$ and the tails of the jet response can be modelled using this to calculate R. Examples for the jet response can be found in Fig. 5.10 where the two-dimensional map of the functions versus the true jet p_{T} is shown together with one jet p_{T} slice from this map. As expected, the detector response has a dominant Gaussian peak centred around one which means that the jet energy is measured correctly most of the time. There are, however, non-Gaussian tails especially to the lower side of the response functions. These reflect the fact that the jet energy can be mismeasured dramatically by more than 30 % with a small but finite probability.

For the smearing, a random number is drawn from the appropriate response function by setting the true p_{T} equal to the reconstructed p_{T} for the jets in the seed events. The momentum vector of the jet is scaled by this number. It was found that it is not sufficient to smear only the magnitude of the momentum vector but also its ϕ direction must be varied. This is due to the fact that the jet axis would not remain the same if a large fraction of the jet energy was missed in the calorimeter measurement. For this, a similar dijet analysis as described above is performed where the jets are not required to be back-to-back any longer. The $\Delta\phi$ distribution of the two jets is fitted with a Gaussian distribution centred around 0. The corrections to the ϕ direction of the smeared jets are taken from this function.

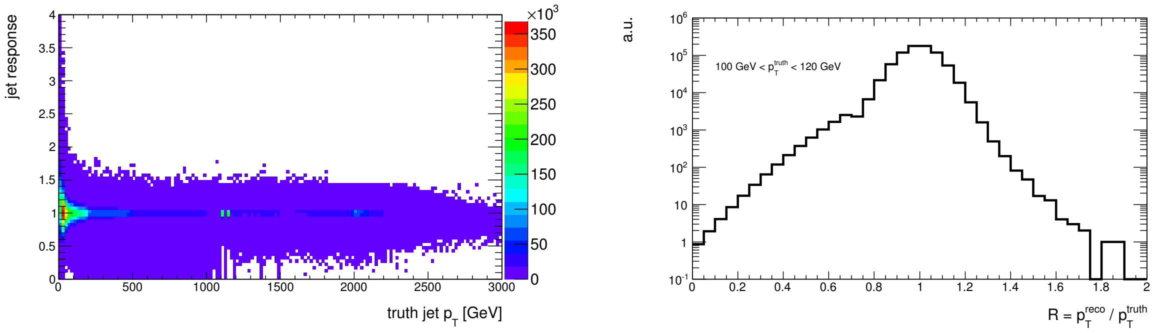

Figure 5.10: The response function map for the jet smearing method for non-b-tagged jets. All bins of the true jet p_{T} are shown on the left, while one slice for $100\,\mathrm{GeV} < p_T^{\mathrm{true}} < 120\,\mathrm{GeV}$ as example is presented on the right.

After the smearing procedure the smeared missing energy, $E_{\mathrm{T,smeared}}^{\mathrm{miss}}$, is calculated in the following way:

$$E_{\mathrm{T,smeared}}^{\mathrm{miss}} = \left| \vec{E}_{\mathrm{T,unsmeared}}^{\mathrm{miss}} - \sum_{\mathrm{jets}} \vec{p}_{\mathrm{T,smeared}} + \sum_{\mathrm{jets}} \vec{p}_{\mathrm{T,unsmeared}} \right| , \tag{5.4}$$

where $\vec{E}_{\mathrm{T,unsmeared}}^{\mathrm{miss}}$ is the missing energy vector of the original unsmeared seed event and $\vec{p}_{\mathrm{T,smeared}}$ ($\vec{p}_{\mathrm{T,unsmeared}}$) are the p_{T} vectors of the jets after (before) smearing. The sum runs over all baseline jets in the seed event. To minimise the statistical uncertainty of the jet smearing method, a high number of pseudo data events, N_{smear}, can be generated from each seed event. N_{smear} was chosen to be 1000 for this analysis. For this reason, the method cannot predict the total normalisation of the fake $E_{\mathrm{T}}^{\mathrm{miss}}$ distribution. Hence, the smeared pseudo data are normalised to data in the low $E_{\mathrm{T}}^{\mathrm{miss}}$ range $10\,\mathrm{GeV} < E_{\mathrm{T}}^{\mathrm{miss}} < 50\,\mathrm{GeV}$ of VRZ, where the influence of large jet mismeasurements is small.

Selection of seed events

The selection of seed events for smearing starts from the Z validation region VRZ, defined in Tab. 5.2, to ensure that the event topology is similar to the signal region. It is essential for the jet smearing method to select only data events with well measured jets as seeds in order not to double count detector effects in the smearing step. To ensure that only jets with a correct energy measurement are used, events with balanced jets and little $E_{\mathrm{T}}^{\mathrm{miss}}$ are selected. However, a direct upper cut on the missing energy can introduce a bias in the jet p_T distribution between seed and validation/signal regions as high fake $E_{\mathrm{T}}^{\mathrm{miss}}$ usually originates from highly energetic jets. The selection of low $E_{\mathrm{T}}^{\mathrm{miss}}$ events as seeds would thus result in a jet p_T spectrum which is too soft. To avoid this, a cut on the $E_{\mathrm{T}}^{\mathrm{miss}}$ significance is applied instead to select seed events. The $E_{\mathrm{T}}^{\mathrm{miss}}$ significance is defined in the following

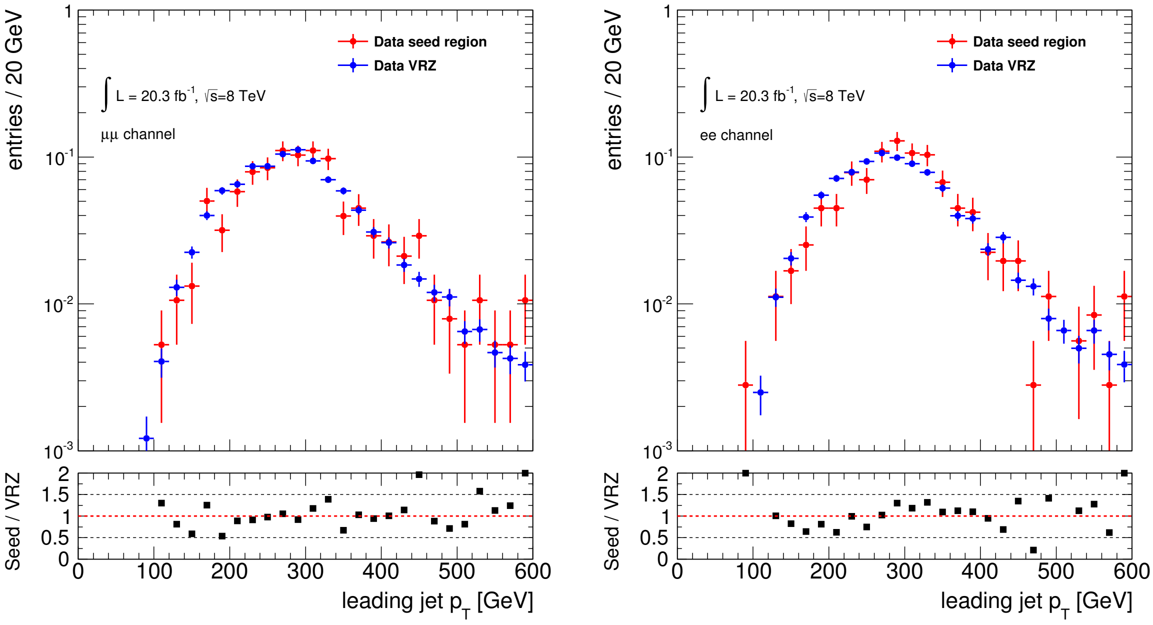

Figure 5.11: Comparison between the shapes of the normalised leading jet p_{T} distribution in the seed region and VRZ for the muon (left) and electron channel (right) in data. The main difference between the two regions is the additional cut on E_T^{miss} significance < 0.9 for the seed region.

way:

$$E_{\mathrm{T}}^{\mathrm{miss}} \text{ significance} = \frac{E_{\mathrm{T}}^{\mathrm{miss}}}{\sqrt{\sum\limits_{\mathrm{jets}} |\vec{E_T}| + \sum\limits_{\mathrm{soft}} |\vec{E_T}|}} \,. \tag{5.5}$$

The denominator is a rough estimate for the uncertainty of the energy measurement in the calorimeter which is proportional to $\sqrt{E}$ for highly energetic jets at first approximation [148]. It takes into account all hadronic energy from jets as well as from soft objects (compare Sec. 4.3.5) by summing up the energy of all jets as well as all energy deposits in the calorimeter not associated with any reconstructed object. A cut on the E_T^{miss} significance does not introduce any shape differences between the jet p_{T} distributions in the seed and the validation region as shown in Fig. 5.11 for the leading jet as example. The main difference between the seed region and VRZ is a cut of E_T^{miss} significance < 0.9. The exact definition of the seed region is discussed below and summarised in Tab. 5.3.

It has to be noted that there is an intrinsic difference between the isolation requirements for electrons and muon in this analysis (see Sec. 4.3.3 and 4.3.4). For high p_{T} electrons a relative isolation is required while for muons an absolute isolation criterion is used. This leads to small differences in the lepton p_T distributions, as can be seen in Fig. 5.12. The electron channel shows a slightly harder p_T spectrum than the muon channel. Also the composition of the missing energy is different for ee and $\mu\mu$ events. Electron events have a much harder $E_T^{\mathrm{miss,soft}}$ spectrum as the electron energy is measured in the calorimeter in contrast to the muons. This is shown in the plots in Fig. 5.13, where the missing energy contribution from

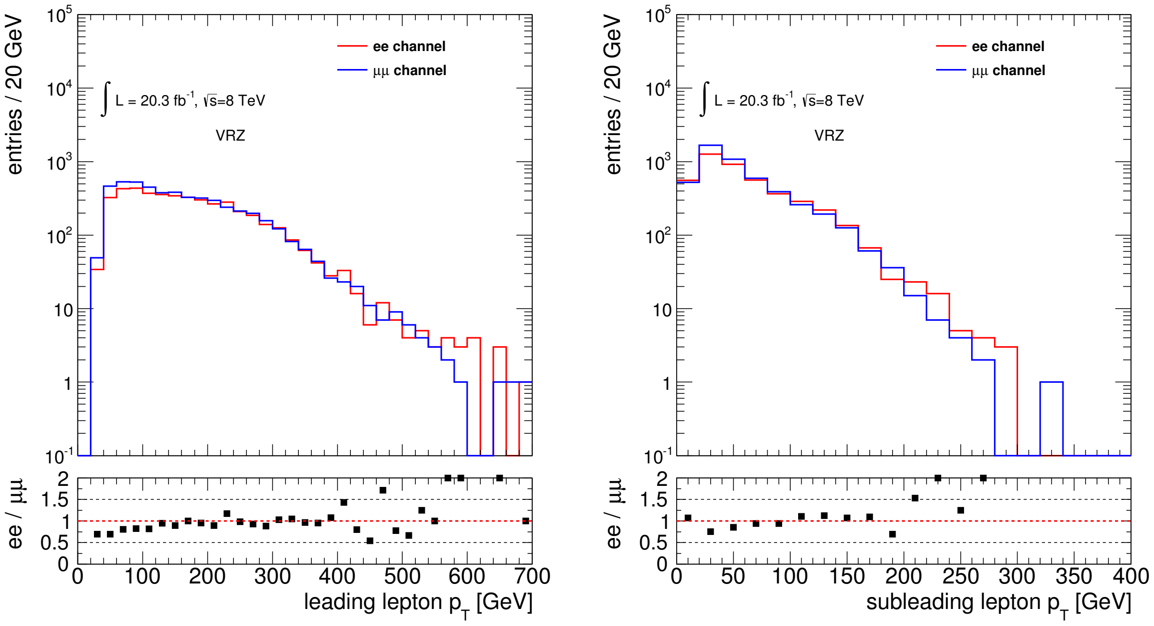

Figure 5.12: Comparison between the p_T distribution of the electron and muon channel for the leading lepton (left) and the subleading lepton (right) for the data in VRZ.

the soft term $E_T^{\text{miss,soft}}$ is shown and compared between MC simulations and data. It can happen that parts of the electron energy leak out of the cone defining the electron in the calorimeter and are therefore counted to the soft term instead of the electron term in the E_T^{miss} calculation. Events from the tail of the soft term distribution in the electron channel can get unnaturally high weights during the smearing procedure, leading to an unphysical asymmetry between the prediction for ee and $\mu\mu$ $Z+$jets background events. To solve this problem an additional cut on the soft term fraction, f_ST, is applied to select seed events. The definition of f_ST is as follows:

$$f_\text{ST} = \frac{E_T^{\text{miss,soft}}}{E_\text{T}^{\text{miss}}} \,. \tag{5.6}$$

A cut of $f_\text{ST} < 0.6$ has been found to be sufficient to avoid this effect.
To get an idea of a suitable value for the E_T^{miss} significance cut, an MC closure test is performed by applying the jet smearing method to simulated $Z+$jets events with a MC response function. As the detector response should be independent of the MC generator, the response function for the closure test was taken also from the Pythia dijet MC with good statistics. Tests were performed to check the impact of using response functions derived from a quark-enhanced $Z+$jets SHERPA sample, rather than gluon-enhanced dijet samples, but no significant differences were observed. Furthermore, ϕ-smearing is applied in the MC closure test to be as close to the nominal method as possible.
The closure test is performed in VRZ with an additional cut on $\Delta\phi(\text{jet}_{1,2}, E_T^{\text{miss}}) > 0.4$. It shows good results and the jet smearing method can reproduce the E_T^{miss} spectrum of simulated $Z+$jets events for a suitable seed selection. This is shown in Fig. 5.14 where the E_T^{miss} spectrum obtained from the MC simulation directly is compared to the spectra from the jet

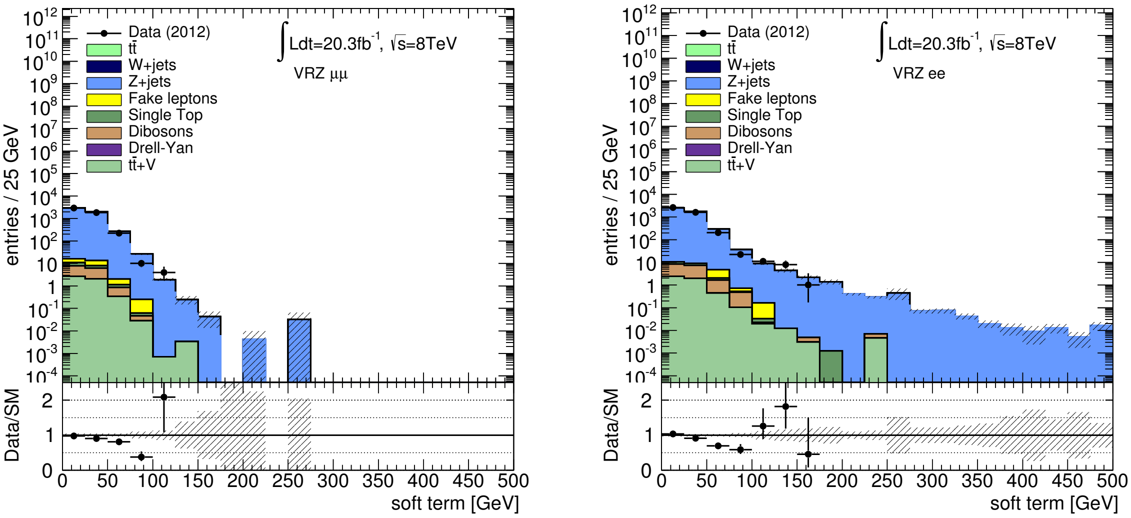

Figure 5.13: MC-to-data comparison of the $E_{\mathrm{T}}^{\mathrm{miss}}$ soft term spectra in the muon (left) and electron channel (right) in VRZ. The distribution of the background is predicted using MC simulations. Only statistical uncertainties are included in the indicated error bands.

$E_{\mathrm{T}}^{\mathrm{miss}}$ [GeV]	H_{T} [GeV]	n_{jets}	$E_{\mathrm{T}}^{\mathrm{miss}}$ sig. [$\sqrt{\mathrm{GeV}}$]	f_{ST}	$\Delta\phi(\mathrm{jet}_{1,2}, E_{T}^{\mathrm{miss}})$
< 150	> 600	≥ 2	< 0.9	< 0.6	-

Table 5.3: Seed event selection for the jet smearing method. In addition a Z candidate is required for all seed events.

smearing method with different E_T^{miss} significance cuts. It can be seen that the best agreement between the direct MC prediction and the result of the smearing method is obtained for a cut around E_T^{miss} significance $\lesssim 1\sqrt{\mathrm{GeV}}$. Still, the exact selection of the E_T^{miss} significance cut remains somehow arbitrary as the shape of the $E_{\mathrm{T}}^{\mathrm{miss}}$ distribution differs slightly between the electron and the muon channel due to the different isolation requirements explained above. Therefore, an uncertainty due to the seed event selection is applied, which is explained in Sec. 5.4.1 in more detail.

The final E_T^{miss} significance cut to select seed events is determined by optimizing the agreement between data and background prediction in VRZ. The best agreement is found for a value of E_T^{miss} significance $< 0.9\sqrt{\mathrm{GeV}}$. As the E_T^{miss} significance is highly correlated with $E_{\mathrm{T}}^{\mathrm{miss}}$ itself, the significance cut ensures that no event which enters the signal region is used as seed for the smearing.

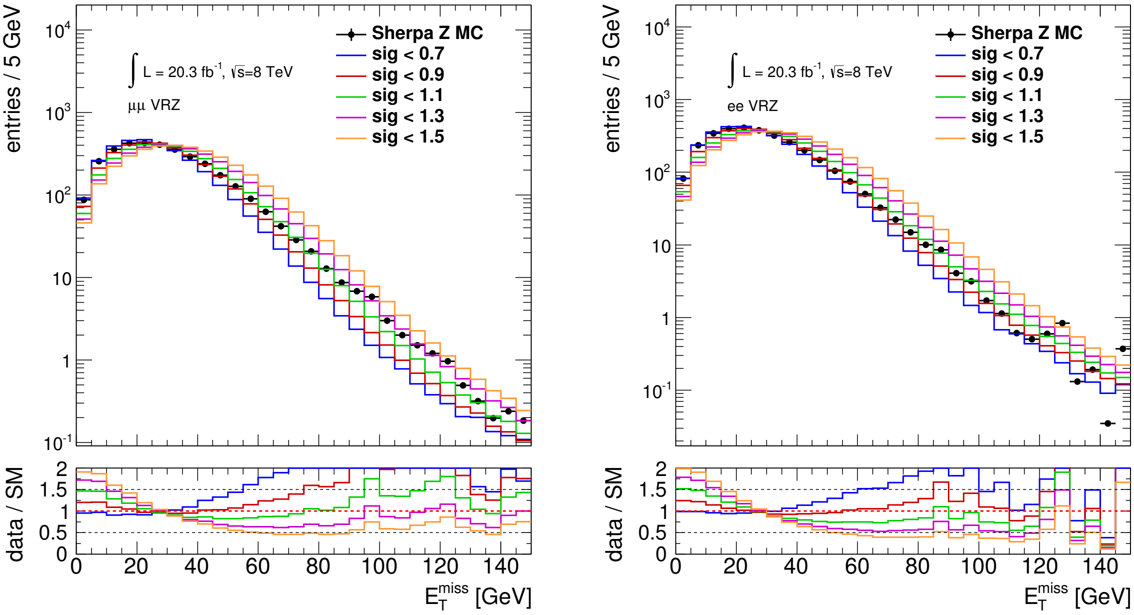

Figure 5.14: MC Closure test for the jet smearing method: the MC $E_{\mathrm{T}}^{\text{miss}}$ distribution shown as black dots is compared to the distributions from the jet smearing method (coloured lines) with different E_T^{miss} significance cuts and $f_{\text{ST}} < 0.6$ in VRZ. The muon channel is shown on the left and the electron channel on the right. A cut of $\Delta\phi(\text{jet}_{1,2}, E_T^{\text{miss}}) > 0.4$ is also applied for this test to be closer to the signal region selection.

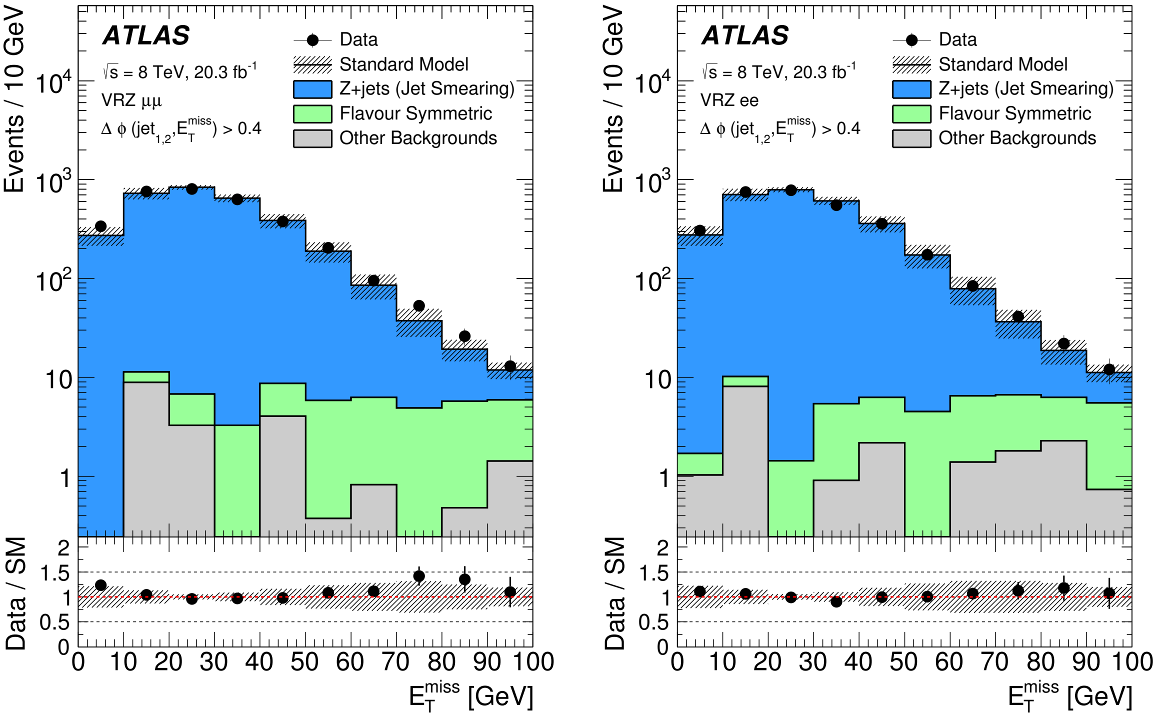

Figure 5.15: Comparison between the background estimate and data in VRZ with an additional cut on $\Delta\phi(\text{jet}_{1,2}, E_T^{\text{miss}}) > 0.4$ for $\mu^+\mu^-$ (left) and e^+e^- events (right) [53]. The blue shaded area represents the fake $E_{\text{T}}^{\text{miss}}$ distribution obtained from the jet smearing method. Background processes with real $E_{\text{T}}^{\text{miss}}$ are added from MC. Flavour symmetric backgrounds include dileptonic $t\bar{t}$, WW, $W + t$ and $Z \rightarrow \tau\tau$ processes. Fake lepton background, WZ and ZZ processes as well as $t\bar{t} + Z/W$, $t\bar{t} + WW$ and $Z + t$ are summarised in the "Other Backgrounds" category. All uncertainties of the jet smearing method described in Sec. 5.4.1 are taken into account in the indicated error bands in addition to the MC statistical error.

Validation and results

The fake $E_{\text{T}}^{\text{miss}}$ distribution obtained from the jet smearing method is compared to the unsmeared data in VRZ, which is dominated by $Z +$ jets background, to validate the results. Additionally, a cut on $\Delta\phi(\text{jet}_{1,2}, E_T^{\text{miss}}) > 0.4$ is applied for this study as this is also required in the signal region. The comparison is shown in Fig. 5.15. As the jet smearing method can only estimate the background contribution from $Z +$ jets events with fake missing energy, backgrounds with real missing energy (like $t\bar{t}$) have to be added from MC in these figures.
The indicated error bands are due to the uncertainty on the response functions, the selection of seed events and the limited seed event statistics. They also contain the statistical error of the backgrounds added from MC. More details about the uncertainties of the jet smearing method will be discussed in Sec. 5.4.1. Good agreement between the $E_{\text{T}}^{\text{miss}}$ distribution from the jet smearing method and the unsmeared data is observed for both channels in the region $E_{\text{T}}^{\text{miss}} < 100$ GeV. Above, $t\bar{t}$ background starts to dominate and the region is not suitable

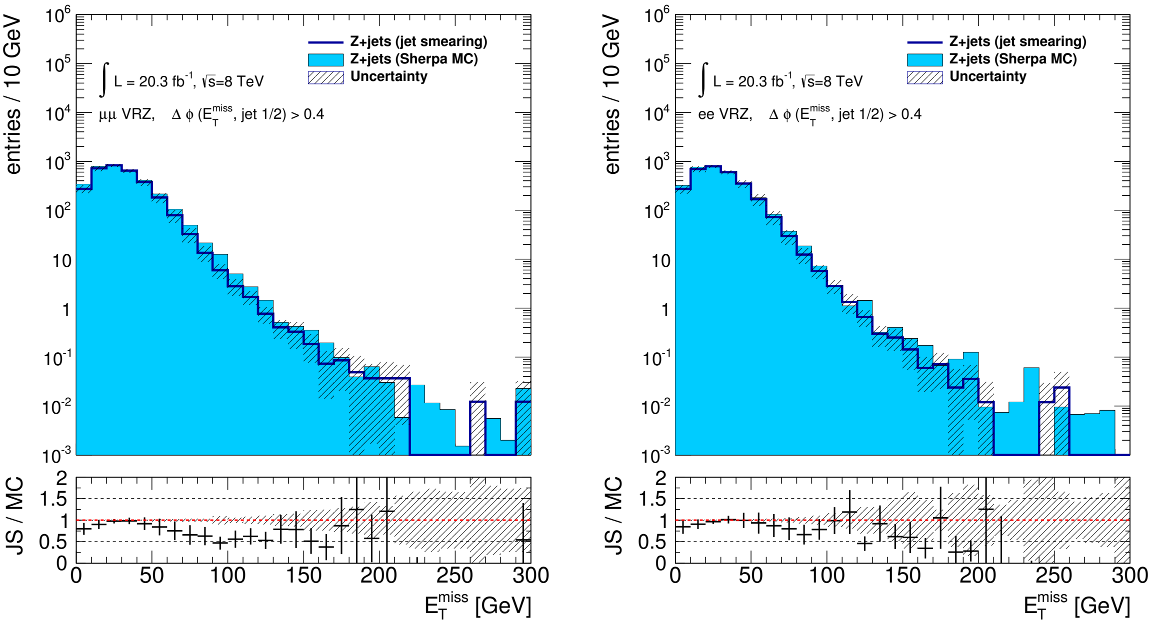

Figure 5.16: Comparison of the jet smearing method to a $Z+$jets MC in VRZ with an additional cut on $\Delta\phi(\text{jet}_{1,2}, E_T^{\text{miss}}) > 0.4$ for the muon (left) and the electron channel (right). The solid line represents the fake $E_{\text{T}}^{\text{miss}}$ distribution estimated from jet smearing, while the shaded blue area shows the yield from Z MC. All uncertainties of the jet smearing method discussed in Sec. 5.4.1 are included in the error band.

anymore to validate the $Z+$ jets background.

Further validation is performed by comparing the $E_{\text{T}}^{\text{miss}}$ distribution from jet smearing to the one of $Z+$jets MC simulations. This is shown in Fig. 5.16. Good agreement is seen in general between the MC and the jet smearing distribution. Some small discrepancies are observed in the intermediate $E_{\text{T}}^{\text{miss}}$ range. A conservative MC non-closure uncertainty is taken into account for the jet smearing estimate based on the difference between jet smearing and MC in the range $100 < E_{\text{T}}^{\text{miss}} < 200$ GeV in the same figure. This is discussed further in Sec. 5.4.1. For completeness, the comparison between data and MC is shown in Fig. C.1 in App. C.

It has been checked in addition that the distribution of the $\Delta\phi$ angle between the two jets with the highest energy and $E_{\text{T}}^{\text{miss}}$ is predicted correctly by the smeared pseudo data before the cut on this angle is applied. The $\Delta\phi(\text{jet}, E_T^{\text{miss}})$ distribution for the leading jet can be seen in Fig. 5.17 and 5.18 in different bins of $E_{\text{T}}^{\text{miss}}$. Good agreement between data and the background prediction is observed in all regions of $E_{\text{T}}^{\text{miss}}$. It has to be stressed that no cut on $\Delta\phi(\text{jet}_{1,2}, E_T^{\text{miss}})$ is applied to select the seed events, but the angle between smeared jets and $E_{\text{T}}^{\text{miss}}$ is calculated after the method has been applied. The jet smearing can reproduce the jet kinematics well also for events with high fake $E_{\text{T}}^{\text{miss}}$. From these plots, it can also be seen that most of the $Z+$ jets background with high fake $E_{\text{T}}^{\text{miss}}$ peaks at small $\Delta\phi$ values. This indicates that it is most probable that only one of the jets is mismeasured dramatically leading to large fake $E_{\text{T}}^{\text{miss}}$ pointing into the direction of this particular jet. The fake $E_{\text{T}}^{\text{miss}}$ background is therefore efficiently suppressed by the cut on $\Delta\phi(\text{jet}_{1,2}, E_T^{\text{miss}}) > 0.4$. The $\Delta\phi$ distributions of Fig. 5.17 and 5.18 have been checked for the second jet as well and show good

Channel	Jet smearing				$Z+$jets MC
	Nominal	Syst.	Stat.	Seed selection	
e^+e^-	0.048	< 0.0001	± 0.034	± 0.014	0.05 ± 0.03
$\mu^+\mu^-$	0.024	< 0.0001	± 0.024	± 0.019	0.09 ± 0.05

Table 5.4: Estimated number of events for the $Z+$jets background in SR-Z obtained from the jet smearing method and from a $Z+$jets MC simulation. All uncertainties of the jet smearing method (see Sec. 5.4.1) are also shown in detail. The uncertainty of the MC estinmate includes the statistical error and all detector related systematic uncertainties.

agreement, too. They are presented in App. C.

The yield for the $Z+$jets background in the signal region is estimated from the fake $E_{\mathrm{T}}^{\mathrm{miss}}$ distribution obtained with the jet smearing method, as shown in Fig. 5.15. The results are summarised in Tab. 5.4 for the electron and muon channel. It can be concluded that the fake $E_{\mathrm{T}}^{\mathrm{miss}}$ background is very small due to the $\Delta\phi(\mathrm{jet}_{1,2}, E_T^{\mathrm{miss}})$ cut. Only 0.05 ± 0.04 and $0.02^{+0.03}_{-0.02}$ background events from $Z+$jets processes are expected in the electron and the muon channel, respectively. This is about 1 % of the total background prediction in the signal region.

The table also shows the statistical error and the systematic uncertainties related to the response function and the seed event selection. The dominant uncertainty comes from the limited statistics in the seed region. The results can be compared to the estimates from $Z+$jets MC simulations, given in the same table. The jet smearing estimate in SR-Z agrees with the MC prediction within the uncertainties in both channels.

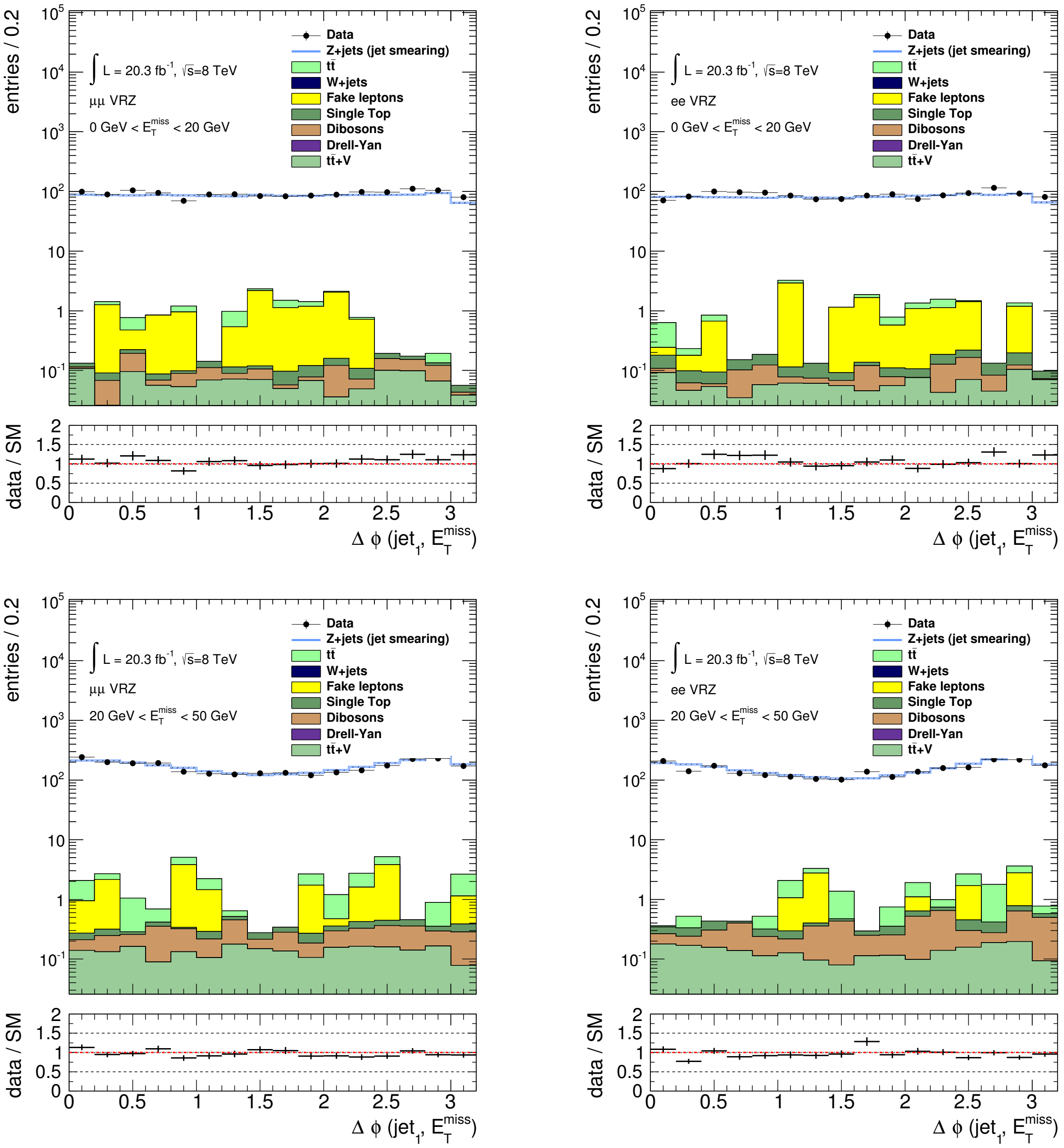

Figure 5.17: Distribution of $\Delta\phi(\mathrm{jet}_1, E_{\mathrm{T}}^{\mathrm{miss}})$ in the muon (left) and electron (right) channel. In the upper row the region $0\,\mathrm{GeV} < E_{\mathrm{T}}^{\mathrm{miss}} < 20\,\mathrm{GeV}$ is shown and in the lower row $20\,\mathrm{GeV} < E_{\mathrm{T}}^{\mathrm{miss}} < 50\,\mathrm{GeV}$. The error band contains only the statistical error of the backgrounds added from MC.

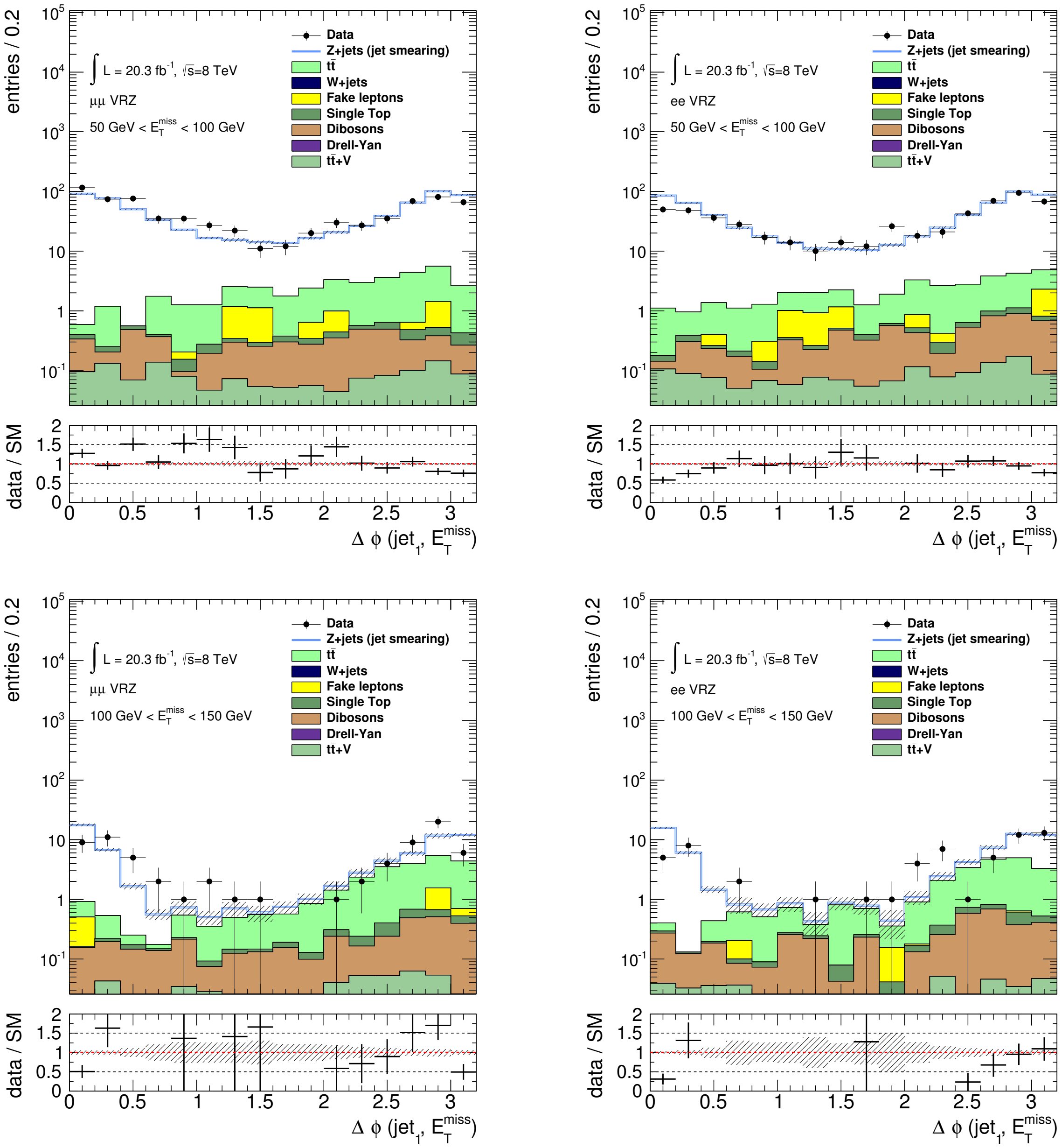

Figure 5.18: Distribution of $\Delta\phi(\text{jet}_1, E_{\mathrm{T}}^{\mathrm{miss}})$ in the muon (left) and electron (right) channel. In the upper row the region $50\,\text{GeV} < E_{\mathrm{T}}^{\mathrm{miss}} < 100\,\text{GeV}$ is shown and in the lower row $100\,\text{GeV} < E_{\mathrm{T}}^{\mathrm{miss}} < 150\,\text{GeV}$. The error band contains only the statistical error of the backgrounds added from MC.

5.3.2 Flavour symmetric backgrounds

For flavour symmetric backgrounds, the number of e^+e^- to $\mu^+\mu^-$ to $e^\pm\mu^\mp$ events is expected to fulfil the relation [53, 132]

$$e^+e^- : \mu^+\mu^- : e^\pm\mu^\mp = 1 : 1 : 2 \tag{5.7}$$

just for reasons of combinatorics. In particular, this includes $t\bar{t}$ events, where both top quarks decay leptonically, but also dileptonic WW, $W+t$ and $Z \to \tau\tau$ processes. These backgrounds can be estimated in the e^+e^- and $\mu^+\mu^-$ channel basically by dividing the number of events in the $e^\pm\mu^\mp$ channel by 2. As the signal models targeted by the Z+jets+E_T^{miss} analysis do not predict signatures involving different-flavour lepton pairs, the $e^\pm\mu^\mp$ channel offers a statistically independent control sample which can be used for the estimate of flavour symmetric backgrounds. This control region is denoted as CReμ in the region overview in Tab. 5.2. It is identical to the signal region except for the requirement of a different-flavour lepton pair. The method has the advantage that it is almost completely based on experimental data and relies only very little on computer simulations.

Due to different reconstruction and identification efficiencies for electrons and muons as well as different efficiencies for the various dilepton triggers discussed in Sec. 4.4, the relation in Eq. (5.7) is not fulfilled perfectly for reconstructed leptons. This is taken into account by correction factors. The estimate for the number of flavour symmetric background events in SR-Z in the e^+e^- and $\mu^+\mu^-$ channel, N_{ee} and $N_{\mu\mu}$, can be derived from the number of events in CReμ, $N_{e\mu}$, in the following way:

$$N_{ee} = \frac{1}{2} N_{e\mu}^{\text{corr}} \cdot k_{ee} \cdot \alpha \,, \tag{5.8}$$

$$N_{\mu\mu} = \frac{1}{2} N_{e\mu}^{\text{corr}} \cdot k_{\mu\mu} \cdot \alpha \,. \tag{5.9}$$

The superscript “corr” following $N_{e\mu}$ indicates that the number must be corrected for the contamination of CReμ with non-flavour symmetric backgrounds. Their contribution is estimated from MC and found to be very small. The factors $k_{ee/\mu\mu}$ correct for the difference in selection efficiency between electrons and muons, while the factor α takes into account that the $e^+e^-/\mu^+\mu^-$ and $e^\pm\mu^\mp$ events are triggered by same-flavour and different-flavour dilepton triggers, respectively, which have different efficiencies. The $k_{ee/\mu\mu}$ factors are derived from the ratio of e^+e^- to $\mu^+\mu^-$ events in VRZ, N_{ee}^{VRZ} and $N_{\mu\mu}^{\text{VRZ}}$, as this region contains well reconstructed $Z+$jets events:

$$k_{ee} = \sqrt{\frac{N_{ee}^{\text{VRZ}}}{N_{\mu\mu}^{\text{VRZ}}}} \,, \tag{5.10}$$

$$k_{\mu\mu} = \sqrt{\frac{N_{\mu\mu}^{\text{VRZ}}}{N_{ee}^{\text{VRZ}}}} \,. \tag{5.11}$$

The α factors are calculated from the different trigger efficiencies discussed in Sec. 4.4 in the following way:

$$\alpha = \frac{\sqrt{\epsilon_{ee}^{\text{trig}} \epsilon_{\mu\mu}^{\text{trig}}}}{\epsilon_{e\mu}^{\text{trig}}} \,, \tag{5.12}$$

Region	N_{ee}^{VRZ}	$N_{\mu\mu}^{\mathrm{VRZ}}$	k_{ee}	$k_{\mu\mu}$
barrel-barrel	2399	1995	1.099 ± 0.017 ± 0.08	0.910 ± 0.014 ± 0.1
barrel-endcap	1215	1667	0.853 ± 0.016 ± 0.08	1.173 ± 0.022 ± 0.1
endcap-endcap	838	1298	0.805 ± 0.018 ± 0.08	1.242 ± 0.028 ± 0.1
Global	4452	4960	0.947 ± 0.010 ± 0.08	1.056 ± 0.011 ± 0.1

Table 5.5: Correction factors k_{ee} and $k_{\mu\mu}$ calculated from the number of events in VRZ, N_{ee}^{VRZ} and $N_{\mu\mu}^{\mathrm{VRZ}}$, according to Eq. (5.10) and (5.11). The results are separated into different detector regions depending on if both leptons are in the barrel region (barrel-barrel), the endcaps (endcap-endcap) or one lepton is in the barrel and the other in the endcaps (barrel-endcap) [132]. The global $k_{ee/\mu\mu}$ factors obtained without this separation are also shown for comparison. The first uncertainty is the statistical error while the second one is due to the $E_{\mathrm{T}}^{\mathrm{miss}}$ dependency of the $k_{ee/\mu\mu}$ factors (see Sec. 5.4.1 for details).

Channel	$\epsilon_{\mathrm{barrel,barrel}}$	$\epsilon_{\mathrm{barrel,endcap}}$	$\epsilon_{\mathrm{endcap,endcap}}$
e^+e^-	0.96	0.94	0.91
$\mu^+\mu^-$	0.88	0.90	0.92
$e^\pm\mu^\mp$	0.80	0.81	0.82
α	1.15	1.14	1.12

Table 5.6: Trigger efficiencies ϵ_i and trigger correction factors α in the e^+e^-, $\mu^+\mu^-$ and $e^\pm\mu^\mp$ channel shown separately for the different detector regions: Both leptons in the barrel region (barrel-barrel), both in the endcaps (endcap-endcap) and one lepton in the barrel and the other in the endcaps (barrel-endcap) [132].

where $\epsilon_{ee}^{\mathrm{trig}}$, $\epsilon_{\mu\mu}^{\mathrm{trig}}$ and $\epsilon_{e\mu}^{\mathrm{trig}}$ are the efficiencies of the ee, $\mu\mu$ and eμ trigger combinations shown in Tab. 4.5. As both the lepton selection efficiencies as well as the trigger efficiencies depend on the η region of the detector, the flavour symmetry method is applied separately for cases where both leptons are in the ATLAS barrel region, where both leptons are in the endcaps and where one lepton is in the barrel and one in the endcaps. In general, the $k_{ee/\mu\mu}$ and the α factors are close to 1 and do not different significantly from global correction factors which would be obtained without barrel-endcap separation. This is shown in Tab. 5.5 for the $k_{ee/\mu\mu}$ factors and in Tab. 5.6 for the α factors.

The estimate for the flavour symmetric backgrounds obtained from this method is summarised in Tab. 5.7. The prediction is 2.8 ± 1.4 events in the e^+e^- channel and 3.3 ± 1.6 events in the $\mu^+\mu^-$ channel, which roughly corresponds to 50 % and 65 % of the total background, respectively. It can be estimated from MC simulations that about 80 % of the flavour symmetric background come from dileptonic $t\bar{t}$ events. The main uncertainty of the estimate is the large statistical error which is due to the limited number of events in CReμ. Besides that also the uncertainty on the contamination of CReμ with non-flavour symmetric backgrounds, which is estimated with MC simulations, is taken into account as well as the uncertainty on the trigger efficiencies. The $k_{ee/\mu\mu}$ factors show a slight dependency on $E_{\mathrm{T}}^{\mathrm{miss}}$, which is considered as an additional systematic uncertainty of the method to be conservative. More details are

Region	$N_{e\mu}$	N_{ee}	$N_{\mu\mu}$
barrel-barrel	2	$0.88 \pm 0.93 \pm 0.10 \pm 0.07$	$0.73 \pm 0.77 \pm 0.09 \pm 0.08$
barrel-endcap	4	$2.02 \pm 0.97 \pm 0.15 \pm 0.20$	$2.78 \pm 1.33 \pm 0.21 \pm 0.23$
endcap-endcap	0	$-0.16 \pm 0.15 \pm 0.01 \pm -0.02$	$-0.24 \pm 0.24 \pm 0.02 \pm -0.02$
$\sum$	6	$2.75 \pm 1.35 \pm 0.18 \pm 0.21$	$3.27 \pm 1.56 \pm 0.23 \pm 0.24$

Table 5.7: Data-driven prediction for the flavour symmetric backgrounds (dileptonic $t\bar{t}$, WW, $W+t$ and $Z \to \tau\tau$) in SR-Z [132]. The results are shown separately for the different detector regions depending on if both leptons are in the barrel region (barrel-barrel), the endcaps (endcap-endcap) or one lepton is in the barrel and the other in the endcaps (barrel-endcap). The first uncertainty corresponds to the statistical error, the second one to the uncertainty due to contamination of CReμ with non-flavour symmetric backgrounds together with the trigger efficiency error and the third one to the uncertainty due to the $E_{\mathrm{T}}^{\mathrm{miss}}$ dependency of $k_{ee/\mu\mu}$ (see 5.4.1 for details).

given in Sec. 5.4.1.

The results of the flavour symmetry method are cross-checked in two ways. First, an MC closure test is performed for which the same method is applied to simulated events. The method can reproduce the MC prediction for the flavour symmetric backgrounds well which validates the correctness of the approach. Also the 1:1:2 ratio for the three lepton flavour combinations (compare Eq. (5.7)) is cross-checked using MC simulations and is fulfilled well for all detector regions after the application of the correction factors.

Second, a fit of the $t\bar{t}$ background, which is the dominant source of flavour symmetric processes, is performed in the $m_{\ell\ell}$ sidebands around the Z mass peak. For this, the normalisation of the POWHEG $t\bar{t}$ MC was fitted to the data observed in CRT, which has the same selection criteria as the signal region, but is defined in the region $m_{\ell\ell}$ <81 GeV or $m_{\ell\ell}$ >101 GeV. All other backgrounds are taken from MC for this cross-check and are left unchanged during the fit. The $t\bar{t}$ background is extrapolated into the signal region using the normalisation factor obtained in the control region. This is illustrated in the sketch in Fig. 5.8: The fit is performed in CRT in the Z sidebands (green box) and then extrapolated into the signal region in the Z mass window (yellow box).

The fit results in slightly higher estimates for the flavour symmetric backgrounds of 4.9 ± 1.5 events in the electron channel and 5.3 ± 1.9 in the muon channel. It has a large uncertainty due to limited statistics in CRT. This translates into a large uncertainty on the top normalisation factor and thus on the extrapolation to the signal region. The results from the fit agree within $\sim 1\,\sigma$ with the ones from the flavour symmetry method. This level of agreement is good regarding the fact that both methods use data from orthogonal regions and very different approaches for the background estimation. They are therefore completely independent from each other. The comparison between the two is summarised in Tab. 5.8.

For the sideband fit, the extrapolation via $m_{\ell\ell}$ is validated by repeating the same fit in a region at lower $E_{\mathrm{T}}^{\mathrm{miss}}$ and H_{T}, which has higher statistics. For this, the $t\bar{t}$ normalisation is fitted in VRT (compare also Fig. 5.8) and the result is extrapolated to VRTZ. This extrapolation is identical to the one from CRT to SR-Z concerning the $m_{\ell\ell}$ selection, but has the advantage that the data in VRTZ can be checked before the signal region is unblinded. Thus,

Channel	flavour symmetry	sideband fit
e^+e^-	2.8 ± 1.4	4.9 ± 1.5
$\mu^+\mu^-$	3.3 ± 1.6	5.3 ± 1.9

Table 5.8: Comparison of the estimate for the flavour symmetric backgrounds (dileptonic $t\bar{t}$, WW, $W+t$ and $Z \to \tau\tau$) between the data-driven flavour symmetry method and the sideband fit of a $t\bar{t}$ MC simulation in SR-Z [53]. The combined statistical and systematic uncertainties are shown in both cases.

it serves as a cross-check for the sideband fit described above. The agreement between the fitted background prediction and the data in VRTZ is within 1σ and gives confidence in the results of the fit from CRT to SR-Z. It has to be noted, that no extrapolation in $m_{\ell\ell}$ is needed in the nominal flavour symmetry method as CReμ is defined in the Z mass window.
The sideband fit is also repeated with different $t\bar{t}$ MC simulations using ALPGEN or POWHEG interfaced with HERWIG instead of the nominal POWHEG +PYTHIA $t\bar{t}$ sample. All generators give consistent results.

5.3.3 Fake lepton backgrounds

Processes with one real prompt lepton, like W+jets or semileptonic $t\bar{t}$ events, can be a source of background in the signal region if there is an additional fake lepton reconstructed. These fake leptons can arise from misidentified jets, heavy flavour decays or converted photons [53]. To place an upper limit on this background contribution, the data-driven matrix method is applied [149], which covers also QCD multijet events with two fake leptons. The method relies on the fact that a control sample enriched with fake leptons can be obtained by dropping the signal lepton requirements defined in Tab. 4.3 and 4.4 and using only the baseline selection. This means that the leptons do not have to be isolated from other objects and do not have to fulfil tight cuts on their impact parameters. For electrons, also the identification criteria are loosened. Otherwise, the selection of the control sample is identical to the signal region, which ensures that the overall event kinematics are comparable between the two samples.
The unknown true number of events with real and fake leptons in the signal region, N_{real} and N_{fake}, can be related to the measurable number of events in the control sample, N_{pass} and N_{fail}, with leptons passing or failing the signal lepton requirements, respectively. For simplicity, the relation between these quantities is first shown for event selections with only one real or fake lepton [150]:

$$\begin{pmatrix} N_{\text{pass}} \\ N_{\text{fail}} \end{pmatrix} = \begin{pmatrix} r & f \\ (1-r) & (1-f) \end{pmatrix} \cdot \begin{pmatrix} N_{\text{real}} \\ N_{\text{fake}} \end{pmatrix} , \tag{5.13}$$

where r (f) is the efficiency with which a real (fake) lepton passing the baseline lepton selection also fulfils the signal lepton requirements. The estimate for the number of fake leptons in the signal region is given by N_{fake} and can be obtained by inverting the matrix in

Eq. (5.13):

$$N_{\text{fake}} = \frac{N_{\text{fail}} - \left(\frac{1}{r} - 1\right) N_{\text{pass}}}{\left(\frac{f}{r} - 1\right)} \tag{5.14}$$

For analyses with 2 leptons, all different combinations with 0, 1 and 2 real or fake leptons have to be considered and the matrix has to be extended to a four-by-four matrix [151]:

$$\begin{pmatrix} N_{\text{pass,pass}} \\ N_{\text{pass,fail}} \\ N_{\text{fail,pass}} \\ N_{\text{fail,fail}} \end{pmatrix} = \begin{pmatrix} rr & rf & fr & ff \\ r(1-r) & r(1-f) & f(1-r) & f(1-f) \\ (1-r)r & (1-r)f & (1-f)r & (1-f)f \\ (1-r)(1-r) & (1-r)(1-f) & (1-f)(1-r) & (1-f)(1-f) \end{pmatrix} \cdot \begin{pmatrix} N_{\text{real,real}} \\ N_{\text{real,fake}} \\ N_{\text{fake,real}} \\ N_{\text{fake,fake}} \end{pmatrix}, \tag{5.15}$$

where the first and second index of N is referring to the first and second lepton, respectively. Analogously, the estimate for the number of events for the different cases with one or two fake leptons can be found by inverting the matrix. The efficiencies r and f, that a real or fake lepton, which passes the baseline lepton selection, also fulfils the signal lepton requirements, must be measured in dedicated data samples.

The identification efficiency for real leptons, r, is measured with a tag-and-probe method from $Z \to \ell\ell$ events and is close to 100 % for muons and about 80-90 % for electrons [152]. The fake efficiency, f, is estimated from a region enriched with multijet background. For this. events with at least one signal jet with $p_{\text{T}} > 60\,\text{GeV}$ and low missing energy ($E_{\text{T}}^{\text{miss}} < 30\,\text{GeV}$) are selected. The background with real leptons (e.g. $W + \text{jets}$) in this region is subtracted using MC predictions. Afterwards, it can be assumed that all remaining leptons are fake leptons. Therefore, the fraction of events in which the leptons pass the signal lepton requirements is an approximation for f. The fake efficiency is on average about 30 % for muons and between $10-20$ % for electrons. Both r and f show a dependency on p_{T} and η of the lepton and can differ significantly from the average values especially at the boarder of the accessible phase space. The p_{T} and η dependencies are taken into account in the matrix method. In this thesis, an implementation of the matrix method common to many ATLAS SUSY searches is used [153]. A region enriched with fake lepton background (denoted as VRQCD) has been defined to show the validity of the method and of the common implementation in case of the Z+jets+E_T^{miss} analysis:

- Two lepton preselection as described in Sec. 4.5 and 5.2 but with two same-sign leptons.
- Requirement of $E_{\text{T}}^{\text{miss}} < 100\,\text{GeV}$.
- Selection of Z mass sidebands: $m_{\ell\ell} < 40\,\text{GeV}$ or $m_{\ell\ell} > 140\,\text{GeV}$.
- Requirement of at least two signal jets.

The $E_{\text{T}}^{\text{miss}}$ distribution in this validation region for the ee, $\mu\mu$ and $e\mu$ channel is shown in Fig. 5.19. There it can be seen that the overall agreement between data and background prediction is good. The events in the dip between 50 GeV $< E_{\text{T}}^{\text{miss}} <$ 70 GeV in the $\mu\mu$ channel have been studied in detail and no problems have been found. This discrepancy is thus probably due to a statistical fluctuation in data as VRQCD suffers from low statistics.

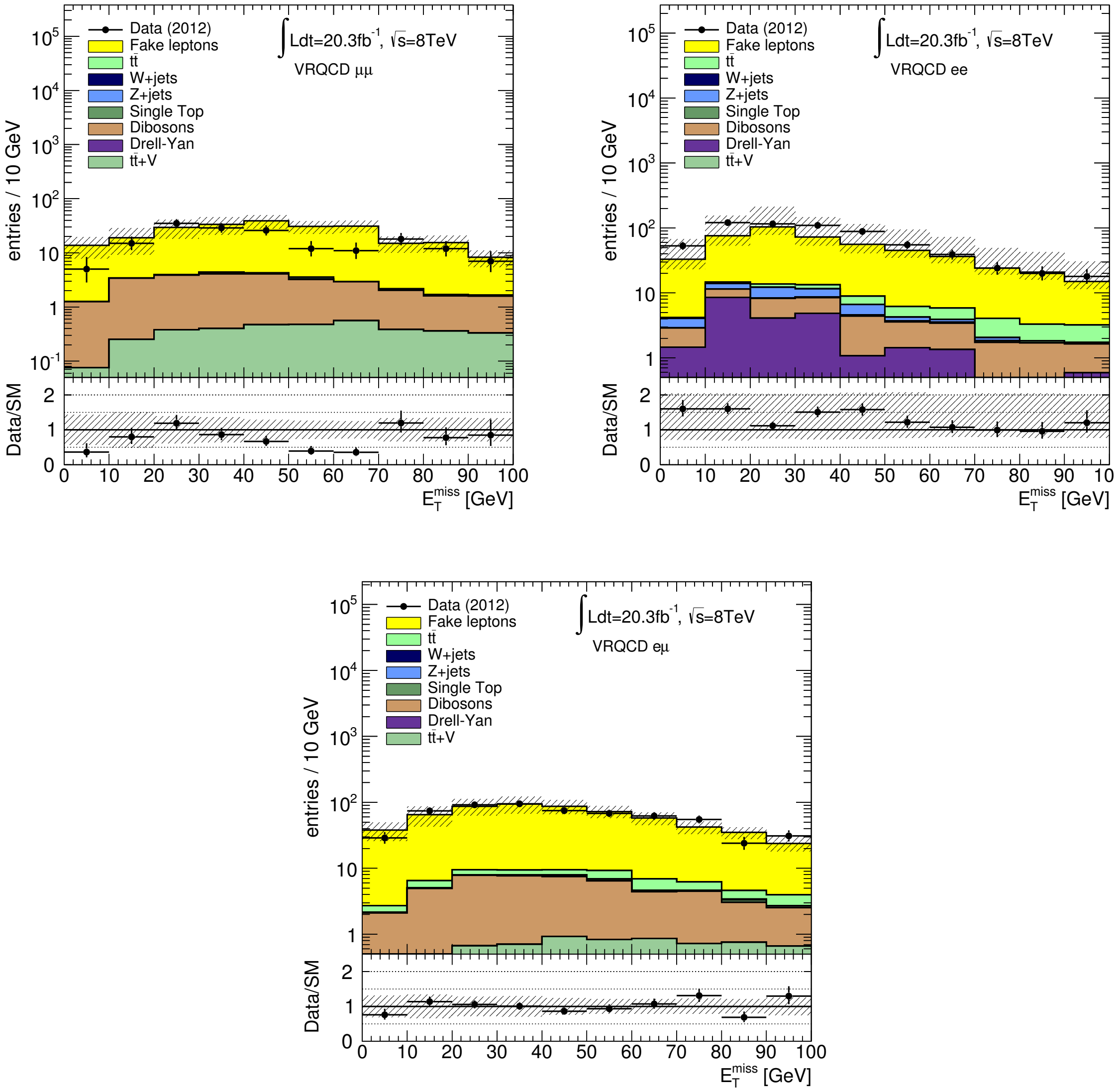

Figure 5.19: $E_{\mathrm{T}}^{\mathrm{miss}}$ distribution in the fake lepton validation region defined VRQCD for the $\mu\mu$ (top left), ee channel (top right) and $e\mu$ channel (bottom). The fake lepton background is estimated with the matrix method, while all other backgrounds are taken from MC simulations. The uncertainty on the matrix method estimate, all detector related systematic uncertainties (see Sec. 5.4.2) as well as the statistical uncertainties of the backgrounds added from MC are included in the indicated error bands.

It can be seen that the Drell-Yan and Z+jets background is higher in the ee channel compared to the $\mu\mu$ channel. This is due to the fact that electron bremsstrahlung can lead to same-sign events when most of the electron energy is transferred to the photon which then converts into an electron-positron pair with one high- and one low-energy lepton. If the highly energetic lepton from the photon conversion has the same charge as the non-decaying lepton from the original Drell-Yan or Z process, the two leading leptons in the event can have the same charge and enter the fake lepton validation region. This effect only occurs in the ee channel as the bremsstrahlung probability is much smaller for muons. For the same reason the $t\bar{t}$ background is higher in the ee and $e\mu$ channels compared to the $\mu\mu$ channel.

5.3.4 WZ/ZZ and rare top backgrounds

The remaining diboson processes, WZ and ZZ, as well as rare processes involving a top quark ($t\bar{t} + W/Z$, $t\bar{t} + WW$ and $t + Z$) are estimated from the MC simulations described in Sec. 4.2.2. The contribution of WZ/ZZ production to the total background estimate in SR-Z is about 30 % in both channels. This comes from WZ events, where the W and the Z boson decay leptonically, and ZZ events, in which one Z decays leptonically and the other one invisible. Rare top processes play only a minor role and contribute less than 5 % to the total background in the signal region.
It has been attempted to define a validation region enriched with diboson background to cross-check the MC estimate. However, due to the small cross-sections for these processes, it is very difficult to find a region dominated by WZ and/or ZZ processes. The following selection results in a purity of about 30 % for WZ and ZZ backgrounds:

- Preselection as described in Sec. 4.5.
- Requirement of at least three leptons with $p_{\mathrm{T}}^{\mathrm{lep1}} > 25\,\mathrm{GeV}$, $p_{\mathrm{T}}^{\mathrm{lep2}} > 10\,\mathrm{GeV}$ and $p_{\mathrm{T}}^{\mathrm{lep3}} > 10\,\mathrm{GeV}$. No cut on the charge or flavour of the leptons is applied.
- Requirement on the invariant mass of the two leading leptons of $m_{\ell\ell} > 15\,\mathrm{GeV}$.
- Requirement of $25\,\mathrm{GeV} < E_{\mathrm{T}}^{\mathrm{miss}} < 225\,\mathrm{GeV}$.
- Requirement of $H_{\mathrm{T}} > 600\,\mathrm{GeV}$.
- Requirement of at least two signal jets.
- Veto on events with a b-tagged jet among the first three signal jets.

This validation region is relatively close to the signal region and the requirement of a third lepton as well as the veto on b-jets helps to suppress the $t\bar{t}$ background. A matrix method for three leptons is out of scope of this thesis. Corresponding events with two real and one fake lepton are estimated from MC simulations and events with two fake leptons are extrapolated using the fake lepton estimate in 2-lepton regions.

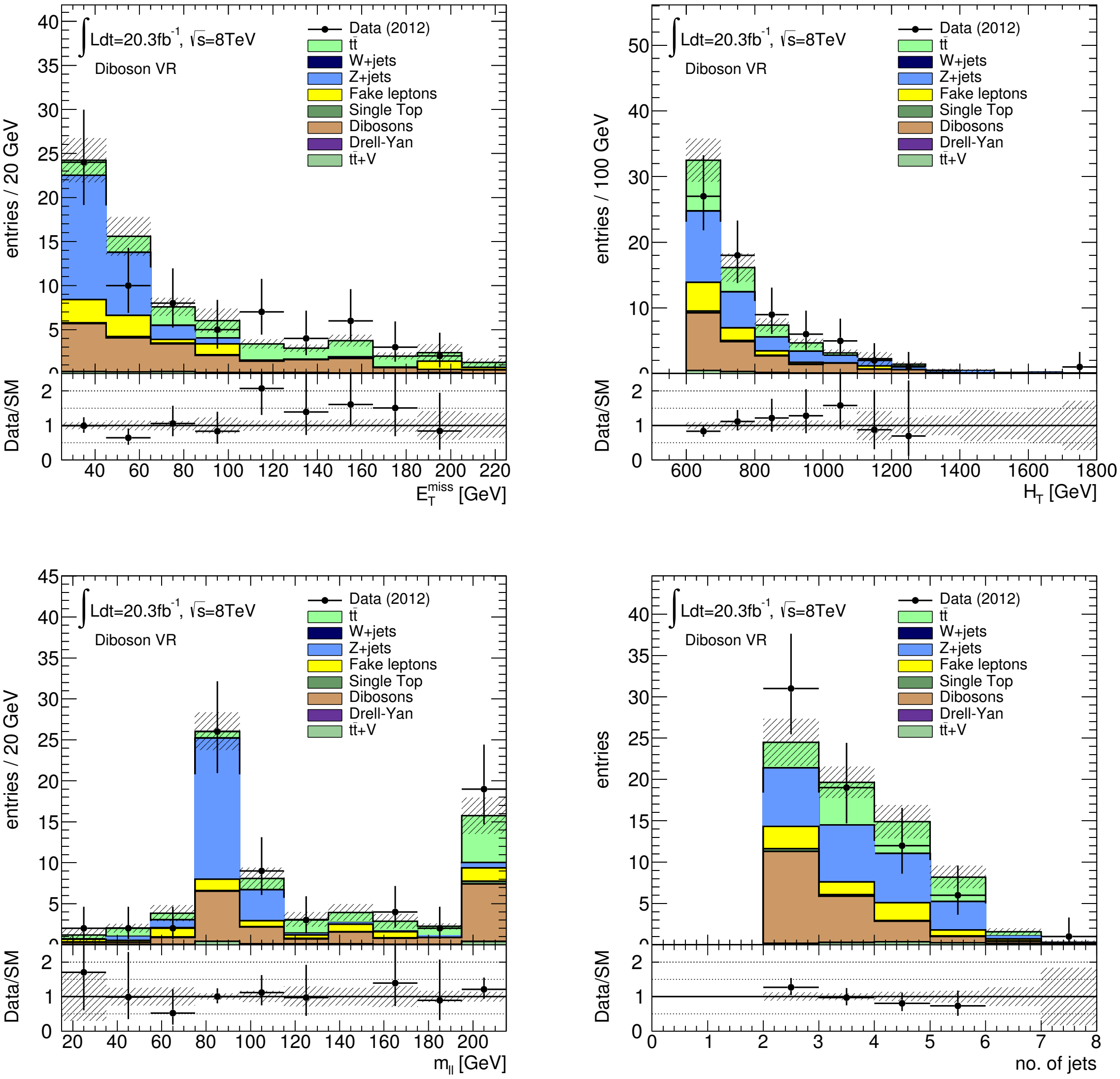

Figure 5.20: Distributions of $E_{\mathrm{T}}^{\mathrm{miss}}$ (top left), H_T (top right), $m_{\ell\ell}$ (bottom left) and the number of signal jets (bottom right) in the diboson validation region described in the text. Only statistical uncertainties are included in the indicated error bands.

Channel	e^+e^-	$\mu^+\mu^-$	SF
Total background prediction	4.2 ± 1.6	6.4 ± 2.2	10.6 ± 3.2
Flavour symmetric backgrounds	2.8 ± 1.4	3.3 ± 1.6	6.0 ± 2.6
$Z +$ jets (jet smearing)	0.05 ± 0.04	$0.02^{+0.03}_{-0.02}$	0.07 ± 0.05
Rare top	0.18 ± 0.06	0.17 ± 0.06	0.35 ± 0.12
WZ/ZZ diboson	1.2 ± 0.5	1.7 ± 0.6	2.9 ± 1.0
Fake leptons	$0.1^{+0.7}_{-0.1}$	$1.2^{+1.3}_{-1.2}$	$1.3^{+1.7}_{-1.3}$

Table 5.9: Total background estimate in SR-Z for the e^+e^- and $\mu^+\mu^-$ channel and their sum [132]. Rare top backgrounds include contributions from $t\bar{t} + W/Z$, $t\bar{t} + WW$ and $t + Z$ processes. The indicated errors include statistical as well as all systematic uncertainties.

The distributions for $E_{\mathrm{T}}^{\mathrm{miss}}$, H_T, m_{ll} and the number of jets in the diboson validation region are shown in Fig. 5.20. Despite the low diboson purity and the fact that the region is statistics limited, it can be concluded that the diboson background is in general modelled correctly by the simulation and is not underestimated by orders of magnitude.

5.3.5 Validation of the background estimate

The total background estimate in SR-Z including all contributions discussed in Sec. 5.3 is summarised for the $\mu^+\mu^-$ channel, the e^+e^- channel and the sum (denoted as SF) in Tab. 5.9. The background prediction is scrutinised carefully in the validation and control regions introduced in Tab. 5.2. In these regions, little signal contamination is expected and the experimental data can be examined before the signal region is unblinded.

The full analysis is repeated systematically in all VRs and CRs. This means that the yield for each background is obtained from the corresponding nominal method. The only exception is the estimate of Z+jets backgrounds in the Z mass sidebands regions (compare right sketch of Fig. 5.8). The nominal jet smearing method cannot be applied there as possible seed regions would suffer from large contamination with non-Z backgrounds. Thus, the $Z +$ jets background is estimated from MC simulations in all regions in the Z mass sidebands. The result of the complete background prediction is compared to data as summarised in Fig. 5.21. Agreement within ~1 σ is generally observed in all VRs and CRs both inside and outside the Z mass window which shows the accuracy of the background estimation.

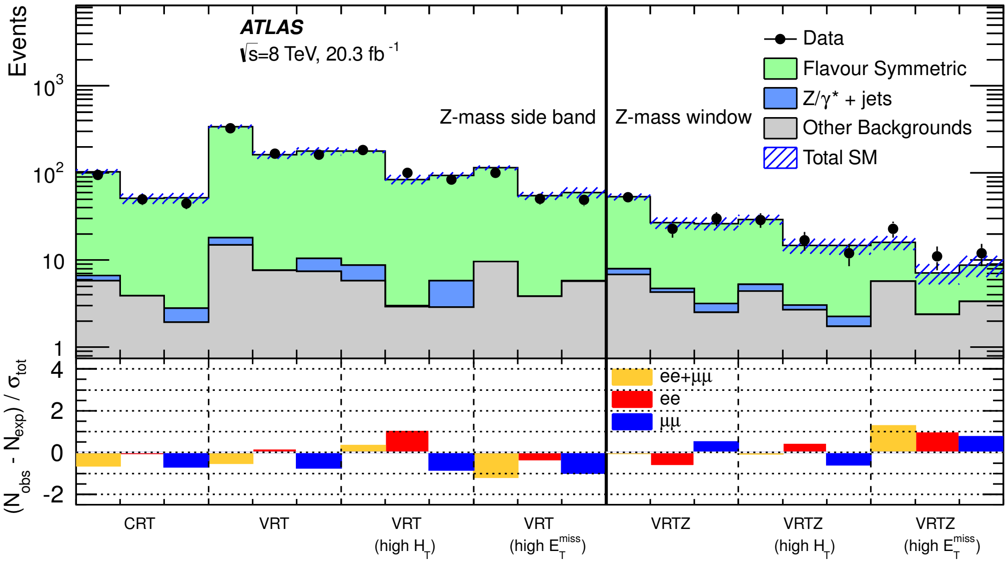

Figure 5.21: Overview over the agreement between background prediction and data in all VRs and CRs of the Z+jets+E_T^{miss} analysis [53]. Regions in the Z mass sidebands are shown on the left, while regions in the Z mass window are shown on the right. The difference between the observed and the expected yields, expressed in number of standard deviations, is shown on bottom. The "Other Backgrounds" category comprises WZ, ZZ, $t\bar{t}+W/Z$, $t\bar{t}+WW$, $t+Z$ and fake lepton processes.

5.4 Systematic uncertainties

Different experimental and theoretical uncertainties affect the background and signal prediction of the Z+jets+E_T^{miss} analysis. They are taken into account in the statistical treatment of the results. The uncertainties are estimated following the recommendations of the ATLAS SUSY group [154] wherever applicable in accordance with the ATLAS performance groups. An overview over the relative size of all considered uncertainties is given in Tab. 5.10 at the end of this section for the $\mu^+\mu^-$ and e^+e^- channels as well as their sum.

5.4.1 Uncertainties of data-driven methods

Since most backgrounds are estimated in a data-driven way, the statistical uncertainty on the control samples dominates the uncertainty on the total background estimate. The statistical error of the flavour symmetry method is ~25-30 % with respect to the total background yield and the one of the matrix method is ~10-20 % in the e^+e^- and the $\mu^+\mu^-$ channel. Nonetheless, additional systematic effects are considered when their impact is not negligible.

Uncertainties of the jet smearing method

There are three sources of uncertainties for $Z+\text{jets}$ background estimation based on the jet smearing method:

- Statistical uncertainty: Due to the limited number of the seed events and as every seed event is used a finite number of times for smearing, the statistical errors related to this have to be propagated to the final background estimation. The statistical uncertainty, σ_{stat}, of the j-th bin of the smeared $E_{\mathrm{T}}^{\mathrm{miss}}$ distribution is given by [147]:

$$\sigma_{\mathrm{stat}}(E_{\mathrm{T,j}}^{\mathrm{miss}}) = \frac{1}{N_{\mathrm{seed}}N_{\mathrm{smear}}}\sqrt{\sum_i n_{ij}(1+n_{ij})},$$

  where N_{seed} is the number of seed events, N_{smear} is the number of events generated from each seed (1000 in this analysis) and n_{ij} is the number of entries from the i-th seed event in the j-th bin of the estimated $E_{\mathrm{T}}^{\mathrm{miss}}$ distribution. The sum runs over all seed events.

- Systematic uncertainties on the response functions: To account for uncertainties due to the response functions the smearing is repeated with three different sets: the nominal response functions are used to get the estimate for the $Z+\text{jets}$ background while sets with a modified Gaussian core as well as a lower or an upper tail, respectively, are used to assess the error of the results. The size of the uncertainties on the response functions are estimated such that they cover the statistical uncertainties in the dijet and 3-jet analyses in which the response functions are fitted to data. To estimate the uncertainty on the $Z+$jets background yield, the difference between the jet smearing result with the nominal response functions and with the functions including upper/lower tails are taken as a systematic uncertainty.

- Systematic uncertainty due to the seed event selection: The results of the jet smearing method depend on the selection criteria for the seed events (compare Fig. 5.14). As the exact E_T^{miss} significance cut cannot be determined with absolute precision, a conservative uncertainty is added to account for it and estimated in two ways:

  - The $E_{\mathrm{T}}^{\mathrm{miss}}$ significance cut is varied between 0.7 and 1.1 (i.e. nominal ± 0.2) in steps of 0.05. The largest up or down deviation between the nominal jet smearing yield in SR-Z and the yields with the modified significance cut is taken as a symmetric uncertainty

  - A MC non-closure uncertainty is estimated by taking the difference between the jet smearing and the direct MC yield in VRZ and VRTZ_highHT in the range $100\,\mathrm{GeV} < E_{\mathrm{T}}^{\mathrm{miss}} < 200\,\mathrm{GeV}$. This is motivated by the fact that the largest deviations occur in this range.

  Only the larger of the two is added as an uncertainty on the jet smearing results as both estimation methods cover the same effect.

- Contamination from non-Z backgrounds in the seed region: The expected contribution from non-Z backgrounds to the seed events is estimated from MC and found to be below 2% in both channels. Therefore this effect is neglected and no additional uncertainty is assigned.

All uncertainties are treated as uncorrelated for the final statistical interpretation.

Uncertainties of the flavour symmetry method

The statistical error is by far the largest uncertainty of the flavour symmetry method as the different-flavour control region CReμ contains only 6 events. The statsitical uncertainty is highly correlated between the e^+e^- and $\mu^+\mu^-$ channel as CReμ is common to both channels. However, the correlation is not 100 % as the flavour symmetry method is applied separately in different detector regions with different efficiencies (compare Tab. 5.7). Additional systematic effects on the yield for the flavour symmetric backgrounds are [132]:

- Correction for non-flavour symmetric backgrounds: The number of events in CReμ is corrected for non-flavour symmetric backgrounds before the flavour symmetry method is applied (compare Eq. (5.8) and (5.9)). Their impact is small (∼10 % of the total number of events in CReμ) and is estimated from MC simulations. All experimental uncertainties (see Sec. 5.4.2) as well as the statistical errors of the simulations are taken into account and propagated to the final flavour symmetry prediction.

- The dependency of $k_{ee/\mu\mu}$ on $E_{\mathrm{T}}^{\text{miss}}$: The correction factors for the lepton selection efficiencies show a slight dependency on the missing energy. To take this into account, k_{ee} and $k_{\mu\mu}$ are calculated in different bins of $E_{\mathrm{T}}^{\text{miss}}$ and the difference between the largest and the smallest value is taken as an uncertainty on the correction factors which is then propagated to the flavour symmetry result.

- Uncertainty of the trigger efficiencies: A conservative flat uncertainty of 5 % is assigned to the trigger efficiencies given in Tab. 5.6 based on observed differences between data and MC in dedicated trigger efficiency studies [155]. This is propagated into the uncertainty on the α factors defined in Eq. (5.12).

For the statistical interpretation of the Z+jets+E_T^{miss} results, these systematic uncertainties are combined assuming no correlations between them.

Uncertainties of the matrix method

Also for the matrix method, the dominant uncertainty comes from the low statistics in the control sample. The uncertainty on the real lepton efficiency is estimated from the difference of the efficiencies in a Z + jets and a $t\bar{t}$ MC. Besides that, the limited number of events of the regions in which the real and fake lepton efficiencies are determined is considered as an additional uncertainty. Eventually, an uncertainty of 20 % is assigned to the subtraction of non-multijet backgrounds in these regions which is determined from MC simulations [53].

5.4.2 Experimental uncertainties

All background predictions based on MC simulations suffer from systematic uncertainties due to detector effects which are not known with absolute precision. This affects the WZ, ZZ, $t\bar{t} + W/Z$, $t\bar{t} + WW$ and $t + Z$ backgrounds in this analysis (compare Sec. 5.3.4). To assess these uncertainties a simulation generated with the nominal (i.e. best) estimate for the detector behaviour is compared to a sample with varied settings. The following sources of uncertainties are taken into account for the Z+jets+E_T^{miss} results:

- The jet energy scale (JES) is measured in MC simulations and in data with different in-situ analyses (Z + jets, γ+jets and multijet balance). These consider the momentum imbalance in an event to estimate the energy scale of a jet relative to another object which is measured with high precision (e.g. a leptonically decaying Z boson, a photon or other jets) [121, 156]. The dependency of the JES on jet p_{T} and η is considered. The JES uncertainty is taken into account by two effective parameters for the statistical treatment of the result (JES 1 and JES 2). Additional JES uncertainties are due to the JES dependency on pile-up, the behaviour of high p_T jets and the η intercalibration. The latter uncertainty is caused by the effect that the response of the ATLAS calorimeter depends on the pseudo-rapidity η. This dependency is measured relative to central jets and corrected for in the jet calibration. Eventually, the energy scale also depends on the flavour composition of the jets and calorimeter response to the different jet flavours, which leads to additional uncertainties. Besides, an extra JES uncertainty for b-tagged jets is considered.

- The jet energy resolution (JER) can be derived from MC simulations where the truth jet p_T is known. In data, JER is measured with the bisector method described in [148]. For this, the vectorial p_T sum of the jets in dijet events is calculated. The two components of this vector float around zero and the width of the fluctuations is a measure for JER. The error of the measurement leads to a systematic uncertainty on this quantity.

- The uncertainty due to the jet vertex fraction cut in the jet definition (compare Tab. 4.2) is assessed by varying the nominal threshold of 0.25 up and down by 0.04 [93].

- As already mentioned in the previous section, a flat uncertainty of 5 % is assigned to the trigger efficiencies in MC simulations and propagated through the analysis.

- Lepton energy scale, resolution and efficiency uncertainties are taken into account by reweighting the simulated events with scale factors which contain these uncertainties. The scale factors are estimated with a tag-and-probe method from $Z \to \ell\ell$ and $J/\psi \to \ell\ell$ decays for electrons [128] and muons [157]. For electrons, also $W \to \ell\nu$ processes are used to assess the energy scale and resolution.

- The uncertainty due to the imperfect knowledge of the pile-up behaviour is taken into account by varying the pile-up reweighting factor introduced in Sec. 4.2.2 up and down by 10 % [93].

- The uncertainties on the energy scale and resolution of jets and leptons are propagated to the missing energy reconstruction. An additional uncertainty accounts for the energy scale of the soft term (compare Eq. 4.6).

The experimental uncertainties of the MC prediction have in general small impact on the final results. The largest one is the uncertainty due to the JES dependency on the flavour composition of a jet which is below 2 % in both the e^+e^- and the $\mu^+\mu^-$ channel.

5.4.3 Theoretical uncertainties

MC predictions are affected by different theoretical uncertainties as the hard scattering process can only be calculated to a fixed order and non-perturbative effects are known with limited precision. The latter uncertainties are estimated in accordance with the PDF4LHC recommendations [158] and follow the description for the MC samples of the SUSY signal discussed in Sec. 5.1 in detail.

For the uncertainties due to the choice of the renormalisation and factorisation scales, MC samples are generated where these scales are varied up and down by a factor of 2. The difference between these samples and the simulation with the nominal scales is considered as an uncertainty. The cross-section uncertainties are 5 % and 7 % for WZ and ZZ processes, respectively, and 22 % for $t\bar{t}+W/Z$. For $t\bar{t}+WW$ and $t+Z$ backgrounds [154], a conservative uncertainty of 50 % is assigned to the LO cross-section [53].

The uncertainty on the number of predicted WZ/ZZ events due to the choice of the MC generator and the parton shower model is estimated by comparing the nominal POWHEG +PYTHIA 8 sample with other simulations using either a different MC generator (MC@NLO [159]) or a different parton shower model (PYTHIA 6 or HERWIG+JIMMY [160, 161]).

For $t\bar{t}+W/Z$ backgrounds, a parton shower uncertainty is derived in a similar way and, additionally, an uncertainty due to the finite number of partons in the MC generation is considered. Samples with different numbers of additional partons are compared to estimate this effect. Only the largest uncertainty among the scale variations, the parton shower uncertainty and the error due to the finite number of partons is used as a combined theoretical uncertainty for the $t\bar{t}+W/Z$ estimate.

The uncertainty due to the limited statistics in the available MC samples is taken into account for all backgrounds derived from simulations. The largest theoretical uncertainty is the combined MC generator and parton shower uncertainty of the WZ/ZZ background prediction which is ~7 % in the signal region in both channels.

5.5 Results of the Z+jets+E_T^{miss} analysis

The results of the search for SUSY in events with a leptonically decaying Z boson, jets and missing energy are summarised in Tab. 5.11. In the e^+e^- channel 4.2 ± 1.6 events are expected from SM backgrounds in SR-Z while 16 events are observed in data. In the $\mu^+\mu^-$ channel the background prediction is 6.4 ± 2.2 events while 13 are observed. A detailed breakdown of all 29 events in SR-Z can be found in App. D.

The p-value (as introduced in Sec. 4.1) for the background only hypothesis can be calculated. It indicates the probability that the background processes lead to result equally or less probable than the observed data. The background prediction is treated as Poisson distributed while most systematic uncertainties are modelled with Gaussian distributions. An exception is the statistical uncertainty of the flavour symmetric background estimate. As this is derived from a control region in the different-flavour channel with very low statistics it is also treated as Poisson distributed which is the correct probability density function for processes with small rates. The p-value can be translated into the number of Gaussian standard deviations and is referred to as the local significance of the result.

The excess of data over the background expectation has a significance of $3.0\,\sigma$ and $1.7\,\sigma$ in the e^+e^- and $\mu^+\mu^-$ channel, respectively. Both channels can be summed up to the same-flavour channel. The significance of the excess in the combination of e^+e^- and $\mu^+\mu^-$ events is also $3.0\,\sigma$ as the result is dominated by the e^+e^- channel. The precision of the background esti-

Channel	e^+e^-	$\mu^+\mu^-$	SF
Total background expectation	4.2	6.4	10.6
Flavour symmetry stat.	±1.35 [31.7%]	±1.57 [24.7%]	±2.53 [23.8%]
Matrix method stat.	±0.38 [9.0%]	±1.25 [19.7%]	±1.51 [14.2%]
WZ, ZZ MC gen. and parton shower	±0.31 [7.2%]	±0.44 [6.9%]	±0.74 [7.0%]
Flavour symmetry syst.	±0.28 [6.5%]	±0.33 [5.1%]	±0.42 [4.0%]
MC stat.	±0.25 [6.0%]	±0.28 [4.4%]	±0.38 [3.6%]
WZ PDF	±0.07 [1.8%]	±0.12 [1.8%]	±0.19 [1.8%]
JES flavour composition	±0.07 [1.6%]	±0.07 [1.1%]	±0.14 [1.3%]
Trigger efficiency	±0.07 [1.6%]	±0.09 [1.5%]	±0.16 [1.5%]
$t\bar{t}+W/Z$ theory	±0.06 [1.5%]	±0.05 [0.77%]	±0.11 [1.1%]
WZ cross-section	±0.06 [1.3%]	±0.09 [1.4%]	±0.15 [1.4%]
JES 1	±0.05 [1.1%]	±0.05 [0.82%]	±0.09 [0.87%]
JES pile-up dependency	±0.04 [1.0%]	±0.02 [0.26%]	±0.06 [0.57%]
JES flavour response	±0.04 [1.0%]	±0.05 [0.80%]	±0.09 [0.89%]
$t\bar{t}+W/Z$ cross-section	±0.04 [0.88%]	±0.03 [0.46%]	±0.07 [0.63%]
JES η intercalibration	±0.04 [0.87%]	±0.04 [0.64%]	±0.08 [0.71%]
lepton energy and efficiency	±0.04 [0.84%]	±0.01 [0.19%]	±0.05 [0.45%]
Jet smearing stat.	±0.03 [0.80%]	±0.02 [0.38%]	±0.04 [0.39%]
WZ renormalisation scale	±0.03 [0.64%]	±0.04 [0.65%]	±0.07 [0.65%]
$t\bar{t}+W/Z$ PDF	±0.03 [0.63%]	±0.02 [0.33%]	±0.05 [0.45%]
JES 2	±0.03 [0.62%]	±0.09 [1.4%]	±0.08 [0.73%]
$Z+t$ PDF	±0.03 [0.60%]	±0.03 [0.47%]	±0.06 [0.52%]
ZZ cross-section	±0.02 [0.42%]	±0.02 [0.33%]	±0.04 [0.37%]
Pile-up	±0.02 [0.36%]	±0.03 [0.46%]	±0.04 [0.42%]
WZ factorisation scale	±0.01 [0.33%]	±0.02 [0.34%]	±0.04 [0.33%]
Jet smearing seed selection	±0.01 [0.33%]	±0.02 [0.30%]	±0.03 [0.30%]
ZZ factorisation scale	±0.01 [0.12%]	±0.01 [0.09%]	±0.01 [0.10%]
$E_{\mathrm{T}}^{\mathrm{miss}}$ soft term scale	±0.00 [0.11%]	±0.01 [0.10%]	±0.01 [0.08%]
$Z+t$ cross-section	±0.00 [0.08%]	±0.02 [0.31%]	±0.02 [0.22%]
ZZ renormalisation scale	±0.00 [0.04%]	±0.00 [0.03%]	±0.00 [0.04%]

Table 5.10: Overview over the size of all systematic uncertainties on the background estimates in SR-Z for the e^+e^- and $\mu^+\mu^-$ channels as well as their sum [132]. The individual uncertainties can be correlated and do not necessarily add up quadratically to the total background uncertainty. The percentages show the size of the uncertainty relative to the total expected background. Effects mentioned in the text but not in this table are negligible for the final results and have been omitted here.

Channel	e^+e^-	$\mu^+\mu^-$	SF
Observed events	16	13	29
Expected background events	4.2 ± 1.6	6.4 ± 2.2	10.6 ± 3.2
Flavour symmetric backgrounds	2.8 ± 1.4	3.3 ± 1.6	6.0 ± 2.6
$Z +$ jets (jet smearing)	0.05 ± 0.04	$0.02^{+0.03}_{-0.02}$	0.07 ± 0.05
Rare top	0.18 ± 0.06	0.17 ± 0.06	0.35 ± 0.12
WZ/ZZ diboson	1.2 ± 0.5	1.7 ± 0.6	2.9 ± 1.0
Fake leptons	$0.1^{+0.7}_{-0.1}$	$1.2^{+1.3}_{-1.2}$	$1.3^{+1.7}_{-1.3}$
Significance	$3.0\,\sigma$	$1.7\,\sigma$	$3.0\,\sigma$

Table 5.11: Results in the signal region of the Z+jets+E_T^{miss} analysis for the e^+e^- and $\mu^+\mu^-$ channel as well as their sum SF [53]. The local significance of the results is also indicated. Background from $t\bar{t} + W/Z$, $t\bar{t} + WW$ and $t + Z$ events are summarised in the "Rare top" category. The uncertainties include all systematic and statistical errors.

mate is also not increased much when the two channels are added together as the statistical error of the flavour symmetry method is the largest uncertainty. This uncertainty is highly correlated between the e^+e^- and the $\mu^+\mu^-$ channel as the dominant background contribution from flavour symmetric processes is estimated from the common control region CReμ.

The data and background distributions for the main variables used for the signal region selection can be compared to the expectations from possible signals. This is shown for $m_{\ell\ell}$ and $E_{\text{T}}^{\text{miss}}$ in Fig. 5.22 and for H_{T} and the jet multiplicity in Fig. 5.23. In these plots, the shape of the background distributions is taken from MC simulations as the data-driven methods used for the nominal background prediction of the Z+jets+E_T^{miss} analysis cannot provide this information. The normalisation of the backgrounds, however, is taken from the flavour symmetry method, the matrix method and the jet smearing method for the respective contributions. In all plots, two signal points from the GGM model with $\tan\beta = 1.5$ are overlaid: one with $m(\tilde{g}) = 700\,\text{GeV}$ and $\mu = 200\,\text{GeV}$ and the other with $m(\tilde{g}) = 900\,\text{GeV}$ and $\mu = 600\,\text{GeV}$. With the limited statistics of SR-Z, no conclusion can be drawn if the data points look more background-like or signal-like. In the e^+e^- channel, the $m_{\ell\ell}$ distribution shows a narrow peak at the Z boson mass around 91 GeV while the distribution in the muon channel has its maximum at higher $m_{\ell\ell}$ values. This is further discussed in Sec. 5.6.1 where a fit of a simple model to the $m_{\ell\ell}$ distribution is performed to disentangle peaking and non-peaking components in SR-Z.

In Fig. 5.24, the distributions of the $\Delta\phi$ angle between the leading/subleading jet and $E_{\text{T}}^{\text{miss}}$ are shown before the final cut of $\Delta\phi(\text{jet}_{1,2}, E_T^{\text{miss}}) > 0.4$ is applied to the signal region selection. It can be seen, that only few data events are rejected by this cut, and so it can be concluded, that the events are not suspect of suffering from large fake $E_{\text{T}}^{\text{miss}}$ from the mismeasurement of a highly energetic jet. In contrast, most of the $Z +$ jets background which can only fulfil the requirements of SR-Z when large $E_{\text{T}}^{\text{miss}}$ is reconstructed mistakenly lies at low $\Delta\phi$ values and is effectively removed by the cut of 0.4. Other backgrounds with real

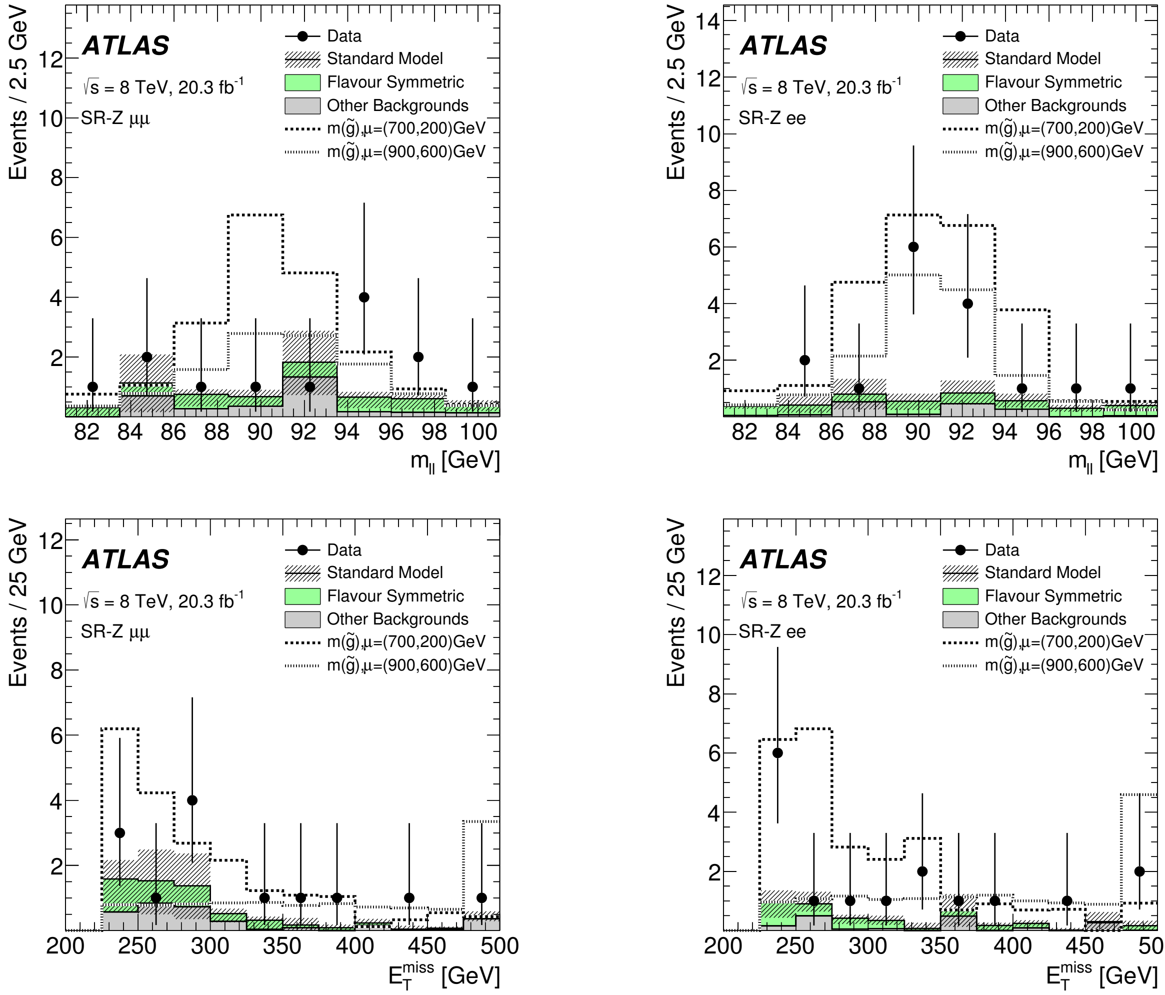

Figure 5.22: Distributions of $m_{\ell\ell}$ (top) and $E_{\mathrm{T}}^{\mathrm{miss}}$ (bottom) in SR-Z for the $\mu^+\mu^-$ (left) and e^+e^- channel (right) [53]. The shape of the background is taken from MC simulations while the normalisation of the backgrounds is derived from the data-driven methods for contributions where applicable. Two signal points from the GGM model with $\tan\beta = 1.5$ are shown for comparison. The "Other backgrounds" category comprises all non-flavour symmetric backgrounds. All experimental systematic uncertainties described in Sec. 5.4.2 as well as the uncertainties due to limited MC statistics are included in the hatched error band.

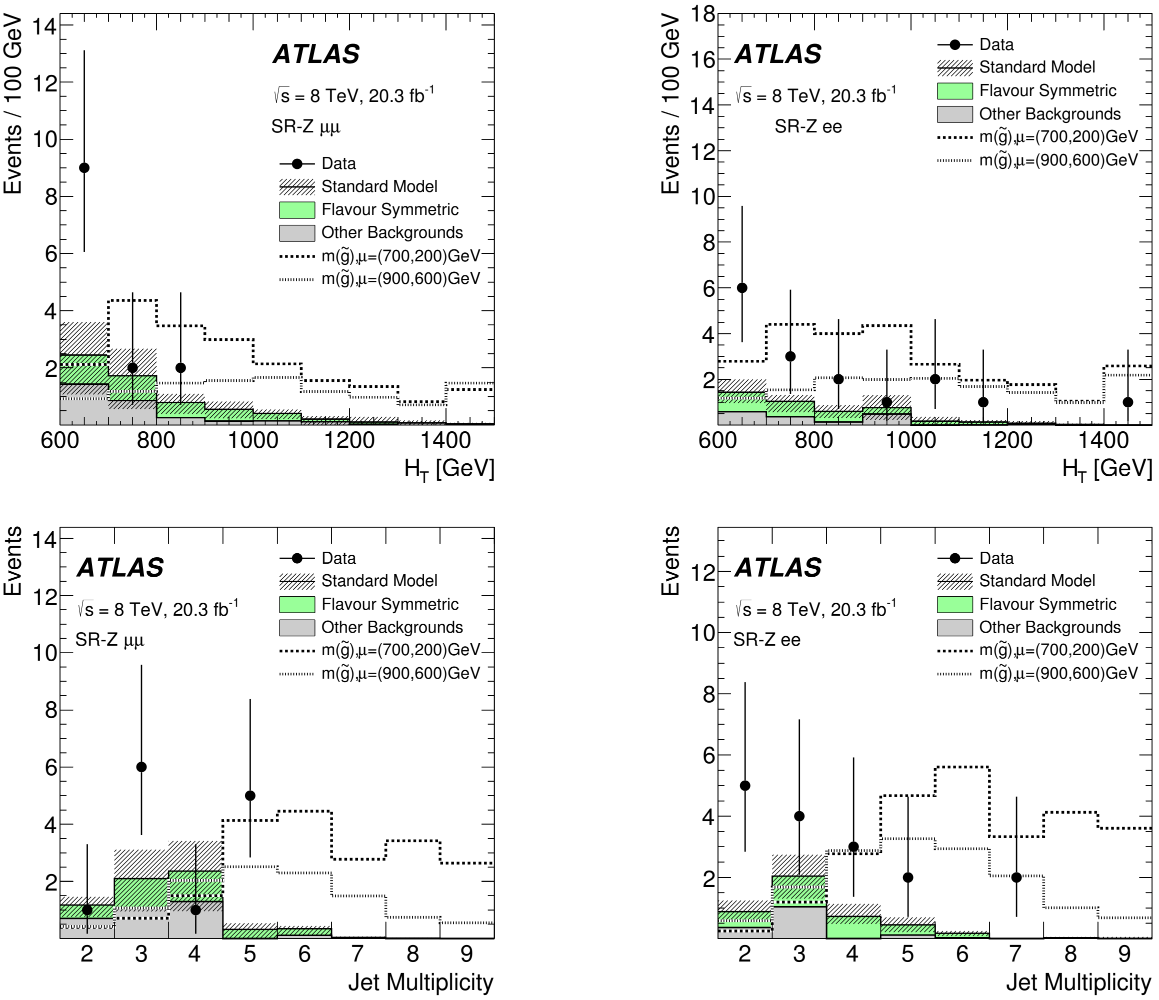

Figure 5.23: Distributions of H_{T} (top) and the jet multiplicity (bottom) in SR-Z for the $\mu^+\mu^-$ (left) and e^+e^- channel (right) [53]. The shape of the background is taken from MC simulations while the normalisation of the backgrounds is derived from the data-driven methods for contributions where applicable. Two signal points from the GGM model with $\tan\beta = 1.5$ are shown for comparison. The “Other backgrounds” category comprises all non-flavour symmetric backgrounds. All experimental systematic uncertainties described in Sec. 5.4.2 as well as the uncertainties due to limited MC statistics are included in the hatched error band.

Cut	**Signal point**			
	$\mathrm{m}(\tilde{g})$ = 700 GeV μ = 200 GeV		$\mathrm{m}(\tilde{g})$ = 900 GeV μ = 600 GeV	
No cuts	4104.3		189.0	
Lepton trigger requirement	3325.1		161.1	
Reject events with bad jets	3315.2		160.6	
Reject events with bad muons	3315.0		160.5	
Primary vertex with $\geq$ 5 tracks	3307.6		160.4	
Veto events with cosmic muons	3286.5		159.2	
At least 2 leptons	1892.2		88.8	
Veto LAr problems	1860.4		86.7	
Channel	e^+e^-	$\mu^+\mu^-$	e^+e^-	$\mu^+\mu^-$
Lepton isolation, trigger matching	775.2	725.6	40.7	29.7
Same-flavour leptons	688.4	640.0	36.1	25.7
Prompt leptons	671.0	639.3	35.3	25.6
Opposite-sign leptons	633.1	609.7	33.6	24.2
At least two signal jets	369.4	323.6	32.2	23.1
Electron crack veto	342.6	322.6	30.0	23.0
$m_{\ell\ell} > 15\,\mathrm{GeV}$	342.3	322.5	30.0	23.0
$\Delta\phi(\mathrm{jet}_1, E_\mathrm{T}^\mathrm{miss}) > 0.4$	323.5	302.6	28.3	21.9
$\Delta\phi(\mathrm{jet}_2, E_\mathrm{T}^\mathrm{miss}) > 0.4$	294.3	272.7	25.7	19.9
$81\,\mathrm{GeV} < m_{\ell\ell} < 101\,\mathrm{GeV}$	244.4	230.6	22.1	16.6
$H_\mathrm{T} > 600\,\mathrm{GeV}$	126.6	92.1	20.5	15.1
$E_\mathrm{T}^\mathrm{miss} > 225\,\mathrm{GeV}$	25.4 ± 1.3	20.0 ± 0.4	15.0 ± 0.4	11.1 ± 0.1

Table 5.12: Predicted number of signal events for the points with ($m(\tilde{g}) = 700$ GeV, $\mu = 200$ GeV) and ($m(\tilde{g}) = 900$ GeV, $\mu = 600$ GeV) from the GGM model with $\tan\beta = 1.5$ after the different selection cuts of the Z+jets+E_T^{miss} analysis described in Sec. 4.5 and 5.2 [134]. The experimental systematic uncertainty is indicated in the last row after the final cut of the signal region selection.

$E_\mathrm{T}^\mathrm{miss}$ are less rejected by the $\Delta\phi$ requirement. Also the signal is not affected much as the jets and $E_\mathrm{T}^\mathrm{miss}$ are expected to be well separated for signal events. More distributions of various kinematic quantities can be found in Sec. 5.6.1.

In all plots it becomes apparent that the signal acceptance is slightly smaller for the $\mu^+\mu^-$ channel compared to the e^+e^- channel which seems to be in disagreement with the lepton universality of the Z boson decay. This is further illustrated in Tab. 5.12 where detailed signal yields for the two GGM points from the plots are shown after the different cuts of the signal region selection. The effect is more pronounced for higher μ values and is due to the fact that different isolation requirements are used for electrons and muons as already discussed in Sec. 5.3.1. As μ increases, the $\tilde{\chi}_1^0$ gets heavier and the p_T of the Z boson from its decay becomes higher. Therefore the two leptons from the Z decay are more collimated. As a absolute isolation of 1.8 GeV criterion is applied to muons with $p_\mathrm{T} > 25$ GeV (compare Tab. 4.3), they are more likely to fail the isolation cut. The fact that the significance of the excess is higher in the e^+e^- channel than in the $\mu^+\mu^-$ channel seems to agree with the expected behaviour of the signal.

The background prediction shows the opposite effect and is higher in $\mu^+\mu^-$ events. However, the background estimates in the two channels agree within their uncertainty and the difference can nearly fully be accounted to the fake lepton estimate which suffers from a very large statistical error of more than 100 %. With the integrated luminosity available for this thesis, no final conclusion about the origin of the excess can be drawn.

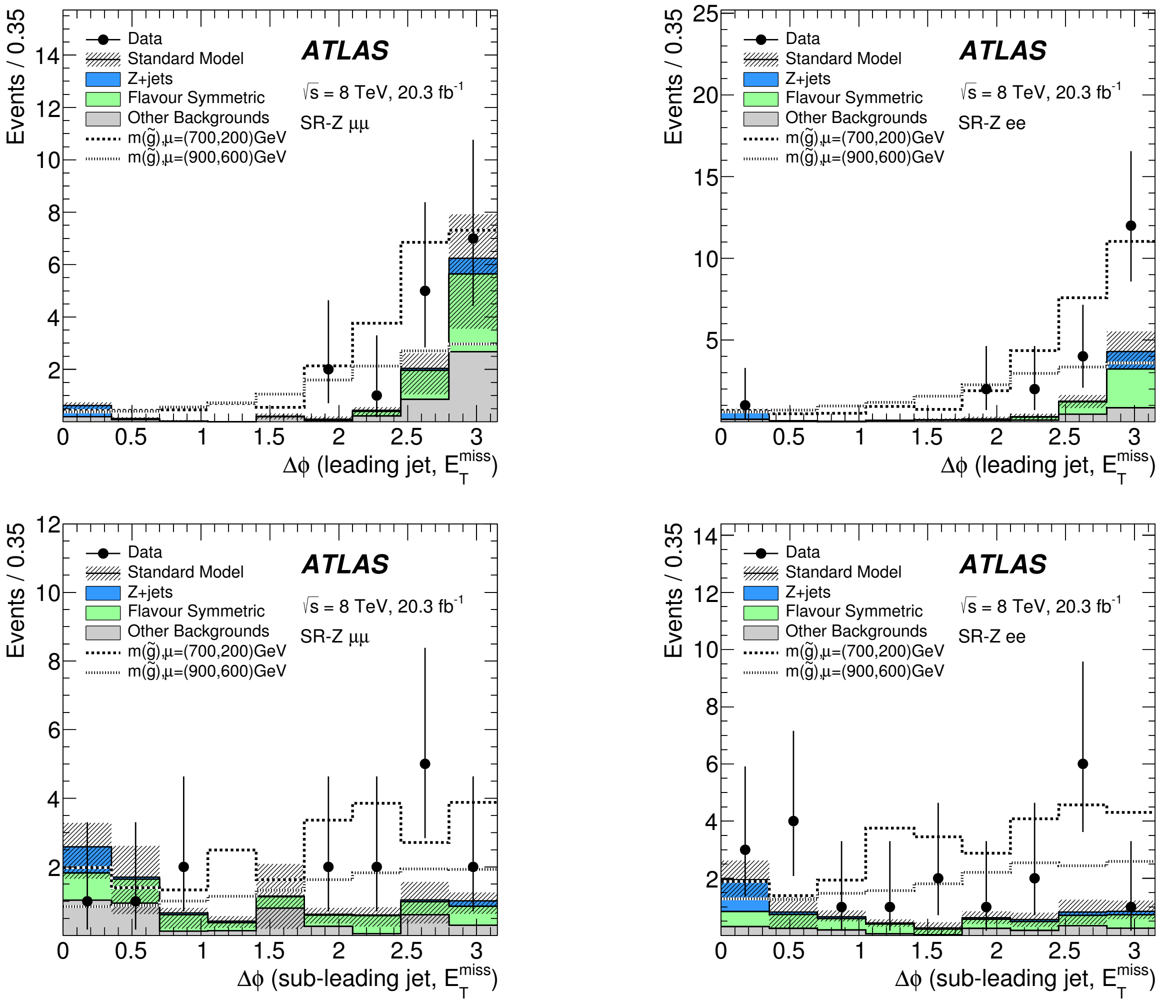

Figure 5.24: Distributions of $\Delta\phi$ between $E_{\mathrm{T}}^{\mathrm{miss}}$ and the leading jet (top) as well as the subleading jet (bottom) in SR-Z for the $\mu^+\mu^-$ (left) and e^+e^- channel (right) [53]. The shape of the background is taken from MC simulations while the normalisation of the backgrounds is derived from the data-driven methods for contributions where applicable. Two signal points from the GGM model with $\tan\beta = 1.5$ are shown for comparison. The "Other backgrounds" category comprises fake lepton, WZ, ZZ, $t\bar{t} + W/Z$, $t\bar{t} + WW$ and $t + Z$ processes. All experimental systematic uncertainties described in Sec. 5.4.2 as well as the uncertainties due to limited MC statistics are included in the hatched error band.

5.6 Validation of the results

The excess of data over the SM prediction observed in SR-Z has been subject to careful investigations to exclude underestimated or missing background contributions or not understood effects in any of the analysis steps as the cause for this excess. The studies can be grouped into three categories:

1. **Cross-checks on the events in SR-Z:**
   - Comparison between background prediction and data for all important kinematic distributions.
   - Investigation on a feature in the ϕ distribution of the leading jet.
   - Fit of the peak in the $m_{\ell\ell}$ distribution.
2. **Validation of the complete background estimation:**
   - Re-running of the full analysis in various validation and control regions.
   - MC-to-data comparison for kinematic distributions in VRs and CRs.
   - Investigation of the Z boson kinematics in the phase space of SR-Z.
3. **Investigations on the physics objects:**
   - Study of the lepton resolution and its dependency on p_{T}.
   - Check of the jet response and resolution.
   - Validation of the $E_{\mathrm{T}}^{\mathrm{miss}}$ reconstruction and calibration.
   - Investigations on the angular separation between the two signal leptons.

These studies will be outlined in the next sections in more detail. Further cross-checks have been performed [132] which are not discussed in this thesis and only mentioned for completeness here and at appropriate places in the other sections:

- Validation of the assumptions and results of the flavour symmetry method.
- Cross-check of the jet smearing results using the data-driven jet-Z balance method [162].
- Careful study of the impact of the $\Delta\phi(\mathrm{jet}_{1,2}, E_T^{\mathrm{miss}}) > 0.4$ cut on the signal acceptance and the background prediction.

- Detailed breakdown of the WZ and ZZ background contribution.

- Study of the impact of poorly reconstructed muons reported by an other ATLAS analysis [155].

- Investigations on the asymmetry between the e^+e^- and $\mu^+\mu^-$ channel observed in the expected signal yields as well as for some of the background predictions caused by different isolation and d_0/z_0 requirements for electrons and muons.

- Independent validation of the background prediction and the number of data events in SR-Z by other ATLAS analysis groups to exclude bugs in the software framework of the Z+jets+E_T^{miss} analysis.

These cross-checks of the analysis results did not identify any problems with the search strategy or the background prediction methods which could serve as a possible explanation for the observed excess.

5.6.1 Events in the Z signal region

Various kinematic distributions of the events in SR-Z are examined to exclude that very rare or poorly understood detector effects cause the excess of data over the background prediction. These could manifest themselves in inexplicable peaks in the angular or p_{T} distributions of the leptons or jets, for example. As already stated in Sec. 5.5, the data-driven methods used for the background estimation in the Z+jets+E_T^{miss} analysis cannot predict the shape of distributions. Instead, they are taken from MC simulations for all background sources for the studies discussed in this section. The only exception is the fake lepton background for which kinematic distributions can be obtained from the matrix method directly. The dominant $t\bar{t}$ background is scaled by a factor of 0.52 in all plots in this section as this is the normalisation factor retrieved from the fit of the $t\bar{t}$ background in the Z mass sidebands (compare Sec. 5.3.2). Although the background is not completely estimated as in the nominal analysis, the plots showing the comparison between data and simulations are still useful to see trends in data and determine if they appear to be more background-like or signal-like. For this reason, three signal samples are overlaid for comparison. They are taken from points from the GGM model with $\tan\beta = 1.5$ and have mass parameters of ($m(\tilde{g}) = 700\,\text{GeV}$, $\mu = 200\,\text{GeV}$), ($m(\tilde{g}) = 900\,\text{GeV}$, $\mu = 600\,\text{GeV}$) and ($m(\tilde{g}) = 1000\,\text{GeV}$, $\mu = 700\,\text{GeV}$), respectively. These signal samples cover a wide range of the parameter space under study and differ in their phenomenology.
Some SUSY models not explicitly considered in this thesis predict the extended production of Z bosons in association with b quarks. Therefore, the number of b-tagged jets among the three jets with the highest momenta is analysed as shown in Fig. 5.25. This distribution is also helpful to reveal possible problems with the $t\bar{t}$ background. The excess of data is spread evenly over all bins and no indication is found that the events in the signal region contain an unexpectedly high amount of b-tagged jets.
The p_{T} and angular distributions for the leading jet and leading lepton are shown in Fig. 5.26 and 5.27, respectively. The same plots for the subleading jet and lepton are presented in

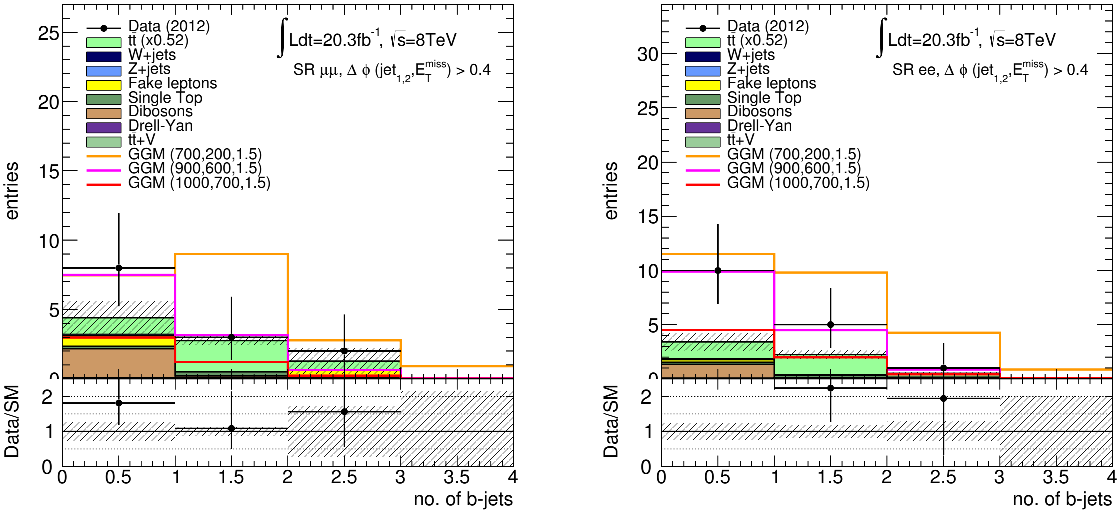

Figure 5.25: Distribution of the number of b-tags among the first three jets for the muon (left) and electron (right) channel in SR-Z. All experimental systematic uncertainties and the statistical error of the MC simulation are included in the indicated error band. The $t\bar{t}$ MC prediction is scaled by a factor of 0.52 according to the results of the sideband fit in CRT.

App. D for completeness. As already discussed in Sec. 5.3.1, the p_{T} spectrum for electrons is a bit harder than for muons due to the different isolation requirements. The statistics is rather low in all distributions which makes it difficult to draw final conclusions. No evidence for detector related problems with any of the ATLAS subsystems is found. The distributions of ϕ or η do not show suspicious peaks or wholes for any of the leptons or jets. The only visible feature is the apparent asymmetry between the positive and the negative half in the ϕ distribution of the leading jet. The same trend is also visible for the second jet (compare Fig. D.1). This means that the jets in the events in SR-Z are on average found more often in the upper half of the ATLAS detector. After detailed investigations, which are explained in the next section, it can be concluded that the effect is most likely caused by a statistical fluctuation.

In addition, it has been checked that the 29 events in SR-Z are not suspicious of being recorded during unusual data taking conditions. The pile-up distribution of the events characterised by the mean number of pp interactions per bunch crossing ranges from 10 to 35 which is expected for the 2012 run of the LHC (compare Fig. 4.2). Furthermore, the 29 events have been found to be spread over the full data taking period in 2012 as it can be seen from the breakdown in App. D.

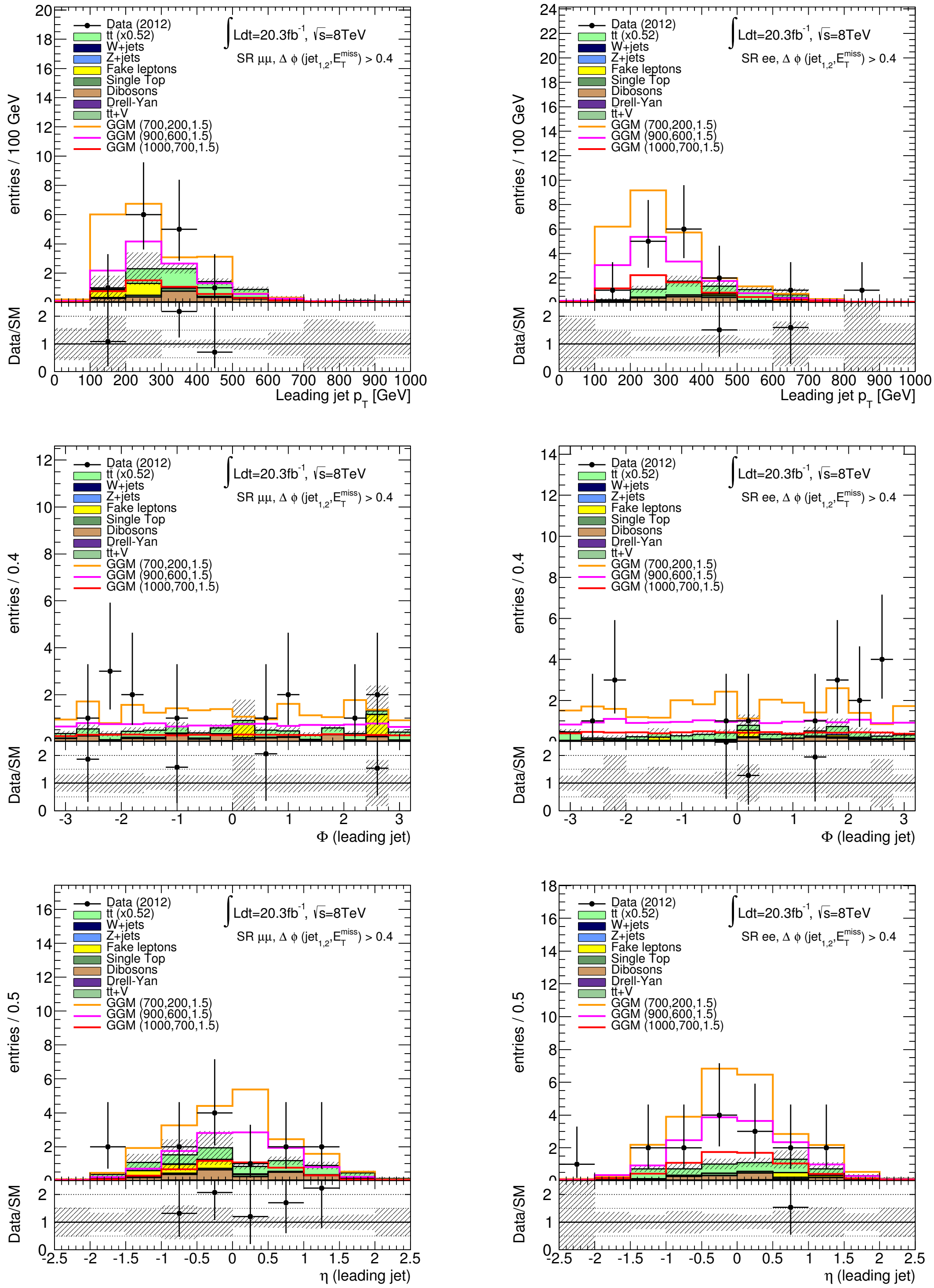

Figure 5.26: Kinematic distributions of the leading jet for the muon (left) and electron (right) channel in SR-Z: p_{T} (top), ϕ angle (middle) and pseudo-rapidity η (bottom). Only the statistical uncertainties of the MC simulation are included in the indicated error bands. The $t\bar{t}$ MC prediction is scaled by a factor of 0.52 according to the results of the sideband fit in CRT.

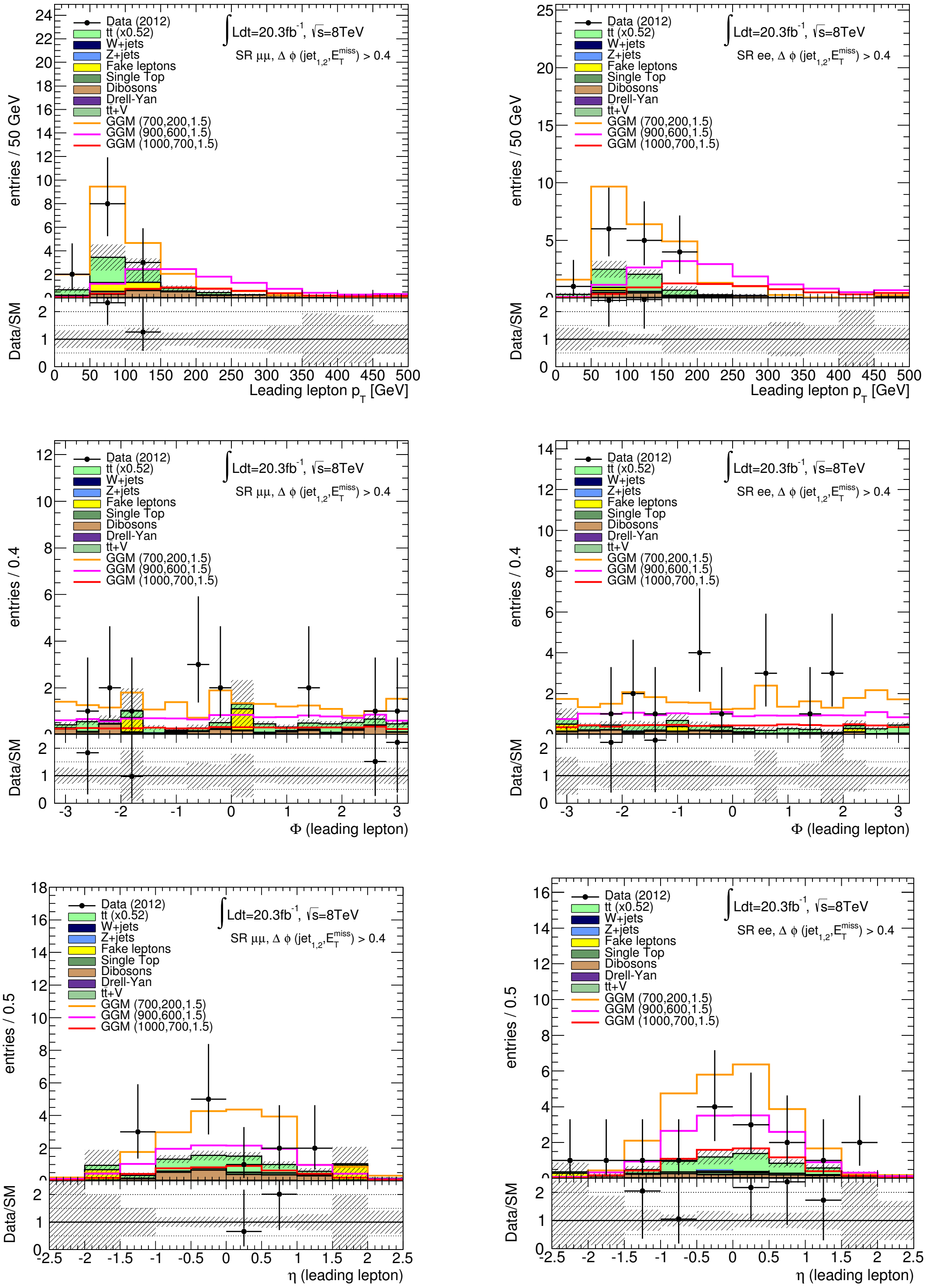

Figure 5.27: Kinematic distributions of the leading lepton for the muon (left) and electron (right) channel in SR-Z: p_{T} (top), ϕ angle (middle) and pseudo-rapidity η (bottom). Only the statistical uncertainties of the MC simulation are included in the indicated error bands. The $t\bar{t}$ MC prediction is scaled by a factor of 0.52 according to the results of the sideband fit in CRT.

Investigation on leading jet ϕ asymmetry

The asymmetry between jets with $\phi > 0$ and $\phi < 0$ (see middle right plot of Fig. 5.26) in the e^+e^- channel might be caused by some beam induced non-collision background (e.g. interactions of the beam with the remaining gas in the beam pipe). These backgrounds normally do not originate from the nominal interaction point. Support, supply and readout structures in the detector which are not evenly distributed in ϕ [73] might affect jets from these processes leading to the observed asymmetry. Although the same effect should also appear in the muon channel in this case and jets from these kind of backgrounds should be completely rejected by the quality requirements described in Sec. 4.3.2, the feature has been scrutinised and is most likely caused by a statistical fluctuation.

This can be concluded from the plots in Fig. 5.28 where the ϕ distributions of the leading jet in SR-Z and VRTZ are shown with a very coarse binning. For this study, the requirement on $\Delta\phi(\mathrm{jet}_{1,2}, E_T^{\mathrm{miss}}) > 0.4$ was removed from the selection requirements for both regions to enhance the statistics. Again, the background distributions are obtained from MC simulations and the $t\bar{t}$ contribution in SR-Z is scaled by a factor of 0.49, which is the normalisation factor retrieved from the sideband fit (see Sec. 5.3.2) for the case without $\Delta\phi(\mathrm{jet}_{1,2}, E_T^{\mathrm{miss}})$ cut.

VRTZ is located in lower $E_{\mathrm{T}}^{\mathrm{miss}}$ region at $150\,\mathrm{GeV} < E_{\mathrm{T}}^{\mathrm{miss}} < 225\,\mathrm{GeV}$ and has a loosened cut on $H_{\mathrm{T}} > 500\,\mathrm{GeV}$ compared to SR-Z but is still very similar with respect to background composition and event kinematics. The statistics in VRTZ is larger than in SR-Z and it can be seen that the effect vanishes there. In addition, the distribution of the jet vertex fraction introduced in Sec. 4.3.2 is cross-checked which quantifies how much of the jet energy is comprised in tracks coming from the primary vertex. This is shown in Fig. 5.29 for the leading jet. All jets in the signal region events have JVF ≈ 1 which indicates that they most likely originate from the primary vertex. Jets from beam induced backgrounds would appear at smaller JVF values. No jets are observed there and it can be concluded that these processes do not play a role in SR-Z.

Fit of the Z mass peak

A model with a peaking and a non-peaking component is fitted to the $m_{\ell\ell}$ distribution in the signal region to quantify to what extent the excess in the signal region appears to be Z-like or $t\bar{t}$-like. The fit is performed for the electron and muon channel separately as well as for the combination of the two channels. A simple model is used: The contribution from processes involving a Z boson (be it signal or background) is modelled by a Gaussian distribution while non-peaking processes, which are expected to come mainly from $t\bar{t}$ production, are fitted with a first order polynomial. The shape of the Z peak is constrained by fitting the Gaussian template in an inclusive region first (denoted as "Z preselection"). The width and the mean of the Z peak obtained there are then used for the subsequent fit in SR-Z where only the normalisation of the Gaussian distribution is allowed to float. For the template fit in the Z preselection region, all events that contain a Z candidate (i.e. e^+e^- or $\mu^+\mu^-$ with $81\,\mathrm{GeV} < m_{\ell\ell} < 101\,\mathrm{GeV}$) and at least two signal jets are used.

The results of the fit in the Z preselection region and SR-Z can be found in Fig. 5.30 for the muon channel, the electron channel and their combination. These plots show that the simple

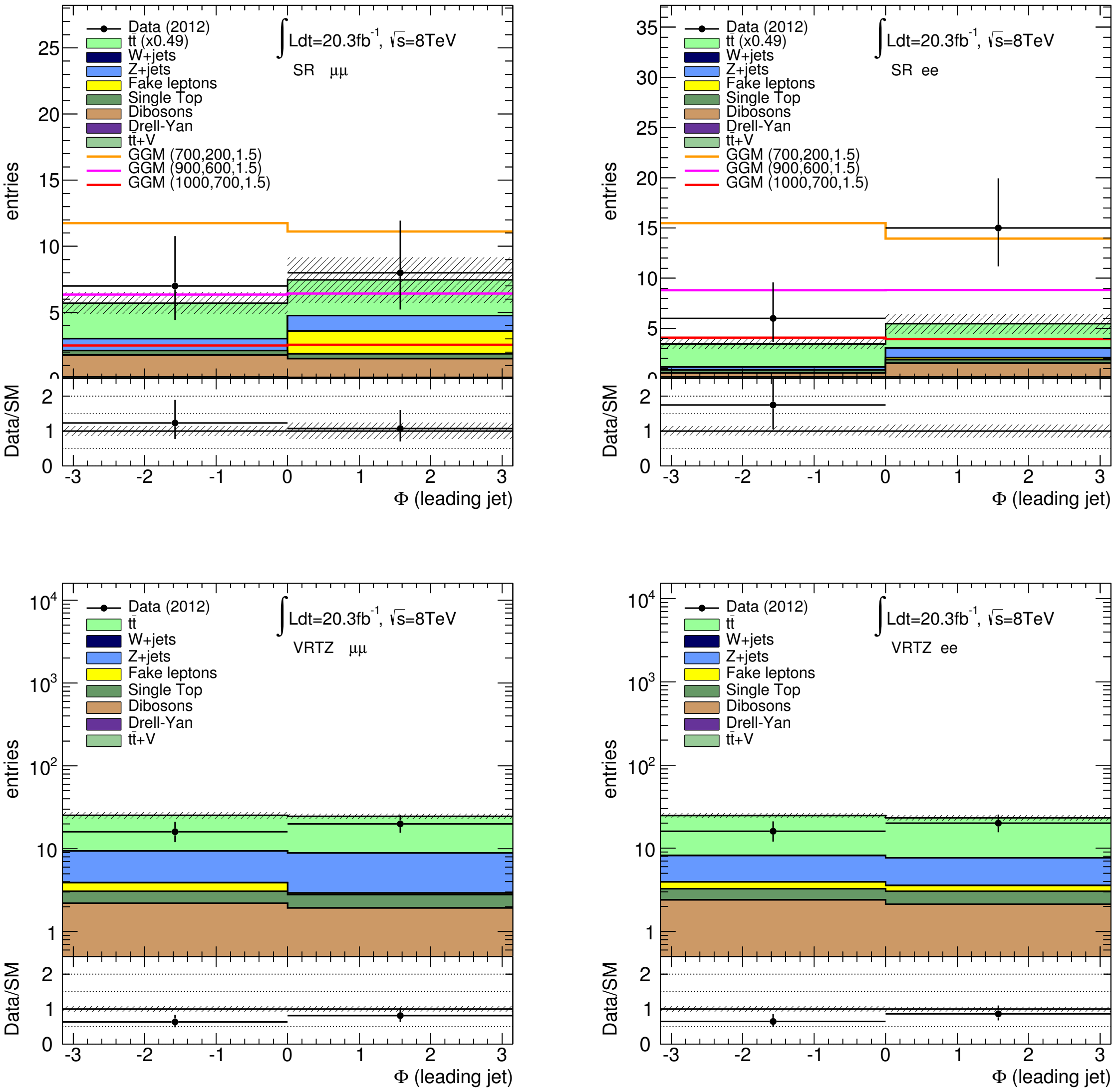

Figure 5.28: Asymmetry between $\phi > 0$ and $\phi < 0$ for the leading jet in SR-Z (top) and VRTZ (bottom) for the muon (left) and electron channel (right). The $\Delta\phi(\text{jet}_{1,2}, E_T^{\text{miss}}) > 0.4$ cut is not applied for these plots. Only the statistical error of the MC simulation is included in the indicated error bands. The $t\bar{t}$ MC prediction in SR-Z has been normalised by 0.49 according to the results of the sideband fit in CRT. In VRTZ, no normalisation factor is applied to $t\bar{t}$.

Channel	peaking	non-peaking
$\mu^+\mu^-$	-0.9 ± 2.8	11.4 ± 4.5
e^+e^-	8.2 ± 5.6	4.8 ± 6.6
SF	10.7 ± 5.3	15.0 ± 5.7

Table 5.13: Results of the fit of the $m_{\ell\ell}$ distribution in SR-Z with a Gaussian peak plus a first order polynomial for non-peaking processes.

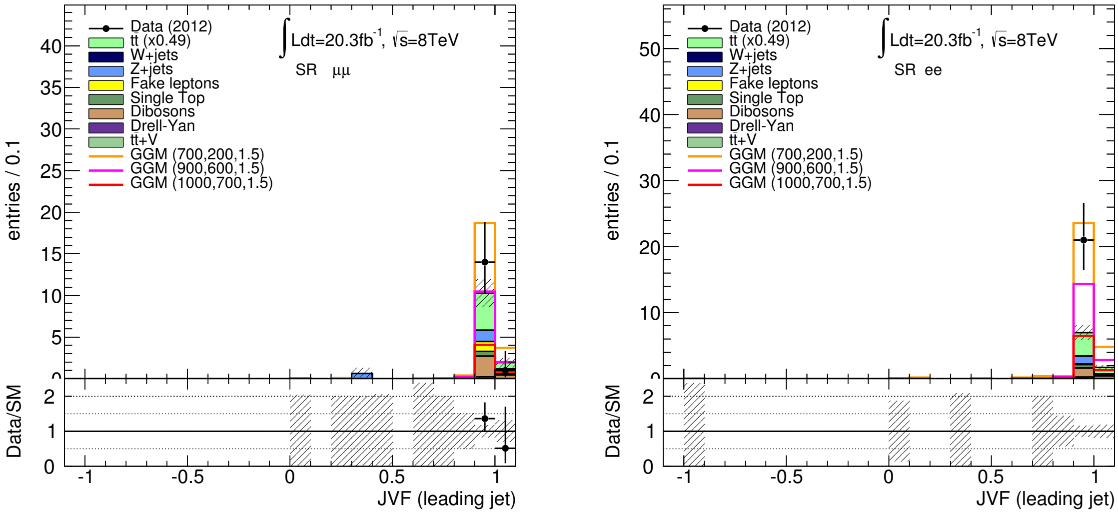

Figure 5.29: Distribution of the leading jet JVF for the muon (left) and electron channel (right) in SR-Z. The $\Delta\phi(\text{jet}_{1,2}, E_T^{\text{miss}}) > 0.4$ cut is not applied for these plots. Only the statistical error of the MC simulation is included in the indicated error bands. The $t\bar{t}$ MC prediction has been normalised by 0.49 according to the results of the sideband fit in CRT.

approach models the data reasonably well although it has some shortcomings (e.g. does not yield the right total number of events). The event yields for the peaking and the non-peaking component derived from the fit in SR-Z are summarised in Tab. 5.13. The excess shows a Z-like appearance especially in the electron channel. By comparing the fit results to the background estimate from Tab. 5.11 it can be seen that only about 1.2 events are predicted from background processes involving a Z boson while the fit yields 8.2 events from peaking processes. The non-peaking component is only slightly above the nominal estimate for non-Z backgrounds.

In the muon channel the highest peak in the $m_{\ell\ell}$ distribution is shifted by $\sim$4 GeV with respect to the mass of the Z boson which might be due to a statistical fluctuation. This is not accounted for by the fit as the Z peak position is fixed to the value retrieved in the Z preselection region. Therefore, the fit yields a negative value for the peaking component in the $\mu^+\mu^-$ channel.

When both channels are added together and fitted simultaneously, more Z processes are observed than predicted by the background estimation of the analysis. However, this is also true for the non-peaking components. Given the errors of the fit, it cannot be concluded at this stage if the excess of data in SR-Z appears to come from the extended production of Z bosons or not.

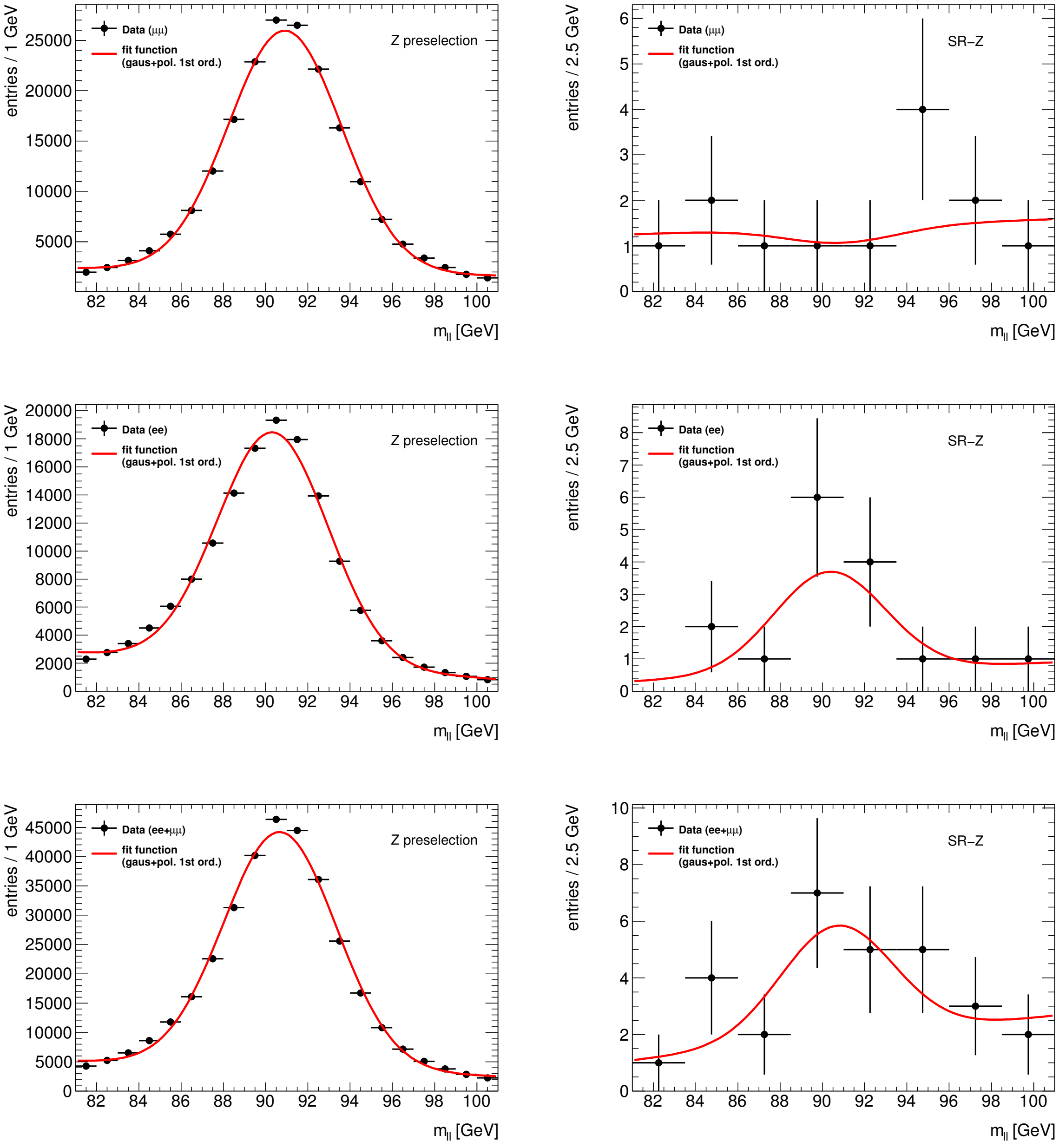

Figure 5.30: Fit of the $m_{\ell\ell}$ distribution in the Z preselection region (left) and in SR-Z (right) for the muon channel (top), the electron channel (middle) and their sum (bottom). A Gaussian distribution plus a first order polynomial is used as model. The shape of the peak in the left plots is used to derive a template for the peak in SR-Z on the right.

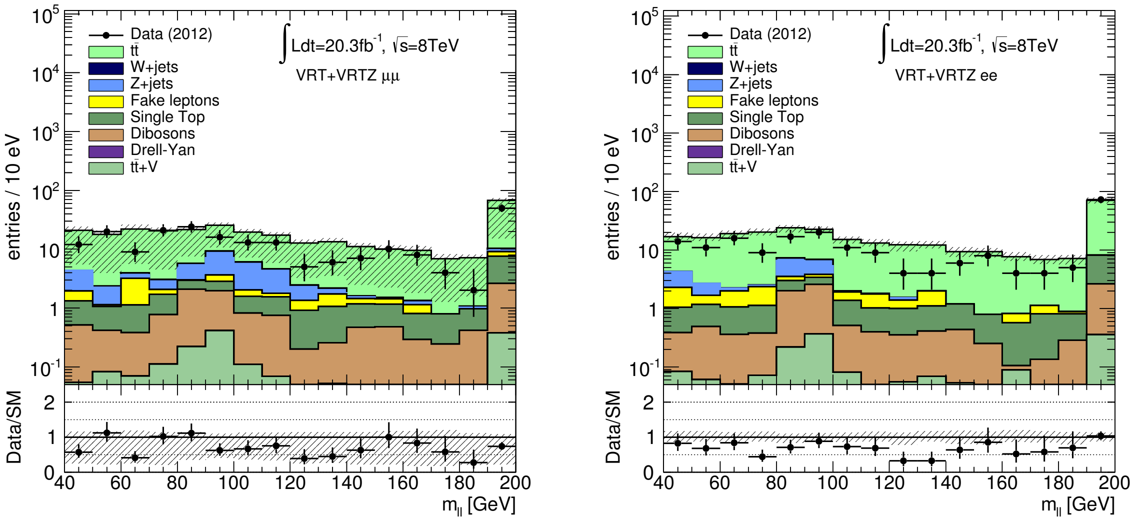

Figure 5.31: MC-to-data comparison for the $m_{\ell\ell}$ distribution for the muon (left) and electron (right) channel in VRTZ (81 GeV $< m_{\ell\ell} <$ 101 GeV) and VRT ($m_{\ell\ell} <$ 81 GeV or $m_{\ell\ell} >$ 101 GeV) without the cut on $\Delta\phi(\mathrm{jet}_{1,2}, E_T^{\mathrm{miss}}) > 0.4$. All experimental systematic uncertainties and the statistical error of the MC simulation are included in the indicated error band.

5.6.2 Background prediction

Various cross-checks and tests are performed to prove the validity and robustness of the background estimation methods. Some of them have already been discussed in Sec. 5.3.

Kinematic distributions in VRs and CRs

Distributions of the most important kinematic variables used for the signal region selection ($m_{\ell\ell}$, $E_{\mathrm{T}}^{\mathrm{miss}}$, H_{T}, jet multiplicity) are compared between background prediction and data in three of the VRs and CRs. The regions differ in their background composition which helps to disentangle effects of the various components. As for most plots in Sec. 5.6.1, the shape of the background distribution is predicted from MC simulations as the data-driven methods cannot be used for this. Still, this comparison is useful to reveal problems at the edges of the accessible phase space at high $E_{\mathrm{T}}^{\mathrm{miss}}$ or high H_{T}. The normalisation of the $t\bar{t}$ MC is scaled by a factor of 0.52 in regions at high $E_{\mathrm{T}}^{\mathrm{miss}} > 225$ GeV, while no scale factor is applied in regions at lower $E_{\mathrm{T}}^{\mathrm{miss}}$ values.

The distribution of the invariant dilepton mass is validated as shown in Fig. 5.31. There, the $m_{\ell\ell}$ range from 40 GeV to 200 GeV is shown. The region around the Z mass peak corresponds to VRTZ while the sidebands are referred to as VRT. The cut on $\Delta\phi(\mathrm{jet}_{1,2}, E_T^{\mathrm{miss}}) > 0.4$ is not applied for this study. It can be seen that the sidebands are dominated by $t\bar{t}$ background while $Z+$jets processes also contribute significantly in the range 81 GeV $< m_{\ell\ell} <$ 101 GeV. Some $Z+$jets background also appears in the low $m_{\ell\ell}$ region. This is due to the fact that the

$Z+$jets MC used in this analysis contains all Drell-Yan processes with $m_{\ell\ell} > 40\,\text{GeV}$. The range $m_{\ell\ell} < 40\,\text{GeV}$ is included in a separate Drell-Yan MC but not visible in the figures due to the plotting range.

From the plots, it becomes apparent that the normalisation of the $t\bar{t}$ background is not predicted correctly by the MC simulation also in VRT and VRTZ. However, the scale factor needed to correct for this is closer to 1 than in the region $E_{\mathrm{T}}^{\mathrm{miss}} > 225\,\text{GeV}$. Besides the discrepancy in the overall normalisation, good agreement is observed between data and the SM prediction and the $m_{\ell\ell}$ distribution is modelled well over the full range.

The $Z+$jets background can be cross-checked in VRZ which is located at low $E_{\mathrm{T}}^{\mathrm{miss}} < 150\,\text{GeV}$ and is dominated by this process. The distributions of $E_{\mathrm{T}}^{\mathrm{miss}}$, H_{T} and the number of jets in VRZ are presented in Fig. 5.32 and no effects which might lead to a incorrect $Z+$jets prediction in the analysis are visible.

Going to higher $E_{\mathrm{T}}^{\mathrm{miss}}$ values, the $Z+$jets background shrinks while $t\bar{t}$ processes start to dominate. This can be seen in Fig. 5.33 where the same distributions are shown for VRTZ, which is located in the range $150\,\text{GeV} < E_{\mathrm{T}}^{\mathrm{miss}} < 225\,\text{GeV}$. Although the H_{T} cut of VRTZ is lowered to 500 GeV compared to VRZ and SR-Z, the statistics is very limited leading to large uncertainties on the background prediction. Good agreement between data and background prediction is observed within the uncertainties.

CRT is defined such that also the region above $E_{\mathrm{T}}^{\mathrm{miss}} > 225\,\text{GeV}$ can be validated. It is positioned in the Z mass sideband to be orthogonal to SR-Z but has the same event selection with respect to all other cuts. The distributions for CRT are summarised in Fig. 5.34. Also there, the statistical uncertainties are large. Data and MC simulations agree well within the uncertainties. The asymmetry in the $Z+$jets background between the e^+e^- and $\mu^+\mu^-$ channel which can be seen best in the tails of the H_{T} distribution is due to the fact that the muon resolution decreases with increasing lepton momentum while for electrons it is vice versa. Thus, the Z peak is wider for decays into highly energetic muons than for electrons and $Z \to \mu\mu$ events can fall out of the window of $81\,\text{GeV} < m_{\ell\ell} < 101\,\text{GeV}$ more easily. This effect is discussed in detail in Sec. 5.6.3.

The good agreement in the various validation and control regions spread over the full $E_{\mathrm{T}}^{\mathrm{miss}}$ range shows the validity of the background modelling. No problems which might hint at an explanation of the excess in SR-Z are discovered anywhere.

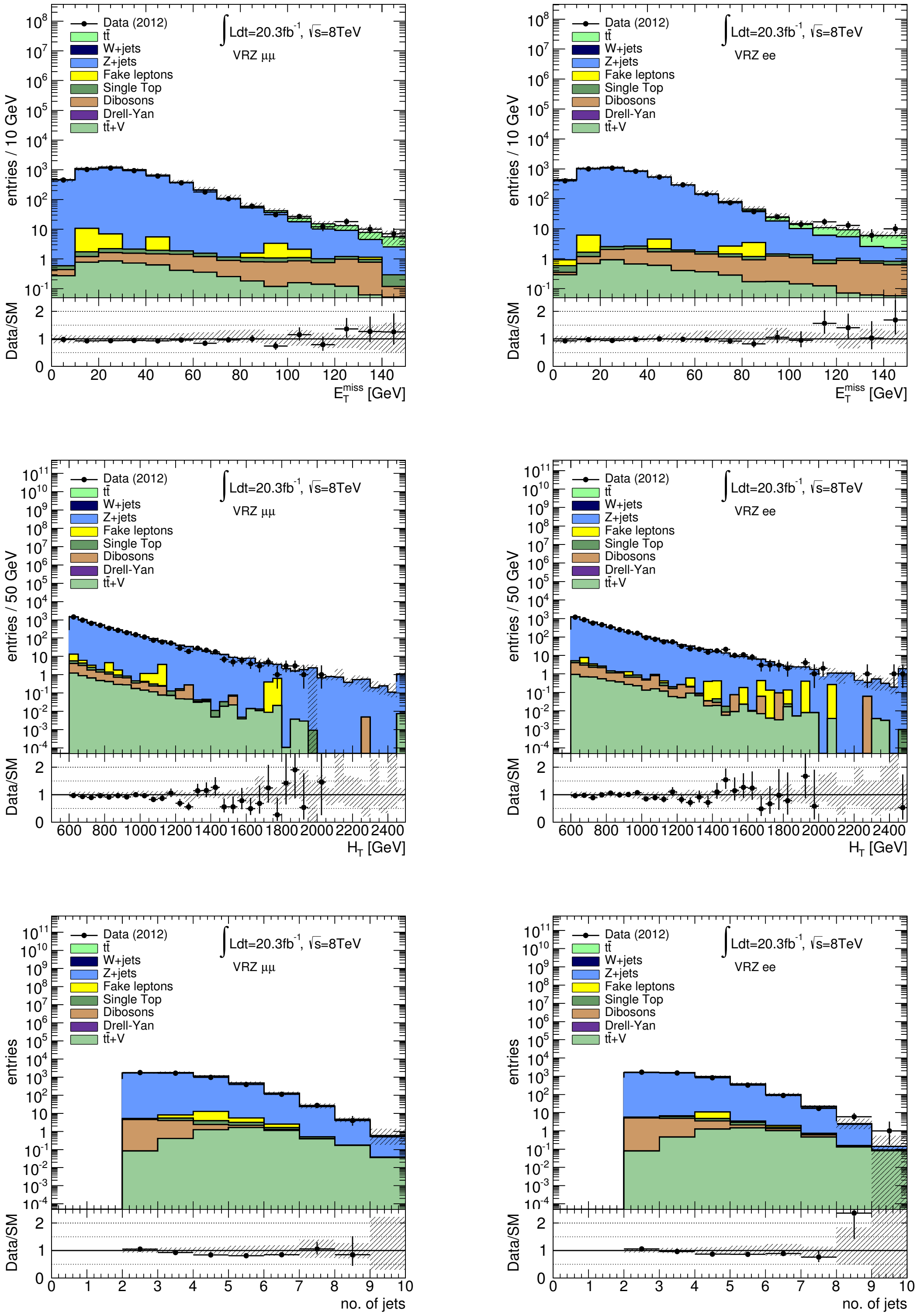

Figure 5.32: MC-to-data comparison for kinematic distributions in VRZ for the muon (left) and electron channel (right): $E_{\mathrm{T}}^{\mathrm{miss}}$ (top), H_{T} (middle) and jet multiplicity (bottom). All experimental systematic uncertainties and the statistical error of the MC simulation are included in the indicated error band.

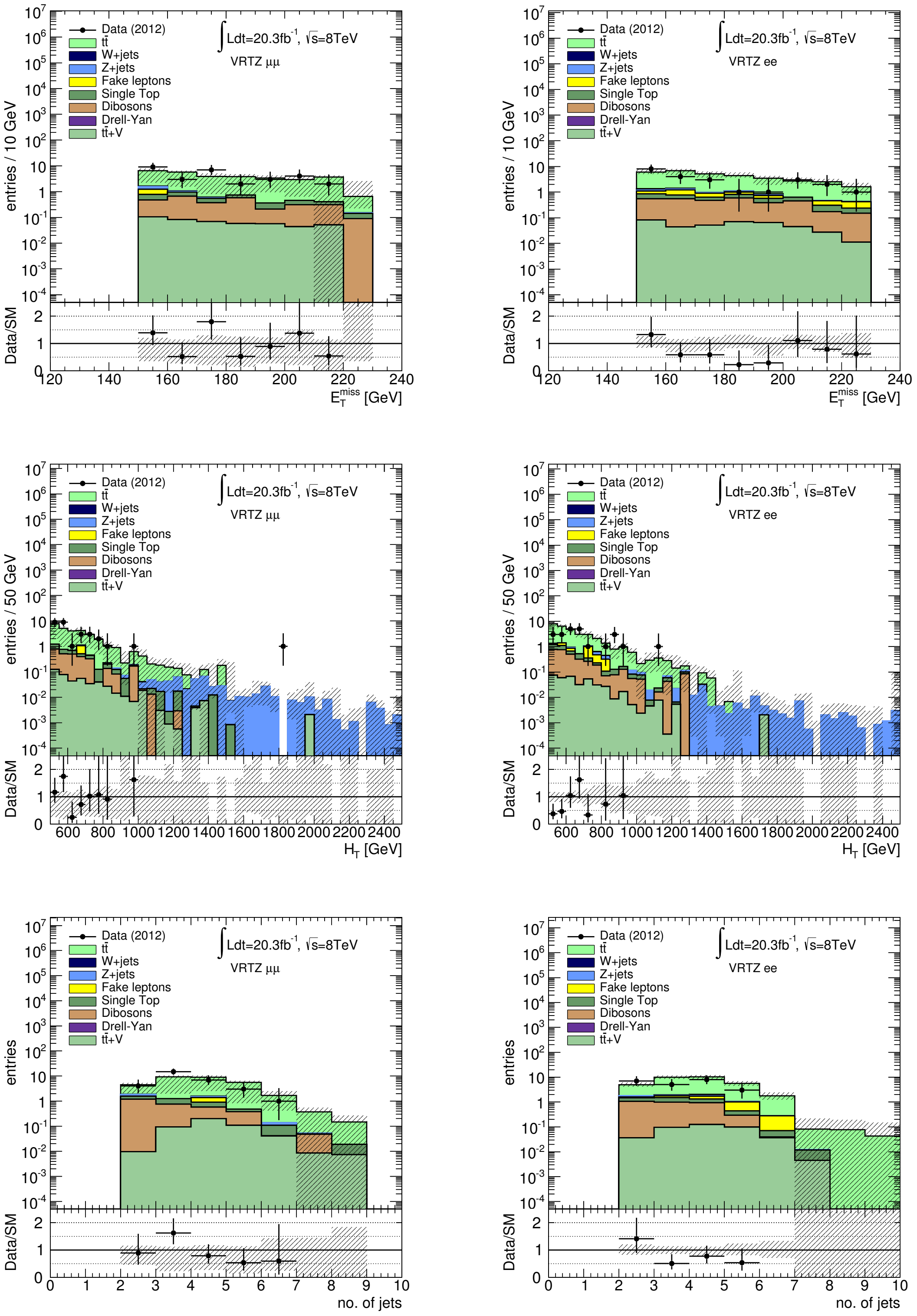

Figure 5.33: MC-to-data comparison for kinematic distributions in VRTZ for the muon (left) and electron channel (right): $E_{\mathrm{T}}^{\mathrm{miss}}$ (top), H_{T} (middle) and jet multiplicity (bottom). All experimental systematic uncertainties and the statistical error of the MC simulation are included in the indicated error band.

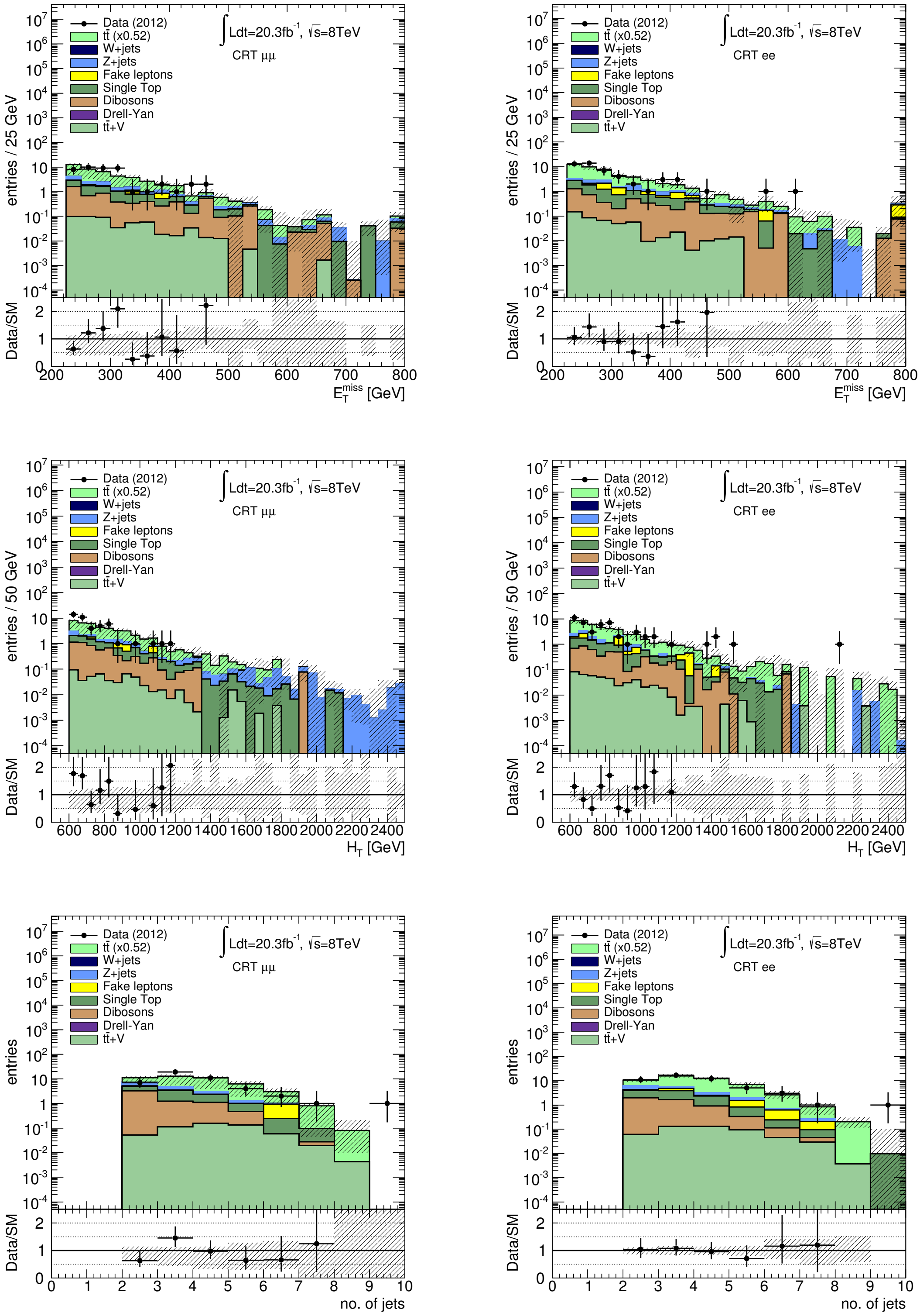

Figure 5.34: MC-to-data comparison for kinematic distributions in CRT for the muon (left) and electron channel (right): $E_{\mathrm{T}}^{\mathrm{miss}}$ (top), H_{T} (middle) and jet multiplicity (bottom). All experimental systematic uncertainties and the statistical error of the MC simulation are included in the indicated error band. The $t\bar{t}$ MC prediction is scaled by a factor of 0.52 according to the results of the sideband.

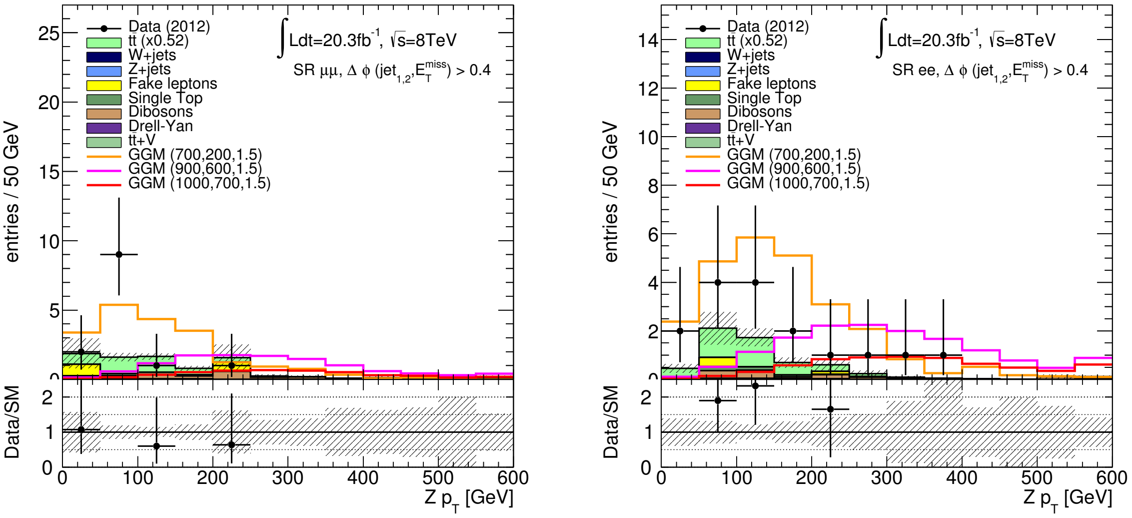

Figure 5.35: Distribution of the reconstructed p_{T} of the Z boson in SR-Z for the muon (left) and electron channel (right). All experimental systematic uncertainties and the statistical error of the MC simulation are included in the indicated error band. The $t\bar{t}$ MC prediction is scaled by a factor of 0.52.

Checks on the kinematics of the Z boson

The excess of data in the signal region appears to be Z-like at first glance especially in the e^+e^- channel. Hence, the kinematics of the Z boson are scrutinised in order to reveal potential problems with the $Z+\text{jets}$ background prediction in the phase space at very high $E_{\mathrm{T}}^{\mathrm{miss}}$. For this, the Lorentz vector of the Z boson is reconstructed from the two leading leptons with opposite-sign and same-flavour assuming that they originate from the Z boson decay. The Z p_{T} distribution in SR-Z can be found in Fig. 5.35. Again, the background is taken from computer simulations and the $t\bar{t}$ MC is scaled by a factor of 0.52 in these plots as discussed before. In events without a Z boson, the "Z" p_{T} can still be reconstructed, but is somehow meaningless, of course, and has a random value.

It can be seen that the transverse momentum of the boson is of the order of the mass of the Z itself. This means that the Z bosons selected by the Z+jets+E_T^{miss} analysis are not at rest but boosted moderately. The leptons from the Z decay are thus collimated. The correlations between the Z p_{T} and various other kinematic quantities in the events are checked to reveal possible features hinting at a problem with the $Z+\text{jets}$ background estimation. These studies are performed in VRTZ with a loosened $E_{\mathrm{T}}^{\mathrm{miss}}$ selection ($125\,\text{GeV} < E_{\mathrm{T}}^{\mathrm{miss}} < 225\,\text{GeV}$) and without the cut on $\Delta\phi(\text{jet}_{1,2}, E_T^{\mathrm{miss}}) > 0.4$ to enhance the statistics and the contribution from $Z+\text{jets}$ processes.

The correlation between H_{T} and Z p_{T} is checked for $Z+\text{jets}$ simulated events as shown in the top row of Fig. 5.36. There is an epxected dependency of H_{T} on the Z p_{T} as bosons with a higher boost lead to objects with higher momenta and thus higher H_{T}. This dependency vanishes for simulated $t\bar{t}$ events which are shown in the middle row of the same figure. As the two leptons in these events do not originate from the same particle decay, there is no correlation between the "Z" p_{T} reconstructed from them and the overall event activity characterised by H_{T}. The correlation observed in data is shown for comparison in the bottom plots. However, the statistics is not large enough to disentangle the effects of $t\bar{t}$ and $Z+$jets events in data.

In Fig. 5.37, the correlation between Z p_{T} and the direction of the missing transverse momentum is shown for a $Z+$jets MC, a $t\bar{t}$ MC as well as for data. The difference in the azimuthal angle between the Z boson and the missing energy, $\Delta\phi(Z, E_{\mathrm{T}}^{\mathrm{miss}})$, is used instead of ϕ angle of $E_{\mathrm{T}}^{\mathrm{miss}}$ for better visibility. In the $Z+$jets simulated events, it can be seen clearly that $\Delta\phi(Z, E_{\mathrm{T}}^{\mathrm{miss}})$ is either close to 0 or close to π. This is consistent with the assumption that $E_{\mathrm{T}}^{\mathrm{miss}}$ in $Z+$jets events is only reconstructed by mistake from the mismeasurement of one of the jets. Depending on whether the jet energy is measured too low or too high, the fake $E_{\mathrm{T}}^{\mathrm{miss}}$ points either in the direction or in the opposite direction of this particular jet. The jets balance the momentum of the Z boson and thus also of the direction of the Z boson is aligned with the missing energy. As expected, the effect is enhanced the higher the boost of the Z boson gets. In dileptonic $t\bar{t}$ processes, the $E_{\mathrm{T}}^{\mathrm{miss}}$ direction is not correlated with the "boson" p_{T} as these contain real missing energy from the two neutrinos. The limited data statistics makes it impossible again to disentangle $Z+$jets and $t\bar{t}$ effects in an unambiguous way.

In all these cross-checks, the simulation of the $Z+$jets background shows the expected behaviour. It can thus be concluded that no strange features appear in the phase space under study and the $Z+$jets background estimation is reliable.

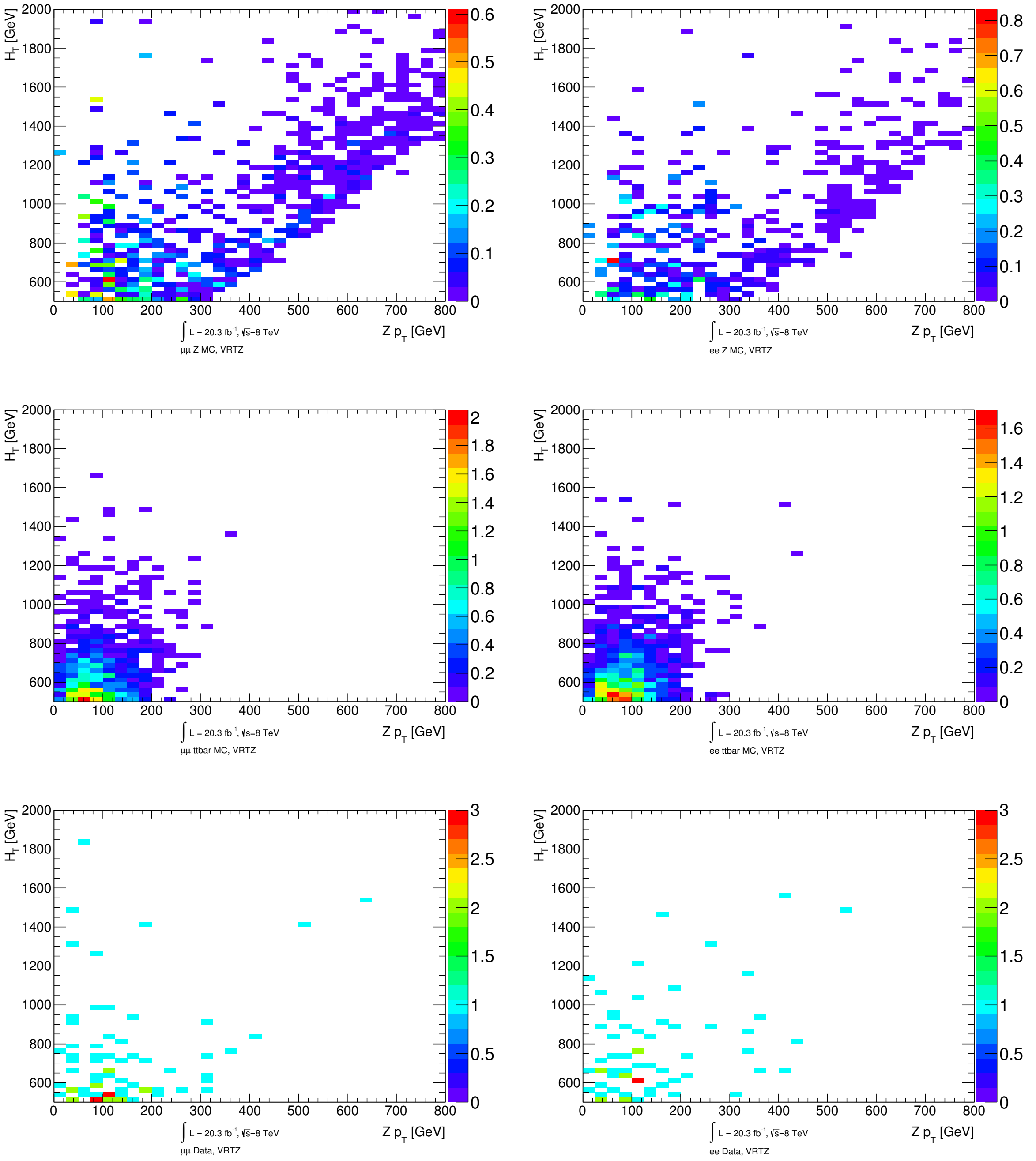

Figure 5.36: Correlations between the reconstructed Z p_{T} and H_{T} for the muon (left) and electron channel (right): $Z+$jets MC (top), $t\bar{t}$ MC (middle) and data (bottom). The plots are shown for VRTZ with a loosened $E_{\mathrm{T}}^{\mathrm{miss}}$ requirement of $125\,\mathrm{GeV} < E_{\mathrm{T}}^{\mathrm{miss}} < 225\,\mathrm{GeV}$ and without the cut on $\Delta\phi(\mathrm{jet}_{1,2}, E_T^{\mathrm{miss}}) > 0.4$.

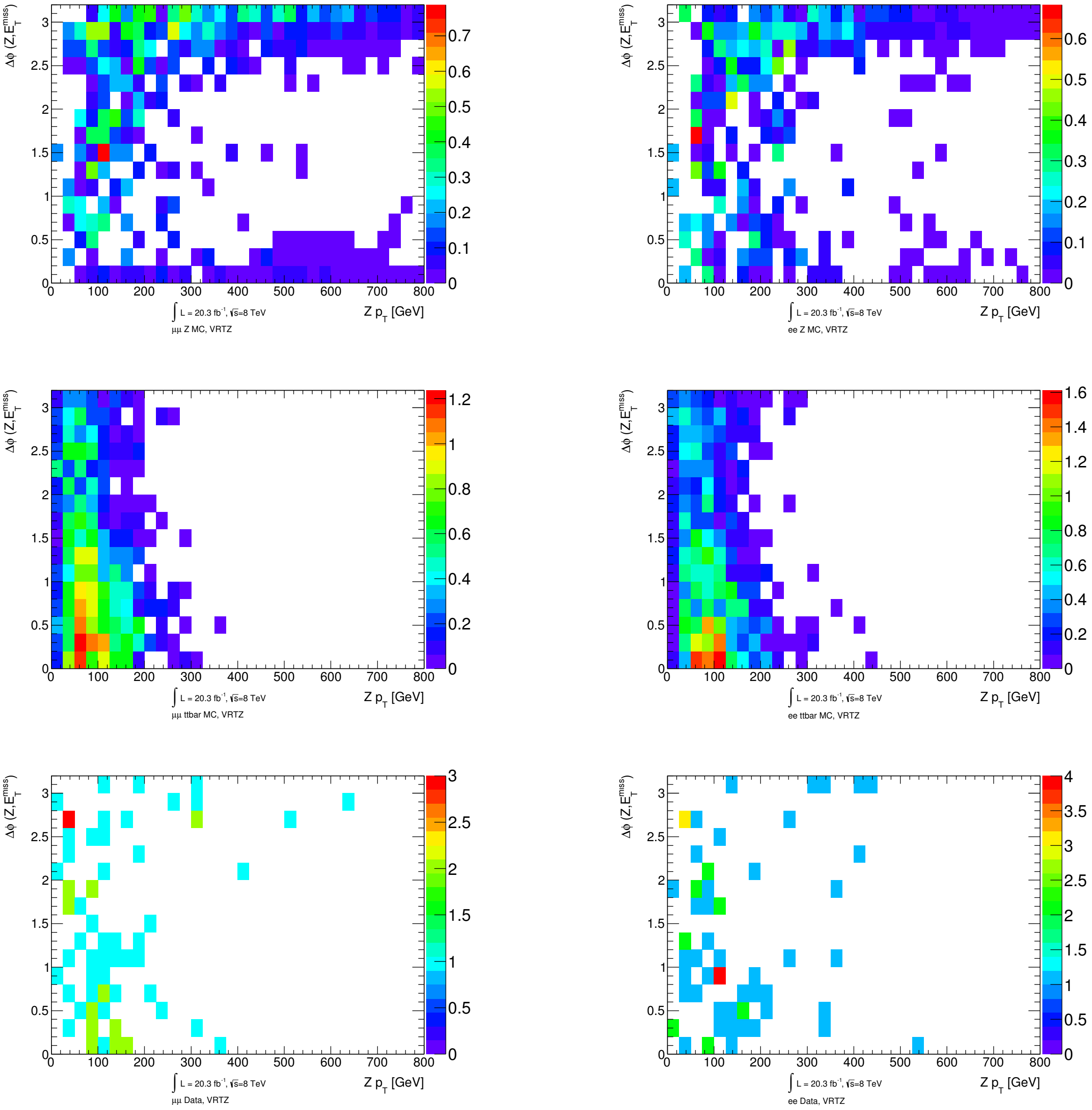

Figure 5.37: Correlations between the reconstructed Z p_{T} and the ϕ angle between the Z boson and $E_{\mathrm{T}}^{\mathrm{miss}}$ for the muon (left) and electron channel (right): Z+jets MC (top), $t\bar{t}$ MC (middle) and data (bottom). The plots are shown for VRTZ with a loosened $E_{\mathrm{T}}^{\mathrm{miss}}$ requirement of $125\,\mathrm{GeV} < E_{\mathrm{T}}^{\mathrm{miss}} < 225\,\mathrm{GeV}$ and without the cut on $\Delta\phi(\mathrm{jet}_{1,2}, E_T^{\mathrm{miss}}) > 0.4$.

5.6.3 Physics objects

All physics objects used in this analysis (electrons, muons, jets and $E_{\mathrm{T}}^{\mathrm{miss}}$) are validated in detail to exclude unexpected detector effects as a source for the observed excess. This includes studies about the resolution, reconstruction and calibration.

Lepton resolution studies

To exclude that the excess in SR-Z is caused by leptons with mismeasured momenta, the muon and electron resolution is studied. The natural decay width of the Z boson of $\Gamma_Z = 2.5\,\mathrm{GeV}$ is smaller than the width of the resonance observed in the experiment due to detector resolution effects. Therefore, the width of the Z peak in the invariant mass distribution can be used as a measurement of the lepton resolution. This has been studied for the e^+e^- and the $\mu^+\mu^-$ channel in different bins of the reconstructed Z p_{T}. The momenta of the leptons from the Z decay get larger with increasing boson p_{T} and the dependency of the detector resolution on the lepton p_{T} can thus be seen in the different Z p_{T} slices. To have enough statistics in the high Z p_{T} region, a loose event selection is used for this cross-check. Events are required to contain a e^+e^- or $\mu^+\mu^-$ pair, at least two signal jets and $H_T > 200\,\mathrm{GeV}$. The $m_{\ell\ell}$ distribution is studied in different bins of the Z p_{T} with increasing bin size to have a sufficient events also in the highest bins. The following eleven ranges are investigated:

- $Z\, p_{\mathrm{T}} \in [0, 20]$, $[20, 40]$, $[40, 55]$, $[55, 70]$, $[70, 105]$, $[105, 140]$, $[140, 210]$, $[210, 280]$, $[280, 390]$, $[390, 500]$ and $[500, \infty[$ GeV

The results for all bins are shown in Fig. 5.38 for the muon channel and in Fig. 5.39 for the electron channel. The width of the Z peak at 91 GeV increases for muons the larger the boson p_{T} is, while it is vice versa for electrons. This behaviour is expected from the tracking and calorimeter resolution, respectively (compare Sec. 3.2). The effect is shown more quantitatively in Fig. 5.40. There, the $m_{\ell\ell}$ distributions in the different Z p_{T} bins are fitted in the range $81\,\mathrm{GeV} < m_{\ell\ell} < 101\,\mathrm{GeV}$ with a simple model of a Gaussian distribution for the peak and a first order polynomial for the non-Z background contribution. The fitted width of the Gaussian as a measure of the lepton resolution is plotted against the boson p_{T} and compared between data and simulation. The theoretical shape of the Z resonance is a Breit-Wigner distribution and a more sophisticated model for the fit would thus include a convolution of a Breit-Wigner with a Gaussian distribution. The pure Gaussian model used here yields smaller values for the width of the Z peak compared to a fit including a Breit-Wigner. Hence, the Gaussian widths shown in the plot are close to Γ_Z and include both the natural decay width of the Z as well as detector resolution effects.

The lepton resolution is modelled well in MC simulations although it is slightly underestimated in the e^+e^- channel. The simple model cannot fit the data in regions with low statistics very well leading to large uncertainties and some discrepancies between data and simulation for $Zp_{\mathrm{T}} > 280\,\mathrm{GeV}$. Still, it can be seen that the lepton resolution shows the expected behaviour up to the highest lepton p_{T} range. One can draw the conclusion that the analysis results are not affected by large mismeasurements of the lepton p_{T}.

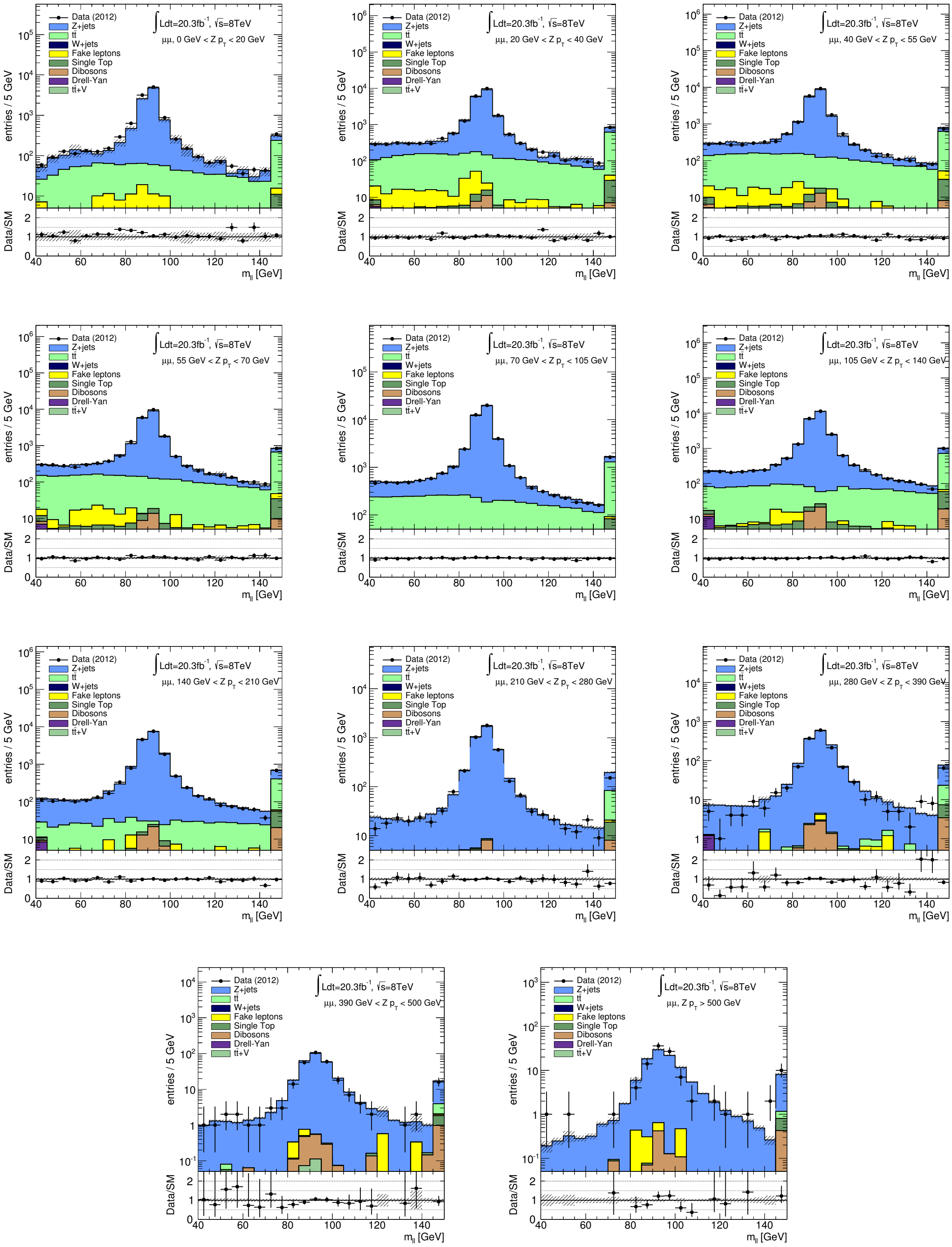

Figure 5.38: The Z peak in the $m_{\ell\ell}$ distribution of the $\mu^+\mu^-$ channel for increasing p_T values of the Z boson. The Z p_T range is indicated in the plots directly. Only the statistical due to the limited number of MC events is included in the error bands.

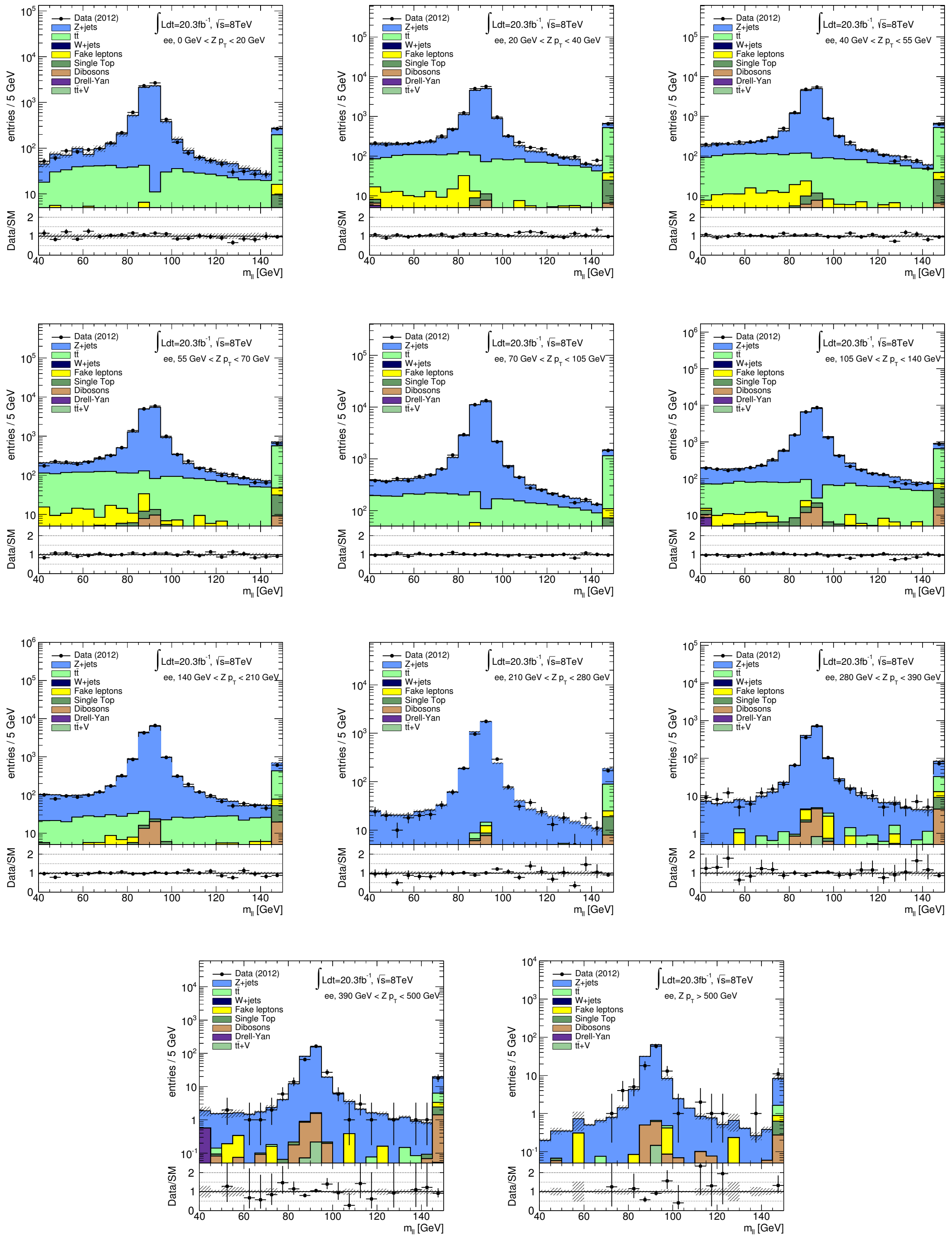

Figure 5.39: The Z peak in the $m_{\ell\ell}$ distribution of the e^+e^- channel for increasing p_{T} values of the Z boson. The Z p_{T} range is indicated in the plots directly. Only the statistical due to the limited number of MC events is included in the error bands.

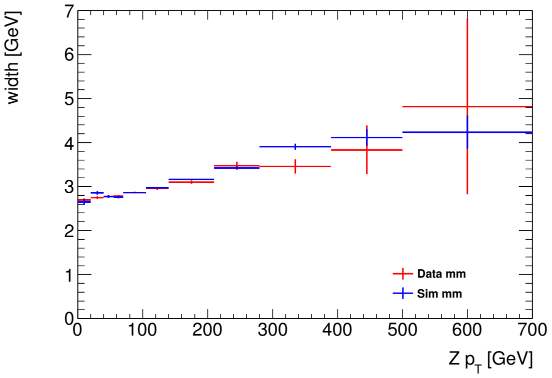

Figure 5.40: Width of the Z peak as a measurement of the lepton resolution in different bins of the Z p_T and thus of the lepton p_T for muons (left) and electrons (right). The resolution is modelled well in simulations (blue curve) when compared to data (red curve).

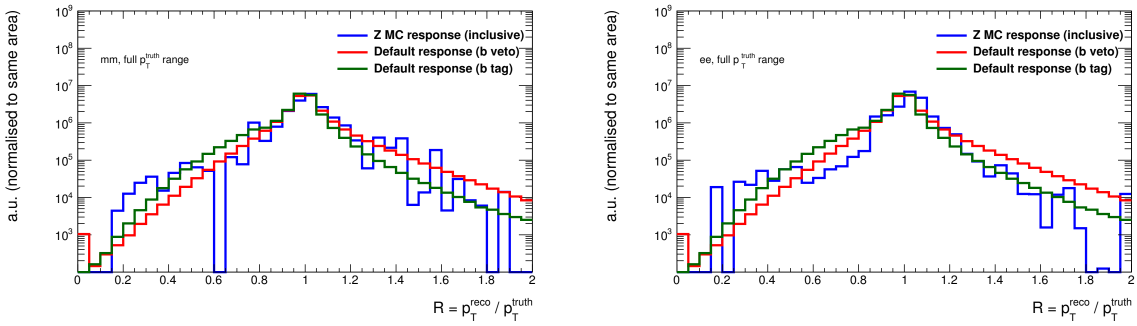

Figure 5.41: Jet response for simulated Z+jets events in a region close to SR-Z (blue curve) compared to the default response function for non-b-tagged (red) and b-tagged jets (green) from the jet smearing method. The muon channel (left) and electron channel (right) are shown separately. The response functions are summed up over the full true jet p_T range to gain statistics.

Jet response studies

The detector response to jets is investigated close to SR-Z to make sure that the jet resolution in this phase space is treated correctly by the jet smearing method (compare Sec. 5.3.1). If this was not the case, it could lead to an underestimation of $Z+$jets backgrounds in SR-Z which could explain the excess. For this study, events with at least two signal jets, $H_\mathrm{T} > 500\,\mathrm{GeV}$, $E_\mathrm{T}^\mathrm{miss} > 200\,\mathrm{GeV}$ and an opposite-sign electron or muon pair with $81\,\mathrm{GeV} < m_{\ell\ell} < 101\,\mathrm{GeV}$ are selected in a MC sample of simulated Z+jets events. The selection is chosen to be slightly looser than SR-Z to enhance the statistics.

The resolution (i.e. the ratio between the reconstructed and true p_T) of the jets in these events is compared to the default response functions used to estimate the $Z+$jets background with fake $E_\mathrm{T}^\mathrm{miss}$. This can be seen in Fig. 5.41. There, the response functions of the jet smearing method are shown for b-tagged and non-b-tagged jets and compared to the jet response in the $Z+$jets events selected for this study. It has to be noted that no cuts on H_T or $E_\mathrm{T}^\mathrm{miss}$ are applied for the jet smearing response functions. All distributions have been normalised to the same area for better comparison, so that the absolute values are meaningless. In the nominal jet smearing method, the response functions are binned in the true jet p_{T}. For this study, all bins are added together to enhance the statistics in the sample of simulated $Z+$jets events. The $Z+$jets events selected for this study must contain a highly energetic jet which was mismeasured dramatically to fulfil the tight cut of $E_{\mathrm{T}}^{\mathrm{miss}} > 200\,\mathrm{GeV}$. This becomes apparent in the enhanced number of events around $R \approx 0.3$ for the blue line in the plots. The default response used in the jet smearing method (red and green curve) cover this region completely. So effects due to large mismeasurements of the jet energy are treated correctly in the fake $E_{\mathrm{T}}^{\mathrm{miss}}$ estimation from the jet smearing method. One can conclude that jet mismeasurement is not underestimated by the $Z+$jets prediction for SR-Z.

Validation of the $E_{\mathrm{T}}^{\mathrm{miss}}$ reconstruction

Large fake $E_{\mathrm{T}}^{\mathrm{miss}}$ from mismeasurements or problems in the $E_{\mathrm{T}}^{\mathrm{miss}}$ calibration could lead to enhanced contributions from $Z+$jets processes in SR-Z. No hints, that effects like this are not covered by the jet smearing method and could explain the excess observed by the Z+jets+E_{T}^{miss} analysis, were found in any of the cross-checks discussed in Sec. 5.3.1 and 5.6.2. Nonetheless, the $E_{\mathrm{T}}^{\mathrm{miss}}$ reconstruction and calibration are scrutinised to reveal problems which might not be visible in the tests performed so far. For this, three different definitions of the missing transverse energy are studied and compared:

- Default $E_{\mathrm{T}}^{\mathrm{miss}}$ (referred to as calorimeter $E_{\mathrm{T}}^{\mathrm{miss}}$ in this section) is the standard definition used in this analysis and has been introduced in Sec. 4.3.5. It is calculated from calibrated calorimeter cells.

- Track $E_{\mathrm{T}}^{\mathrm{miss}}$ is calculated analogously to Eq. 4.6 as the momentum imbalance of all tracks from the primary vertex with $p_T > 500\,\mathrm{MeV}$ [163]. It is more robust against pile-up effects than the calorimeter $E_{\mathrm{T}}^{\mathrm{miss}}$ and it is less affected by large mismeasurements of single objects as the tracking resolution is in general better than the calorimeter resolution. The energy of neutral particles is not taken into account as they are not detected in the tracking system.

- Object $E_{\mathrm{T}}^{\mathrm{miss}}$ is calculated as the momentum imbalance of the final calibrated analysis objects (i.e. jets and leptons):

  $$(E_T^{\mathrm{miss}})^{\mathrm{object}} = \left| - \left(\sum_{\text{baseline jets}} \vec{p}_T + \sum_{\text{lepton 1,2}} \vec{p}_T \right) \right| . \tag{5.16}$$

  Object $E_{\mathrm{T}}^{\mathrm{miss}}$ does not include any contribution from soft objects that are normally included in the soft term for the calorimeter $E_{\mathrm{T}}^{\mathrm{miss}}$.

The comparison between the calorimeter and track based definition of $E_{\mathrm{T}}^{\mathrm{miss}}$ is shown in Fig. 5.42. The event selection of SR-Z is used without the cut on $\Delta\phi(\mathrm{jet}_{1,2}, E_T^{\mathrm{miss}}) > 0.4$ to enhance statistics. The two-dimensional correlation plots are shown separately for a $t\bar{t}$ MC, a $Z+$jets simulation and data. It can be seen that the track $E_{\mathrm{T}}^{\mathrm{miss}}$ is on average smaller than the calorimeter $E_{\mathrm{T}}^{\mathrm{miss}}$ in events with real missing energy from neutrinos (such as $t\bar{t}$ processes shown in the top row). This is expected as the contribution from neutral hadrons to the jet energy as well as photons are not included in the track based $E_{\mathrm{T}}^{\mathrm{miss}}$ definition.

In processes without genuine missing energy (like $Z+$jets shown in the middle), the track based $E_{\mathrm{T}}^{\mathrm{miss}}$ reconstruction and the calorimeter $E_{\mathrm{T}}^{\mathrm{miss}}$ are not correlated. The missing energy is only caused by detector effects in these events and the track measurement is approximately independent from the calorimeter measurement.

The number of events in data is too small to draw any definite conclusions from the correlation plots (shown in the bottom row). For most of the data events, track $E_{\mathrm{T}}^{\mathrm{miss}}$ is smaller than calorimeter $E_{\mathrm{T}}^{\mathrm{miss}}$. As this case can occur in events with real as well as with fake missing energy, the different contributions can not be disentangled completely.

Also the correlation between the directions of track and calorimeter $E_{\mathrm{T}}^{\mathrm{miss}}$ does not allow distinguishing between real and fake $E_{\mathrm{T}}^{\mathrm{miss}}$, which is shown in Fig. 5.43. There is a strong correlation between the ϕ angle of track and calorimeter $E_{\mathrm{T}}^{\mathrm{miss}}$ for $t\bar{t}$ as well as for $Z+$jets simulated events. For the former, this is expected as the direction of the missing energy coincides with the p_{T} weighted direction of the two neutrinos. This does not change no matter if the missing energy is measured from tracks or calorimeter cells. In $Z+$jets events, the fake $E_{\mathrm{T}}^{\mathrm{miss}}$ is caused by the mismeasurement of one of the two jets with the highest energy in most of the cases (compare Fig. 5.24). Therefore, the missing energy is aligned with the direction of the mismeasured jet and the direction of $E_{\mathrm{T}}^{\mathrm{miss}}$ is correlated with the jet direction for the track based as well as for the calorimeter based definition. In some cases, the energy of the jet is underestimated in the calorimeter while it is overestimated in the tracking system (or vice versa). This results in events where the difference in the azimuthal angle between track and calorimeter $E_{\mathrm{T}}^{\mathrm{miss}}$ is $\sim\pi$ (compare Fig. 5.43 middle).

Although no distinct conclusions can be drawn from the study of track $E_{\mathrm{T}}^{\mathrm{miss}}$, no implications are found that the data in SR-Z are suspicious of being affected by fake $E_{\mathrm{T}}^{\mathrm{miss}}$ to a larger extent than assumed in the background prediction.

The calorimeter based $E_{\mathrm{T}}^{\mathrm{miss}}$ definition can also be compared to the object based calculation introduced in Eq. (5.16). Large differences between the two definitions would point to the fact that the jets and leptons are calibrated very differently in the default $E_{\mathrm{T}}^{\mathrm{miss}}$ calculation and the physics objects selection.

Strong correlations between calorimeter and object $E_{\mathrm{T}}^{\mathrm{miss}}$ are observed both in the magnitude as well as in the direction which can be seen from Fig. 5.44 and 5.45, respectively. No hints of problems with the calibration of either the default $E_{\mathrm{T}}^{\mathrm{miss}}$ or the jets and leptons used in this analysis are found. This is studied in more detail for the single terms of the missing energy as introduced in Eq. 4.6 which can be found in App. E. Also there, strong correlations are observed between both $E_{\mathrm{T}}^{\mathrm{miss}}$ definitions. Thus, no problems with the object calibration are found which might explain the observed excess in SR-Z.

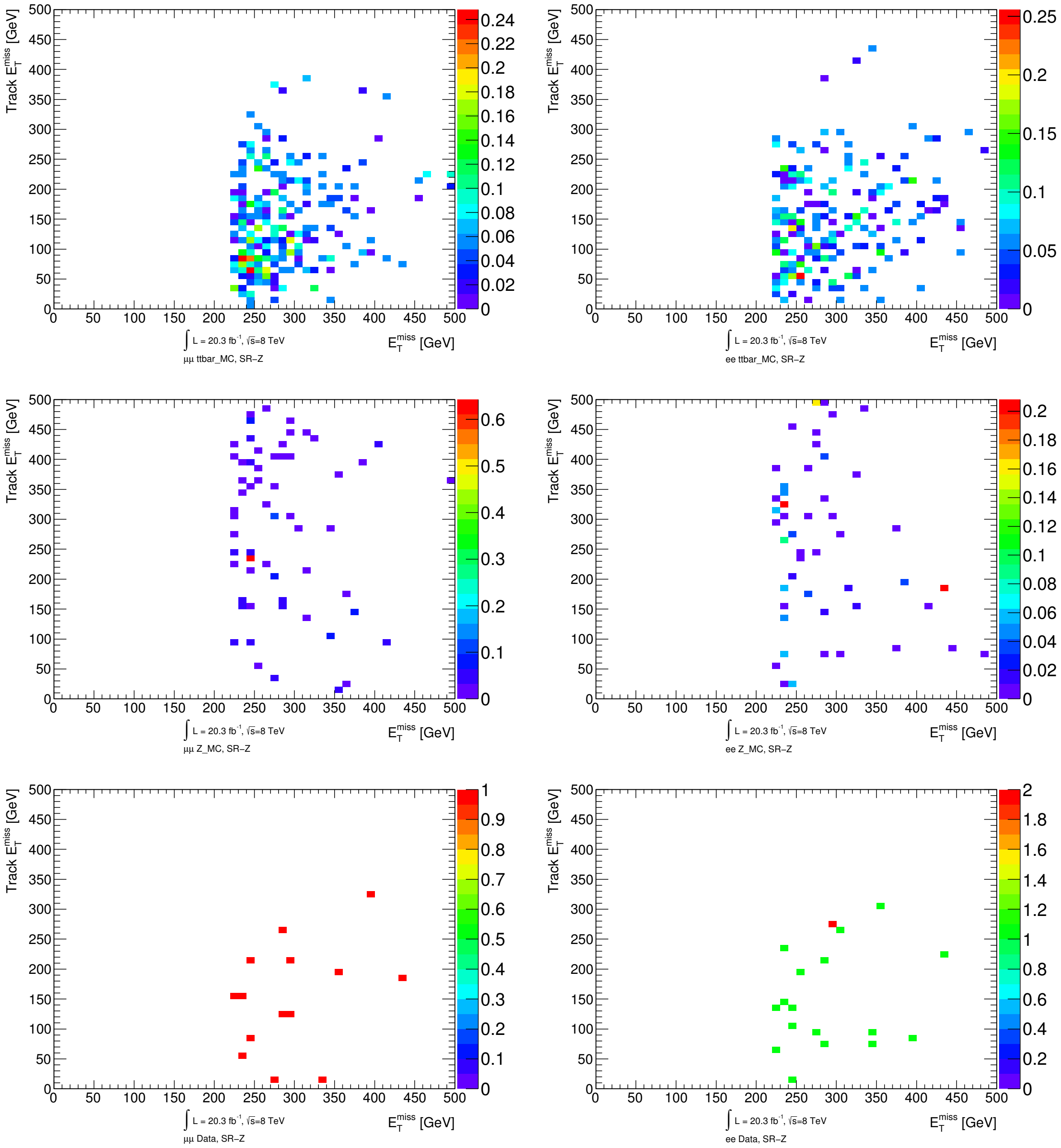

Figure 5.42: Correlation between the magnitudes of the calorimeter and track based $E_{\mathrm{T}}^{\mathrm{miss}}$ definition in the muon (left) and electron channel (right) for a $t\bar{t}$ MC (top), $Z+$jets MC (middle) and data (bottom). All plots use the event selection of SR-Z without the cut on $\Delta\phi(\mathrm{jet}_{1,2}, E_T^{\mathrm{miss}}) > 0.4$.

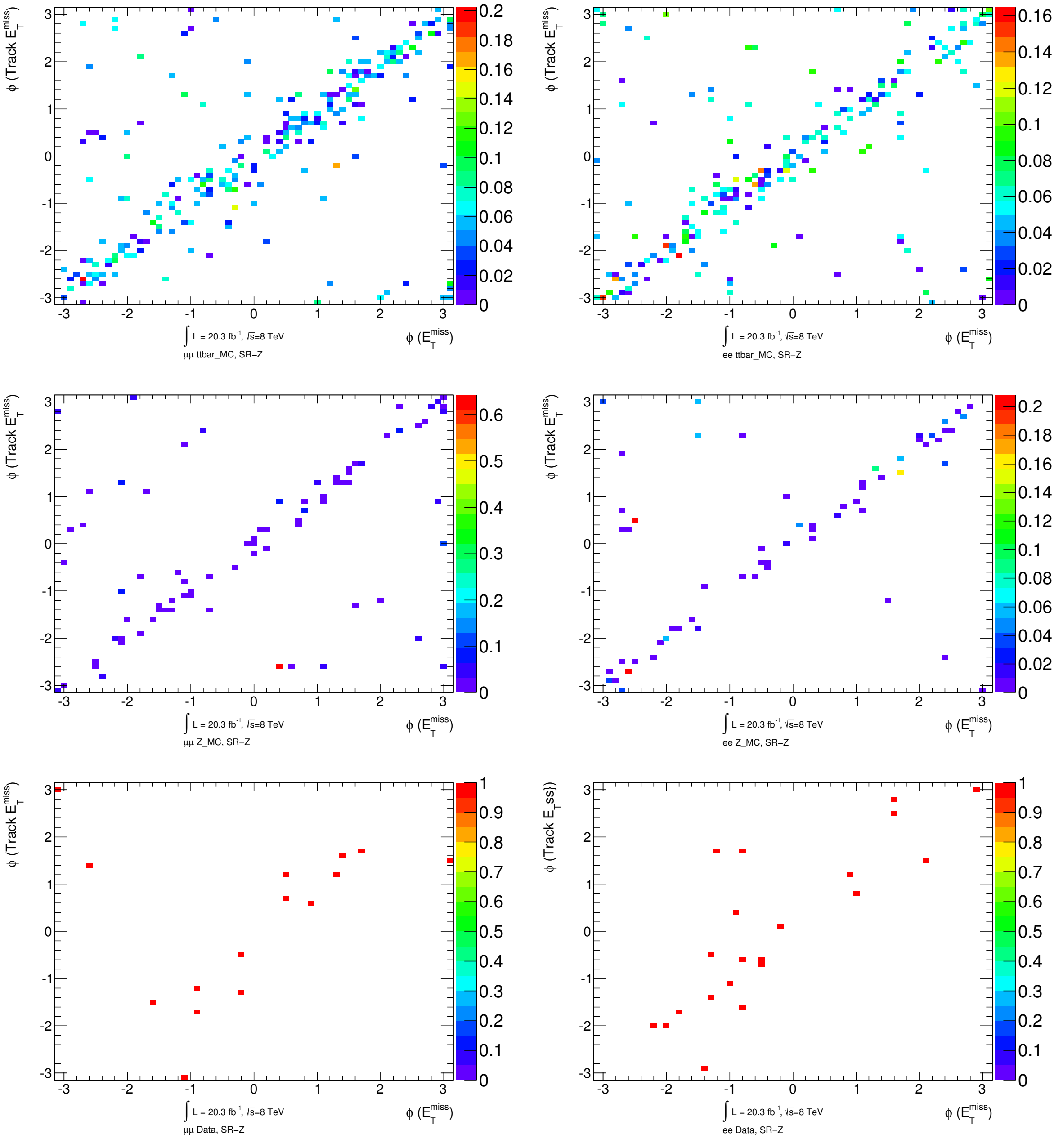

Figure 5.43: Correlation between the directions of the calorimeter and track based $E_{\mathrm{T}}^{\mathrm{miss}}$ definition in the muon (left) and electron channel (right) for a $t\bar{t}$ MC (top), $Z+$jets MC (middle) and data (bottom). All plots use the event selection of SR-Z without the cut on $\Delta\phi(\mathrm{jet}_{1,2}, E_T^{\mathrm{miss}}) > 0.4$.

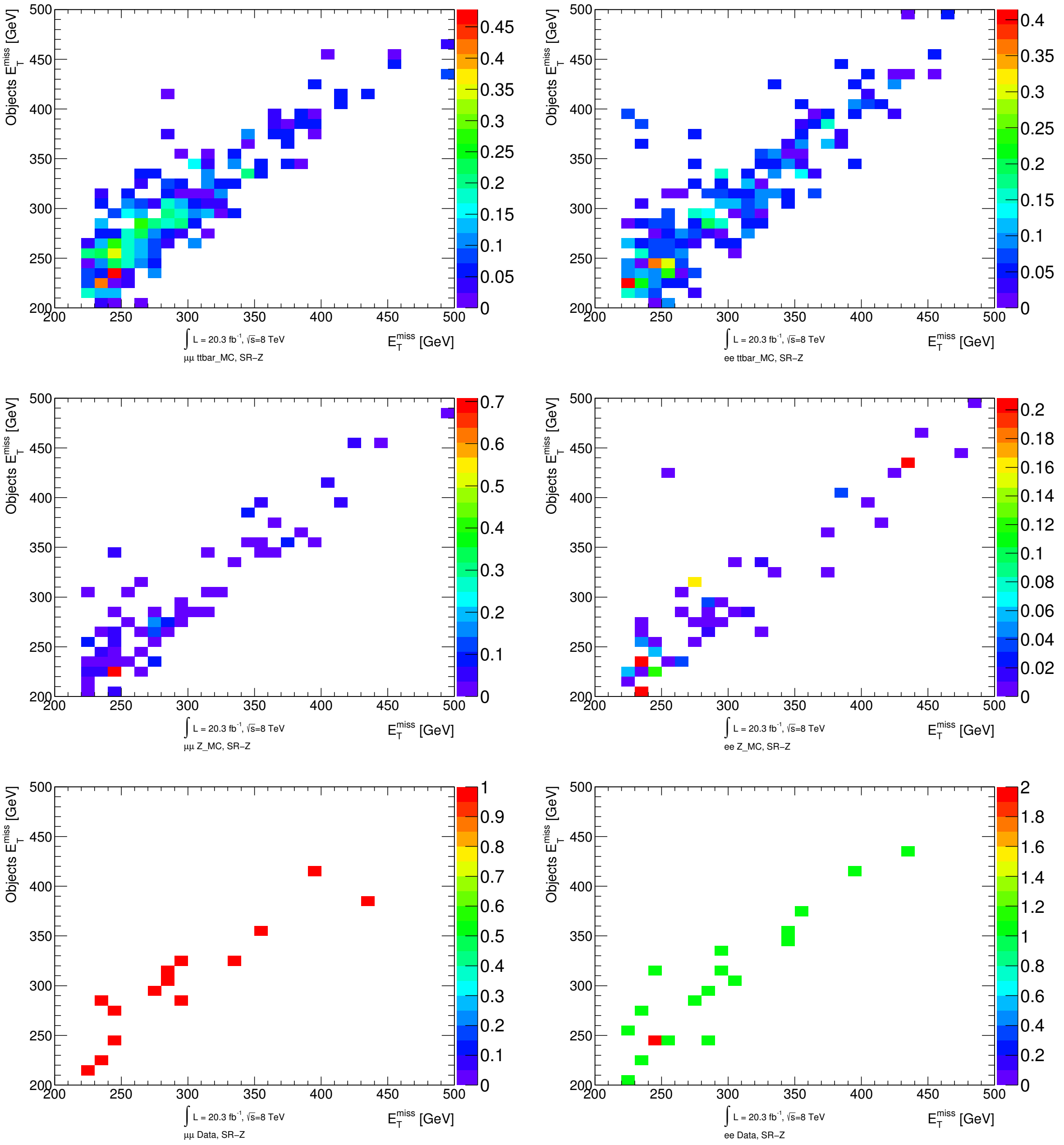

Figure 5.44: Correlation between the magnitudes of the calorimeter and object based $E_{\mathrm{T}}^{\mathrm{miss}}$ definition in the muon (left) and electron channel (right) for a $t\bar{t}$ MC (top), $Z+$jets MC (middle) and data (bottom). All plots use the event selection of SR-Z without the cut on $\Delta\phi(\mathrm{jet}_{1,2}, E_T^{\mathrm{miss}}) > 0.4$.

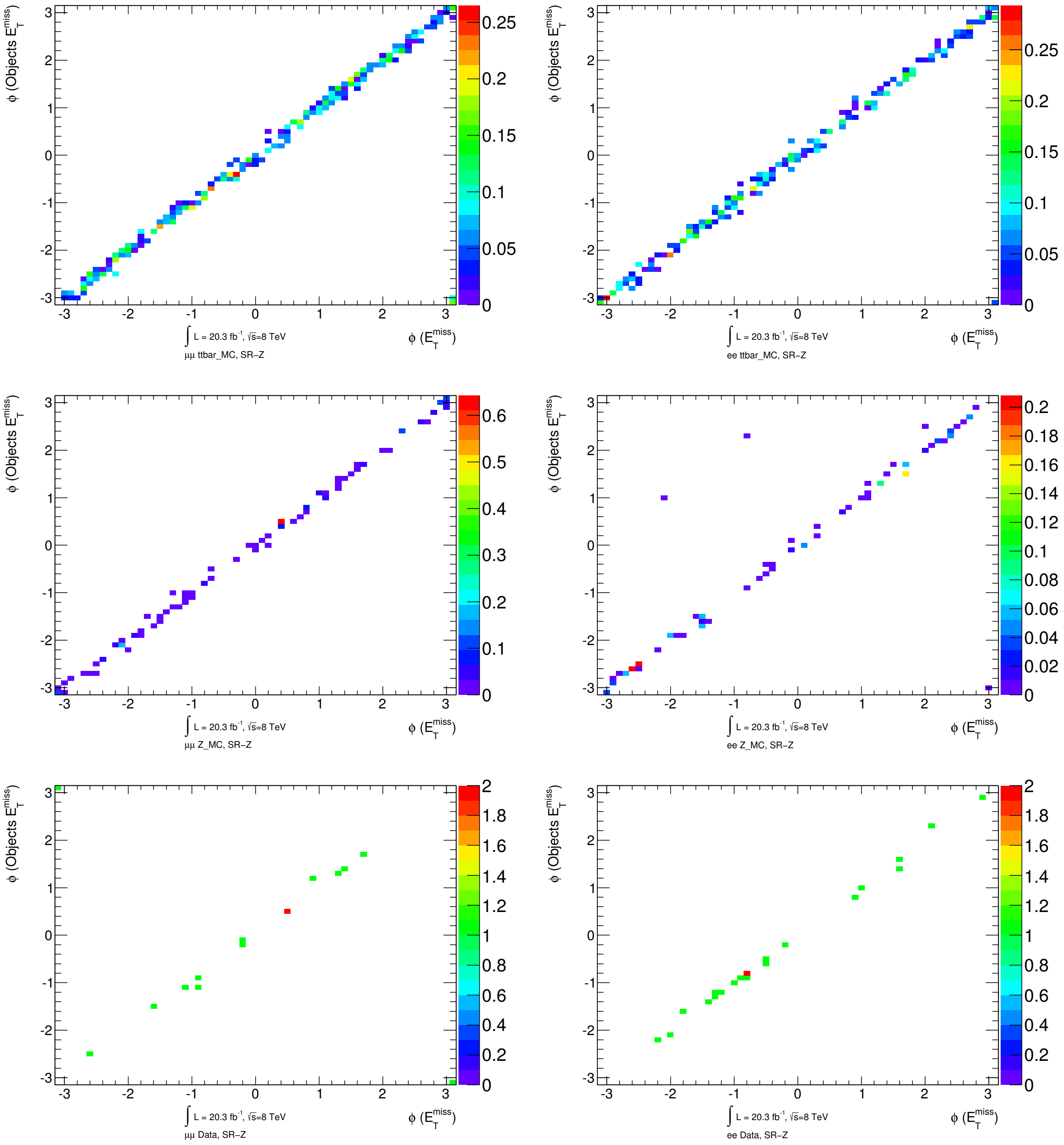

Figure 5.45: Correlation between the directions of the calorimeter and object based $E_{\mathrm{T}}^{\mathrm{miss}}$ definition in the muon (left) and electron channel (right) for a $t\bar{t}$ MC (top), $Z+$jets MC (middle) and data (bottom). All plots use the event selection of SR-Z without the cut on $\Delta\phi(\mathrm{jet}_{1,2}, E_T^{\mathrm{miss}}) > 0.4$.

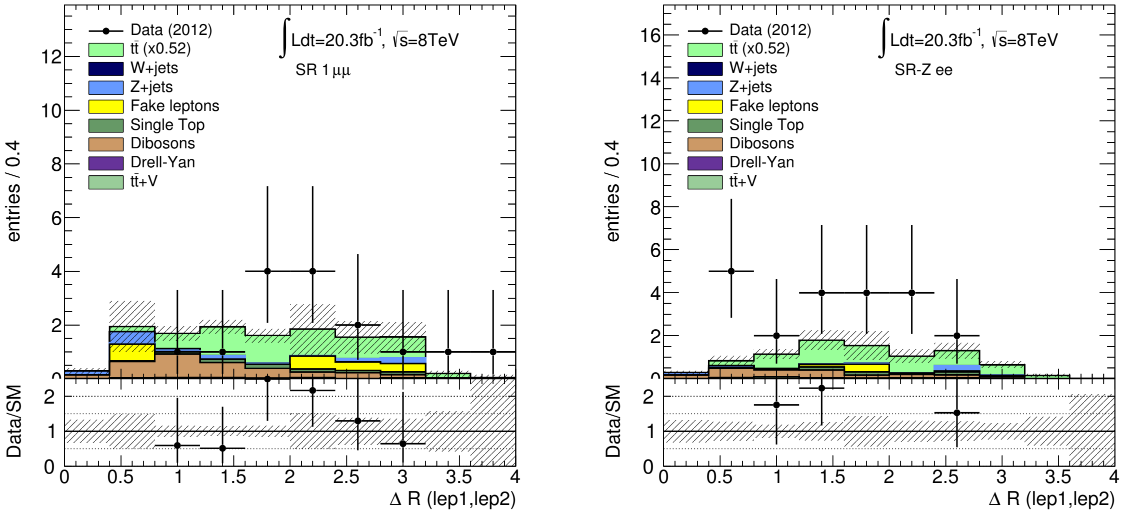

Figure 5.46: Distribution of ΔR between the two leading leptons in SR-Z without the $\Delta\phi(\mathrm{jet}_{1,2}, E_T^{\mathrm{miss}}) > 0.4$ cut for the muon (left) and electron channel (right). Only the uncertainties due to limited MC statistics are included in the error band. The $t\bar{t}$ MC prediction is scaled by a factor of 0.49.

Angular separation between leptons

The angular separation, ΔR, between the two leading leptons is compared between data and the background prediction from MC simulations. This is to exclude that the excess in SR-Z could be accounted for by topologies where the two leptons have a large spatial overlap leading to problems in their reconstruction. The results from this study are shown in Fig. 5.46 for SR-Z without the cut on $\Delta\phi(\mathrm{jet}_{1,2}, E_T^{\mathrm{miss}}) > 0.4$ to enhance statistics. The MC estimate for the $t\bar{t}$ background in SR-Z is scaled by a factor of 0.49 as this is the normalisation factor without the $\Delta\phi(\mathrm{jet}_{1,2}, E_T^{\mathrm{miss}})$ cut. It can be seen that the two leptons are always well separated. This means that the events selected in the Z+jets+E_T^{miss} analysis do not originate from processes where the two leptons arise from the decay of a very boosted object.

5.7 Interpretation and conclusion

As no problems with the results of the Z+jets+E_T^{miss} analysis have been found, they are used to constrain the parameter space of the GGM models under study. The CL_s method introduced in Sec. 4.1 is applied to calculate upper limits on the model parameters. This means that a hypothesis test is performed how well the data observed in SR-Z fit the background only hypothesis or different signal hypotheses. The number of expected events E in channel i can be written as follows:

$$E_i = \mu\, s_i + b_i\,, \tag{5.17}$$

where b_i is the background expectation obtained from the methods described in Sec. 5.3 and s_i is the signal expectation predicted by the SUSY model under study. An additional parameter μ is introduced here which quantifies the signal strength. A value of $\mu = 0$ corresponds to the background only hypothesis, while $\mu = 1$ is the nominal signal hypothesis. The likelihood $\mathcal{L}$ is constructed taking into account all experimental and theoretical uncertainties on the prediction of b_i (compare Sec. 5.4) and all experimental uncertainties on s_i. The uncertainty on the nominal signal cross-section is not included in the likelihood. The uncertainties are treated as described in Sec. 5.5 and $\mathcal{L}$ contains the signal strength μ as an additional free parameter. A test statistic q is required to perform the hypothesis test. The profile likelihood ratio $\lambda(\mu)$ from which q can be constructed is defined in the following way [88]:

$$\lambda(\mu) = \frac{\mathcal{L}(\mu, \hat{\hat{\theta}})}{\mathcal{L}(\hat{\mu}, \hat{\theta})}\,, \tag{5.18}$$

where θ represents all free parameters of $\mathcal{L}$ besides μ (e.g. b_i and its uncertainties). $\hat{\mu}$ and $\hat{\theta}$ in the denominator are the values maximizing the likelihood. $\hat{\hat{\theta}}$ in the numerator is the value of θ maximizing $\mathcal{L}$ for a specific μ, so it is a function of the signal strength. λ is always between 0 and 1. A convenient definition for q can be derived from $\lambda(\mu)$ as a measurement of the disagreement between the value $\hat{\mu}$ maximizing the likelihood and a specific signal hypothesis:

$$q_\mu = -2\ln\lambda(\mu)\,. \tag{5.19}$$

Larger values of q imply larger disagreement, so the p-values, p_b and p_{s+b}, for the background only and the signal+background hypothesis for a given μ value can be computed as the probability to get a value of q equal or greater than the observed one, $q_{\mu,\text{obs}}$ (analogously to the description in Sec. 4.1). The nominal signal model is regarded as being excluded by the data if the CL_s value for $\mu = 1$ is greater than 95 %.

To set limits on the GGM parameters, a scan in the $m(\tilde{g})$-μ-plane is performed, where μ is now again the higgsino mass parameter. All points with $CL_s > 0.95$ are excluded by the Z+jets+E_T^{miss} analysis. This is shown in Fig. 5.47 for the two GGM models under study. For the final limits, the e^+e^- and $\mu^+\mu^-$ channels are added together. The definition of the test statistic q is modified slightly compared to Eq. 5.19 in order to avoid non physical negative values for E_i. This is described in [88] together with an asymptotic prescription of the CL_s method implemented in the HistFitter program [164] which was used to calculate the limits.

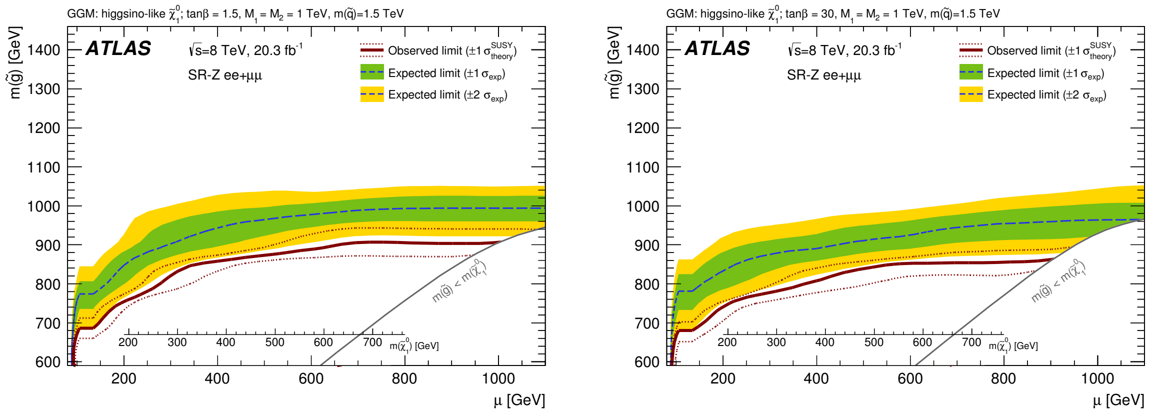

Figure 5.47: Exclusion limits in the $m(\tilde{g})$-μ-plane for the GGM model with $\tan\beta = 1.5$ (left) and $\tan\beta = 30$ (right) calculated from sum of the $\mu^+\mu^-$ and e^+e^- channel in SR-Z [53]. The physical mass of the lightest neutralino is indicated as a second x-axis in the plots. The region in the lower right corner has $m(\tilde{g}) < m(\tilde{\chi}_1^0)$ and is not considered by this search.

The Z+jets+E_T^{miss} analysis can exclude gluino masses up to ~900 GeV for $\mu > 500$ GeV in the GGM model with $\tan\beta = 1.5$. For the $\tan\beta = 30$ scenario, the limits are slightly weaker and gluino masses up to ~840 GeV can be excluded for $\mu > 550$ GeV. This is due to the fact that the $BR(\tilde{\chi}_1^0 \rightarrow Z + \tilde{G})$ is significantly smaller there. Still, the Z+jets+E_T^{miss} analysis shows good sensitivity also to these kind of models.

The green ($1\,\sigma$) and yellow ($2\,\sigma$) bands in Fig 5.47 indicate the size of the fluctuations of the expected limits around the median. In addition, it is shown by the red dashed lines how the observed limit would changes when the nominal signal cross-section is varied up and down by its estimated uncertainty.

The observed limits for the Z+jets+E_T^{miss} analysis are weaker than the expected ones due to the excess of data over the SM prediction. As it can be seen, this affects all regions of parameter space more or less equally. In the region of very low μ values, this analysis looses its sensitivity for the reasons discussed in Sec. 5.2. Details about the CL_s values for the individual GGM signal points as well as about the signal acceptance and efficiency can be found in App. B.

The results of this analysis performed with the ATLAS data of 2012 can be compared to recently published results of the CMS experiment [165]. The SUSY search described there uses a similar analysis strategy as the one presented in this thesis although the details of the search region selection are different. CMS also searches for SUSY in events with a lepton pair with opposite sign and same flavour, at least two jets and missing transverse momentum. The analysis targets models where the two leptons do not come from the decay of a Z boson and considers the full range of the invariant dilepton mass $20\,\text{GeV} < m_{\ell\ell} < 300\,\text{GeV}$ in different bins. The signal region which is most similar to the ATLAS Z+jets+E_T^{miss} analysis is defined in the same $m_{\ell\ell}$ range between 81 GeV and 101 GeV, requires also two jets and has a cut of $E_{\text{T}}^{\text{miss}} > 300$ GeV. However, no explicit requirement on H_{T} or a similar quantity is applied which makes the comparison between ATLAS and CMS difficult. CMS expects 12.8 ± 4.3 events from background processes and observes 7 events in data. The overlap between the ATLAS and the CMS search region is rather small due to the higher $E_{\text{T}}^{\text{miss}}$

requirement of the CMS analysis. Only 10 out of 29 events observed in SR-Z fulfil also the cut on $E_{\mathrm{T}}^{\mathrm{miss}} > 300$ GeV. Therefore, it is not possible at this stage to conclude if the excess observed by the ATLAS analysis also shows up in the CMS data which would be a distinct hint of new physics.

More data will be recorded by ATLAS and CMS in the run-II of the LHC at an increased centre of mass energy and luminosity from spring 2015 onwards. This will hopefully reveal the origin of the excess.

6 Reinterpretation of the ATLAS 1L+jets+E_T^{miss} analysis in the context of SUSY with RPV via $LQ\bar{D}$ operators

As described in Sec. 2.2.2, SUSY with R-parity violation is equally motivated as R-parity-conserving models and might well be realized in nature. However, most ATLAS searches focus on RPC models and only contain interpretations for special cases of RPV theories - if at all. In principle, many of the existing ATLAS SUSY analyses are also sensitive to a wide range of RPV models. In this thesis, the results of the 1L+jets+E_T^{miss} analysis [19] are reinterpreted in the context of SUSY models with RPV via the $LQ\bar{D}$ operators in the superpotential (compare Eq. (2.6)). Signatures with one light lepton (electron or muon), jets and large missing transverse momentum arise from many of the λ'_{ijk} couplings. The analysis strategy, background estimation and observed results of the 1L+jets+E_T^{miss} analysis can thus be used to constrain the parameter space of the $LQ\bar{D}$ model. Other ATLAS analyses have already set limits on some dedicated $LQ\bar{D}$ models. The search for multitrack displaced vertices [166] has put constraints on long-lived decays of supersymmetric particles via λ'_{i11}, λ'_{i13} and λ'_{i23} (with $i = 1, 2$) couplings. A search for signatures with two light leptons and two b quarks [167] has set limits on the decays of the stop quark via RPV operators.
However, no ATLAS results are available for prompt decays of SUSY particles via λ'_{ijk} couplings where all three quark and lepton generations are covered in a systematic way. The reinterpretation of the 1L+jets+E_T^{miss} analysis helps to close this gap. This analysis was part of a major effort to combine various ATLAS searches and constrain SUSY with lepton number violating couplings in a systematic way [54, 133]. Besides the $LQ\bar{D}$ operators, also models with R-parity violation via $LL\overline{E}$ operators and bRPV couplings have been considered there, but will not be discussed in this thesis in detail.

6.1 The $LQ\bar{D}$ model

The theoretical basics of SUSY with R-parity-violating couplings have been introduced in Sec. 2.2.2. For the reinterpretation of the 1L+jets+E_T^{miss} analysis, the $LQ\bar{D}$ operators are implemented in two simplified models which focus on the strong production of SUSY particles. One model contains the production of squark pairs, the other one considers gluino pair production. In both cases, the NLSPs (which are the squarks or gluinos) decay directly into the lightest neutralino $\tilde{\chi}_1^0$ (which is the LSP) via $\tilde{q} \to q\tilde{\chi}_1^0$ or $\tilde{g} \to qq\tilde{\chi}_1^0$, respectively. There, q includes all quarks of the first and second generation. Top and bottom quarks are omitted

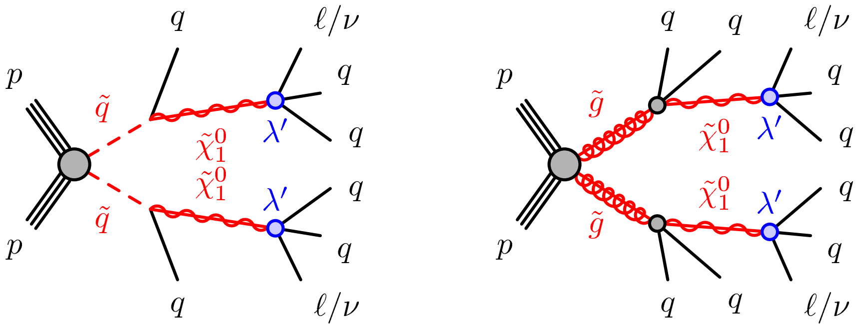

Figure 6.1: Example diagrams for the SUSY model with R-parity violation via $LQ\bar{D}$ operators [54]: Production of squarks (left) and gluinos (right) which decay into the lightest neutralino $\tilde{\chi}_1^0$ under the emission of quarks. The $\tilde{\chi}_1^0$ decays via λ'_{ijk} couplings into charged or neutral leptons and quarks.

in this decay step for reasons of simplicity. Especially top quarks would enhance the jet multiplicity of the final state and the sensitivity of the analysis would be improved further. Each $\tilde{\chi}_1^0$ then decays into a charged or neutral lepton and a pair of quarks via the λ'_{ijk} couplings. Example diagrams for the $LQ\bar{D}$ squark and gluino model are shown in Fig. 6.1.

Signal samples for the two production modes are simulated using the HERWIG++ 2.6.3 MC generator [168] with the CTEQ6L1 PDF set [169] and the UEEE3 tune [170] for the underlying event. The squark mass $m(\tilde{q})$ or the gluino mass $m(\tilde{g})$, respectively, are free parameters as well as the neutralino mass $m(\tilde{\chi}_1^0)$. All other SUSY particle masses are set to 4.5 TeV and effectively decoupled as they are beyond the reach of the LHC.

The simulated events are passed through a fast simulation of the ATLAS detector (compare Sec. 4.2.2). The signal cross-sections were calculated at NLO+NLL accuracy [138–142] including both left-handed and right-handed squarks. The nominal cross-section and its uncertainty is retrieved according to the recommendations of the ATLAS SUSY group described in Sec. 5.1.

In the $LQ\bar{D}$ model, the $\tilde{\chi}_1^0$ can either decay to $\tilde{\chi}_1^0 \to \ell_i u_j d_k$ or to $\tilde{\chi}_1^0 \to v_i d_j d_k$, where ℓ/ν are charged/neutral leptons and u/d are up-/down-type quarks. The indices i, j, k indicate the lepton or quark family. Each term with a specific λ'_{ijk} coupling in the superpotential leads to dedicated decay modes of the $\tilde{\chi}_1^0$. Due to the large number of possible $LQ\bar{D}$ operators it is not feasible to generate separate signal MC simulations for all different combinations and values of the λ'_{ijk}. Many of the decay modes cannot be distinguished by the detector anyhow (e.g. jets originating from u, d or s quarks are indistinguishable). Therefore, inclusive high statistics MC samples with different SUSY mass spectra are generated in which nearly all possible decays of the $\tilde{\chi}_1^0$ are allowed at the same time with arbitrary branching fraction, BR_{MC}. The samples can be reweighted to a specific model with fixed branching fractions, BR_{model}, by applying the ratio $BR_{\mathrm{model}}/BR_{\mathrm{MC}}$ as a weight to each LSP decay. The weight for the whole event is the product of the weights for the two $\tilde{\chi}_1^0$ decays.

As the efficiency for charged leptons of the first two generations (i.e. electrons and muons) as well as for the first two quark families (i.e. u,d,s and c) is very similar, no distinction between first and second generation fermions is made in the reweighting procedure. In contrast, τ

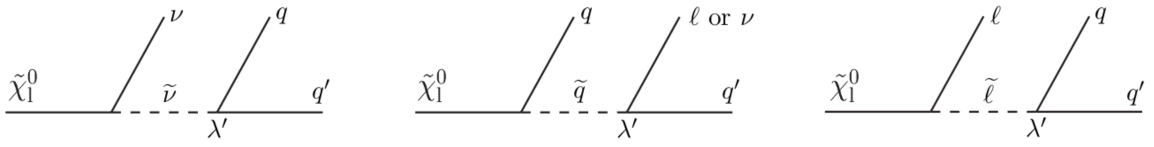

Figure 6.2: Example Feynman diagrams for decay of the $\tilde{\chi}_1^0$ via λ'_{ijk} couplings and a virtual sneutrino (left), squark (middle) or slepton (right) [30].

leptons and b quarks in the final state can change the sensitivity of the analysis significantly. This effectively leads to six considered decay modes for the LSP which incorporate nearly all possible $LQ\bar{D}$ operators:

$$\tilde{\chi}_1^0 \to \ell qq\,, \tag{6.1}$$

$$\tilde{\chi}_1^0 \to \tau qq\,, \tag{6.2}$$

$$\tilde{\chi}_1^0 \to \nu qq\,, \tag{6.3}$$

$$\tilde{\chi}_1^0 \to \ell qb\,, \tag{6.4}$$

$$\tilde{\chi}_1^0 \to \tau qb\,, \tag{6.5}$$

$$\tilde{\chi}_1^0 \to \nu qb\,, \tag{6.6}$$

where ℓ and q stand for the first and second generation charged leptons and quarks, respectively. The Feynman diagrams for some of the $\tilde{\chi}_1^0$ decays are shown in Fig. 6.2. It is assumed that the branching fractions for decays with charged and neutral leptons are equal. Furthermore, the $\tilde{\chi}_1^0$ decays to muons or to electrons, respectively, are assumed to have the same branching fraction. All λ'_{ijk} couplings with $i, j, k = 1, 2$, which give signatures without third generation fermions are covered by this implementation of the model. Also, all λ'_{3jk} ($j = 1, 2$, $k = 1, 2, 3$) which lead to final states with τ leptons and all λ'_{ij3} ($i = 1, 2, 3,\ j = 1, 2$) which involve $\tilde{\chi}_1^0$ decays to b quarks are included in the model implementation. The only couplings not considered in this analysis are λ'_{i3k} ($i, k = 1, 2, 3$) as they involve third generation left-handed squarks. The relative rates of the $\tilde{\chi}_1^0$ decays into charged and neutral leptons are more complicated as they are affected by the large mass of the top quark and not only by the mass of the virtual sleptons/sneutrinos/squarks. Therefore, this case is not taken into account in this thesis. Under the assumptions discussed above, the branching fractions of the $\tilde{\chi}_1^0$ decays can be related to the underlying λ'_{ijk} couplings for a specific SUSY model.

For the reinterpretation of the 1L+jets+E_T^{miss} results, the MC samples of the $LQ\bar{D}$ model are reweighted to 11×11 combinations of branching fractions in a two-dimensional coupling plane. There, the branching fraction for $\tilde{\chi}_1^0$ decays with b quarks, $BR(b)$, is increased from 0 to 1.0 in steps of 0.1 and the branching fraction for LSP decays involving τ leptons, $BR(\tau)$, is varied between 0 and 0.5 in steps of 0.05. A maximum value of $BR(\tau) = 0.5$ is chosen as the 1L+jets+E_T^{miss} analysis is not sensitive to higher values as will be discussed in Sec. 6.4.1. The branching fraction plane is illustrated in the sketch in Fig. 6.3. Each point in the plane corresponds to a specific combination of λ'_{ijk} couplings. This can be seen most easily in the four corners of the grid which represent cases where one single $LQ\bar{D}$ operator dominates.

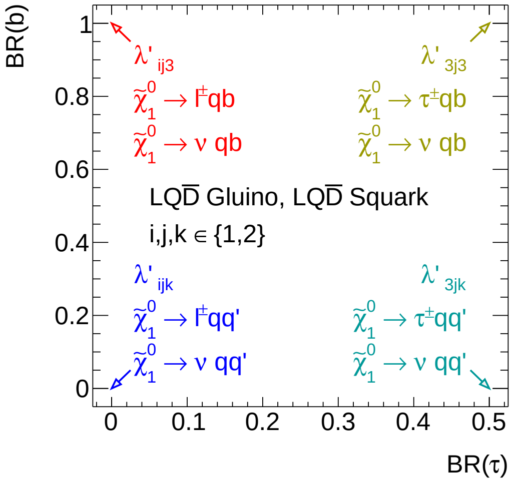

Figure 6.3: Overview over the branching fractions for the $\tilde{\chi}_1^0$ decay considered in the reinterpreation of the 1L+jets+$E_T^{\rm miss}$ analysis [54]. In the two-dimensional coupling plane, the branching fraction for $\tilde{\chi}_1^0$ decays with τ leptons, $BR(\tau)$, is given on the x-axis, while the branching fraction for LSP decays involving b quarks, $BR(b)$, is indicated on the y-axis. Each point in the plane can be mapped to concrete $\lambda^{'}_{ijk}$ values in a model-dependent way. This is indicated in the four corners where this connection can be illustrated most easily.

- Bottom left corner with $BR(\tau)$=0 and $BR(b)$=0: $\lambda^{'}_{ijk}$ $(i, j, k = 1, 2)$ couplings dominate leading to $\tilde{\chi}_1^0 \to \ell qq$ and $\tilde{\chi}_1^0 \to \nu qq$ decays.

- Bottom right corner with $BR(\tau)$=0.5 and $BR(b)$=0: $\lambda^{'}_{3jk}$ $(j, k = 1, 2)$ couplings dominate leading to $\tilde{\chi}_1^0 \to \tau qq$ and $\tilde{\chi}_1^0 \to \nu qq$ decays.

- Top left corner with $BR(\tau)$=0 and $BR(b)$=1: $\lambda^{'}_{ij3}$ $(i, j = 1, 2)$ couplings dominate leading to $\tilde{\chi}_1^0 \to \ell qb$ and $\tilde{\chi}_1^0 \to \nu qb$ decays.

- Top right corner with $BR(\tau)$=0.5 and $BR(b)$=1: $\lambda^{'}_{3j3}$ $(j = 1, 2)$ couplings dominate leading to $\tilde{\chi}_1^0 \to \tau qb$ and $\tilde{\chi}_1^0 \to \nu qb$ decays.

$LQ\bar{D}$ models with different mass spectra are considered and the two-dimensional branching fraction reweighting described above is performed for each sample individually. Simulated signal events are generated for three different ratios, R, of $m(\tilde{\chi}_1^0)$ to m(NLSP): $R = 0.1$, 0.5 and 0.9. The squark and gluino masses are varied in a range between 600 GeV and 1400 GeV although not the full mass range is considered for each value of R. A summary of the $\tilde{q}$ and $\tilde{g}$ masses taken into account can be found in Tab. 6.1. MC samples are generated between the lowest and highest considered NLSP mass in steps of 200 GeV.
By fixing the mass of the NLSP and the ratio R, the speed of the LSP in the rest frame of the squark or gluino is approximately constant no matter what the absolute mass scale is. As R increases, a higher amount of the available energy is contained in the decay products

NLSP	R	m(NLSP)
$\tilde{g}$	0.1	600 GeV – 1400 GeV
$\tilde{g}$	0.5	800 GeV – 1400 GeV
$\tilde{g}$	0.9	800 GeV – 1400 GeV
$\tilde{q}$	0.1	600 GeV – 1000 GeV
$\tilde{q}$	0.5	600 GeV – 1200 GeV
$\tilde{q}$	0.9	800 GeV – 1400 GeV

Table 6.1: Overview over the mass ranges taken into account for the different values of $R = m(\tilde{\chi}_1^0)/m(\text{NLSP})$ in the two $LQ\bar{D}$ simplified models with gluino and squark production [54]. MC samples are generated between the lowest and highest NLSP mass in steps of 200 GeV for each value of R

of the LSP while the quarks from the NLSP decay are less energetic. This means that the higher R the harder is the p_T spectrum of the charged leptons and neutrinos. The higher neutrino momentum becomes apparent in larger E_T^miss. In contrast, the lower R the more highly energetic jets arise from the NLSP decay.

6.2 Analysis overview

The search for SUSY in events with one isolated lepton (electron or muon), jets and missing transverse momentum [19, 131] was originally optimized for strong production within R-parity-conserving SUSY models. There, leptons can arise from the decay chains of the squarks and gluinos into the LSP. In the R-parity-violating $LQ\bar{D}$ model, the same signature can occur if one of the $\tilde{\chi}_1^0$ decays involves a charged lepton and the other one a neutrino.

The basic object and event selection of the 1L+jets+E_T^miss analysis is harmonized with the Z+jets+E_T^miss analysis and can be found in Sec. 4. The 1L+jets+E_T^miss analysis has three signal regions which were designed for a high discovery reach and three signal regions optimized for good exclusion power. For this reinterpretation of the results, only the exclusion regions are used. They are denoted as SR3J (#jets $\geq$ 3), SR5J (#jets $\geq$ 5) and SR6J (#jets $\geq$ 6) and their event selection is summarised in Tab. 6.2. Exactly one isolated hard lepton with $p_\text{T} > 25$ GeV is required in all signal regions. Additional stringent cuts on E_T^miss, m_T (see Eq. (4.3)), m_eff (see Eq. (4.2)) and $E_\text{T}^\text{miss}/m_\text{eff}$ are applied to achieve a good signal to background ratio. The regions are designed to have no overlap so that they are statistically independent and can be combined for the final interpretation of the results.

Unlike in the Z+jets+E_T^miss analysis, not only the total number of expected and observed events in the signal regions is used to contrain the parameters space of new physics. Instead, a shape fit to either the m_eff (SR3J and SR5J) or the E_T^miss distribution (SR6J) is performed. This means that different bins of the shape fit variable are statistically combined taking into account correlations between them. This procedure is illustrated in Fig. 6.4 where the E_T^miss distribution in SR6J is shown for the background prediction, the observed data and one RPC signal example. It can be seen that the shape of the distribution differs for background and signal events. Therefore, the fit has an increased sensitivity by taking into account the shape

	SR3J (exclusion)	SR5J (exclusion)	SR6J (exclusion)
#leptons	=1		
leading lepton p_{T}	> 25 GeV		
subleading lepton p_{T}	< 10 GeV		
#jets	≥ 3	≥ 5	≥ 6
jet p_{T} [GeV]	$> 80, 80, 30$	$> 80, 50, 40, 40 ,40$	$> 80, 50, 40, 40, 40 ,40$
	$p_T^{\text{5th jet}} < 40$ GeV	$p_T^{\text{6th jet}} < 40$ GeV	
$E_{\text{T}}^{\text{miss}}$	> 300 GeV	> 300 GeV	> 250 GeV
m_{T}	> 150 GeV	> 150 GeV	> 150 GeV
$E_{\text{T}}^{\text{miss}}/m_{\text{eff}}$	> 0.3	-	-
m_{eff}	> 800 GeV	> 800 GeV	> 600 GeV
shape fit variable	m_{eff}	m_{eff}	$E_{\text{T}}^{\text{miss}}$
binning, bin size	4 bins, 200 GeV	4 bins, 200 GeV	3 bins, 100 GeV

Table 6.2: Overview over the selection criteria for the exclusion signal regions of the 1L+jets+E_T^{miss} analysis as well as the details of the shape fit [19].

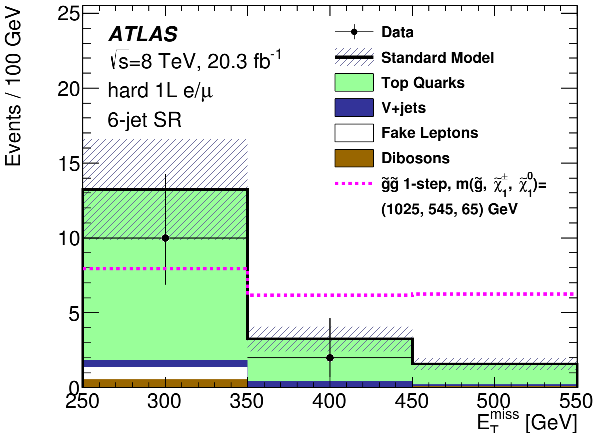

Figure 6.4: $E_{\text{T}}^{\text{miss}}$ distribution in SR6J of the 1L+jets+E_T^{miss} analysis for the expected background, the experimental data and one signal benchmark point [19]. This is taken from a simplified RPC model with the production of gluinos which decay via $\tilde{g} \to qq\tilde{\chi}_1^{\pm} \to qqW^{\pm}\tilde{\chi}_1^0$. The last bin includes the overflow.

information. Details about the shape fit variables and their binning can be also found in Tab. 6.2.

Standard Model $t\bar{t}$ and W + jets events are the dominant source of background in the 1L+jets+E_T^{miss} analysis. They are predicted by fitting MC simulations of the corresponding processes to data in dedicated control regions enriched with $t\bar{t}$ and W + jets background, respectively. The control regions are located at lower $E_{\text{T}}^{\text{miss}}$ and m_{T} values compared to the signal regions. For each SR, one CR for $t\bar{t}$ and one for W + jets background is defined which mainly differ by their requirement/veto on b-jets. Their event selection can be found in Tab. 6.3. The background prediction is extrapolated from the control to the signal region using transfer factors obtained from MC. Validation regions positioned between the CRs and the SRs are used to validate the correctness of the extrapolation. Other backgrounds in the 1L+jets+E_T^{miss} analysis arise from diboson, $t\bar{t} + W/Z$, $t\bar{t} + WW$, single top and $Z/\gamma^* +$ jets processes and are estimated from MC simulations. The fake lepton contribution to the different regions is predicted with the 1-lepton matrix method described in Sec. 5.3.3.

	$W+\text{jets}$ / $t\bar{t}$		
	3-jet	5-jet	6-jet
#leptons	=1		
leading lepton p_{T}	$> 25\,\mathrm{GeV}$		
subleading lepton p_{T}	$< 10\,\mathrm{GeV}$		
#jets	≥ 3	≥ 5	≥ 6
jet p_{T} [GeV]	$> 80, 80, 30$ $p_T^{\text{5th jet}} < 30$ GeV	$> 80, 50, 30, 30 ,30$ $p_T^{\text{6th jet}} < 30$ GeV	$> 80, 50, 30, 30, 30 ,30$
#b-tagged jets	$= 0 \;/ \geq 1$		
$E_{\mathrm{T}}^{\mathrm{miss}}$	$\in [150, 300]$ GeV	$\in [150, 300]$ GeV	$\in [100, 200]$ GeV / $\in [150, 250]$ GeV
m_{T}	$\in [80, 150]$ GeV	$\in [60, 150]$ GeV	$\in [40, 80]$ GeV / $\in [40, 150]$ GeV
m_{eff}	$> 800\,\mathrm{GeV}$	$> 800\,\mathrm{GeV}$	$> 600\,\mathrm{GeV}$

Table 6.3: Control region definitions for the 3-jets, 5-jets and 6-jets $W+\text{jets}$ and $t\bar{t}$ control regions of the 1L+jets+E_T^{miss} analysis [19]. For cuts with different selections, the first value belongs to the $W+\text{jets}$ CR and the second value to the $t\bar{t}$ CR.

For the final exclusion fit, the likelihood is built from the probability density functions of the background and signal expectation as well as of the uncertainties on both quantities. The number of observed events in all CRs and SRs is plugged in the likelihood. It then contains three parameters of interest: The normalisation of the $t\bar{t}$ as well as the $W+\text{jets}$ background and the signal strength. They are constrained by using the information from all control and signal regions simultaneously. Various systematic uncertainties are taken into account which are estimated analogously to the methods described in Sec. 5.4.2 and 5.4.3. The expected and observed results in the three exclusion SRs of the 1L+jets+E_T^{miss} analysis are shown in Tab. 6.4. No significant excess of data over the Standard Model prediction is found.

SR3J was originally designed for RPC models with squark production while the high jet multiplicity regions target gluino production. SR6J contributes the most to the sensitivity of the 1L+jets+E_T^{miss} analysis for the RPV models under study. This is due to the fact that additional jets arise from the LSP decay in the $LQ\bar{D}$ model while the expected missing energy is lower with respect to RPC models. Therefore, the results benefit from the loosened $E_{\mathrm{T}}^{\mathrm{miss}}$ requirement of SR6J with respect to the other signal regions.

Expected signal yields in this region are shown in Fig. 6.5 for the $BR(\tau)$–$BR(b)$ plane. Mass points with $m(\tilde{\chi}_1^0) = 500\,\mathrm{GeV}$ and $m(\tilde{g}/\tilde{q}) = 1000\,\mathrm{GeV}$ are used for this study and all $E_{\mathrm{T}}^{\mathrm{miss}}$ bins of the shape fit are summed up. It can be seen that the 1L+jets+E_T^{miss} analysis has the highest sensitivity in the region of low $BR(\tau)$ as expected. Here, the LSP dominantly decays into leptons of the first and second generation. As the hadronic decay modes of the τ lepton, which have a branching ratio of $\sim$60 % [22], are not considered here, the signal acceptance decreases as the branching fraction for $\tilde{\chi}_1^0$ decay with τ leptons increases. In contrast, nearly no dependence of the expected signal yield on $BR(b)$ is visible as the SR selection does not distinguish between b-tagged and non-b-tagged jets.

6.3 Validation of the analysis assumptions

Signal contamination of control regions and additional uncertainties on the signal acceptance might affect the reinterpretation of the 1L+jets+E_T^{miss} analysis in the context of the $LQ\bar{D}$

	SR3J	SR5J	SR6J
Observed events	75	16	12
Expected background	82.5 ± 7.2	17.7 ± 4.0	18.1 ± 4.3
$t\bar{t}$	35.0 ± 6.2	12.3 ± 4.1	13.9 ± 4.7
Other top backgrounds	7.6 ± 3.0	2.1 ± 0.5	1.7 ± 0.5
W/Z+jets	24.4 ± 3.6	1.8 ± 0.6	0.99 ± 0.80
WW, WZ, ZZ	14.3 ± 4.3	1.5 ± 1.0	0.70 ± 0.36
Fake leptons	$1.2^{+1.3}_{-1.2}$	$0.00^{+0.09}_{-0.00}$	$0.82^{+0.87}_{-0.82}$

Table 6.4: Results in the three exclusion SRs of the 1L+jets+E_T^{miss} analysis for the sum over all bins of the shape fit. The numbers are shown for the background fit configuration which means that only the CRs are used to constrain the background and the signal strength is set to 0. The uncertainties include both the statistical as well as all experimental and theoretical systematic uncertainties. $t\bar{t}+W/Z$, $t\bar{t}+WW$ and single top processes are contained in the "Other top background" category.

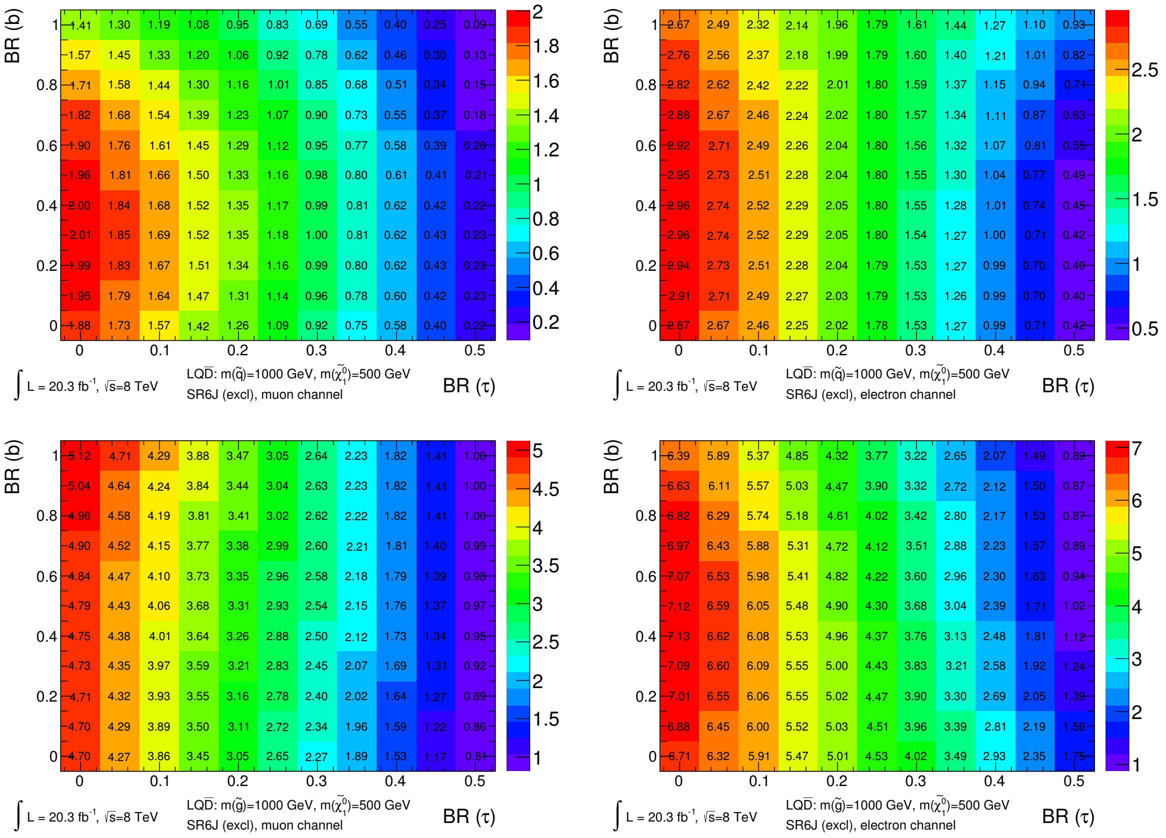

Figure 6.5: Expected number of signal events in the $BR(\tau)$–$BR(b)$ plane for the $LQ\bar{D}$ model with squark (top) and gluino production (bottom) in the muon (left) and electron channel (right) of SR6J. The results are for the mass point with $m(\tilde{\chi}_1^0) = 500\,\mathrm{GeV}$ and $m(\tilde{q}/\tilde{g}) = 1000\,\mathrm{GeV}$. All $E_{\mathrm{T}}^{\mathrm{miss}}$ bins of the 1L+jets+E_T^{miss} shape fit are summed up for this study.

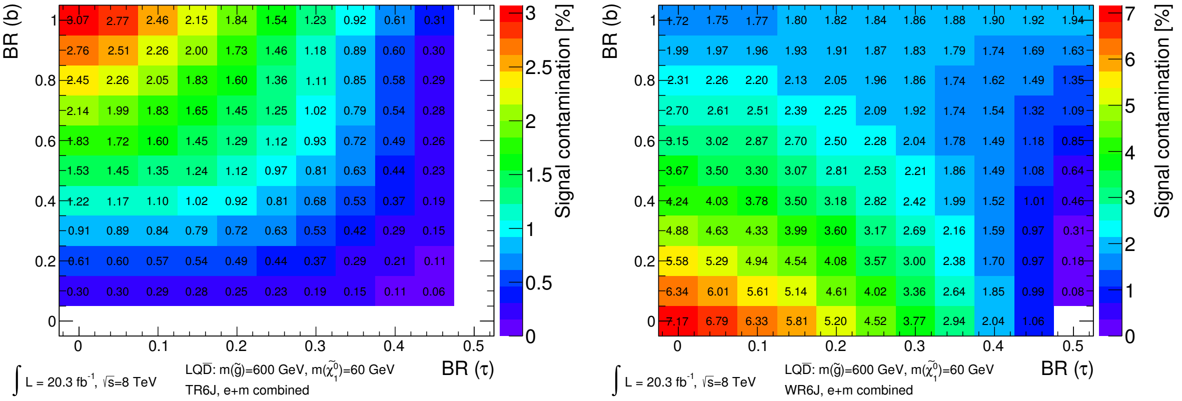

Figure 6.6: Expected signal contamination in the $t\bar{t}$ 6-jet CR (left) and the W+jets 6-jet CR (right) for the $LQ\bar{D}$ simplified model with gluino production and mass parameters $m(\tilde{g}) = 600\,\text{GeV}$ and $m(\tilde{\chi}_1^0) = 60\,\text{GeV}$. Electron and muon channel are summed up for this study. Bins without entry have a signal yield of zero.

model. These effects have been found to be negligible for the RPC models which the analysis was targeting originally. This is re-checked for the simplified RPV models used in this thesis.

6.3.1 Signal contamination of control regions

Backgrounds from $t\bar{t}$ and $W+$jets processes are estimated by fitting the normalisation of the corresponding MC simulation to data in two dedicated control regions for each SR (defined in Tab. 6.3). A contamination of the CRs with signal events might lead to an underestimation of the SM background in the SRs. The 1L+jets+E_T^{miss} exclusion fit simultaneously constrains the two background contributions as well as the signal strength in the CRs and SRs. In principle, a possible signal contamination is thus taken into account in the fit configuration. Nevertheless, the effect is double-checked for the mass points of the $LQ\bar{D}$ model which is expected to contribute the most to the CRs. For this study, the signal contamination is defined as the ratio of the number of expected signal events to the observed number of data events. It is highest in the regions which require at least six jets. This is expected as these regions have the highest sensitivity for the $LQ\bar{D}$ models. But even in the 6-jet CRs, the signal contamination is below 3 % nearly for the complete parameter space under study, which can be seen in Fig. 6.6. There, the signal contamination of the 6-jet $t\bar{t}$ and $W+$jets CR is shown for the $LQ\bar{D}$ gluino model with mass parameters $m(\tilde{g}) = 600\,\text{GeV}$ and $m(\tilde{\chi}_1^0) = 60\,\text{GeV}$. This is a benchmark point where the effect is rather large. The expected signal contamination reaches 7 % for low values of BR(b) and BR(τ) and is of the order of a few percent for most of the branching fraction plane. Therefore, it can be concluded that a possible signal contamination does not have a big influence on the sensitivity of the 1-lepton analysis for the $LQ\bar{D}$ models under study. Nonetheless, it is taken into account in the fit as mentioned above.

BR(τ)	BR(b)	signal region	dominant uncertainty	relative size [%]
		$LQ\bar{D}$ gluino model		
0.0	0.0	SR3J	FSR down	10.4
0.0	0.0	SR5J	FSR down	5.4
0.0	0.0	SR6J	FSR up	2.6
0.0	1.0	SR3J	FSR up	7.3
0.0	1.0	SR5J	ISR up	6.5
0.0	1.0	SR6J	ISR up	1.8
		$LQ\bar{D}$ squark model		
0.0	0.0	SR3J	ISR up	14.3
0.0	0.0	SR5J	ISR down	6.3
0.0	0.0	SR6J	Scale up	2.6
0.0	1.0	SR3J	FSR up	17.2
0.0	1.0	SR5J	ISR down	8.1
0.0	1.0	SR6J	FSR up	4.0

Table 6.5: Theoretical uncertainties on the signal acceptance of the 1L+jets+E_T^{miss} analysis due to ISR/FSR and scale effects for the mass points with $m(\tilde{g}/\tilde{q}) = 1000\,\text{GeV}$ and $m(\tilde{\chi}_1^0) = 900\,\text{GeV}$.

6.3.2 Theoretical signal uncertainties

For SUSY models simulated with HERWIG++, it is recommended by the ATLAS SUSY group [171] to check the impact of initial- or final-state radiation (ISR/FSR) and additional scale uncertainties on the signal acceptance. These can play a role particularly for compressed mass spectra. Their effect on the expected signal yields of the $LQ\bar{D}$ models in the 1L+jets+E_T^{miss} SRS is checked by comparing different MC simulations generated with MADGRAPH5 1.5.12 [108] and showered with PYTHIA 6.427 [97]. The renormalisation scale, the factorisation scale or the amount of ISR/FSR is varied up and down in the individual MC samples. The size of the uncertainties is estimated from the difference to the MC simulation with nominal settings. This is done at particle level without detector simulation as the amount of ISR/FSR is expected to be not affected by detector effects. A higher number of events can be simulated without the detector simulation as the latter is very time consuming.

All uncertainties have been found to be negligible which can be seen from the numbers in Tab. 6.5 for the mass points with a gluino/squark mass of 1000 GeV and a neutralino mass of 900 GeV. Only the corners of the branching fraction plane are cross-checked where the 1L+jets+E_T^{miss} analysis is sensitive (i.e. with $BR(\tau)$=0). All other mass points under consideration have less compressed mass spectra. Hence, these uncertainties are even smaller for them. Although the ISR/FSR and scale uncertainties can be as high as 17 % for the 3-jet region, they are $\leq$ 4 % in SR6J which contributes the most to the sensitivity of the analysis. In SR3J, the expected signal yield is very small and an additional signal uncertainty of the order of 10 % would not change the final exclusion limits significantly as the background is much higher than the signal prediction there.

6.4 Constraints on the $LQ\bar{D}$ model

The 1L+jets+E_T^{miss} analysis can set strong limits on SUSY models with R-parity violation via $LQ\bar{D}$ operators. However, it is not sensitive to the full parameter space as for high $BR(\tau)$ only a small number of light leptons is expected. The results can be combined with new physics searches in signatures without leptons to gain sensitivity in this area.

6.4.1 Results

The shape fit in the three signal regions of the 1L+jets+E_T^{miss} analysis is used to constrain the parameters of $LQ\bar{D}$ model. A hypothesis test is performed using the profile likelihood method (described in Sec. 5.7) for each mass point of the two $LQ\bar{D}$ models and each point in the branching fraction plane. The signal strength μ is fitted with respect to the theoretical cross-section of the model reduced by one standard deviation. The maximum signal strength μ^{95} which can be excluded at 95 % confidence level is retrieved from each of the hypothesis tests. A model is regarded as being excluded when the obtained value of μ^{95} is smaller than one.

The maximum squark or gluino mass, which can be excluded at 95 % confidence level, is calculated by interpolating the $\ln(\mu^{95})$ values between the generated signal samples (compare Tab. 6.1) linearly. For $R = 0.5$ and $R = 0.9$, the results from the $LQ\bar{D}$ model with squark or gluino production are shown in Fig. 6.7 and Fig. 6.8, respectively. The highest exclusion limits are obtained for low values of $BR(\tau)$ as expected while the results only depend a little on $BR(b)$ (compare Sec. 6.2). Squark masses up to ~1100 GeV and gluino masses up to ~1050 GeV can be excluded for a mass ratio of $R = 0.5$, while the mass limits exceed 1200 GeV in the case of $R = 0.9$ both for the squark and the gluino model. The observed limits are always stronger than the expected limits as the 1L+jets+E_T^{miss} analysis observes less data than predicted from the SM background (compare Tab. 6.4). With increasing $BR(\tau)$ the mass limits become weaker as the sensitivity of the 1L+jets+E_T^{miss} analysis decreases. For some points at the edge of the branching fraction plane at $BR(\tau) \approx 0.5$, the sensitivity of the analysis is so weak that the fit cannot set any limits on the model at 95 % confidence level as indicated by the white points in the plots. This can partially be recovered by combining the results with other analyses which are more sensitive to this region as will be discussed in Sec. 6.4.2.

No mass limits can be set at 95 % confidence level in the case of $R = 0.1$. There, the particles from the $\tilde{\chi}_1^0$ decay become so soft that the neutrinos do not have sufficient p_{T} to fulfil the tight $E_{\text{T}}^{\text{miss}}$ cuts of the 1L+jets+E_T^{miss} signal regions. The expected number of events from the $LQ\bar{D}$ model becomes so small that the signal cross-section which could be excluded with $CL_s > 0.95$ exceeds the theoretical cross-section of the model at least by a factor of 3. This is illustrated in Fig. 6.9 for the mass point with $m(\tilde{q}) = 600$ GeV and $m(\tilde{\chi}_1^0) = 60$ GeV from the squark $LQ\bar{D}$ model. New physics with cross-section of the order of 1000 fb could be excluded while the theoretical cross-section for this point is 285 fb.

Additionally, the fit configuration of the 1L+jets+E_T^{miss} analysis becomes unstable and does not converge to consistent μ values anymore on reasonable time scales. This is due to the fact

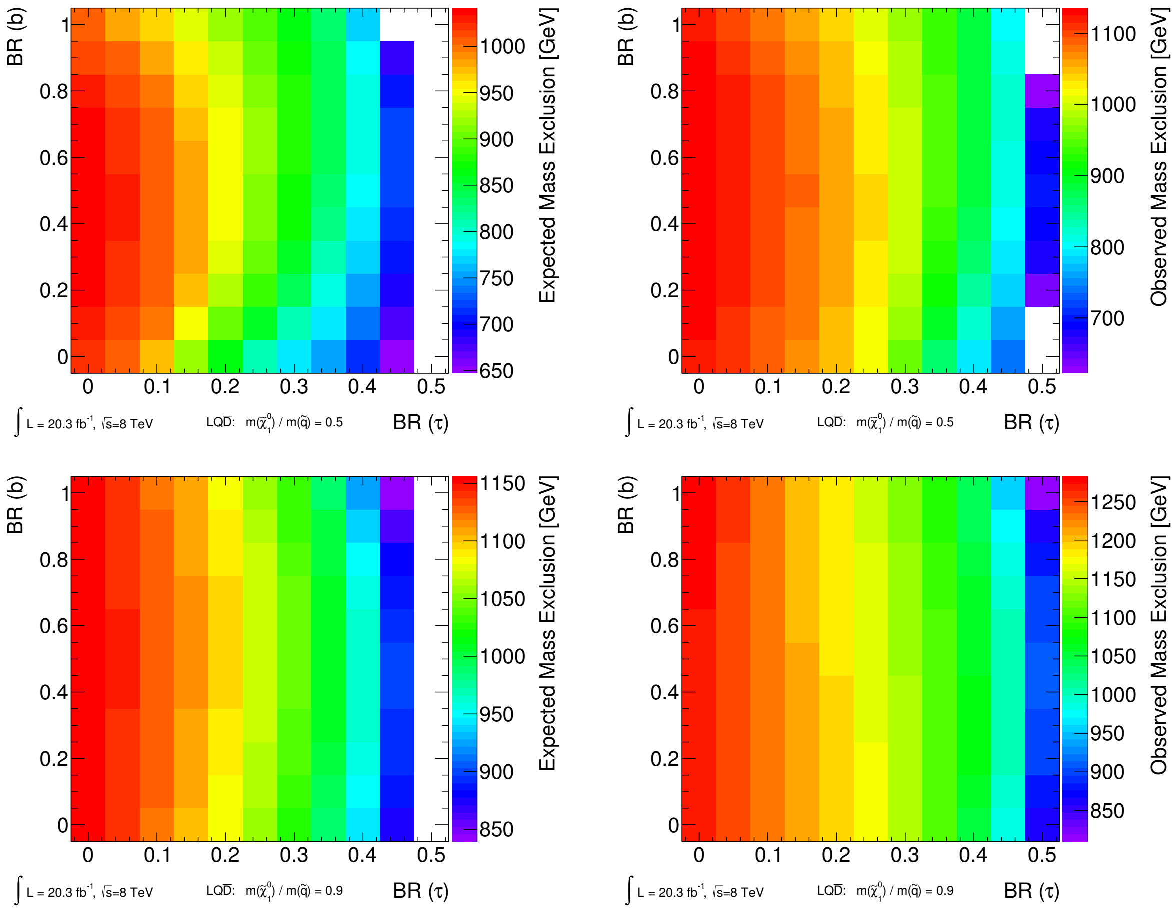

Figure 6.7: Results from the reinterpretation of the 1L+jets+E_T^{miss} analysis in the context of the $LQ\bar{D}$ model with squark production: Expected (left) and observed (right) mass limits for $R = 0.5$ (top) and $R = 0.9$ (bottom). Points in the branching fraction plane for which no mass limit can be set by the 1L+jets+E_T^{miss} analysis alone are shown in white.

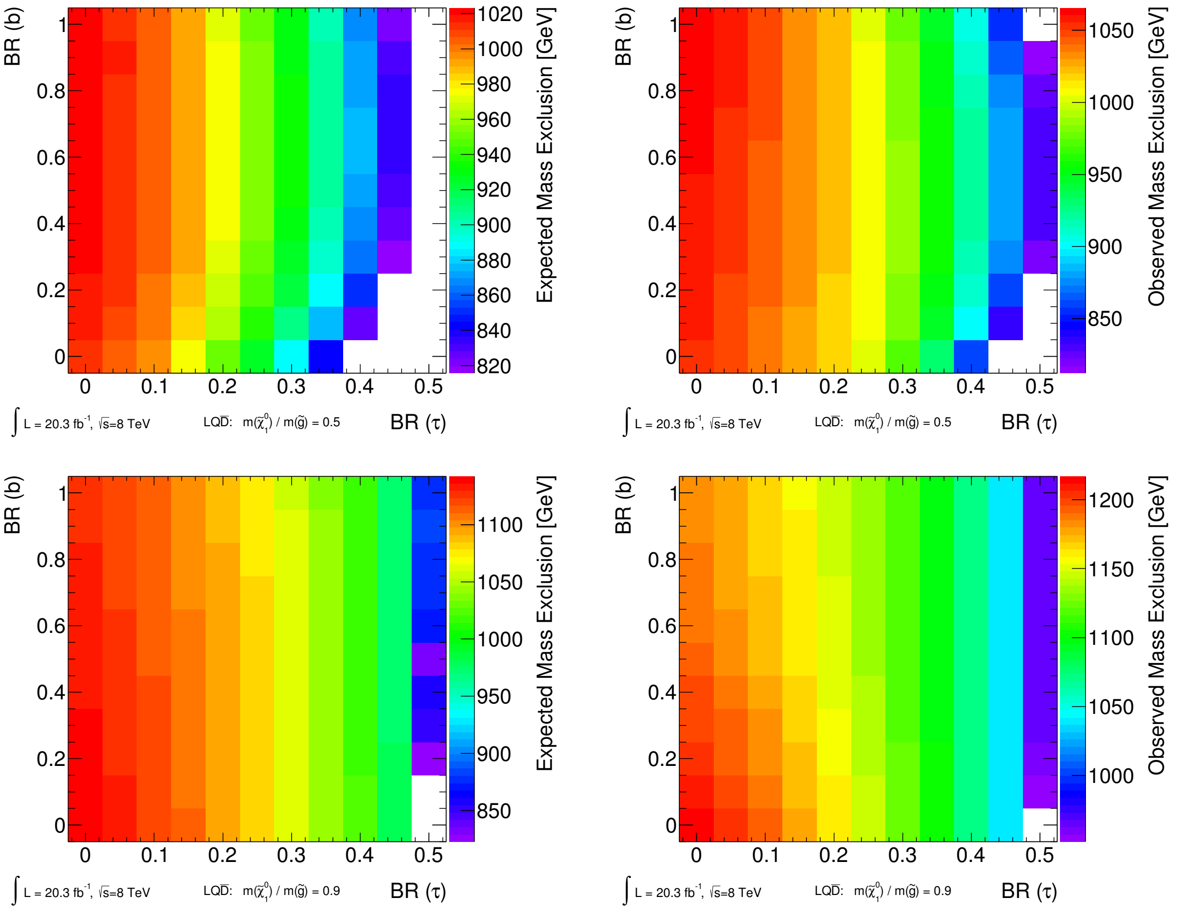

Figure 6.8: Results from the reinterpretation of the 1L+jets+E_T^{miss} analysis in the context of the $LQ\bar{D}$ model with gluino production: Expected (left) and observed (right) mass limits for $R = 0.5$ (top) and $R = 0.9$ (bottom). Points in the branching fraction plane for which no mass limit can be set by the 1L+jets+E_T^{miss} analysis alone are shown in white.

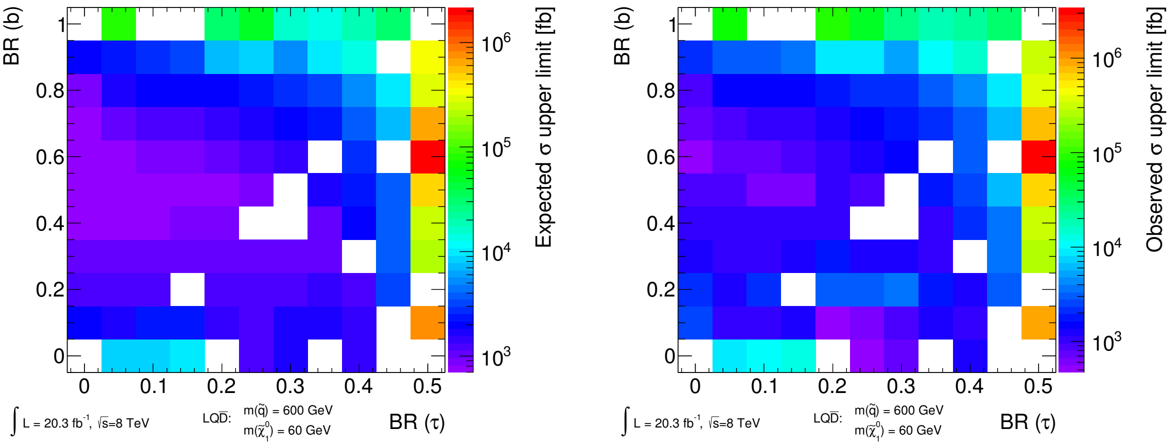

Figure 6.9: Results from the reinterpretation of the 1L+jets+$E_T^{\rm miss}$ analysis in the context of the $LQ\bar{D}$ model with squark production and $m(\tilde{q}) = 600\,\mathrm{GeV}$, $m(\tilde{\chi}_1^0) = 60\,\mathrm{GeV}$. Points in the branching fraction plane for which the 1L+jets+$E_T^{\rm miss}$ fit fails are shown in white.

that the fit uses the shape information and cannot yield meaningful results in cases where the signal expectation is 0 for most of the bins and has large uncertainties of up to 100 % in the others. Failed fits are indicated as white points in the plots. The range between R=0.1 and 0.5 has not been invastigated as other analyses show better sensitivity in this area of phase space which will be discussed in the next section in more detail.

It can be concluded that if SUSY with RPV via $LQ\bar{D}$ operators and mass spectra similar to the $R = 0.1$ case was realized in nature it would not be discovered by the 1L+jets+$E_T^{\rm miss}$ analysis. Other analyses can recover some efficiency for low R values, but dedicated search strategies have to be developed in cases where this is not possible. Details about the excluded signal strength for all generated mass points in the two $LQ\bar{D}$ models can be found in App. F. The information there has been used for the interpolated mass limits shown in Fig. 6.7 and 6.8.

6.4.2 Combinations with other analyses

It becomes apparent from the results in Sec. 6.4.1 that the 1L+jets+$E_T^{\rm miss}$ analysis loses more and more sensitivity the higher the branching fraction for $\tilde{\chi}_1^0$ decays with τ leptons gets. SUSY searches in signatures with jets and large missing energy but without electrons or muons can be used to gain sensitivity in this region. A combination of the 1L+jets+$E_T^{\rm miss}$ results with two ATLAS searches in events with zero leptons, missing energy and $2-6$ jets [172] or $7-10$ jets [173] is presented in [54]. The latter analysis exceeds the 1L+jets+$E_T^{\rm miss}$ limits in the case of the $LQ\bar{D}$ gluino model with $R = 0.5$ over the full branching fraction plane. It can also set limits in the case of $R = 0.1$ where the 1L+jets+$E_T^{\rm miss}$ analysis has no sensitivity at all.

For $R = 0.9$, the jets from the gluino decay become too soft and the requirement of at least seven highly energetic jets is not suitable any more. Here a combination of the 1L+jets+$E_T^{\rm miss}$

results with the 0-lepton analysis with $2-6$ jets gives the best exclusion limits which can be seen in Fig. 6.10. A full statistical combination of the different searches is out of scope of this thesis. Instead, the result from the analysis with the better expected exclusion limit is used at each point of the branching fraction plane. The plot at the bottom illustrates which analysis performs better. The search in 0-lepton signatures recovers the loss of efficiency for values of $BR(\tau) \gtrsim 0.3$, while the 1L+jets+E_T^{miss} analysis sets the highest limits for $BR(\tau) \lesssim 0.1$. In the region in between, the two analyses show comparable sensitivity leading to almost constant mass limits.

Also for the squark model, the results of the 1L+jets+E_T^{miss} analysis can be combined with the 0-lepton results. The search in signatures with very high jet multiplicities ($7-10$ jets) is omitted from the combination as fewer than seven jets are expected from the squark decay chain. The limits for $R = 0.5$ and $R = 0.9$ are shown in Fig. 6.11. Again, the results of the 1L+jets+E_T^{miss} analysis dominate for the region at low $BR(\tau)$, while the 0-lepton analysis has better sensitivity at high $BR(\tau)$ with a range in between where both analysis set comparable limits. Therefore, a combination of the analyses helps to improve the stand-alone constraints on the model parameters. The squark $LQ\bar{D}$ model with $R = 0.1$, however, escapes detection by any of the analyses used in the combination. This leaves a gap in the ATLAS SUSY search program which might be closed with dedicated searches in regions at lower $E_{\mathrm{T}}^{\text{miss}}$, although the estimation of the backgrounds from QCD multijet events becomes more and more difficult there.

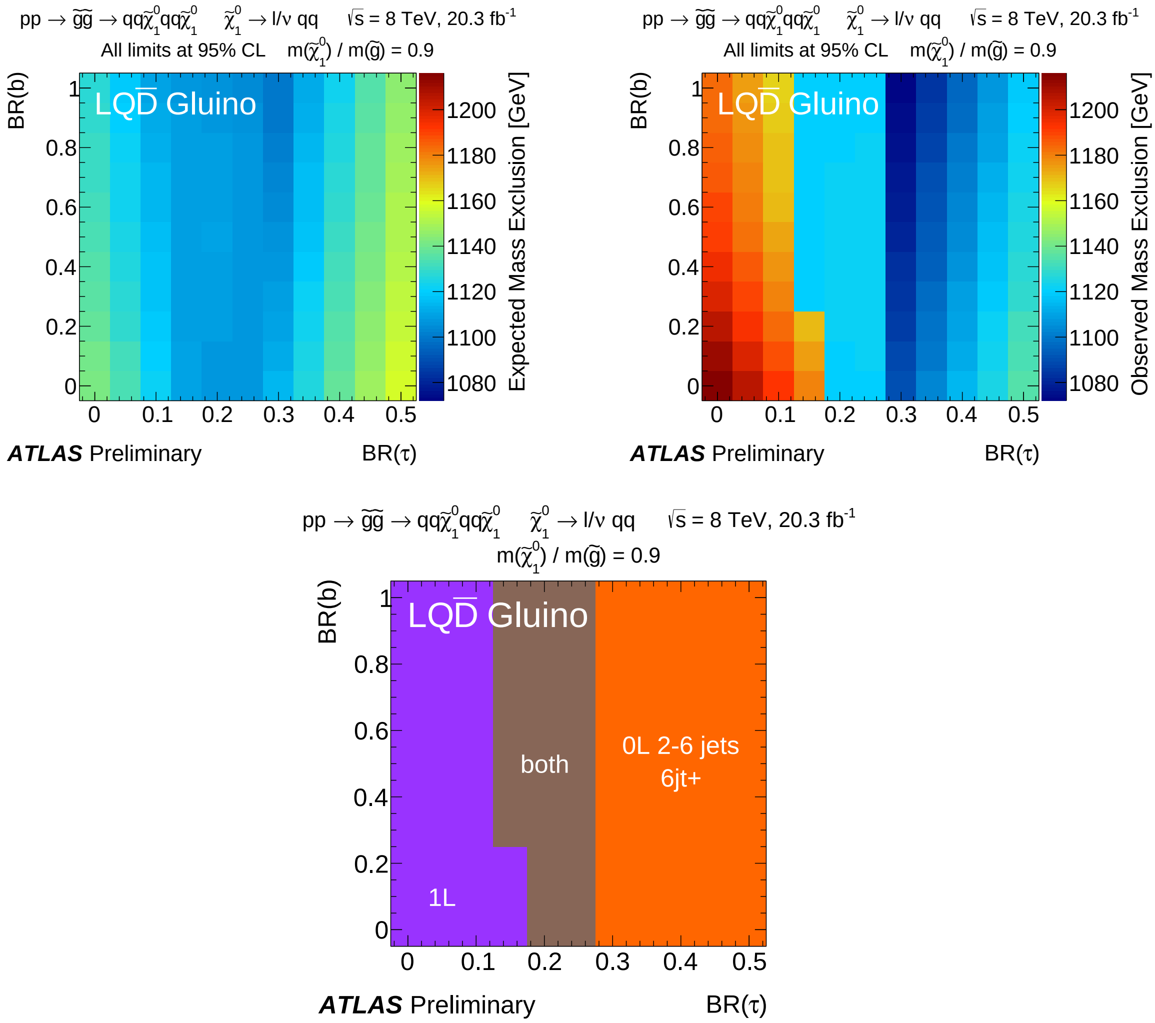

Figure 6.10: Combination of the 1L+jets+E_T^{miss} analysis (referred to as “1L”) and the SUSY search in 0-lepton signatures with 2-6 jets [172] (“0L 2-6 jets 6jt+”) for the $LQ\bar{D}$ gluino model with $R = 0.9$ [54]: The expected limits are shown on top left, the observed limits on top right, while the sketch on bottom illustrates which analysis dominates the sensitivity in the different regions of the branching fraction plane.

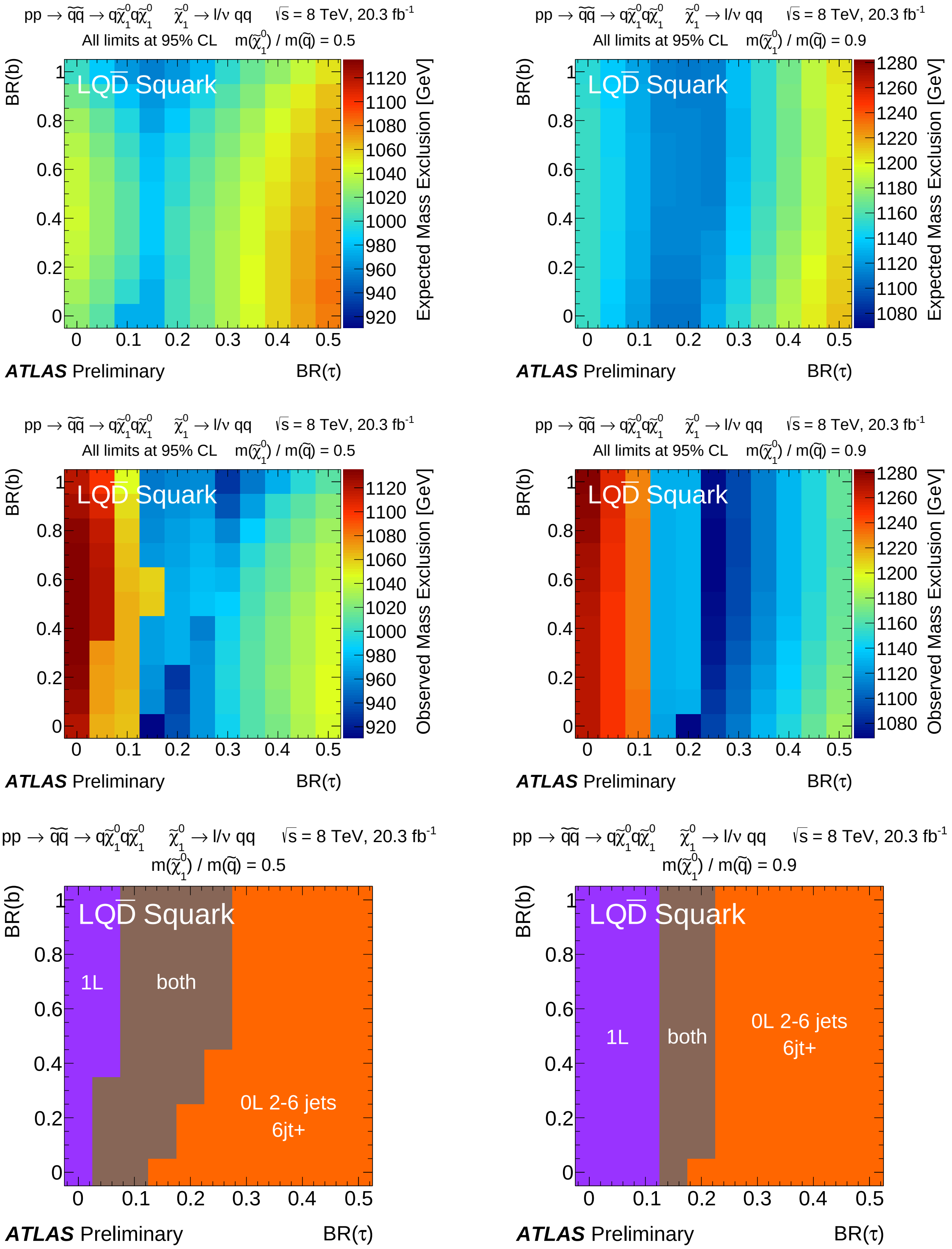

Figure 6.11: Combination of the 1L+jets+E_T^{miss} analysis (referred to as "1L") and the SUSY search in 0-lepton signatures with 2-6 jets [172] ("0L 2-6 jets 6jt+") for the $LQ\bar{D}$ squark model with $R = 0.5$ (left) and $R = 0.9$ (right) [54]: The expected limits are shown on top, the observed limits in the middle, while the sketches on bottom illustrate which analysis dominates the sensitivity in the different regions of the branching fraction plane.

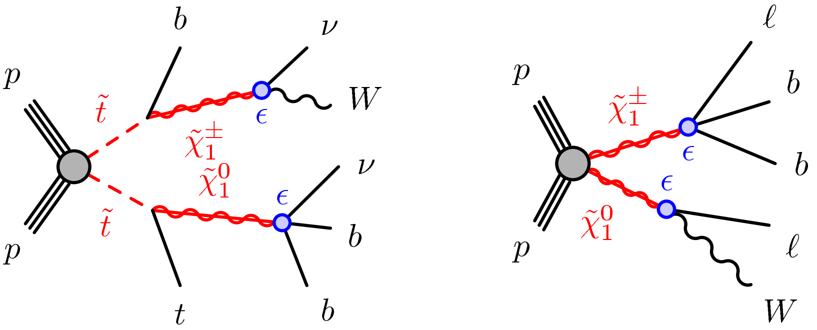

Figure 6.12: Example Feynman diagrams for the pMSSM with R-parity violation via bRPV operators: Production of stop quarks (left) and gauginos (right) [54].

6.5 Sensitivity of the signal selection to bRPV models

In principle, signatures with one lepton, jets and missing energy can also occur in models with bRPV introduced in Sec. 2.2.2. The sensitivity of the 1L+jets+E_T^{miss} analysis is studied for bRPV implemented in a natural SUSY scenario within the pMSSM (compare Sec. 2.2.3). Constraints from neutrino oscillation data and the Higgs mass of 125 GeV are taken into account in the pMSSM by construction. The LSP is a higgsino-like $\tilde{\chi}_1^0$ in this model where the masses of the $\tilde{\chi}_2^0$ and the lightest charginos $\tilde{\chi}_1^{\pm}$ are very close [54]. The masses of the gauginos are governed by the higgsino mass parameter μ which is treated as a free parameter for this study. In addition, the mass parameter for the left-handed third generation squarks, $m_{\tilde{q}_{\text{L}},3}$, is varied in a range compatible with a natural SUSY spectrum. The masses of all other SUSY particles are adjusted to be high enough so that their production is suppressed at LHC energies. Thus, the strong production of third generation squarks and the electroweak production of the light gauginos are the dominant production modes in the pMSSM parameter space considered here. The gauginos can decay via the bRPV couplings into SM particles. Example Feynman diagrams for typical bRPV signatures studied here are shown in Fig. 6.12.

The bRPV parameters ϵ_i $(i = 1, 2, 3)$ (compare Eq. (2.6)) can be determined from current neutrino oscillation data [45, 174]. The decay properties of the supersymmetric particles are calculated with Spheno 3.3.2 [175,176]. MC samples of the model are simulated with Pythia 6.423 [97] using the CTEQ6L1 PDF set [169] and a fast simulation of the ATLAS detector is applied to the generated events. For this sensitivity study, average LO cross-sections as retrieved from the MC generator are used to normalise the signal expectation.

The CL_s values of the reinterpretation of the 1L+jets+E_T^{miss} analysis in the context of eight pMSSM mass points with additional bRPV terms are shown in Tab. 6.6 together with some details about considered mass spectra. None of the models can be excluded with a confidence level of 95 % and the obtained p-values are very weak which means that the sensitivity of the 1L+jets+E_T^{miss} analysis for these models is poor. This can also be seen from the signal yields after the different cuts of SR6J which has the best sensitivity among all SRs. These numbers are given in Tab. 6.7 for one pMSSM point as example. The signal efficiency is very small and only a few events are expected to fulfil all selection requirements. This is especially due to the

μ [GeV]	$m_{\tilde{q}_\mathrm{L},3}$ [GeV]	$m(\tilde{\chi}_1^0)$ [GeV]	$m(\tilde{\chi}_1^\pm)$ [GeV]	$m(\tilde{t}_1)$ [GeV]	CL_s
160	350	156	160	355	0.62
160	650	154	158	534	0.13
160	950	154	158	533	0.38
310	450	311	313	415	0.15
310	650	311	313	541	0.37
310	950	311	313	539	0.67
460	650	464	465	540	0.10
460	950	464	465	545	0.29

Table 6.6: CL_s values for the reinterpretation of the 1L+jets+E_T^miss analysis in the context of eight parameter points of the pMSSM with additional bRPV couplings.

Cut	muon channel	electron channel
Preselection	54.0 ± 1.5	66.6 ± 1.7
#leptons $= 1$ leading lepton $p_\mathrm{T} > 25$ GeV subleading lepton $p_\mathrm{T} < 10$ GeV	23.3 ± 1.0	29.5 ± 1.1
#jets ≥ 6 p_T^jet [GeV] > 80, 50, 40, 40, 40 ,40	13.4 ± 0.8	17.4 ± 0.9
$E_\mathrm{T}^\mathrm{miss} > 250$ GeV	2.3 ± 0.3	2.8 ± 0.3
$m_\mathrm{T} > 150$ GeV	0.83 ± 0.19	0.97 ± 0.21
$m_\mathrm{eff} > 600$ GeV	0.83 ± 0.19	0.97 ± 0.21

Table 6.7: Signal yields for the pMSSM point with $m_{\tilde{q}_\mathrm{L},3} = 650$ GeV and $\mu = 310$ GeV after the different selection requirements of the 1L+jets+E_T^miss signal region SR6J. The indicated uncertainties are due to limited MC statistics and do not include any systematic uncertainties. Only the cuts after the event preselection are shown here.

high $E_\mathrm{T}^\mathrm{miss}$ cut of the analysis and the veto on events with more than one electron or muon. Analyses, which allow for more leptons in the final state and can therefore apply looser cuts on $E_\mathrm{T}^\mathrm{miss}$, have better sensitivity for the bRPV model under study. A reinterpretation of a SUSY search in events with two same-sign or three leptons [146] can be found in [54]. This analysis can exclude the full pMSSM parameter space considered here.

7 Summary and Outlook

A nice graphical illustration of the main result presented in this thesis can be seen in the event display in Fig. 7.1. One of the 29 events from the signal region of the Z+jets+E_T^{miss} analysis which was recorded on 24th August 2012 is shown there. It contains two muons with an invariant dilepton mass of 92.3 GeV, two highly energetic jets, 593.4 GeV of missing transverse energy and has $H_{\mathrm{T}} = 667.4$ GeV.
The Z+jets+E_T^{miss} analysis presented in Sec. 5 targets SUSY models in which the enhanced production of Z bosons in association with jets and large missing transverse momentum is predicted. A total background of 10.6 ± 3.2 events is expected from SM processes in the combination of the e^+e^- and $\mu^+\mu^-$ channel while 29 events are observed in data. The excess has a local significance of $3.0\,\sigma$. Gluino masses up to ~900 GeV can be excluded for a higgsino mass parameter μ above 500 GeV in the case of a GGM model with $\tan\beta = 1.5$ and up to ~840 GeV for $\mu > 550$ GeV in a $\tan\beta = 30$ model.

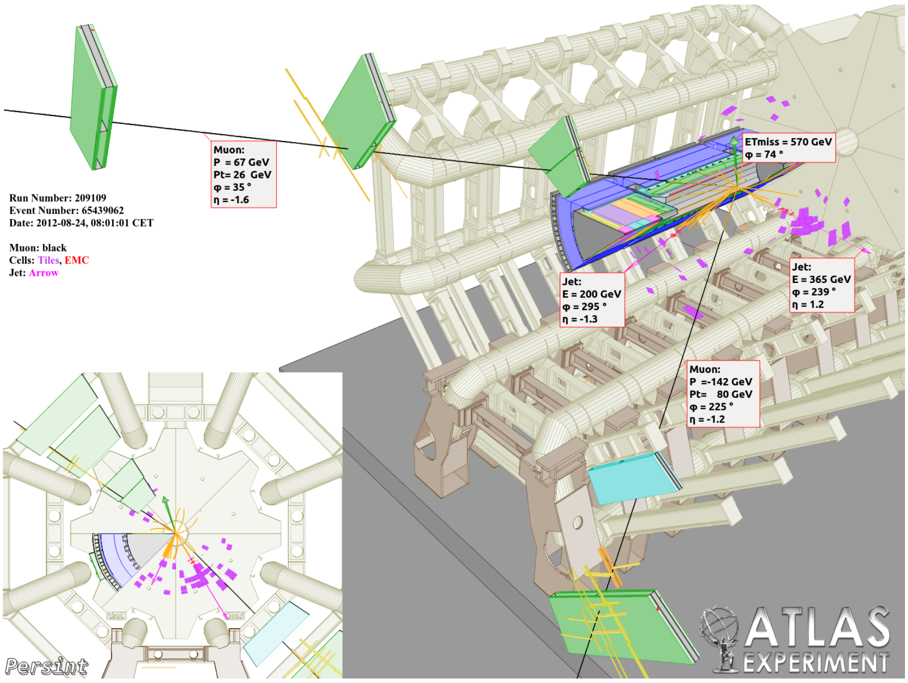

Figure 7.1: One of the 29 events from the signal region of the Z+jets+E_T^{miss} analysis [134]. It contains two muons with an invariant dilepton mass of 92.3 GeV, two highly energetic jets, large missing energy and large H_{T}. The value for $E_{\mathrm{T}}^{\mathrm{miss}}$ shown in the figure differs slightly from the number given in the text as a different $E_{\mathrm{T}}^{\mathrm{miss}}$ definition is applied in the program used to draw the event display.

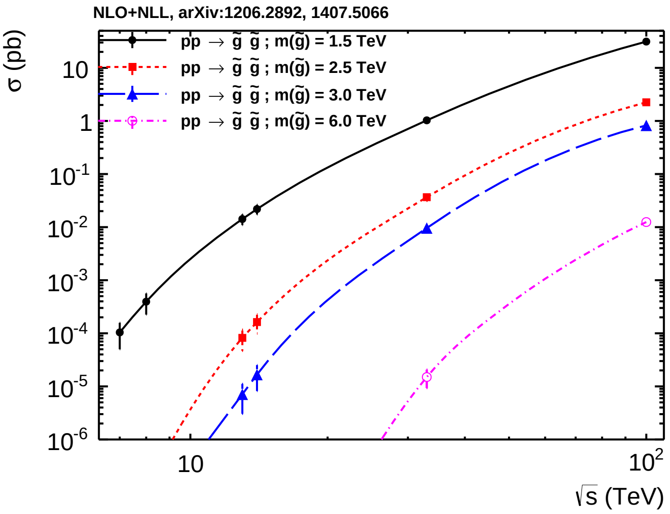

Figure 7.2: Dependency of the cross-sections for the gluino pair production on the centre of mass energy $\sqrt{s}$ for different gluino mass hypotheses [143, 177, 178].

No definite conclusion can be drawn about the origin of the observed excess. Plenty of cross-checks and validation studies were performed to exclude unconsidered detector effects or mismodelled backgrounds as an explanation for the excess. None of these revealed any problems with the analysis strategy or object selection. The question, if the excess appears to be more signal-like or more background-like, remains open with the statistics which was available for this thesis. Also a comparison with a similar CMS search in events with a same-flavour opposite-sign lepton pair is difficult as the details of the CMS event selections are different and the overlap with the ATLAS Z+jets+E_T^{miss} analysis is small.

The other analysis presented in Sec. 6 of this thesis targets SUSY models with R-parity violation via additional $LQ\bar{D}$ operators in the superpotential, where prompt decays of the LSP into jets and leptons are allowed. The results of an ATLAS search for SUSY in events with one isolated lepton, jets and missing transverse momentum were used to constrain the parameters of the model. The limits on the squark and gluino mass extend up to 1200 GeV for particular mass spectra and combinations of open LSP decay modes. The results can be combined with an ATLAS search for SUSY in events without leptons to recover sensitivity in areas of the parameter space where only few electrons or muons are expected from the R-parity-violating operators. However, it becomes apparent that even the combination of different results is not sensitive to some $LQ\bar{D}$ models. Dedicated search strategies have to be developed (e.g. involving low $E_{\mathrm{T}}^{\mathrm{miss}}$ signal regions) to close this gap in the ATLAS search program.

The upcoming run-II of the LHC which has started in spring 2015 offers excellent conditions to continue the searches for new physics and hopefully discover first hints of new particles. The increased centre of mass energy of $\sqrt{s} = 13$ TeV allows the production of heavy particles with higher cross-sections. This can be seen in Fig. 7.2. There, the dependency of the gluino production cross-section on $\sqrt{s}$ is shown as an example. It increases by one order of magnitude for gluinos with mass of 1.5 TeV, which are beyond the exclusion limits of the run-I analyses, when going from $\sqrt{s} = 8$ TeV to 13 TeV. The gain is even higher for particles with masses too high to be produced in 8 TeV collisions.

The LHC can deliver about $10\,\mathrm{fb}^{-1}$ of data by the end of 2015 and the expected integrated luminosity until the end of run-II in 2018 is of the order of $100\,\mathrm{fb}^{-1}$ [179]. There are good reasons to believe that new physics exists at the TeV scale and the signatures of squarks and gluinos will become visible even in the first few fb^{-1} if they are within the new energy regime. Signs of more exotic SUSY models (like the $LQ\bar{D}$ model) will need more data to show up, but the vast expected dataset and optimized analysis strategies ensure that they can also be discovered over a wide range of their hypothetical masses with run-II data. This will also clarify if the excess observed in the Z+jets+E_T^{miss} signal region was caused by a statistical fluctuation in data or if it was a first glimpse at the signs of new elementary particles.

Bibliography

[1] ATLAS Collaboration, *Observation of a new particle in the search for the Standard Model Higgs boson with the ATLAS detector at the LHC*, Phys. Lett. B **716** (2012) 1–29, `arXiv:1207.7214 [hep-ex]`.

[2] CMS Collaboration, *Observation of a new boson at a mass of 125 GeV with the CMS experiment at the LHC*, Phys. Lett. B **716** (2012) 30–61, `arXiv:1207.7235 [hep-ex]`.

[3] P. W. Higgs, *Broken Symmetries and the Masses of Gauge Bosons*, Phys. Rev. Lett. **13** (1964) 508–509.

[4] P. W. Higgs, *Broken symmetries, massless particles and gauge fields*, Phys. Lett. **12** (1964) 132–133.

[5] P. W. Higgs, *Spontaneous Symmetry Breakdown without Massless Bosons*, Phys. Rev. **145** (1966) 1156–1163.

[6] F. Englert and R. Brout, *Broken Symmetry and the Mass of Gauge Vector Mesons*, Phys. Rev. Lett. **13** (1964) 321–323.

[7] G. S. Guralnik, C. R. Hagen, and T. W. B. Kibble, *Global Conservation Laws and Massless Particles*, Phys. Rev. Lett. **13** (1964) 585–587.

[8] T. W. B. Kibble, *Symmetry Breaking in Non-Abelian Gauge Theories*, Phys. Rev. **155** (1967) 1554–1561.

[9] H. Miyazawa, *Baryon Number Changing Currents*, Prog. Theor. Phys. **36** (1966) 1266–1276.

[10] P. Ramond, *Dual Theory for Free Fermions*, Phys. Rev. D **3** (1971) 2415–2418.

[11] Y. A. Gol'fand and E. P. Likhtman, *Extension of the Algebra of Poincare Group Generators and Violation of p Invariance*, JETP Lett. **13** (1971) 323–326.

[12] A. Neveu and J. H. Schwarz, *Factorizable dual model of pions*, Nucl. Phys. B **31** (1971) 86–112.

[13] A. Neveu and J. H. Schwarz, *Quark Model of Dual Pions*, Phys. Rev. D **4** (1971) 1109–1111.

[14] J. Gervais and B. Sakita, *Field theory interpretation of supergauges in dual models*, Nucl. Phys. B **34** (1971) 632–639.

[15] D. V. Volkov and V. P. Akulov, *Is the Neutrino a Goldstone Particle?*, Phys. Lett. B **46** (1973) 109–110.

[16] J. Wess and B. Zumino, *A Lagrangian Model Invariant Under Supergauge Transformations*, Phys. Lett. B **49** (1974) 52.

[17] J. Wess and B. Zumino, *Supergauge Transformations in Four-Dimensions*, Nucl. Phys. B **70** (1974) 39–50.

[18] ATLAS Collaboration, *Search for supersymmetry in final states with jets, missing transverse momentum and a Z boson at* $\sqrt{s} = 8$ TeV *with the ATLAS detector*, ATLAS-CONF-2012-152. `http://cds.cern.ch/record/1493491`.

[19] ATLAS Collaboration, *Search for squarks and gluinos in events with isolated leptons, jets and missing transverse momentum at* $\sqrt{s} = 8$ *TeV with the ATLAS detector*, JHEP **1504** (2015) 116, `arXiv:1501.03555 [hep-ex]`.

[20] Y. Nagashima, *Beyond the Standard Model of Elemetary Particle Physics.* Wiley-VCH, 2014.

[21] D. Griffiths, *Introduction to Elementary Particles.* WILEY-VCH, 2008.

[22] Olive, K.A. et al (Particle Data Group) Chin. Phys. C **38** (2014) 090001.

[23] M. A. Dobbs et al., *Les Houches Guidebook to Monte Carlo Generators for Hadron Collider Physics*, `arXiv:hep-ph/0403045`.

[24] S. F. Novaes, *Standard Model: An Introduction*, `arXiv:hep-ph/0001283`.

[25] A. Djouadi, *The anatomy of electroweak symmetry breaking: Tome I: The Higgs boson in the Standard Model*, Phys. Rep. **457** (2008) 1–216, `arXiv:hep-ph/0503172`.

[26] The ATLAS and CMS Collaborations, *Combined Measurement of the Higgs Boson Mass in pp Collisions at* $\sqrt{s} = 7$ *and 8 TeV with the ATLAS and CMS Experiments*, Phys. Rev. Lett. **114** (2015) 191803, `arXiv:1503.07589 [hep-ex]`.

[27] Planck Collaboration, *Planck 2013 results. XVI. Cosmological parameters*, A&A **571** (2014) A16, `arXiv:1303.5076 [astro-ph.CO]`.

[28] F. Capozzi et al., *Status of three-neutrino oscillation parameters, circa 2013*, Phys. Rev. D **89** (2014) 093018, `arXiv:1312.2878 [hep-ph]`.

[29] E. K. Akhmedov, G. Branco, and M. Rebelo, *Seesaw mechanism and structure of neutrino mass matrix*, Phys. Lett. B **478** (2000) 215–223, `arXiv:hep-ph/9911364`.

[30] S. P. Martin, *A Supersymmetry Primer*, `arXiv:hep-ph/9709356`.

[31] S. Dimopoulos and H. Georgi, *Softly Broken Supersymmetry and SU(5)*, Nucl. Phys. B **193** (1981) 150.

[32] E. Witten, *Dynamical Breaking of Supersymmetry*, Nucl. Phys. B **188** (1981) 513.

[33] M. Dine, W. Fischler, and M. Srednicki, *Supersymmetric Technicolor*, Nucl. Phys. B **189** (1981) 575–593.

[34] S. Dimopoulos and S. Raby, *Supercolor*, Nucl. Phys. B **192** (1981) 353.

[35] N. Sakai, *Naturalness in Supersymmetric Guts*, Zeit. Phys. C **11** (1981) 153.

[36] R. Kaul and P. Majumdar, *Cancellation of Quadratically Divergent Mass Corrections in Globally Supersymmetric Spontaneously Broken Gauge Theories*, Nucl. Phys. B **199** (1982) 36.

[37] H. Goldberg, *Constraint on the photino mass from cosmology*, Phys. Rev. Lett. **50** (1983) 1419.

[38] J. Ellis et al., *Supersymmetric relics from the big bang*, Nucl. Phys. B **238** (1984) 453–476.

[39] H. Dreiner and G. G. Ross, *R-parity violation at hadron colliders*, Nucl. Phys. B **365** (1991) 597–613.

[40] M. Asano, K. Rolbiecki, and K. Sakurai, *Can R-parity violation hide vanilla supersymmetry at the LHC?*, JHEP **01** (2013) 128, `arXiv:1209.5778 [hep-ph]`.

[41] B. Allanach and B. Gripaios, *Hide and seek with natural supersymmetry at the LHC*, JHEP **05** (2012) 062, `arXiv:1202.6616 [hep-ph]`.

[42] H. Dreiner et al., *General MSSM signatures at the LHC with and without R-parity*, Phys. Rev. D **86** (2012) 035021, `arXiv:1205.0557 [hep-ph]`.

[43] R. N. Mohapatra, *Supersymmetry and R-parity: An overview*, `arXiv:1503.06478 [hep-ph]`.

[44] M. Chemtob, *Phenomenological constraints on broken R parity symmetry in*

supersymmetry models, Prog. Part. Nucl. Phys. **54** (2005) 71–191, `arXiv:hep-ph/0406029 [hep-ph]`.

[45] W. Porod et al., *Testing neutrino mixing at future collider experiments*, Phys. Rev. D **63** (2001) 115004, `arXiv:hep-ph/0011248`.

[46] M. Hirsch and W. Porod, *Neutrino properties and the decay of the lightest supersymmetric particle*, Phys. Rev. D **68** (2003) 115007, `arXiv:hep-ph/0307364`.

[47] M. Diaz et al., *Solar neutrino masses and mixing from bilinear R parity broken supersymmetry: Analytical versus numerical results*, Phys. Rev. D **68** (2003) 013009, `arXiv:hep-ph/0302021`.

[48] ATLAS Collaboration, *Measurement of the top pair production cross-section in 8 TeV proton-proton collisions using kinematic information in the lepton+jets final state with ATLAS*, `arXiv:1504.04251 [hep-ex]`.

[49] W.Beenakker, R.Hoepker, and M.Spira, *PROSPINO: A Program for the Production of Supersymmetric Particles in Next-to-leading Order QCD*, `arXiv:hep-ph/9611232`.

[50] T. Plehn, *Prospino2*, `http://www.thphys.uni-heidelberg.de/~plehn/index.php?show=prospino&visible=tools`.

[51] R. Barbieri and G. Giudice, *Upper Bounds on Supersymmetric Particle Masses*, Nucl. Phys. B **306** (1988) 63.

[52] B. de Carlos and J. Casas, *One loop analysis of the electroweak breaking in supersymmetric models and the fine tuning problem*, Phys. Lett. B **309** (1993) 320–328, `arXiv:hep-ph/9303291`.

[53] ATLAS Collaboration, *Search for supersymmetry in events containing a same-flavour opposite-sign dilepton pair, jets, and large missing transverse momentum in* $\sqrt{s} = 8$ *TeV pp collisions with the ATLAS detector*, `arXiv:1503.03290 [hep-ex]`. accepted for publication by Eur. Phys. J. C.

[54] ATLAS Collaboration, *Constraints on promptly decaying supersymmetric particles with lepton-number- and R-parity-violating interactions using Run I ATLAS data*, ATLAS-CONF-2015-018. `http://cds.cern.ch/record/2017303`.

[55] J. Alwall, P. Schuster, and N. Toro, *Simplified Models for a First Characterization of New Physics at the LHC*, Phys. Rev. D **79** (2009) 075020, `arXiv:0810.3921 [hep-ph]`.

[56] D. Alves et al., *Simplified Models for LHC New Physics Searches*, J. Phys. G: Nucl. Part. Phys. **39** (2012) 105005, `arXiv:1105.2838 [hep-ph]`.

[57] P. Meade, N. Seiberg, and D. Shih, *General Gauge Mediation*, Prog. Theo. Phys. Suppl. **177** (2009) 143–158, `arXiv:0801.3278 [hep-ph]`.

[58] M. Buican et al., *Exploring general gauge mediation*, JHEP **0903** (2009) 016, `arXiv:0812.3668 [hep-ph]`.

[59] A. H. Chamseddine, R. L. Arnowitt, and P. Nath, *Locally Supersymmetric Grand Unification*, Phys. Rev. Lett. **49** (1982) 970.

[60] R. Barbieri, S. Ferrara, and C. A. Savoy, *Gauge Models with Spontaneously Broken Local Supersymmetry*, Phys. Lett. B **119** (1982) 343.

[61] L. E. Ibanez, *Locally Supersymmetric SU(5) Grand Unification*, Phys. Lett. B **118** (1982) 73.

[62] L. J. Hall, J. D. Lykken, and S. Weinberg, *Supergravity as the Messenger of Supersymmetry Breaking*, Phys. Rev. D **27** (1983) 2359–2378.

[63] N. Ohta, *Grand unified theories based on local supersymmetry*, Prog. Theor. Phys. **70** (1983) 542.

[64] G. L. Kane et al., *Study of constrained minimal supersymmetry*, Phys. Rev. D **49** (1994) 6173–6210, `arXiv:hep-ph/9312272`.

[65] C. F. Berger et al., *Supersymmetry without prejudice*, JHEP **0902** (2009) 023, `arXiv:0812.0980 [hep-ph]`.

[66] J. A. Conley et al., *Supersymmetry without prejudice at the LHC*, Eur. Phys. J. C **71** (2011) 1697, `arXiv:1009.2539 [hep-ph]`.

[67] ATLAS SUSY Group, *Summary plots from the ATLAS Supersymmetry physics group*, `https://atlas.web.cern.ch/Atlas/GROUPS/PHYSICS/CombinedSummaryPlots/SUSY/index.html#ATLAS_SUSY_Summary`.

[68] LHCb Collaboration, *Measurement of the* $B_s^0 \to \mu^+\mu^-$ *Branching Fraction and Search for* $B^0 \to \mu^+\mu^-$ *Decays at the LHCb Experiment*, Phys. Rev. Lett. **111** (2013) 101805, `arXiv:1307.5024 [hep-ex]`.

[69] CMS Collaboration, *Measurement of the* $B_s^0 \to \mu^+\mu^-$ *Branching Fraction and Search for* $B^0 \to \mu^+\mu^-$ *with the CMS Experiment*, Phys. Rev. Lett. **111** (2013) 101804, `arXiv:1307.5025 [hep-ex]`.

[70] L. Evans and P. Bryant, *LHC Machine*, JINST **3** (2008) S08001.

[71] CERN, *The CERN accelerator complex*, OPEN-PHO-ACCEL-2013-056. `https://cds.cern.ch/record/1621894`.

[72] M. Lamont, *Status of the LHC*, J. Phys.: Conf. Ser. **455** (2013) 012001.

[73] ATLAS Collaboration, *The ATLAS Experiment at the CERN Large Hadron Collider*, JINST **3** (2008) S08003.

[74] CMS Collaboration, *The CMS experiment at the CERN LHC*, JINST **3** (2008) S08004.

[75] ALICE Collaboration, *The ALICE experiment at the CERN LHC*, JINST **3** (2008) S08002.

[76] LHCb Collaboration, *The LHCb Detector at the LHC*, JINST **3** (2008) S08005.

[77] TOTEM Collaboration, *The TOTEM Experiment at the CERN Large Hadron Collider*, JINST **3** (2008) S08007.

[78] LHCf Collaboration, *The LHCf detector at the CERN Large Hadron Collider*, JINST **3** (2008) S08006.

[79] MoEDAL Collaboration, *Technical Design Report of the MoEDAL Experiment*, CERN-LHCC-2009-006. `https://cds.cern.ch/record/1181486`.

[80] ATLAS Collaboration, *Computer generated image of the whole ATLAS detector*, CERN-GE-0803012-01. `https://cds.cern.ch/record/1095924`.

[81] ATLAS Collaboration, *Computer generated image of the ATLAS inner detector*, CERN-GE-0803014-01. `http://cds.cern.ch/record/1095926`.

[82] C. Grupen and B. Shwartz, *Particle Detectors.* Cambridge University Press, 2008.

[83] ATLAS Collaboration, *Expected Performance of the ATLAS Experiment - Detector, Trigger and Physics*, `arXiv:0901.0512 [hep-ex]`.

[84] ATLAS Collaboration, *Computer Generated image of the ATLAS calorimeter*, CERN-GE-0803015-01. `http://cds.cern.ch/record/1095927`.

[85] ATLAS Collaboration, *Computer generated image of the ATLAS Muons subsystem*, CERN-GE-0803017-01. `http://cds.cern.ch/record/1095929`.

[86] ATLAS Collaboration, *Performance of the ATLAS Trigger System in 2010*, Eur. Phys. J. C **72** (2012) 1849, `arXiv:1110.1530 [hep-ex]`.

[87] ATLAS Statistics Forum, *The CL_s method: information for conference speakers*, `https://twiki.cern.ch/twiki/pub/AtlasProtected/StatisticsTools/CLsInfo.pdf`.

[88] G. Cowan et al., *Asymptotic formulae for likelihood-based tests of new physics*, Eur. Phys. J. C **71** (2011) 1554, `arXiv:1007.1727 [physics.data-an]`.

[89] A. L. Read, *Presentation of search results: the CL s technique*, Journal of Physics G: Nuclear and Particle Physics **28** (2002) 2693.

[90] ATLAS Collaboration, *Improved luminosity determination in pp collisions at $\sqrt{s} = 7$ TeV using the ATLAS detector at the LHC*, Eur. Phys. J. C **73** (2013) 2518, `arXiv:1302.4393 [hep-ex]`.

[91] ATLAS Collaboration, *Luminosity Public Results*, `https://twiki.cern.ch/twiki/bin/view/AtlasPublic/LuminosityPublicResults`.

[92] T. Sjostrand, S. Mrenna, and P. Skands, *A Brief Introduction to PYTHIA 8.1*, Comput. Phys. Comm. **178** (2008) 852, `arXiv:0710.3820 [hep-ph]`.

[93] A. Chitan et al., *Search for strongly produced supersymmetric particles in decays with leptons at $\sqrt{s} = 8$ TeV (supporting INT note - Combination)*, ATL-COM-PHYS-2013-1493. `https://cds.cern.ch/record/1624335`.

[94] P. Nason, *A new method for combining NLO QCD with shower Monte Carlo algorithms*, JHEP **0411** (2004) 040, `arXiv:hep-ph/0409146`.

[95] S. Frixione, P. Nason, and C. Oleari, *Matching NLO QCD computations with parton shower simulations: the POWHEG method*, JHEP **0711** (2007) 070, `arXiv:0709.2092 [hep-ph]`.

[96] S. Alioli et al., *A general framework for implementing NLO calculations in shower Monte Carlo programs: the POWHEG BOX*, JHEP **1006** (2010) 043, `arXiv:1002.2581 [hep-ph]`.

[97] T. Sjostrand, S. Mrenna, and P. Skands, *PYTHIA 6.4 Physics and Manual*, JHEP **0605** (2006) 026, `arXiv:hep-ph/0603175`.

[98] B. Cooper et al., *Importance of a consistent choice of α_s in the matching of AlpGen and PYTHIA*, Eur. Phys. J. C **72** (2011) 2078, `arXiv:1109.5295 [hep-ph]`.

[99] H.-L. Lai et al., *New parton distributions for collider physics*, Phys. Rev. D **82** (2010) 074024, `arXiv:1007.2241 [hep-ph]`.

[100] M. Czakon, P. Fiedler, and A. Mitov, *Total Top-Quark Pair-Production Cross Section at Hadron Colliders Through $O(\alpha_s^4)$*, Phys. Rev. Lett. **110** (2013) 252004, `arXiv:1303.6254 [hep-ph]`.

[101] M. Czakon and A. Mitov, *Top++: A Program for the Calculation of the Top-Pair*

Cross-Section at Hadron Colliders, Comput. Phys. Commun. **185** 2930, `arXiv:1112.5675 [hep-ph]`.

[102] T. Gleisberg et al., *Event generation with Sherpa 1.1*, JHEP **0902** (2009) 007, `arXiv:0811.4622 [hep-ph]`.

[103] S. Catani et al., *Vector boson production at hadron colliders: a fully exclusive QCD calculation at NNLO*, Phys. Rev. Lett. **103** (2009) 082001, `arXiv:0903.2120 [hep-ph]`.

[104] S. Catani and M. Grazzini, *An NNLO subtraction formalism in hadron collisions and its application to Higgs boson production at the LHC*, Phys. Rev. Lett. **98** (2007) 222002, `arXiv:hep-ph/0703012`.

[105] ATLAS Collaboration, *New ATLAS event generator tunes to 2010 data*, ATL-PHYS-PUB-2011-008. `http://cdsweb.cern.ch/record/1345343`.

[106] J. M. Campbell and R. K. Ellis, *An update on vector boson pair production at hadron colliders*, Phys. Rev. D **60** (1999) 113006, `arXiv:hep-ph/9905386`.

[107] J. M. Campbell, R. K. Ellis, and C. Williams, *Vector boson pair production at the LHC*, JHEP **1107** (2011) 018, `arXiv:1105.0020 [hep-ph]`.

[108] J. Alwall et al., *MadGraph 5 : Going Beyond*, JHEP **1106** (2011) 128, `arXiv:1106.0522 [hep-ph]`.

[109] J. Pumplin et al., *New generation of parton distributions with uncertainties from global QCD analysis*, JHEP **0207** (2002) 012, `arXiv:hep-ph/0201195`.

[110] J. M. Campbell and R. K. Ellis, *$t\bar{t}$ W production and decay at NLO*, JHEP **1207** (2012) 052, `arXiv:1204.5678 [hep-ph]`.

[111] A. Lazopoulos et al., *Next-to-leading order QCD corrections to $t\bar{t}Z$ production at the LHC*, Phys. Lett. B **666** (2008) 62, `arXiv:0804.2220 [hep-ph]`.

[112] N. Kidonakis, *NNLL resummation for s-channel single top quark production*, Phys. Rev. D **81** (2010) 054028, `arXiv:1001.5034 [hep-ph]`.

[113] N. Kidonakis, *Two-loop soft anomalous dimensions for single top quark associated production with a W- or H-*, Phys. Rev. D **82** (2010) 054018, `arXiv:1005.4451 [hep-ph]`.

[114] B. P. Kersevan and E. Richter-Was, *The Monte Carlo event generator AcerMC versions 2.0 to 3.8 with interfaces to PYTHIA 6.4, HERWIG 6.5 and ARIADNE 4.1*, Comput. Phys. Commun. **184** (2004) 919–985, `arXiv:hep-ph/0405247`.

[115] N. Kidonakis, *Next-to-next-to-leading-order collinear and soft gluon corrections for t-channel single top quark production*, Phys. Rev. D **83** (2011) 091503, `arXiv:1103.2792 [hep-ph]`.

[116] ATLAS Collaboration, *Further ATLAS tunes of PYTHIA 6 and Pythia 8*, ATL-PHYS-PUB-2011-014. `http://cds.cern.ch/record/1400677`.

[117] ATLAS Collaboration, *The ATLAS Simulation Infrastructure*, Eur. Phys. J. C **70** (2010) 823–874, `arXiv:1005.4568 [physics.ins-det]`.

[118] GEANT4 Collaboration, S. Agostinelli et al., *GEANT4: A simulation toolkit*, Nucl. Instrum. Meth. A **506** (2003) 250–303.

[119] ATLAS Collaboration, *The simulation principle and performance of the ATLAS fast calorimeter simulation FastCaloSim*, ATL-PHYS-PUB-2010-013. `http://cds.cern.ch/record/1300517`.

[120] ATLAS SUSY Group, *Release 17 (8 TeV) object selection recommendations*, `https://twiki.cern.ch/twiki/bin/view/AtlasProtected/SusyObjectDefinitionsr178TeV`.

[121] ATLAS Collaboration, *Jet energy measurement and its systematic uncertainty in proton-proton collisions at $\sqrt{s} = 7$ TeV with the ATLAS detector*, Eur.Phys.J. C **75** (2015) 17, `arXiv:1406.0076 [hep-ex]`.

[122] M. Cacciari, G. P. Salam, and G. Soyez, *The anti-k_t jet clustering algorithm*, JHEP **0804** (2008) 063, `arXiv:0802.1189 [hep-ph]`.

[123] ATLAS Collaboration, *Characterisation and mitigation of beam-induced backgrounds observed in the ATLAS detector during the 2011 proton-proton run*, JINST **8** (2013) P07004, `arXiv:1303.0223 [hep-ex]`.

[124] ATLAS Collaboration, *Selection of jets produced in proton-proton collisions with the ATLAS detector using 2011 data*, ATLAS-CONF-2012-020. `http://cds.cern.ch/record/1430034`.

[125] ATLAS Collaboration, *Calibration of the performance of b-tagging for c and light-flavour jets in the 2012 ATLAS data*, ATLAS-CONF-2014-046. `http://cds.cern.ch/record/1741020`.

[126] ATLAS Collaboration, *Muon reconstruction efficiency and momentum resolution of the ATLAS experiment in proton-proton collisions at $\sqrt{s}$=7 TeV in 2010*, Eur. Phys. J. C **74** (2014) 3034, `arXiv:1404.4562 [hep-ex]`.

[127] ATLAS Collaboration, *Search for supersymmetry in final states with jets, missing*

transverse momentum and one isolated lepton in sqrts = 7 TeV pp collisions using 1 fb^{-1} of ATLAS data, Phys. Rev. D **85** (2012) 012006, `arXiv:1109.6606 [hep-ex]`.

[128] ATLAS Collaboration, *Electron reconstruction and identification efficiency measurements with the ATLAS detector using the 2011 LHC proton-proton collision data*, Eur. Phys. J. C **74** (2014) 2941, `arXiv:1404.2240 [hep-ex]`.

[129] ATLAS Collaboration, *Performance of Missing Transverse Momentum Reconstruction in Proton-Proton Collisions at 7 TeV with ATLAS*, Eur. Phys. J. C **72** (2012) 1844, `arXiv:1108.5602 [hep-ex]`.

[130] ATLAS Collaboration, *Measurements of the photon identification efficiency with the ATLAS detector using 4.9 fb^{-1} of pp collision data collected in 2011*, ATLAS-CONF-2012-123. `https://cds.cern.ch/record/1473426`.

[131] A. Chitan et al., *Search for strongly produced supersymmetric particles in decays with leptons at* $\sqrt{s} = 8$ TeV *(supporting INT note - 1 hard lepton)*, ATL-COM-PHYS-2013-1517. `https://cds.cern.ch/record/1626588`.

[132] E. Torro et al., *Search for supersymmetry in events with a Z boson and large missing transverse momentum with the full 2012 ATLAS dataset (supporting INT note - Z + MET)*, ATL-COM-PHYS-2013-1565. `https://cds.cern.ch/record/1630804`.

[133] W. J. Fawcett et al., *Constraints on promptly decaying supersymmetric particles with lepton-number- and R-parity-violating interactions using Run I ATLAS data*, ATL-COM-PHYS-2014-1019. `http://cds.cern.ch/record/1749965`.

[134] ATLAS Collaboration, *Auxiliary figures and tables related to the paper 'Search for supersymmetry in events containing a same-flavour opposite-sign dilepton pair, jets, and large missing transverse momentum in $\sqrt{s} = 8$ TeV pp collisions with the ATLAS detector'*, `https://atlas.web.cern.ch/Atlas/GROUPS/PHYSICS/PAPERS/SUSY-2014-10`.

[135] A. Djouadi, J.-L. Kneur, and G. Moultaka, *SuSpect: A Fortran code for the supersymmetric and Higgs particle spectrum in the MSSM*, Comput. Phys. Commun. **176** (2007) 426–455, `arXiv:hep-ph/0211331`.

[136] M. Muhlleitner, A. Djouadi, and Y. Mambrini, *SDECAY: A Fortran code for the decays of the supersymmetric particles in the MSSM*, Comput. Phys. Commun. **168** (2005) 46–70, `arXiv:hep-ph/0311167`.

[137] A. Sherstnev and R. Thorne, *Parton Distributions for LO Generators*, Eur. Phys. J. C **55** (2008) 553–575, `arXiv:0711.2473 [hep-ph]`.

[138] Beenakker et al., *Squark and gluino production at hadron colliders*, Nucl. Phys. B **492** (1997) 51–103, `arXiv:hep-ph/9610490`.

[139] A. Kulesza and L. Motyka, *Threshold resummation for squark-antisquark and gluino-pair production at the LHC*, Phys. Rev. Lett. **102** (2009) 111802, `arXiv:0807.2405 [hep-ph]`.

[140] A. Kulesza and L. Motyka, *Soft gluon resummation for the production of gluino-gluino and squark-antisquark pairs at the LHC*, Phys. Rev. D **80** (2009) 095004, `arXiv:0905.4749 [hep-ph]`.

[141] W. Beenakker et al., *Soft-gluon resummation for squark and gluino hadroproduction*, JHEP **0912** (2009) 041, `arXiv:0909.4418 [hep-ph]`.

[142] W. Beenakker et al., *Squark and gluino hadroproduction*, Int. J. Mod. Phys. A **26** (2011) 2637–2664, `arXiv:1105.1110 [hep-ph]`.

[143] M. Krämer et al., *Supersymmetry production cross sections in pp collisions at $\sqrt{s} = 7$ TeV*, `arXiv:1206.2892 [hep-ph]`.

[144] ATLAS SUSY Group, *SUSY Signal Uncertainties*, `https://twiki.cern.ch/twiki/bin/view/AtlasProtected/SUSYSignalUncertainties`.

[145] ATLAS Collaboration, *Search for supersymmetry in events with four or more leptons in $\sqrt{s} = 8$ TeV pp collisions with the ATLAS detector*, Phys. Rev. D **90** (2014) 052001, `arXiv:1405.5086 [hep-ex]`.

[146] ATLAS Collaboration, *Search for supersymmetry at $\sqrt{s} = 8$ TeV in final states with jets and two same-sign leptons or three leptons with the ATLAS detector*, JHEP **06** (2014) 35, `arXiv:1404.2500 [hep-ex]`.

[147] G. Fletcher et al., *A data-driven method for measuring the mismeasured jet background for missing transverse energy searches in multijet, Z+jet and γ+jet events*, ATL-COM-PHYS-2014-1243. `http://cds.cern.ch/record/1950335`.

[148] ATLAS Collaboration, *Jet energy resolution in proton-proton collisions at $\sqrt{s} = 7$ TeV recorded in 2010 with the ATLAS detector*, Eur.Phys.J. C **73** (2013) 2306, `arXiv:1210.6210 [hep-ex]`.

[149] ATLAS Collaboration, *Measurement of the top quark-pair production cross section with ATLAS in pp collisions at $\sqrt{s} = 7$ TeV*, Eur. Phys. J. C **71** (2011) 1577, `arXiv:1012.1792 [hep-ex]`.

[150] S. Asai et al., *Search for Supersymmetry with jets and missing transverse momentum and one lepton at sqrts = 7 TeV (supporting INT note)*, ATL-PHYS-INT-2011-008. `https://cds.cern.ch/record/1327968`.

[151] C. Clement et al., *Searching for direct gaugino production and direct slepton*

production with two leptons and missing transverse momentum at sqrts $= 8$ *TeV*, ATL-COM-PHYS-2012-1437. `https://cds.cern.ch/record/1482107`.

[152] A. Chitan et al., *Search for strongly produced supersymmetric particles in decays with leptons at* $\sqrt{s} = 8$ *TeV (supporting INT note)*, ATL-PHYS-INT-2013-017. `https://cds.cern.ch/record/1610179`.

[153] ATLAS SUSY Group, *Fake lepton background estimation*, `https://twiki.cern.ch/twiki/bin/view/AtlasProtected/BackgroundStudies#Fake_lepton_background_estimatio`.

[154] ATLAS SUSY Group, *SUSY Systematic Uncertainties 2012*, `https://twiki.cern.ch/twiki/bin/view/AtlasProtected/SUSYSystematicUncertainties2012`.

[155] E. S. Kuwertz and Z. L. Marshall, *Search for strongly produced supersymmetric particles in decays with at least two leptons at* $\sqrt{s} = 8$ *TeV with the ATLAS detector*, ATL-COM-PHYS-2013-1539. `https://cds.cern.ch/record/1627071`.

[156] ATLAS Jet/EtMiss Performance Group, *Jet Uncertainties 2012: 2012 data recommendations*, `https://twiki.cern.ch/twiki/bin/view/AtlasProtected/JetUncertainties2012`.

[157] ATLAS Collaboration, *Measurement of the muon reconstruction performance of the ATLAS detector using 2011 and 2012 LHC proton–proton collision data*, Eur. Phys. J. C **74** (2014) 3130, `arXiv:1407.3935 [hep-ex]`.

[158] M. Botje et al., *The PDF4LHC Working Group Interim Recommendations*, `arXiv:1101.0538 [hep-ph]`.

[159] S. Frixione and B. R. Webber, *Matching NLO QCD computations and parton shower simulations*, JHEP **0206** (2002) 029, `arXiv:hep-ph/0204244`.

[160] G. Corcella et al., *HERWIG 6: An event generator for hadron emission reactions with interfering gluons (including supersymmetric processes)*, JHEP **0101** (2001) 010, `arXiv:hep-ph/0011363`.

[161] J. Butterworth, J. R. Forshaw, and M. Seymour, *Multiparton interactions in photoproduction at HERA*, Z. Phys. C **72** (1996) 637–646, `arXiv:hep-ph/9601371`.

[162] CMS Collaboration, *Search for physics beyond the standard model in events with a Z boson, jets, and missing transverse energy in pp collisions at* $\sqrt{s} = 7$ *TeV*, Phys.Lett. **B716** (2012) 260–284, `arXiv:1204.3774 [hep-ex]`.

[163] ATLAS Jet/EtMiss Performance Group, *TrackMET 2011/2012*, `http://twiki.cern.ch/twiki/bin/viewauth/AtlasProtected/TrackMET`.

[164] M. Baak et al., *HistFitter software framework for statistical data analysis*, Eur. Phys. J. C **75** (2015) 153, `arXiv:1410.1280 [hep-ex]`.

[165] CMS Collaboration, *Search for physics beyond the standard model in events with two leptons, jets, and missing transverse momentum in pp collisions at $\sqrt{s} = 8$ TeV*, JHEP **1504** (2015) 124, `arXiv:1502.06031 [hep-ex]`.

[166] ATLAS Collaboration, *Search for massive, long-lived particles using multitrack displaced vertices or displaced lepton pairs in pp collisions at $\sqrt{s} = 8$ TeV with the ATLAS detector*, `arXiv:1504.05162 [hep-ex]`.

[167] ATLAS Collaboration, *A search for $B - L$ R-Parity violating scalar top decays in $\sqrt{s} = 8$ TeV pp collisions with the ATLAS experiment*, ATLAS-CONF-2015-015. `http://cds.cern.ch/record/2002885`.

[168] M. Bähr et al., *Herwig++ physics and manual*, Eur. Phys. J. C **58** (2008) 639–707, `arXiv:0803.0883 [hep-ph]`.

[169] P. M. Nadolsky et al., *Implications of CTEQ global analysis for collider observables*, Phys. Rev. D **78** (2008) 013004, `arXiv:0802.0007 [hep-ph]`.

[170] S. Gieseke and A. Rohr, *Colour reconnections in Herwig++*, Eur. Phys. J. C **72** (2012) 2225, `arXiv:1206.0041 [hep-ph]`.

[171] ATLAS SUSY Group, *SUSY Mad Graph Uncertainty*, `https://twiki.cern.ch/twiki/bin/viewauth/AtlasProtected/SUSYMadGraphUncertainty`.

[172] ATLAS Collaboration, *Search for squarks and gluinos with the ATLAS detector in final states with jets and missing transverse momentum using $\sqrt{s} = 8$ TeV proton–proton collision data*, JHEP **09** (2014) 176, `arXiv:1405.7875 [hep-ex]`.

[173] ATLAS Collaboration, *Search for new phenomena in final states with large jet multiplicities and missing transverse momentum at $\sqrt{s} = 8$ TeV proton-proton collisions using the ATLAS experiment*, JHEP **10** (2013) 130, `arXiv:1308.1841 [hep-ex]`.

[174] J. Romao et al., *A Supersymmetric solution to the solar and atmospheric neutrino problems*, Phys.Rev. **D61** (2000) 071703, `arXiv:hep-ph/9907499`.

[175] W. Porod, *SPheno, a program for calculating supersymmetric spectra, SUSY particle decays and SUSY particle production at e^+e^- colliders*, Comput. Phys. Commun. **153** (2003) 275–315, `arXiv:hep-ph/0301101`.

[176] W. Porod and F. Staub, *SPheno 3.1: Extensions including flavour, CP-phases and models beyond the MSSM*, Comput. Phys. Commun. **183** (2012) 2458–2469, `arXiv:1104.1573 [hep-ph]`.

[177] LHC SUSY Cross Section Working Group, *SUSY Cross Sections*, `https://twiki.cern.ch/twiki/bin/view/LHCPhysics/SUSYCrossSections`.

[178] C. Borschensky et al., *Squark and gluino production cross sections in pp collisions at* $\sqrt{s} = 13, 14, 33$ *and 100 TeV*, Eur. Phys. J. C **74** (2014) 3174, `arXiv:1407.5066 [hep-ph]`.

[179] ATLAS Collaboration, *Expected sensitivity studies for gluino and squark searches using the early LHC 13 TeV Run-2 dataset with the ATLAS experiment*, ATL-PHYS-PUB-2015-005. `https://cds.cern.ch/record/2002608`.

A Overview over the Monte-Carlo datasets

In this appendix, the details about the official ATLAS MC samples used in this thesis can be found. The datasets are characterised by their ID number. The cross-sections σ, corrected for NLO effects by the application of k-factors in some cases, and the generator efficiencies when different from one are also indicated in the tables for all samples. In addition, it is specified if a full detector simulation with GEANT4 or a fast simulation was applied.

ID	Name	Det. sim.	σ [pb]
117050	ttbar	fast	253 × 0.543

Table A.1: The $t\bar{t}$ Monte-Carlo samples used in this thesis. σ is a NLO+NLL cross-section times the fraction of none hadronic top decay.

ID	Name	Det. sim.	σ [pb]
110101	singletop_tchan_l	full	25.8 × 1.10
110119	st_schan_lep	fast	1.64 × 1.10
110141	st_Wtchan_dilepton_DR	fast	2.15 × 1.09
179991	tZ_Wtchan_Zll	fast	0.0041
179992	tZ_stchan_Zll	fast	0.0312

Table A.2: The single top and $W/Z{+}t$ Monte-Carlo samples used in this thesis. σ is a LO cross-section times k-factor where applicable.

ID	Name	Det. sim.	σ [pb]
119353	ttbarW	full	0.104 × 1.17
174830	ttbarWjExcl	full	0.0534 × 1.17
174831	ttbarWjjIncl	full	0.0415 × 1.17
119355	ttbarZ	full	0.0677 × 1.35
174832	ttbarZjExcl	full	0.0454 × 1.35
174833	ttbarZjjIncl	full	0.0398 × 1.35
119583	ttbarWW	full	0.00092

Table A.3: The $t\bar{t}{+}W/Z$ and $t\bar{t}{+}WW$ Monte-Carlo samples used in this thesis. σ is a LO cross-section times k-factor where applicable.

ID	Name	Det. sim.	σ [pb]
126928	WpWm_ee	full	$0.598 \times 1.08 \times 1$
126929	WpWm_me	full	$0.597 \times 1.08 \times 1$
126930	WpWm_te	full	$0.598 \times 1.08 \times 1$
126931	WpWm_em	full	$0.598 \times 1.08 \times 1$
126932	WpWm_mm	full	$0.597 \times 1.08 \times 1$
126933	WpWm_tm	full	$0.597 \times 1.08 \times 1$
126934	WpWm_et	full	$0.597 \times 1.08 \times 1$
126935	WpWm_mt	full	$0.598 \times 1.08 \times 1$
126936	WpWm_tt	full	$0.598 \times 1.08 \times 1$
126937	ZZ_4e_mll4_2pt5	full	$0.0769 \times 1 \times 0.908$
126938	ZZ_2e2mu_mll4_2pt5	full	$0.176 \times 1 \times 0.827$
126939	ZZ_2e2tau_mll4_2pt5	full	$0.175 \times 1 \times 0.583$
126940	ZZ_4mu_mll4_2pt5	full	$0.0769 \times 1 \times 0.912$
126941	ZZ_2mu2tau_mll4_2pt5	full	$0.175 \times 1 \times 0.587$
126942	ZZ_4tau_mll4_2pt5	full	$0.0769 \times 1 \times 0.106$
126949	ZZllnunu_ee_mll4	full	$0.0543 \times 3 \times 1$
126950	ZZllnunu_mm_mll4	full	$0.0543 \times 3 \times 1$
126951	ZZllnunu_tt_mll4	full	$0.0543 \times 3 \times 1$
129477	WZ_Wm11Z11_mll0p250d0_2LeptonFilter5	full	$1.41 \times 1.12 \times 0.295$
129478	WZ_Wm11Z13_mll0p4614d0_2LeptonFilter5	full	$0.938 \times 1.12 \times 0.352$
129479	WZ_Wm11Z15_mll3p804d0_2LeptonFilter5	full	$0.175 \times 1.12 \times 0.167$
129480	WZ_Wm13Z11_mll0p250d0_2LeptonFilter5	full	$1.40 \times 1.12 \times 0.294$
129481	WZ_Wm13Z13_mll0p4614d0_2LeptonFilter5	full	$0.954 \times 1.12 \times 0.351$
129482	WZ_Wm13Z15_mll3p804d0_2LeptonFilter5	full	$0.175 \times 1.12 \times 0.169$
129483	WZ_Wm15Z11_mll0p250d0_2LeptonFilter5	full	$1.40 \times 1.12 \times 0.143$
129484	WZ_Wm15Z13_mll0p4614d0_2LeptonFilter5	full	$0.938 \times 1.12 \times 0.183$
129485	WZ_Wm15Z15_mll3p804d0_2LeptonFilter5	full	$0.172 \times 1.12 \times 0.0585$
129486	WZ_W11Z11_mll0p250d0_2LeptonFilter5	full	$0.980 \times 1.14 \times 0.297$
129487	WZ_W11Z13_mll0p4614d0_2LeptonFilter5	full	$0.639 \times 1.14 \times 0.353$
129488	WZ_W11Z15_mll3p804d0_2LeptonFilter5	full	$0.113 \times 1.14 \times 0.160$
129489	WZ_W13Z11_mll0p250d0_2LeptonFilter5	full	$0.936 \times 1.14 \times 0.298$
129490	WZ_W13Z13_mll0p4614d0_2LeptonFilter5	full	$0.649 \times 1.14 \times 0.354$
129491	WZ_W13Z15_mll3p804d0_2LeptonFilter5	full	$0.113 \times 1.14 \times 0.160$
129492	WZ_W15Z11_mll0p250d0_2LeptonFilter5	full	$0.936 \times 1.14 \times 0.148$
129493	WZ_W15Z13_mll0p4614d0_2LeptonFilter5	full	$0.639 \times 1.14 \times 0.187$
129494	WZ_W15Z15_mll3p804d0_2LeptonFilter5	full	$0.111 \times 1.14 \times 0.0567$

Table A.4: The WW,WZ and ZZ Monte-Carlo samples used in this thesis. σ is a LO cross-section times k-factor times event filter efficiency of the W/Z decay.

ID	Name	Det. sim.	σ [pb]
147910	jetjet_JZ0W	full	$7.18 \cdot 10^{10}$
147911	jetjet_JZ1W	full	$9.26 \cdot 10^{6}$
147912	jetjet_JZ2W	full	$1.05 \cdot 10^{5}$
147913	jetjet_JZ3W	full	$6.63 \cdot 10^{2}$
147914	jetjet_JZ4W	full	4.56
147915	jetjet_JZ5W	full	$8.55 \cdot 10^{-2}$
147916	jetjet_JZ6W	full	$1.95 \cdot 10^{-3}$
147917	jetjet_JZ7W	full	$5.93 \cdot 10^{-4}$

Table A.5: The dijet Monte-Carlo samples used in this thesis. σ is a LO cross-section including the the generator filter efficiency.

ID	Name	Det. sim.	σ [pb]
167749	ZeeMassiveCBPt0_BFilter	fast	1.11 × 1.12 × 0.0280
167750	ZeeMassiveCBPt0_CFilterBVeto	fast	1.11 × 1.12 × 0.283
167751	ZeeMassiveCBPt0_CVetoBVeto	fast	1.11 × 1.12 × 0.686
167752	ZmumuMassiveCBPt0_BFilter	fast	1.11 × 1.12 × 0.0280
167753	ZmumuMassiveCBPt0_CFilterBVeto	fast	1.11 × 1.12 × 0.283
167754	ZmumuMassiveCBPt0_CVetoBVeto	fast	1.11 × 1.12 × 0.690
167755	ZtautauMassiveCBPt0_BFilter	fast	1.11 × 1.12 × 0.0278
167756	ZtautauMassiveCBPt0_CFilterBVeto	fast	1.11 × 1.12 × 0.284
167757	ZtautauMassiveCBPt0_CVetoBVeto	fast	1.11 × 1.12 × 0.689

Table A.6: The $Z+$jets Monte-Carlo samples used in this thesis. σ is the cross-section times k-factor times event filter efficiency. These samples are used in combination with the samples sliced in Z p_{T} defined in Tab. A.7 and A.8, where events with $p_{\mathrm{T}}(Z) > 40$ GeV and with truth $H_{\mathrm{T}} < 500\,\mathrm{GeV}$ are omitted to avoid duplication.

ID	Name	Det. sim.	σ [pb]
180543	ZeeMassiveCBPt40_70_BFilter	fast	$70.5 \times 1.12 \times 0.0706$
180544	ZeeMassiveCBPt40_70_CFilterBVeto	fast	$70.5 \times 1.12 \times 0.342$
180545	ZeeMassiveCBPt40_70_CVetoBVeto	fast	$70.4 \times 1.12 \times 0.588$
180546	ZmumuMassiveCBPt40_70_BFilter	fast	$70.5 \times 1.12 \times 0.0707$
180547	ZmumuMassiveCBPt40_70_CFilterBVeto	fast	$70.5 \times 1.12 \times 0.341$
180548	ZmumuMassiveCBPt40_70_CVetoBVeto	fast	$70.5 \times 1.12 \times 0.588$
180549	ZtautauMassiveCBPt40_70_BFilter	fast	$70.4 \times 1.12 \times 0.0709$
180550	ZtautauMassiveCBPt40_70_CFilterBVeto	fast	$70.5 \times 1.12 \times 0.342$
180551	ZtautauMassiveCBPt40_70_CVetoBVeto	fast	$70.5 \times 1.12 \times 0.588$
167797	ZeeMassiveCBPt70_140_BFilter	fast	$29.5 \times 1.12 \times 0.0825$
167798	ZeeMassiveCBPt70_140_CFilterBVeto	fast	$29.5 \times 1.12 \times 0.355$
167799	ZeeMassiveCBPt70_140_CVetoBVeto	fast	$29.5 \times 1.12 \times 0.563$
167800	ZmumuMassiveCBPt70_140_BFilter	fast	$29.5 \times 1.12 \times 0.0826$
167801	ZmumuMassiveCBPt70_140_CFilterBVeto	fast	$29.4 \times 1.12 \times 0.355$
167802	ZmumuMassiveCBPt70_140_CVetoBVeto	fast	$29.5 \times 1.12 \times 0.562$
167803	ZtautauMassiveCBPt70_140_BFilter	full	$29.5 \times 1.12 \times 0.0826$
167804	ZtautauMassiveCBPt70_140_CFilterBVeto	full	$29.5 \times 1.12 \times 0.355$
167805	ZtautauMassiveCBPt70_140_CVetoBVeto	full	$29.5 \times 1.12 \times 0.562$
167809	ZeeMassiveCBPt140_280_BFilter	fast	$3.99 \times 1.12 \times 0.0952$
167810	ZeeMassiveCBPt140_280_CFilterBVeto	fast	$3.98 \times 1.12 \times 0.369$
167811	ZeeMassiveCBPt140_280_CVetoBVeto	fast	$3.99 \times 1.12 \times 0.534$
167812	ZmumuMassiveCBPt140_280_BFilter	fast	$3.98 \times 1.12 \times 0.0954$
167813	ZmumuMassiveCBPt140_280_CFilterBVeto	fast	$3.99 \times 1.12 \times 0.370$
167814	ZmumuMassiveCBPt140_280_CVetoBVeto	fast	$3.98 \times 1.12 \times 0.534$
167815	ZtautauMassiveCBPt140_280_BFilter	full	$3.99 \times 1.12 \times 0.0958$
167816	ZtautauMassiveCBPt140_280_CFilterBVeto	full	$3.99 \times 1.12 \times 0.370$
167817	ZtautauMassiveCBPt140_280_CVetoBVeto	full	$3.99 \times 1.12 \times 0.533$
167821	ZeeMassiveCBPt280_500_BFilter	full	$0.242 \times 1.12 \times 0.109$
167822	ZeeMassiveCBPt280_500_CFilterBVeto	full	$0.241 \times 1.12 \times 0.387$
167823	ZeeMassiveCBPt280_500_CVetoBVeto	full	$0.242 \times 1.12 \times 0.506$
167824	ZmumuMassiveCBPt280_500_BFilter	full	$0.242 \times 1.12 \times 0.108$
167825	ZmumuMassiveCBPt280_500_CFilterBVeto	full	$0.242 \times 1.12 \times 0.386$
167826	ZmumuMassiveCBPt280_500_CVetoBVeto	full	$0.243 \times 1.12 \times 0.505$
167827	ZtautauMassiveCBPt280_500_BFilter	full	$0.241 \times 1.12 \times 0.107$
167828	ZtautauMassiveCBPt280_500_CFilterBVeto	full	$0.241 \times 1.12 \times 0.385$
167829	ZtautauMassiveCBPt280_500_CVetoBVeto	full	$0.241 \times 1.12 \times 0.507$
167833	ZeeMassiveCBPt500_BFilter	full	$0.0132 \times 1.12 \times 0.116$
167834	ZeeMassiveCBPt500_CFilterBVeto	full	$0.0135 \times 1.12 \times 0.398$
167835	ZeeMassiveCBPt500_CVetoBVeto	full	$0.0133 \times 1.12 \times 0.485$
167836	ZmumuMassiveCBPt500_BFilter	full	$0.0132 \times 1.12 \times 0.114$
167837	ZmumuMassiveCBPt500_CFilterBVeto	full	$0.0135 \times 1.12 \times 0.399$
167838	ZmumuMassiveCBPt500_CVetoBVeto	full	$0.0133 \times 1.12 \times 0.487$
167839	ZtautauMassiveCBPt500_BFilter	full	$0.0132 \times 1.12 \times 0.115$
167840	ZtautauMassiveCBPt500_CFilterBVeto	full	$0.0133 \times 1.12 \times 0.393$
167841	ZtautauMassiveCBPt500_CVetoBVeto	full	$0.0133 \times 1.12 \times 0.486$

Table A.7: The $Z+$jets Monte-Carlo samples used in this thesis. σ is the cross-section times k-factor times event filter efficiency. These samples are used in combination with the samples defined in Tab. A.6 and A.8, where events with truth $H_\mathrm{T} < 500\,\mathrm{GeV}$ are omitted to avoid duplication

ID	Name	Det. sim.	σ [pb]
204659	ZeeMassiveCBPt0_40_HT500	full	$1006 \times 1.12 \times 3.75{\cdot}10^{-4}$
204660	ZeeMassiveCBPt40_70_HT500	full	$70.5 \times 1.12 \times 4.36{\cdot}10^{-3}$
204661	ZeeMassiveCBPt70_140_HT500	full	$29.5 \times 1.12 \times 3.30{\cdot}10^{-2}$
204662	ZeeMassiveCBPt140_280_HT500	full	$4.01 \times 1.12 \times 0.632$
204663	ZmumuMassiveCBPt0_40_HT500	full	$1110 \times 1.12 \times 1.20{\cdot}10^{-3}$
204664	ZmumuMassiveCBPt40_70_HT500	full	$70.5 \times 1.12 \times 1.85{\cdot}10^{-3}$
204665	ZmumuMassiveCBPt70_140_HT500	full	$29.5 \times 1.12 \times 1.02{\cdot}10^{-2}$
204666	ZmumuMassiveCBPt140_280_HT500	full	$3.99 \times 1.12 \times 0.137$

Table A.8: The $Z +$jets Monte-Carlo samples used in this thesis. σ is the cross-section times k-factor times event filter efficiency. A generator level cut on truth $H_\mathrm{T} > 500\,\mathrm{GeV}$ is applied to gain statistics in the high H_T and high $E_\mathrm{T}^\mathrm{miss}$ regions. These samples are used in combination with the samples defined in Tab. A.6 and A.7.

ID	Name	Det. sim.	σ [pb]
173041	DYeeM08to15	fast	92.2
173042	DYeeM15to40	fast	279
173043	DYmumuM08to15	fast	92.1
173044	DYmumuM15to40	fast	279
173045	DYtautauM08to15	full	92.1
173046	DYtautauM15to40	full	279

Table A.9: The Drell-Yan Monte-Carlo samples used in this thesis. σ is the cross-section times k-factor.

ID	Name	Det. sim.	σ [pb]
167740	WenuMassiveCBPt0_BFilter	fast	$11.0 \times 1.11 \times 0.0128$
167741	WenuMassiveCBPt0_CJetFilterBVeto	fast	$11.0 \times 1.11 \times 0.0490$
167742	WenuMassiveCBPt0_CJetVetoBVeto	fast	$11.0 \times 1.11 \times 0.938$
167743	WmunuMassiveCBPt0_BFilter	fast	$11.0 \times 1.11 \times 0.0128$
167744	WmunuMassiveCBPt0_CJetFilterBVeto	fast	$11.0 \times 1.11 \times 0.0425$
167745	WmunuMassiveCBPt0_CJetVetoBVeto	fast	$11.0 \times 1.11 \times 0.945$
167746	WtaunuMassiveCBPt0_BFilter	fast	$11.0 \times 1.11 \times 0.0128$
167747	WtaunuMassiveCBPt0_CJetFilterBVeto	fast	$11.0 \times 1.11 \times 0.0461$
167748	WtaunuMassiveCBPt0_CJetVetoBVeto	fast	$11.0 \times 1.11 \times 0.941$

Table A.10: The $W +$ jets Monte-Carlo samples used in this thesis. σ is the cross-section times k-factor times event filter efficiency. These samples are used in combination with the samples sliced in W p_T defined in Tab. A.11, where events with $p_\mathrm{T}(W) > 40$ GeV are omitted to avoid duplication.

ID	Name	Det. sim.	σ [pb]
180534	WenuMassiveCBPt40_70_BFilter	fast	653 × 1.11 × 0.0345
180535	WenuMassiveCBPt40_70_CJetFilterBVeto	fast	653 × 1.11 × 0.171
180536	WenuMassiveCBPt40_70_CJetVetoBVeto	fast	653 × 1.11 × 0.793
180537	WmunuMassiveCBPt40_70_BFilter	fast	653 × 1.11 × 0.0346
180538	WmunuMassiveCBPt40_70_CJetFilterBVeto	fast	653 × 1.11 × 0.166
180539	WmunuMassiveCBPt40_70_CJetVetoBVeto	fast	653 × 1.11 × 0.800
180540	WtaunuMassiveCBPt40_70_BFilter	fast	653 × 1.11 × 0.0346
180541	WtaunuMassiveCBPt40_70_CJetFilterBVeto	fast	653 × 1.11 × 0.169
180542	WtaunuMassiveCBPt40_70_CJetVetoBVeto	fast	653 × 1.11 × 0.796
167761	WenuMassiveCBPt70_140_BFilter	fast	251 × 1.11 × 0.0459
167762	WenuMassiveCBPt70_140_CJetFilterBVeto	fast	251 × 1.11 × 0.201
167763	WenuMassiveCBPt70_140_CJetVetoBVeto	fast	250 × 1.11 × 0.753
167764	WmunuMassiveCBPt70_140_BFilter	fast	251 × 1.11 × 0.0459
167765	WmunuMassiveCBPt70_140_CJetFilterBVeto	fast	251 × 1.11 × 0.199
167766	WmunuMassiveCBPt70_140_CJetVetoBVeto	fast	251 × 1.11 × 0.759
167767	WtaunuMassiveCBPt70_140_BFilter	full	251 × 1.11 × 0.0459
167768	WtaunuMassiveCBPt70_140_CJetFilterBVeto	full	251 × 1.11 × 0.199
167769	WtaunuMassiveCBPt70_140_CJetVetoBVeto	full	251 × 1.11 × 0.755
167770	WenuMassiveCBPt140_280_BFilter	fast	31.2 × 1.11 × 0.0632
167771	WenuMassiveCBPt140_280_CJetFilterBVeto	fast	31.2 × 1.11 × 0.222
167772	WenuMassiveCBPt140_280_CJetVetoBVeto	fast	31.1 × 1.11 × 0.715
167773	WmunuMassiveCBPt140_280_BFilter	fast	31.2 × 1.11 × 0.0631
167774	WmunuMassiveCBPt140_280_CJetFilterBVeto	fast	31.2 × 1.11 × 0.216
167775	WmunuMassiveCBPt140_280_CJetVetoBVeto	fast	31.2 × 1.11 × 0.720
167776	WtaunuMassiveCBPt140_280_BFilter	full	31.2 × 1.11 × 0.0631
167777	WtaunuMassiveCBPt140_280_CJetFilterBVeto	full	31.2 × 1.11 × 0.220
167778	WtaunuMassiveCBPt140_280_CJetVetoBVeto	full	31.2 × 1.11 × 0.716
167779	WenuMassiveCBPt280_500_BFilter	full	1.84 × 1.11 × 0.0829
167780	WenuMassiveCBPt280_500_CJetFilterBVeto	full	1.84 × 1.11 × 0.235
167781	WenuMassiveCBPt280_500_CJetVetoBVeto	full	1.84 × 1.11 × 0.682
167782	WmunuMassiveCBPt280_500_BFilter	full	1.84 × 1.11 × 0.0829
167783	WmunuMassiveCBPt280_500_CJetFilterBVeto	full	1.84 × 1.11 × 0.228
167784	WmunuMassiveCBPt280_500_CJetVetoBVeto	full	1.84 × 1.11 × 0.688
167785	WtaunuMassiveCBPt280_500_BFilter	full	1.84 × 1.11 × 0.0830
167786	WtaunuMassiveCBPt280_500_CJetFilterBVeto	full	1.84 × 1.11 × 0.233
167787	WtaunuMassiveCBPt280_500_CJetVetoBVeto	full	1.84 × 1.11 × 0.684
167788	WenuMassiveCBPt500_BFilter	full	0.102 × 1.11 × 0.100
167789	WenuMassiveCBPt500_CJetFilterBVeto	full	0.101 × 1.11 × 0.244
167790	WenuMassiveCBPt500_CJetVetoBVeto	full	0.101 × 1.11 × 0.657
167791	WmunuMassiveCBPt500_BFilter	full	0.102 × 1.11 × 0.100
167792	WmunuMassiveCBPt500_CJetFilterBVeto	full	0.102 × 1.11 × 0.239
167793	WmunuMassiveCBPt500_CJetVetoBVeto	full	0.102 × 1.11 × 0.658
167794	WtaunuMassiveCBPt500_BFilter	full	0.102 × 1.11 × 0.0997
167795	WtaunuMassiveCBPt500_CJetFilterBVeto	full	0.101 × 1.11 × 0.242
167796	WtaunuMassiveCBPt500_CJetVetoBVeto	full	0.102 × 1.11 × 0.660

Table A.11: The W + jets Monte-Carlo samples used in this thesis. σ is the cross-section times k-factor times event filter efficiency. These samples are used in combination with the samples defined in Tab. A.10.

B Details about the GGM model

The cross-sections of all generated signal points of the GGM model used for the optimization and interpretation of the Z+jets+E_T^{miss} analysis can be found in the first part of this appendix. In the second part, the observed and expected CL_s values for the individual signal point can be found as well as details about the signal acceptance and efficiency.

Signal cross-sections and uncertainties

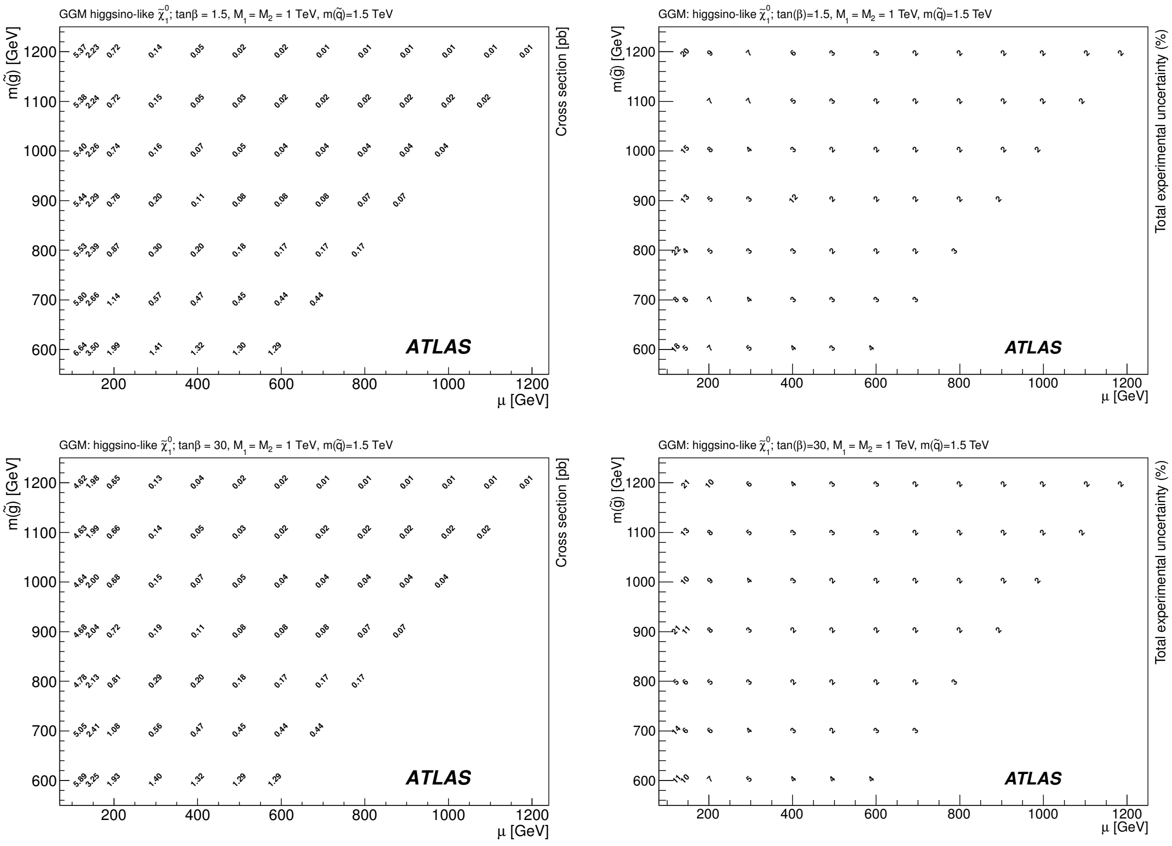

Figure B.1: Signal cross-section (left) and its total experimental uncertainty (right) for the GGM model with $\tan\beta = 1.5$ (top) and $\tan\beta = 30$ (bottom) [134]

CL_s values, signal acceptance and efficiency

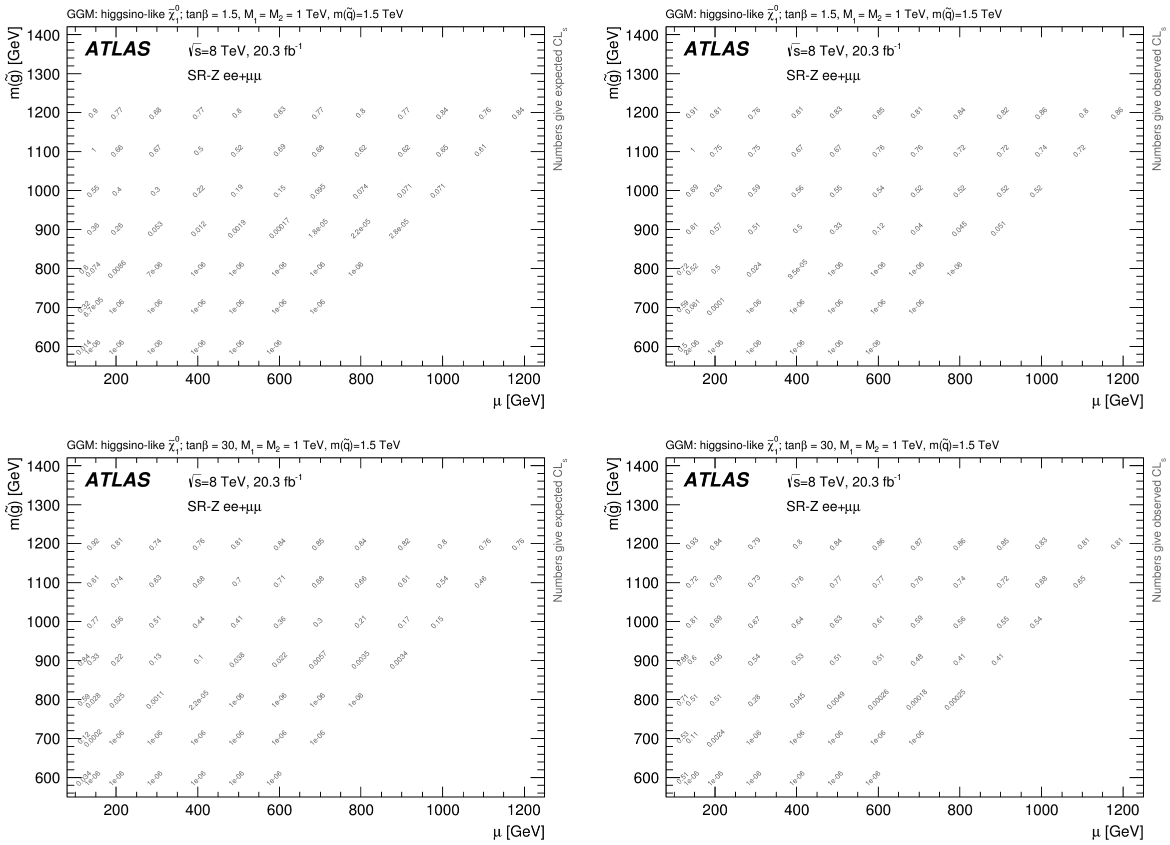

Figure B.2: Expected (left) and observed (right) CL_s values retrieved from the interpretation of the Z+jets+E_T^{miss} results for the GGM model with $\tan\beta = 1.5$ (top) and $\tan\beta = 30$ (bottom) [134]

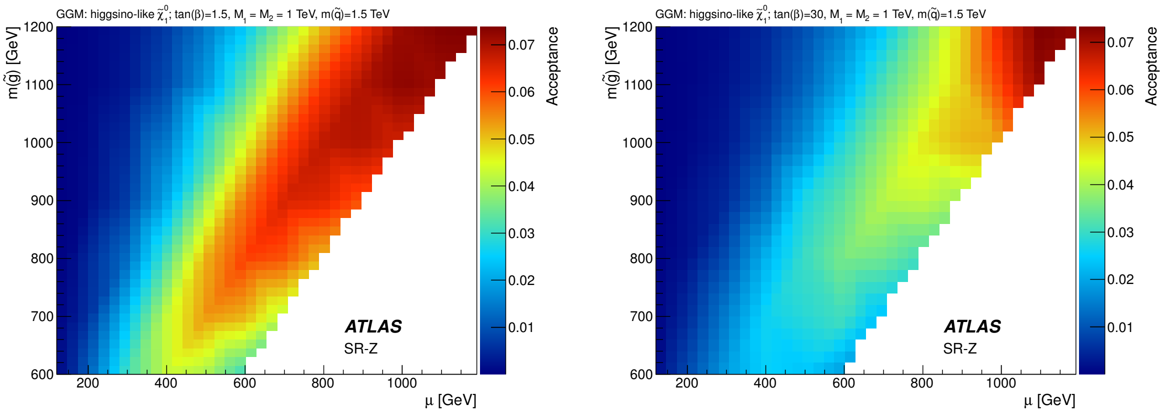

Figure B.3: Signal acceptance for the GGM model with $\tan\beta = 1.5$ (left) and $\tan\beta = 30$ (right) for the sum of the electron and muon channel [134]

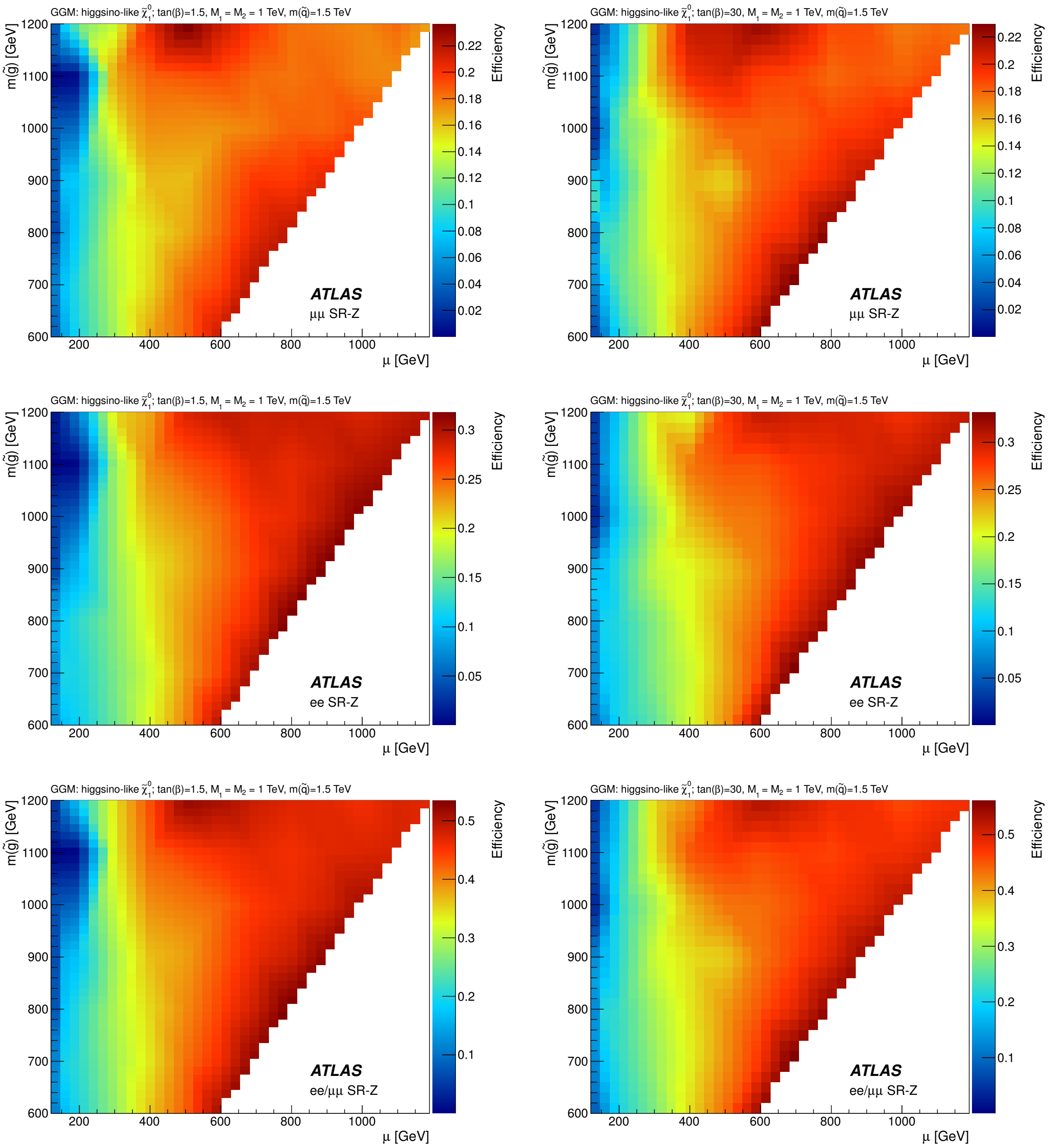

Figure B.4: Signal efficiency for the GGM model with $\tan\beta = 1.5$ (left) and $\tan\beta = 30$ (right) in the muon channel on top, the electron channel in the middle and the sum of the two on bottom [134].

C Further plots on the $Z+$jets background

In this appendix, additional material about the jet smearing method and the $Z+$jets background estimation can be found. In Fig. C.1, the comparison between the background prediction obtained from MC simulations and the data in VRZ with an additional cut on $\Delta\phi(\text{jet}_{1,2}, E_T^{\text{miss}}) > 0.4$ is shown. It has to be stressed that the data-driven jet smearing method is used for the nominal prediction of the $Z+$jets background in the Z+jets+E_T^{miss} analysis.

The ϕ angle between the subleading jet and the estimate for the fake $E_{\text{T}}^{\text{miss}}$ obtained from the jet smearing method is compared to data in different bins of $E_{\text{T}}^{\text{miss}}$ in Fig. C.2 and C.3. Good agreement is observed as for the leading jet as already discussed in Sec. 5.3.1.

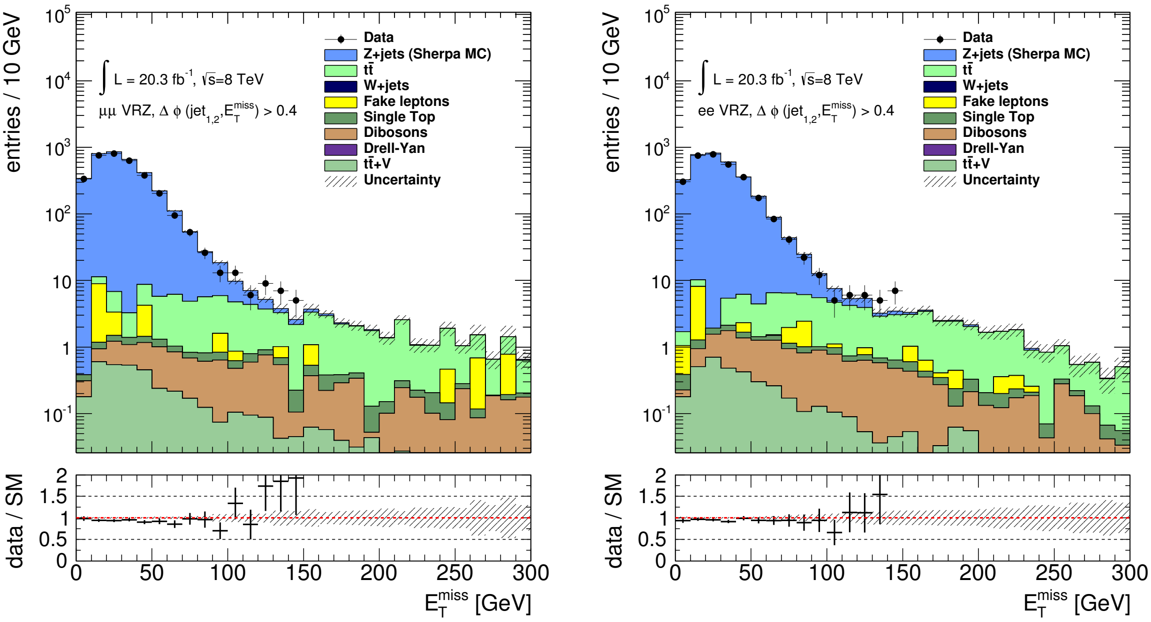

Figure C.1: Comparison between the background estimate obtained from MC simulations and data in VRZ with an additional cut on $\Delta\phi(\text{jet}_{1,2}, E_T^{\text{miss}}) > 0.4$ for $\mu^+\mu^-$ (left) and e^+e^- events (right). Only the statistical error of the MC simulation is included in the error bands. The region $E_{\text{T}}^{\text{miss}} > 150$ GeV is not part of VRZ as it is dominated by $t\bar{t}$ background. The data points are thus omitted there.

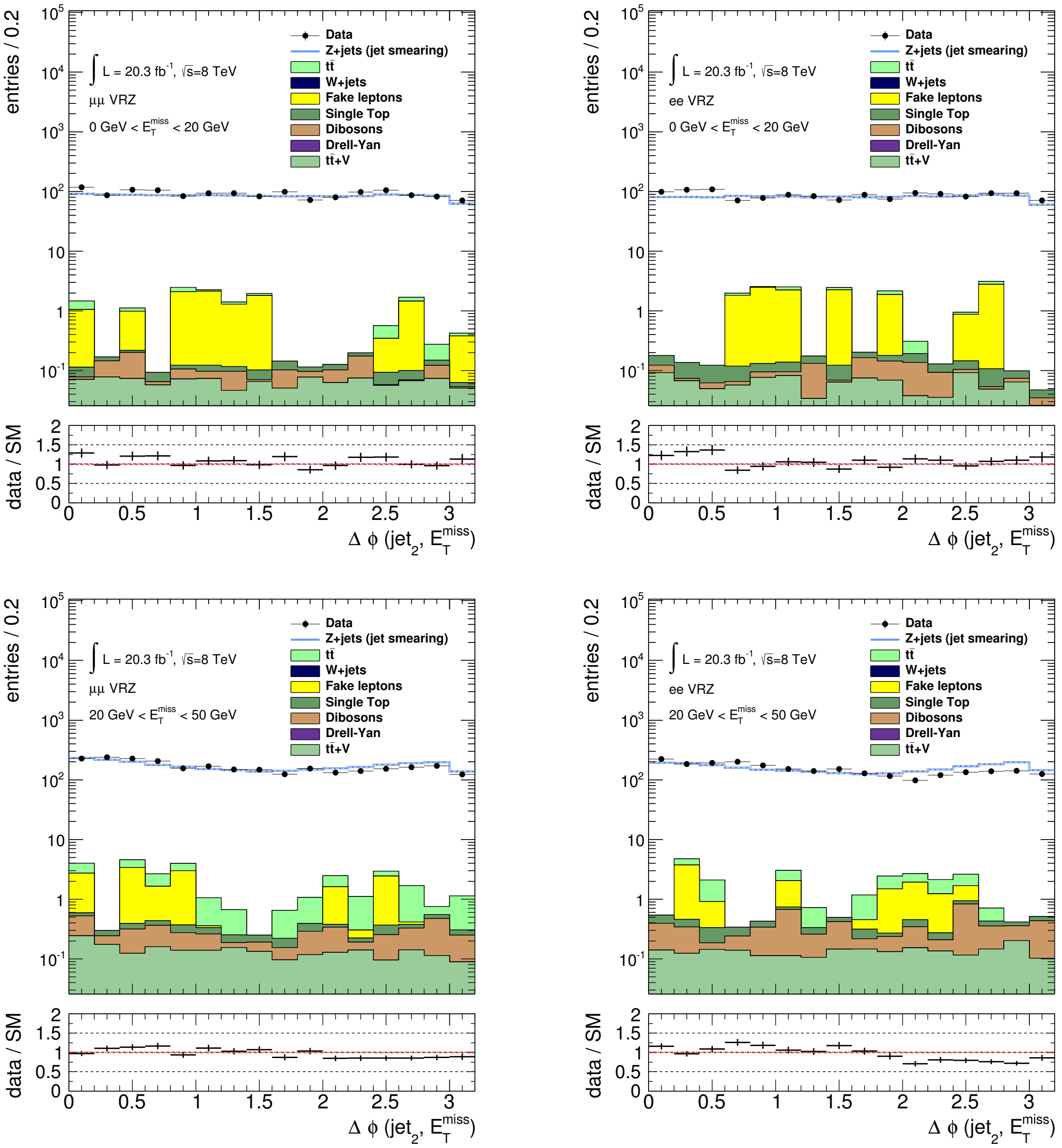

Figure C.2: Distribution of $\Delta\phi(\text{jet}_2, E_{\text{T}}^{\text{miss}})$ in the muon (left) and electron (right) channel. In the upper row the region $0\,\text{GeV} < E_{\text{T}}^{\text{miss}} < 20\,\text{GeV}$ is shown and in the lower row $20\,\text{GeV} < E_{\text{T}}^{\text{miss}} < 50\,\text{GeV}$. The error band contains only the statistical error of the backgrounds added from MC.

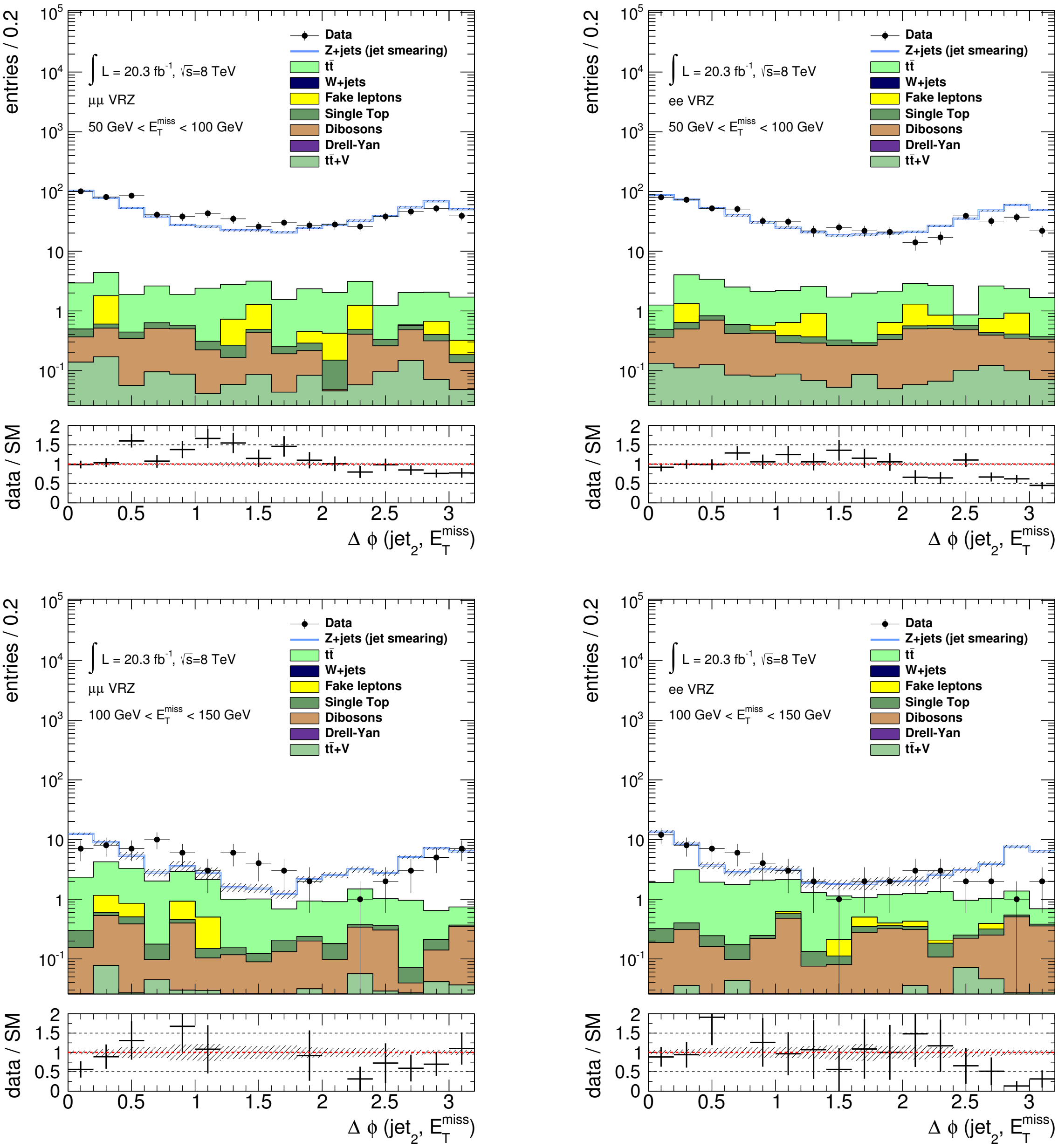

Figure C.3: Distribution of $\Delta\phi(\mathrm{jet}_2, E_{\mathrm{T}}^{\mathrm{miss}})$ in the muon (left) and electron (right) channel. In the upper row the region $50\,\mathrm{GeV} < E_{\mathrm{T}}^{\mathrm{miss}} < 100\,\mathrm{GeV}$ is shown and in the lower row $100\,\mathrm{GeV} < E_{\mathrm{T}}^{\mathrm{miss}} < 150\,\mathrm{GeV}$. The error band contains only the statistical error of the backgrounds added from MC.

D Details about the events in the Z signal region

Details about different properties of all events in the signal region of the Z+jets+E_T^{miss} analysis are collected in the first part of this appendix. The values for the 13 events in the muon channel are shown in Tab. D.1, while the 16 events in the electron channel can be found in Tab. D.2.
In the second part, the p_{T} distributions of the subleading jet and lepton in SR-Z are shown in Fig. D.1 and D.2, respectively. No suspicious features hinting at possible detector problems are visible as for the leading jet and lepton discussed in Sec. 5.6.1.

run number	event number	μ	$m_{\ell\ell}$	# jets	H_T	$E_\mathrm{T}^\mathrm{miss}$	$p_{\mathrm{T,jet1}}$	$p_{\mathrm{T,jet2}}$	$p_{\mathrm{T,lep1}}$	$p_{\mathrm{T,lep2}}$
204633	8011863	28.5	83.6	3	665.1	271.4	359.4	100.4	118.4	34.8
207306	40197306	19.2	94.5	3	721.7	298.0	255.9	229.9	54.3	50.9
207332	165410899	9.0	94.3	5	849.9	283.3	260.1	188.0	55.3	29.7
207582	2050009	26.3	87.9	3	640.8	283.4	384.2	94.5	58.2	47.4
207664	55925060	19.2	98.0	3	637.0	356.1	263.9	192.3	103.6	23.8
208811	145242853	13.2	97.8	4	624.8	246.5	262.3	131.2	53.4	45.8
209109	65439062	33.3	92.3	2	667.4	593.4	364.1	198.7	78.5	26.1
209787	73149960	27.5	84.8	3	669.7	332.9	343.6	150.2	75.4	15.2
211867	135732363	26.4	81.7	5	650.0	295.3	183.1	179.9	75.8	35.2
212199	33863309	29.5	93.6	3	851.7	232.1	339.3	248.9	116.1	105.2
212721	108085311	20.2	99.7	5	619.3	225.2	259.5	87.3	76.5	53.9
212815	32928273	29.4	90.4	5	687.3	436.7	246.1	116.7	38.6	18.7
213754	189058793	21.6	94.0	5	767.3	392.6	400.8	131.4	26.2	22.8

Table D.1: Details of the data events in SR-Z for the muon channel. $m_{\ell\ell}$, H_T, $E_\mathrm{T}^\mathrm{miss}$ and all p_T values are given in units of GeV.

run number	event number	μ	$m_{\ell\ell}$	# jets	H_T	$E_\mathrm{T}^\mathrm{miss}$	$p_{\mathrm{T,jet1}}$	$p_{\mathrm{T,jet2}}$	$p_{\mathrm{T,lep1}}$	$p_{\mathrm{T,lep2}}$
201494	27828022	14.1	89.2	5	1000.9	435.3	328.3	249.0	44.0	43.4
203524	5360108	24.5	90.2	2	654.0	248.6	366.3	68.6	124.8	94.3
203524	27421377	21.2	83.6	3	625.6	273.6	374.2	87.0	78.6	35.8
204474	73848585	17.9	89.7	4	808.6	349.2	271.1	160.7	98.5	18.3
204763	55797530	21.0	89.1	3	727.2	226.5	245.2	218.7	181.1	46.6
206962	58522498	18.3	91.2	2	1145.2	292.2	727.5	74.1	287.0	56.6
206962	87899000	15.9	92.4	2	839.0	254.0	396.4	56.5	262.7	123.4
207304	84037870	14.3	81.6	3	604.5	225.7	155.5	136.7	161.6	21.7
207696	2544548	28.5	98.9	3	613.7	241.6	302.8	104.9	108.2	26.0
208982	163756243	20.5	92.3	7	924.3	241.2	216.9	105.9	147.1	146.7
209736	147304703	14.7	96.7	7	1022.5	286.0	298.0	185.1	129.2	18.0
212144	132600702	18.2	90.8	2	661.9	532.8	203.1	67.9	199.4	191.4
212172	196073153	11.8	92.7	4	1104.7	399.5	635.6	220.1	67.1	41.9
214523	65799808	25.5	91.1	2	644.9	509.8	432.3	111.2	54.1	47.4
214777	149603363	22.0	84.7	3	790.4	296.5	460.4	155.3	117.5	16.9
215464	46088347	23.2	94.4	2	711.2	230.6	428.2	121.8	123.8	37.5

Table D.2: Details of the data events in SR for the electron channel. $m_{\ell\ell}$, H_T, $E_\mathrm{T}^\mathrm{miss}$ and all p_T values are given in units of GeV.

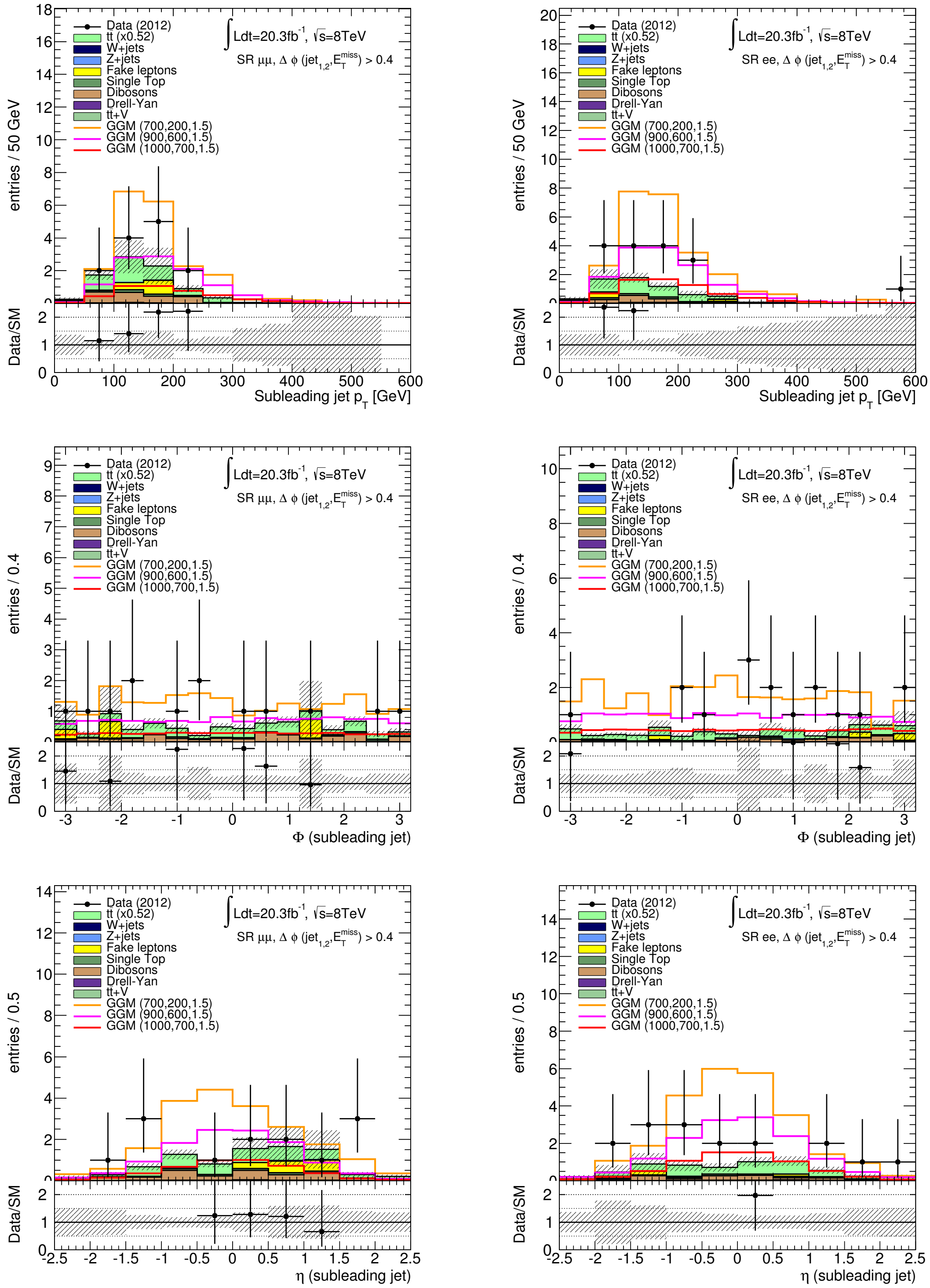

Figure D.1: Kinematic distributions of the subleading jet for the muon (left) and electron (right) channel in SR-Z: p_{T} (top), ϕ angle (middle) and pseudo-rapidity η (bottom). Only the statistical uncertainties of the MC simulation are included in the indicated error bands. The $t\bar{t}$ MC prediction has been normalised by 0.52 according to the results of the sideband fit in CRT.

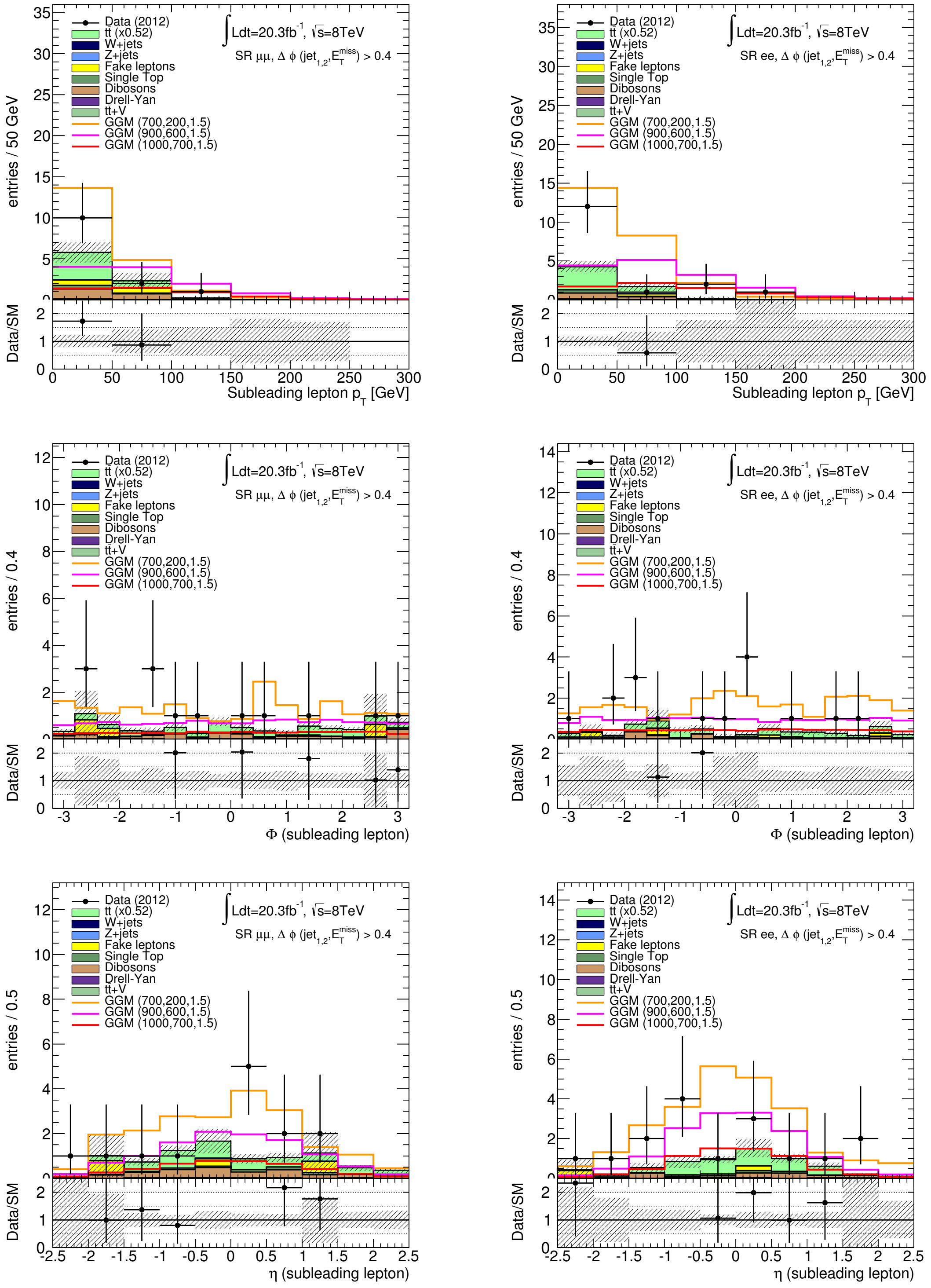

Figure D.2: Kinematic distributions of the subleading lepton for the muon (left) and electron (right) channel in SR-Z: p_{T} (top), ϕ angle (middle) and pseudo-rapidity η (bottom). Only the statistical uncertainties of the MC simulation are included in the indicated error bands. The $t\bar{t}$ MC prediction has been normalised by 0.52 according to the results of the sideband fit in CRT.

E Further cross-checks on the $E_{\mathrm{T}}^{\mathrm{miss}}$ calibration

Correlation plots for the single terms of calorimeter and object $E_{\mathrm{T}}^{\mathrm{miss}}$ are shown in this appendix. For calorimeter $E_{\mathrm{T}}^{\mathrm{miss}}$, this referrs to the single terms in Eq. (4.6). The equivalent terms for object $E_{\mathrm{T}}^{\mathrm{miss}}$ are retrieved if only the sum over all jets or leptons, respectively, is included in Eq. 5.16. A strong correlation between the two definitions is visible in all plots both for the absolute magnitude as well as for the direction of the missing energy. It can thus be concluded that the calibration and selection of the objects used for the $E_{\mathrm{T}}^{\mathrm{miss}}$ reconstruction is correct.

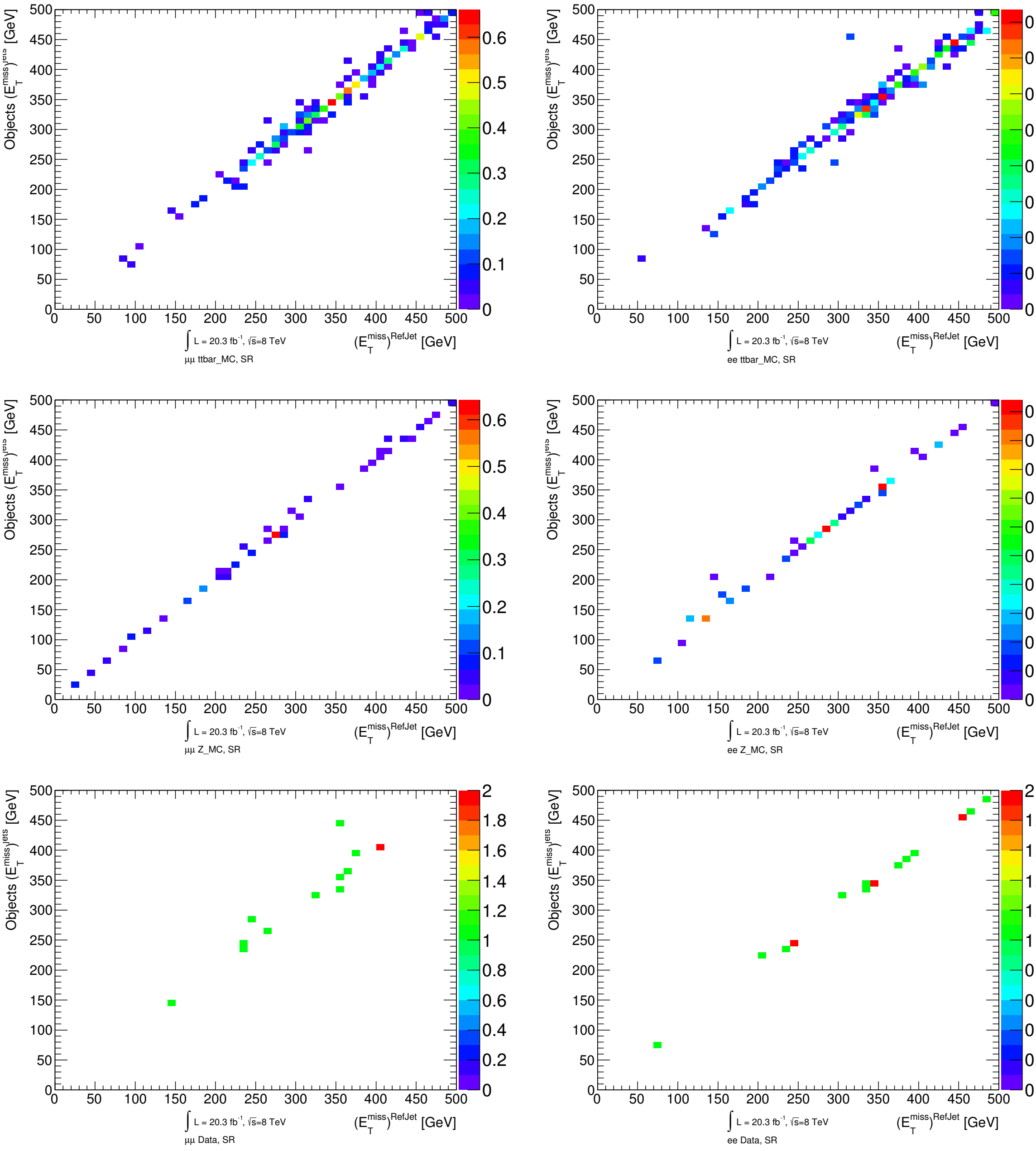

Figure E.1: Correlation between the magnitudes of the jet term of the calorimeter and the object based $E_{\mathrm{T}}^{\mathrm{miss}}$ definition in the muon (left) and electron channel (right) for a $t\bar{t}$ MC (top), Z+jets MC (middle) and data (bottom). All plots use the event selection of SR-Z without the cut on $\Delta\phi(\mathrm{jet}_{1,2}, E_T^{\mathrm{miss}}) > 0.4$.

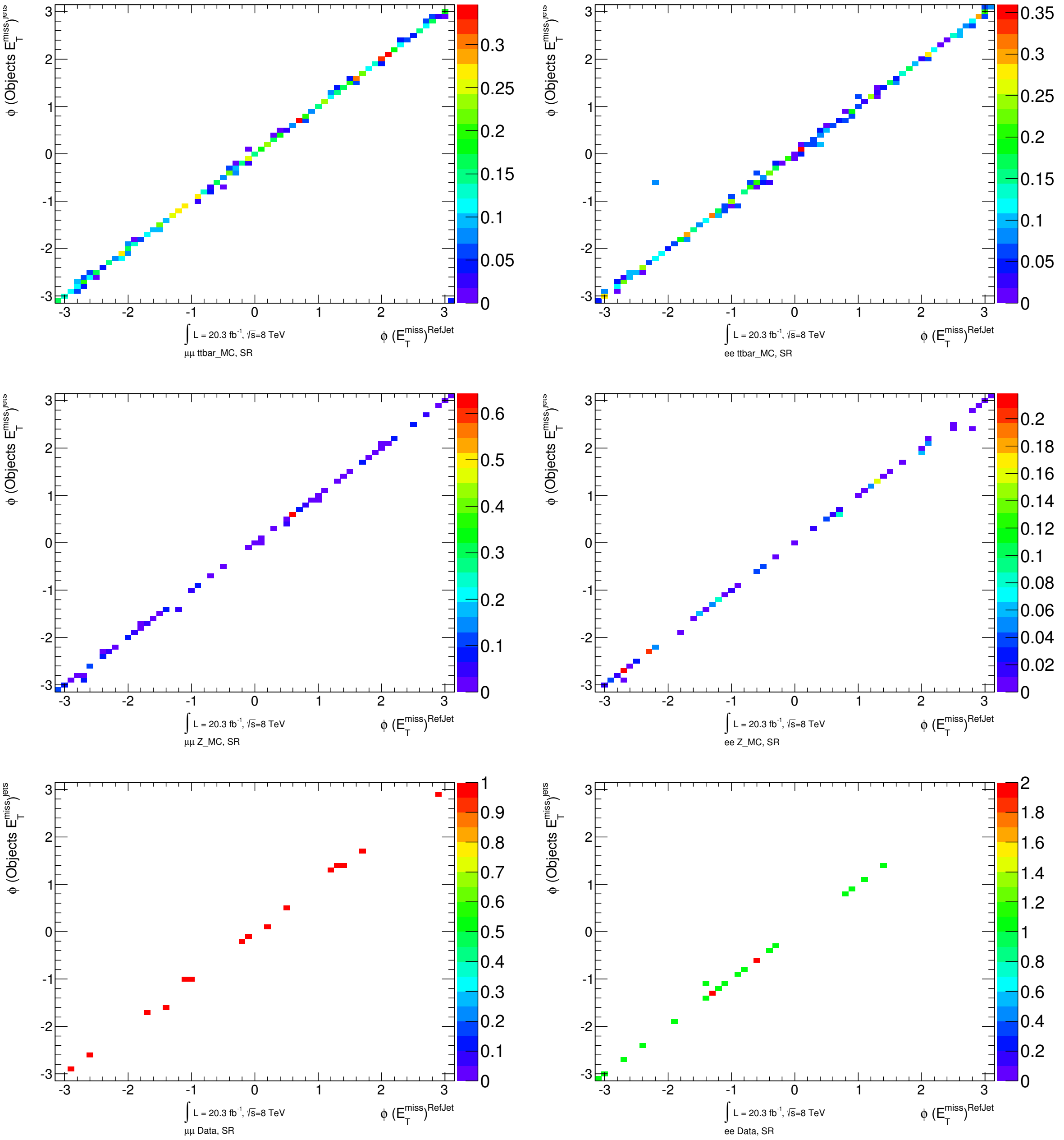

Figure E.2: Correlation between the directions of the jet term of the calorimeter and the object based $E_{\mathrm{T}}^{\mathrm{miss}}$ definition in the muon (left) and electron channel (right) for a $t\bar{t}$ MC (top), $Z+$jets MC (middle) and data (bottom). All plots use the event selection of SR-Z without the cut on $\Delta\phi(\mathrm{jet}_{1,2}, E_T^{\mathrm{miss}}) > 0.4$.

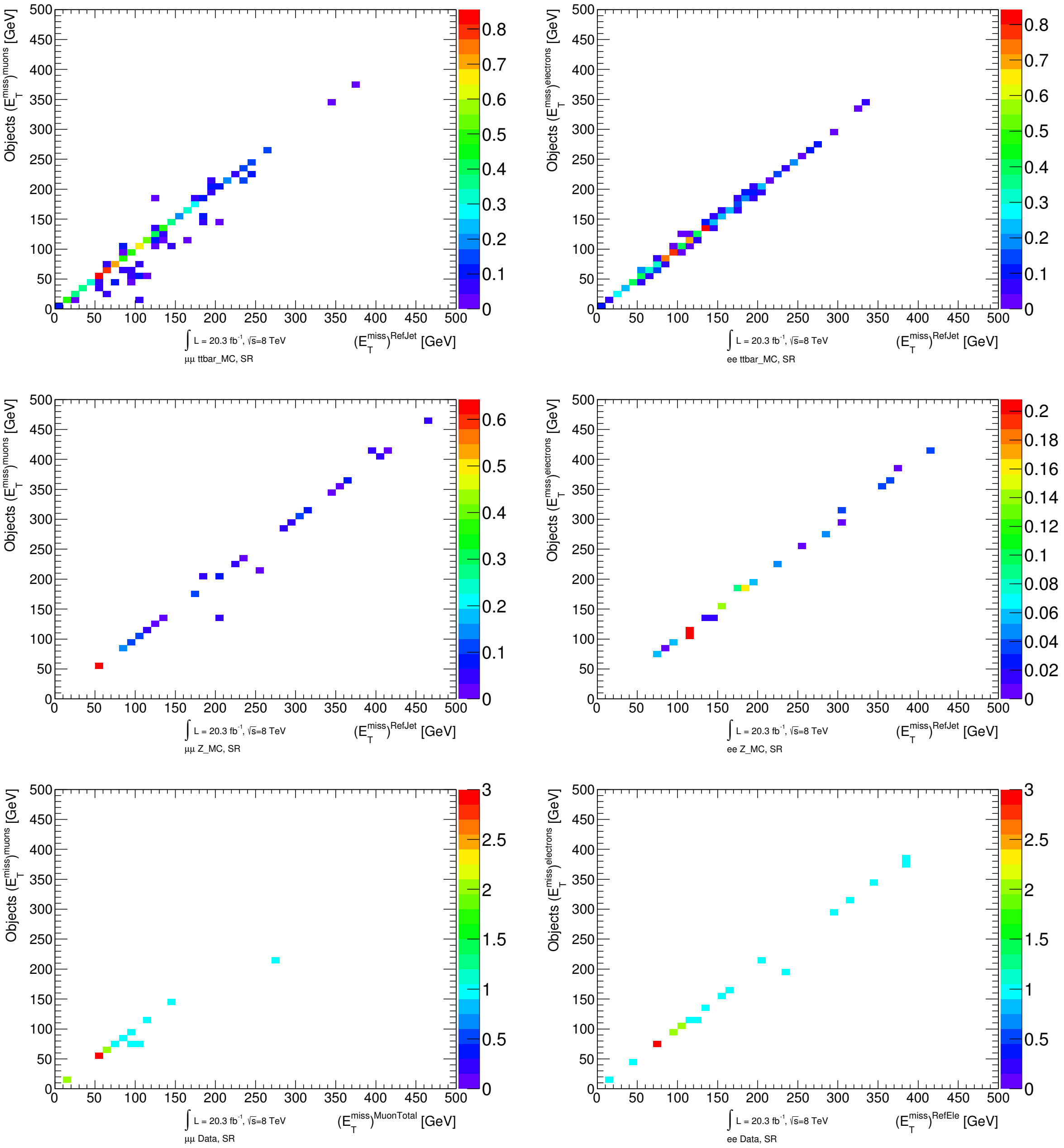

Figure E.3: Correlation between the magnitudes of the lepton term of the calorimeter and the object based $E_{\mathrm{T}}^{\mathrm{miss}}$ definition in the muon (left) and electron channel (right) for a $t\bar{t}$ MC (top), Z+jets MC (middle) and data (bottom). All plots use the event selection of SR-Z without the cut on $\Delta\phi(\mathrm{jet}_{1,2}, E_T^{\mathrm{miss}}) > 0.4$.

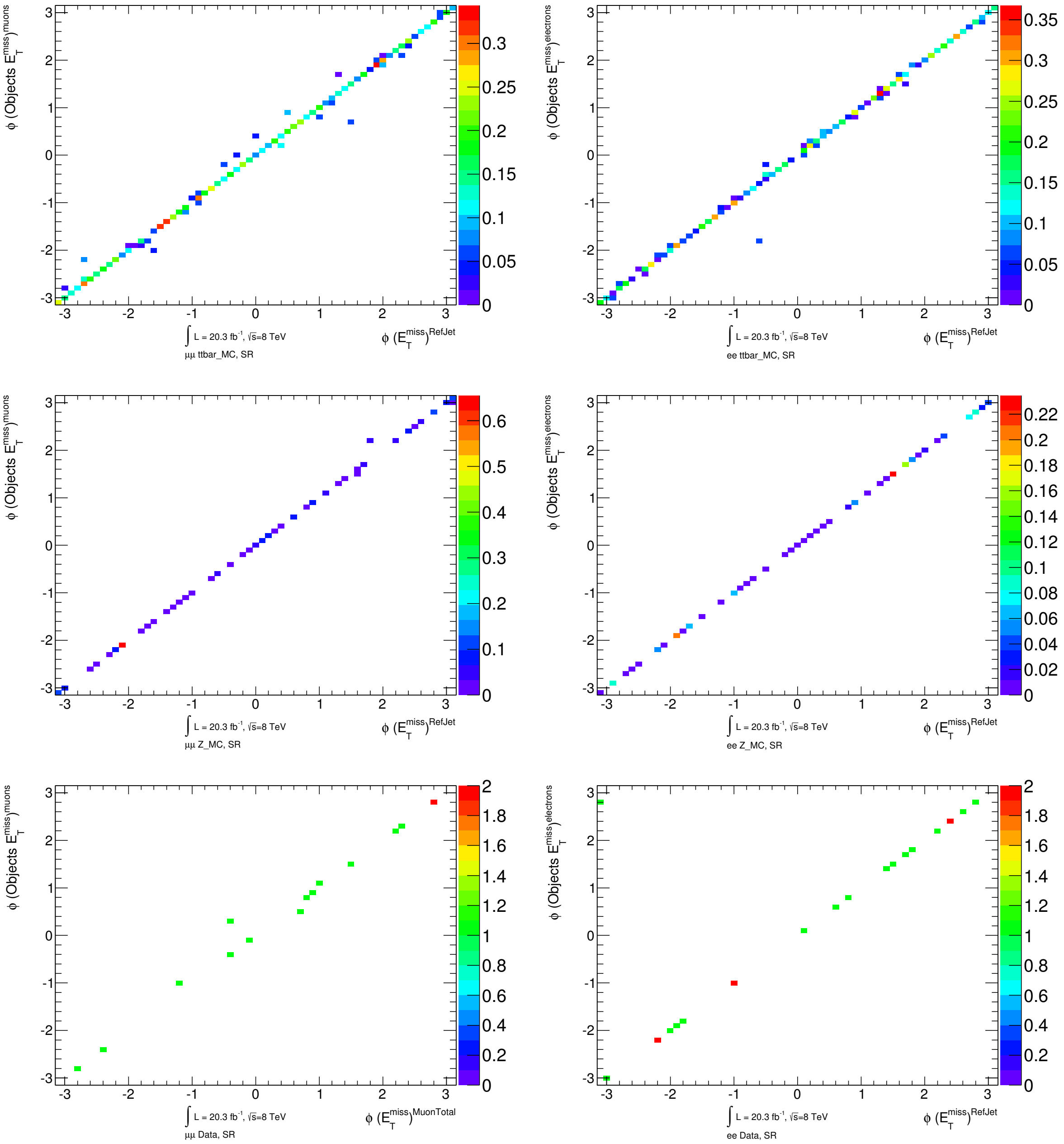

Figure E.4: Correlation between the directions of the lepton term of the calorimeter and the object based $E_{\mathrm{T}}^{\mathrm{miss}}$ definition in the muon (left) and electron channel (right) for a $t\bar{t}$ MC (top), Z+jets MC (middle) and data (bottom). All plots use the event selection of SR-Z without the cut on $\Delta\phi(\mathrm{jet}_{1,2}, E_T^{\mathrm{miss}}) > 0.4$. The scattering around the diagonal is due to events with more than two leptons as only the first two leptons are taken into account in the object $E_{\mathrm{T}}^{\mathrm{miss}}$ definition (compare Eq. (5.16)).

F Further results of the $LQ\bar{D}$ reinterpretation

In this appendix, the maximum signal strengths which can be excluded at 95 % confidence level are shown for all mass points and branching fraction combinations considered in the reinterpretation of the 1L+jets+E_T^{miss} analysis in the context of the $LQ\bar{D}$ model. The squark model is presented in the first part, while the gluino model results are given in the second part. White areas in the plots indicate points where it was not possible to retrieve a meaningful result from the fit configuration of the analysis due to the low signal efficiency.

Futher exclusion plots for the $LQ\bar{D}$ squark model

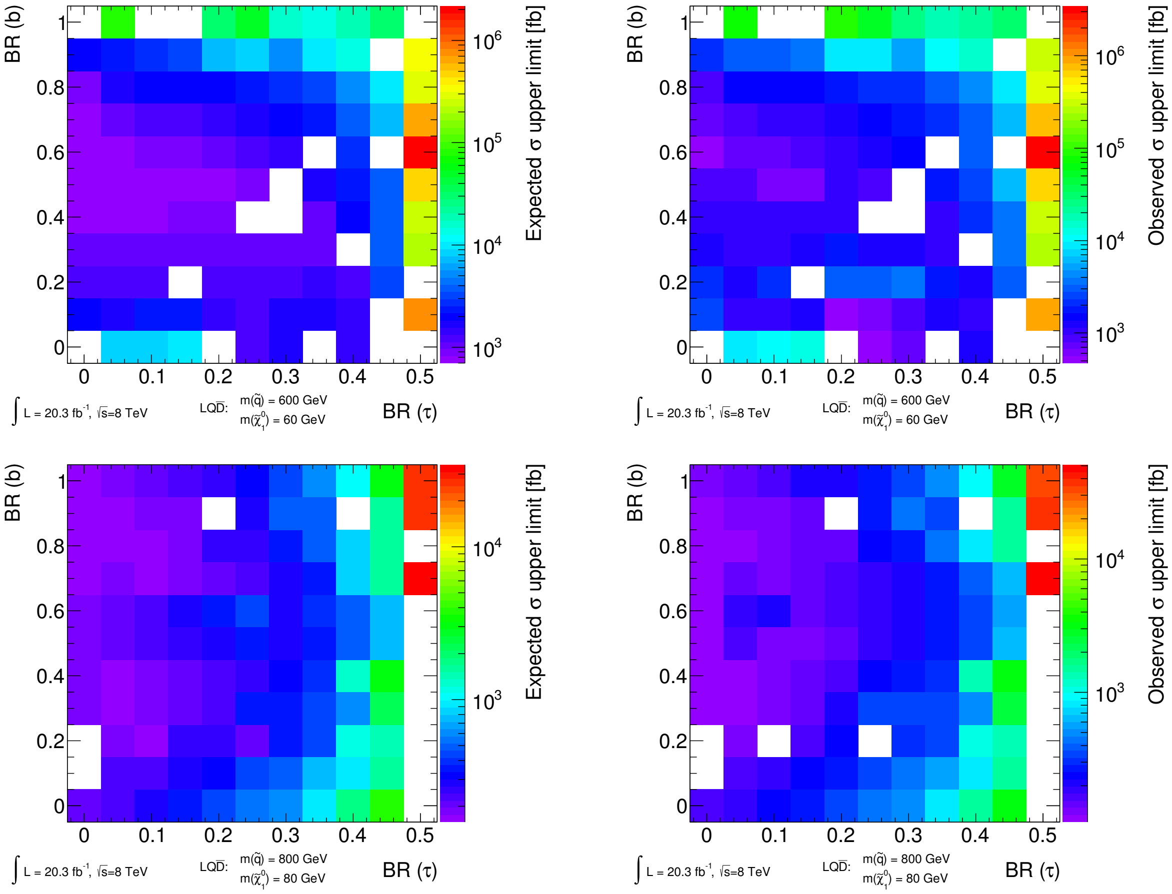

Figure F.1: Results of the reinterpretation of the 1L+jets+E_T^{miss} analysis in the context of the $LQ\bar{D}$ model with squark production: Expected (left) and observed (right) cross-section limits for for $m(\tilde{q}) = 600\,\text{GeV}$, $m(\tilde{\chi}_1^0) = 60\,\text{GeV}$ (top) and $m(\tilde{q}) = 800\,\text{GeV}$, $m(\tilde{\chi}_1^0) = 80\,\text{GeV}$ (bottom).

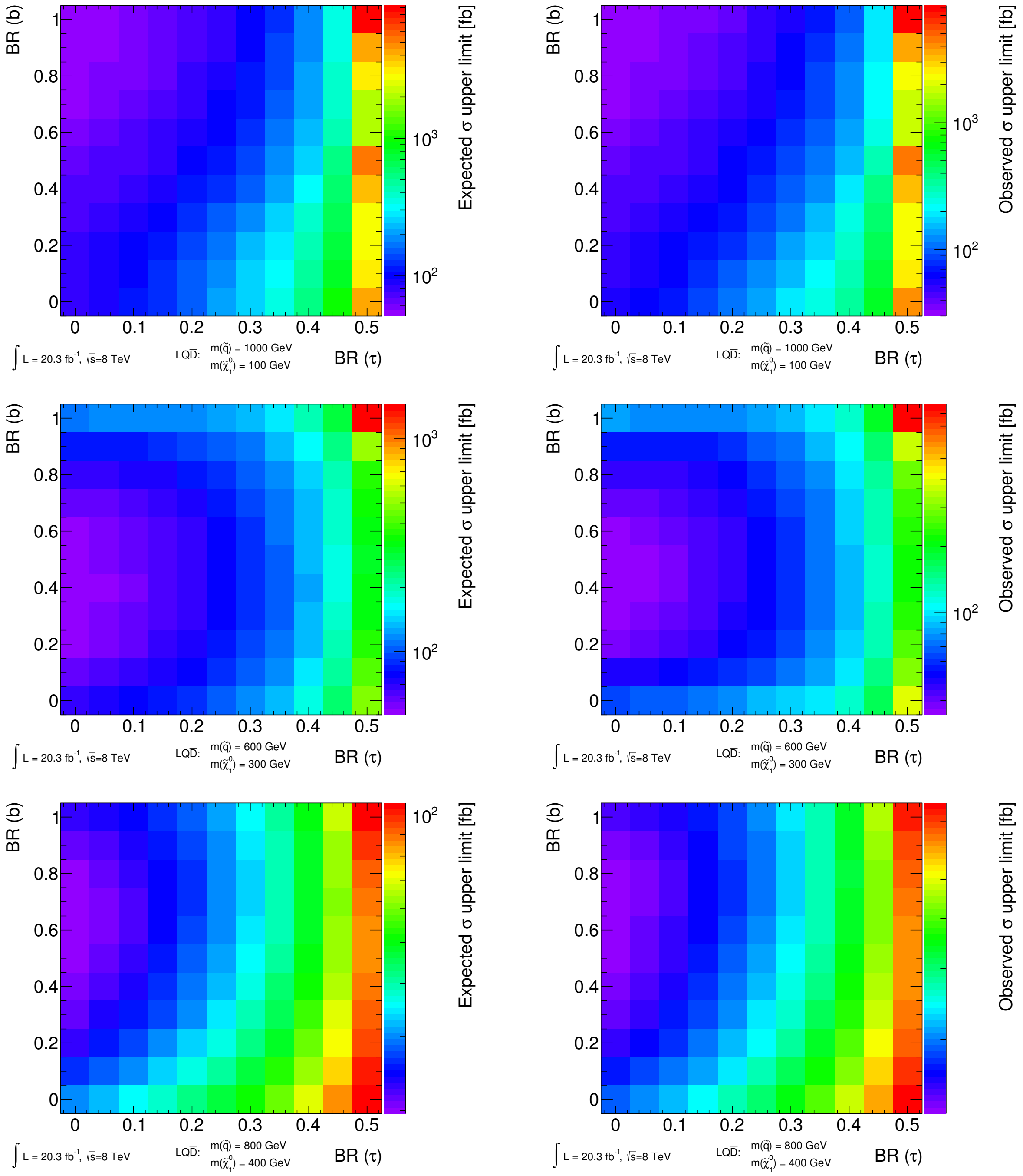

Figure F.2: Results of the reinterpretation of the 1L+jets+E_T^{miss} analysis in the context of the $LQ\bar{D}$ model with squark production: Expected (left) and observed (right) cross-section limits for for $m(\tilde{q}) = 1000\,\text{GeV}$, $m(\tilde{\chi}_1^0) = 100\,\text{GeV}$ (top), $m(\tilde{q}) = 600\,\text{GeV}$, $m(\tilde{\chi}_1^0) = 300\,\text{GeV}$ (middle) and $m(\tilde{q}) = 800\,\text{GeV}$, $m(\tilde{\chi}_1^0) = 400\,\text{GeV}$ (bottom).

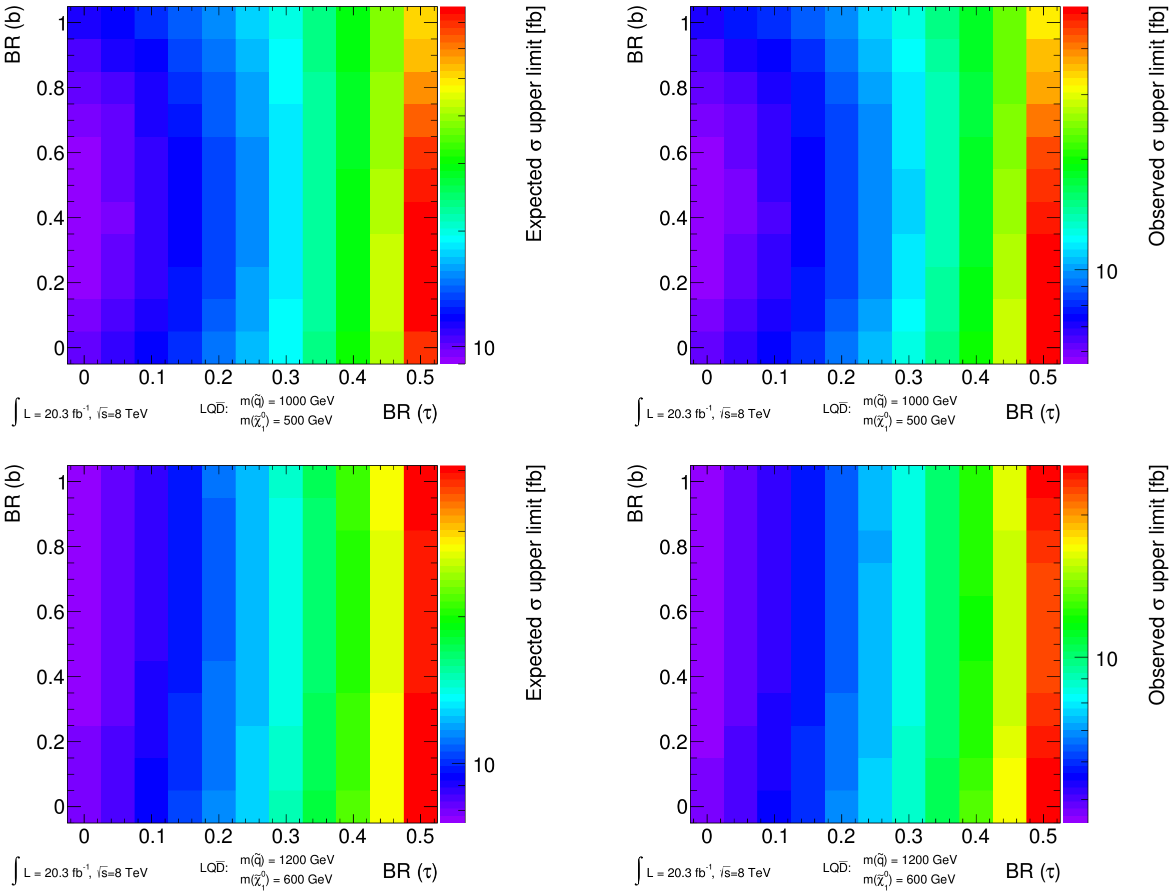

Figure F.3: Results of the reinterpretation of the 1L+jets+E_T^{miss} analysis in the context of the $LQ\bar{D}$ model with squark production: Expected (left) and observed (right) cross-section limits for for $m(\tilde{q}) = 1000\,\mathrm{GeV}$, $m(\tilde{\chi}_1^0) = 500\,\mathrm{GeV}$ (top) and $m(\tilde{q}) = 1200\,\mathrm{GeV}$, $m(\tilde{\chi}_1^0) = 600\,\mathrm{GeV}$ (bottom).

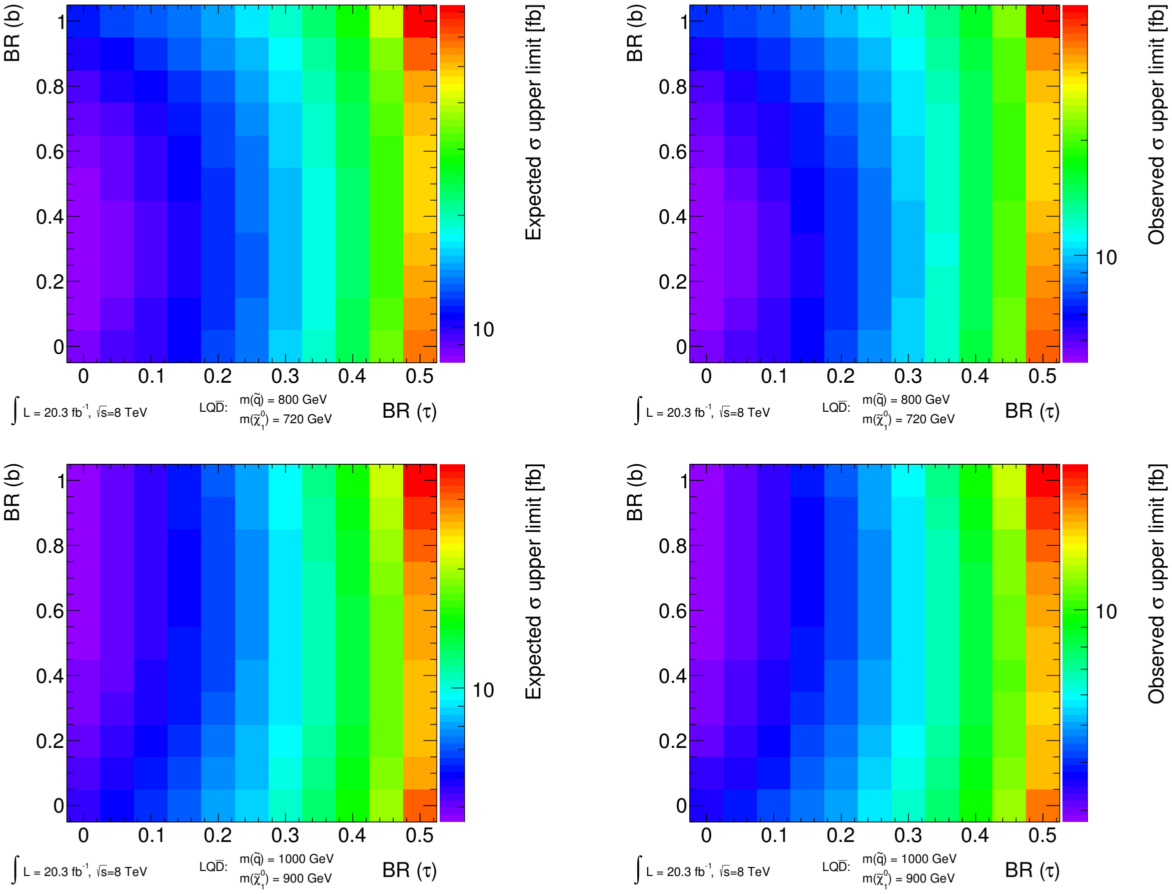

Figure F.4: Results of the reinterpretation of the 1L+jets+E_T^{miss} analysis in the context of the $LQ\bar{D}$ model with squark production: Expected (left) and observed (right) cross-section limits for for $m(\tilde{q}) = 800\,\text{GeV}$, $m(\tilde{\chi}_1^0) = 720\,\text{GeV}$ (top) and $m(\tilde{q}) = 1000\,\text{GeV}$, $m(\tilde{\chi}_1^0) = 900\,\text{GeV}$ (bottom).

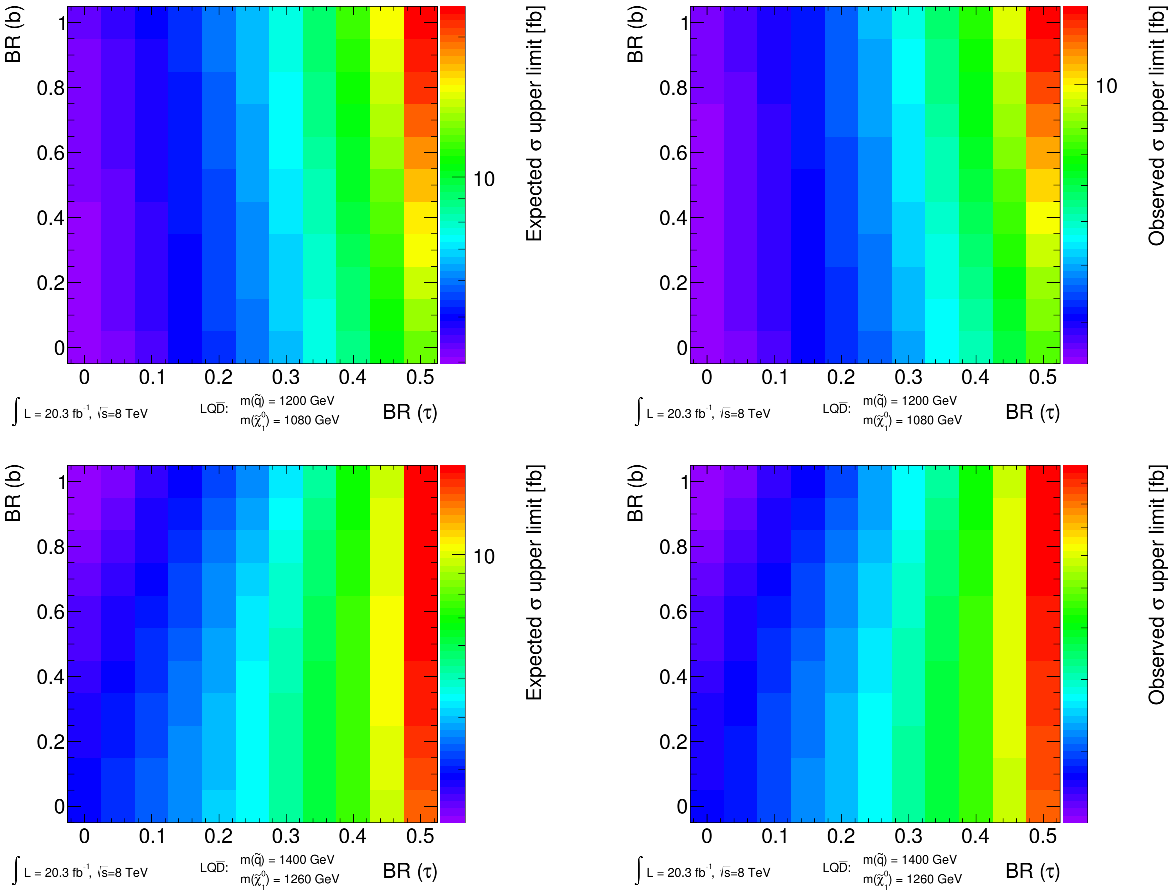

Figure F.5: Results of the reinterpretation of the 1L+jets+E_T^{miss} analysis in the context of the $LQ\bar{D}$ model with squark production: Expected (left) and observed (right) cross-section limits for for $m(\tilde{q}) = 1200\,\mathrm{GeV}$, $m(\tilde{\chi}_1^0) = 1080\,\mathrm{GeV}$ (top) and $m(\tilde{q}) = 1400\,\mathrm{GeV}$, $m(\tilde{\chi}_1^0) = 1260\,\mathrm{GeV}$ (bottom).

Futher exclusion plots for the $LQ\bar{D}$ gluino model

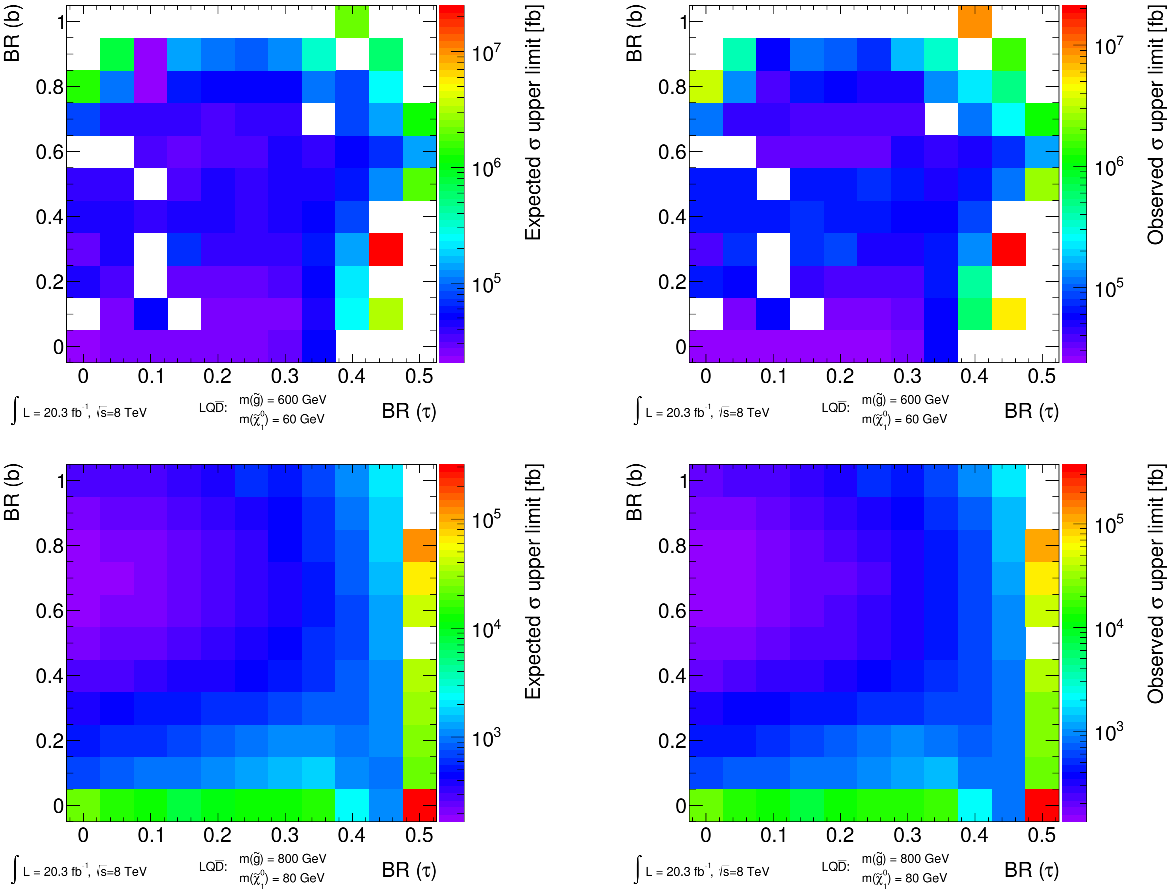

Figure F.6: Results of the reinterpretation of the 1L+jets+E_T^{miss} analysis in the context of the $LQ\bar{D}$ model with gluino production: Expected (left) and observed (right) cross-section limits for for $m(\tilde{g}) = 600\,\text{GeV}$, $m(\tilde{\chi}_1^0) = 60\,\text{GeV}$ (top) and $m(\tilde{g}) = 800\,\text{GeV}$, $m(\tilde{\chi}_1^0) = 80\,\text{GeV}$ (bottom).

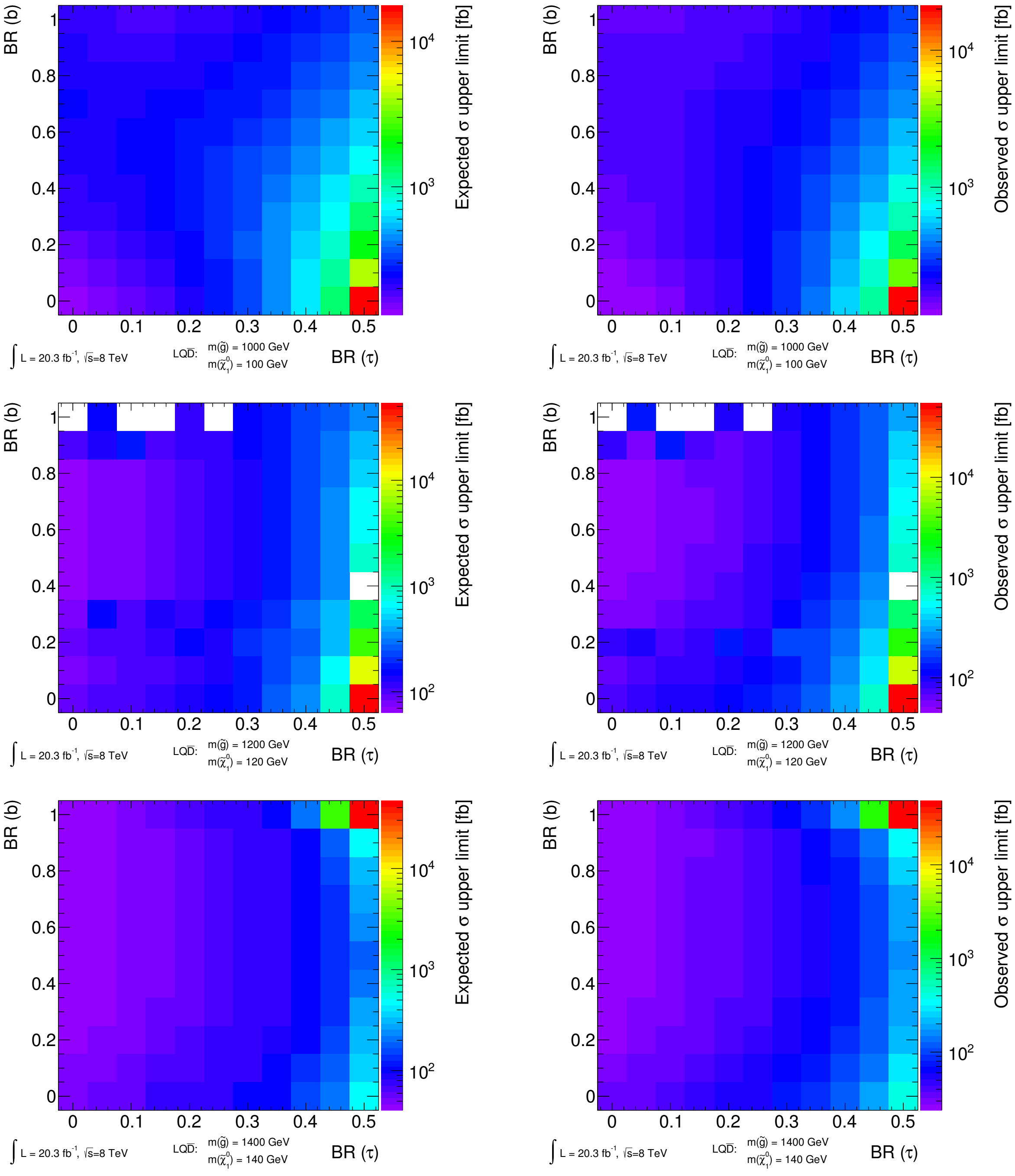

Figure F.7: Results of the reinterpretation of the 1L+jets+E_T^{miss} analysis in the context of the $LQ\bar{D}$ model with gluino production: Expected (left) and observed (right) cross-section limits for for $m(\tilde{g}) = 1000\,\text{GeV}$, $m(\tilde{\chi}_1^0) = 100\,\text{GeV}$ (top), $m(\tilde{g}) = 1200\,\text{GeV}$, $m(\tilde{\chi}_1^0) = 120\,\text{GeV}$ (middle) and $m(\tilde{g}) = 1400\,\text{GeV}$, $m(\tilde{\chi}_1^0) = 140\,\text{GeV}$ (bottom).

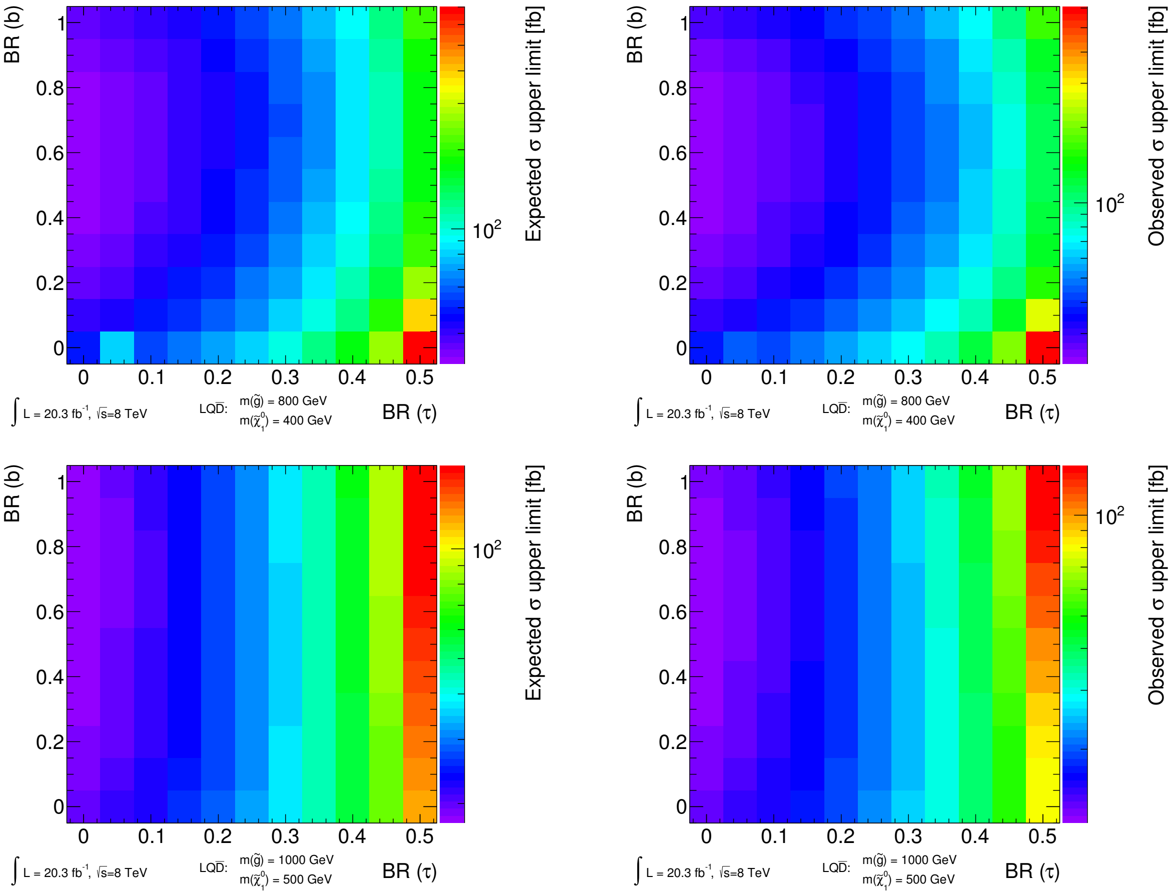

Figure F.8: Results of the reinterpretation of the 1L+jets+E_T^{miss} analysis in the context of the $LQ\bar{D}$ model with gluino production: Expected (left) and observed (right) cross-section limits for for $m(\tilde{g}) = 800\,\mathrm{GeV}$, $m(\tilde{\chi}_1^0) = 400\,\mathrm{GeV}$ (top) and $m(\tilde{g}) = 1000\,\mathrm{GeV}$, $m(\tilde{\chi}_1^0) = 500\,\mathrm{GeV}$ (bottom).

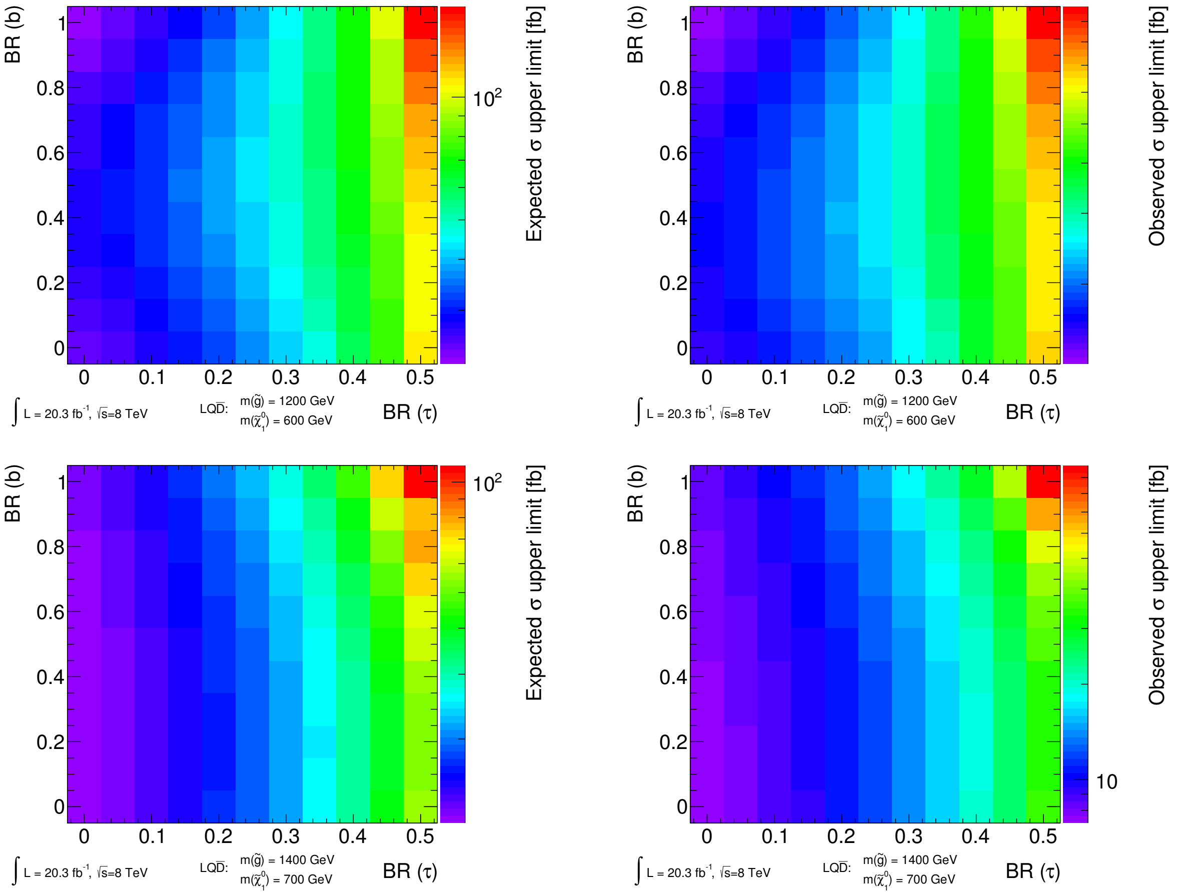

Figure F.9: Results of the reinterpretation of the 1L+jets+E_T^{miss} analysis in the context of the $LQ\bar{D}$ model with gluino production: Expected (left) and observed (right) cross-section limits for for $m(\tilde{g}) = 1200\,\text{GeV}$, $m(\tilde{\chi}_1^0) = 600\,\text{GeV}$ (top) and $m(\tilde{g}) = 1400\,\text{GeV}$, $m(\tilde{\chi}_1^0) = 700\,\text{GeV}$ (bottom).

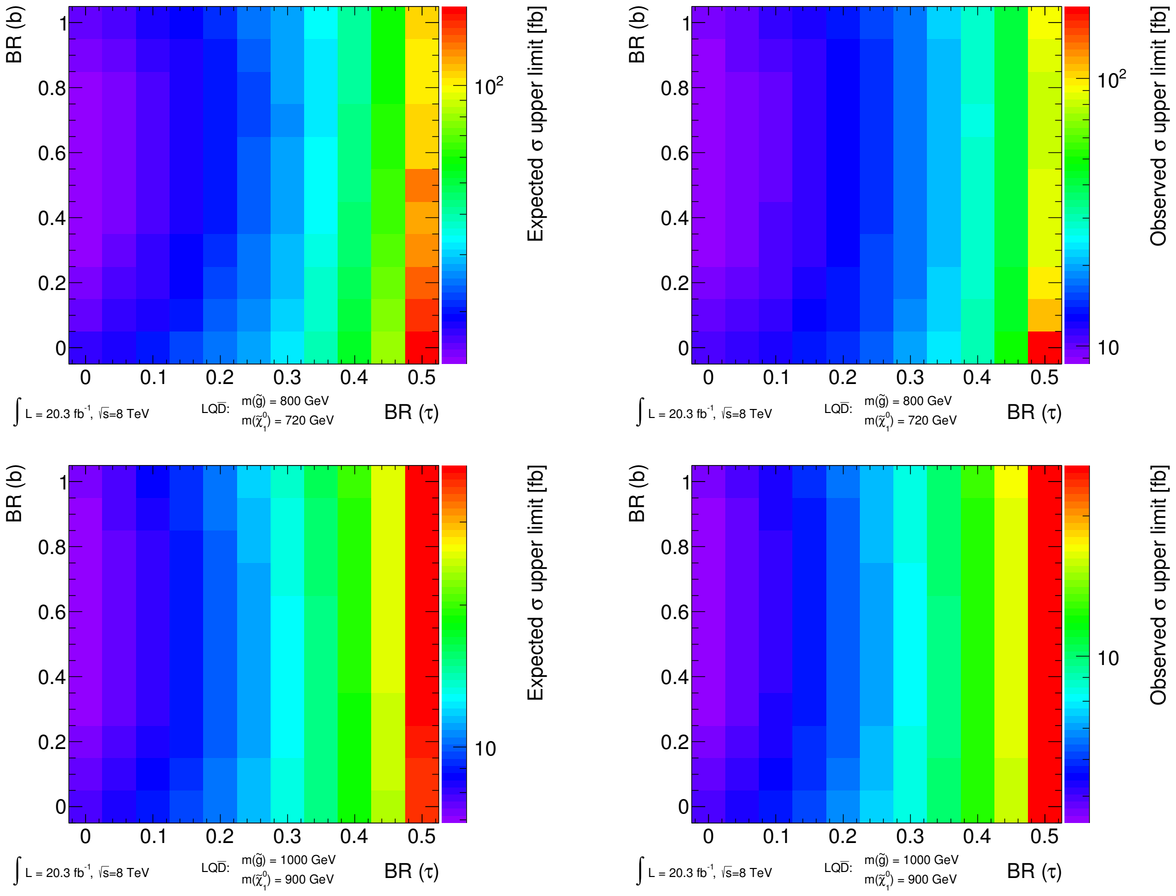

Figure F.10: Results of the reinterpretation of the 1L+jets+E_T^{miss} analysis in the context of the $LQ\bar{D}$ model with gluino production: Expected (left) and observed (right) cross-section limits for for $m(\tilde{g}) = 800\,\mathrm{GeV}$, $m(\tilde{\chi}_1^0) = 720\,\mathrm{GeV}$ (top) and $m(\tilde{g}) = 1000\,\mathrm{GeV}$, $m(\tilde{\chi}_1^0) = 900\,\mathrm{GeV}$ (bottom).

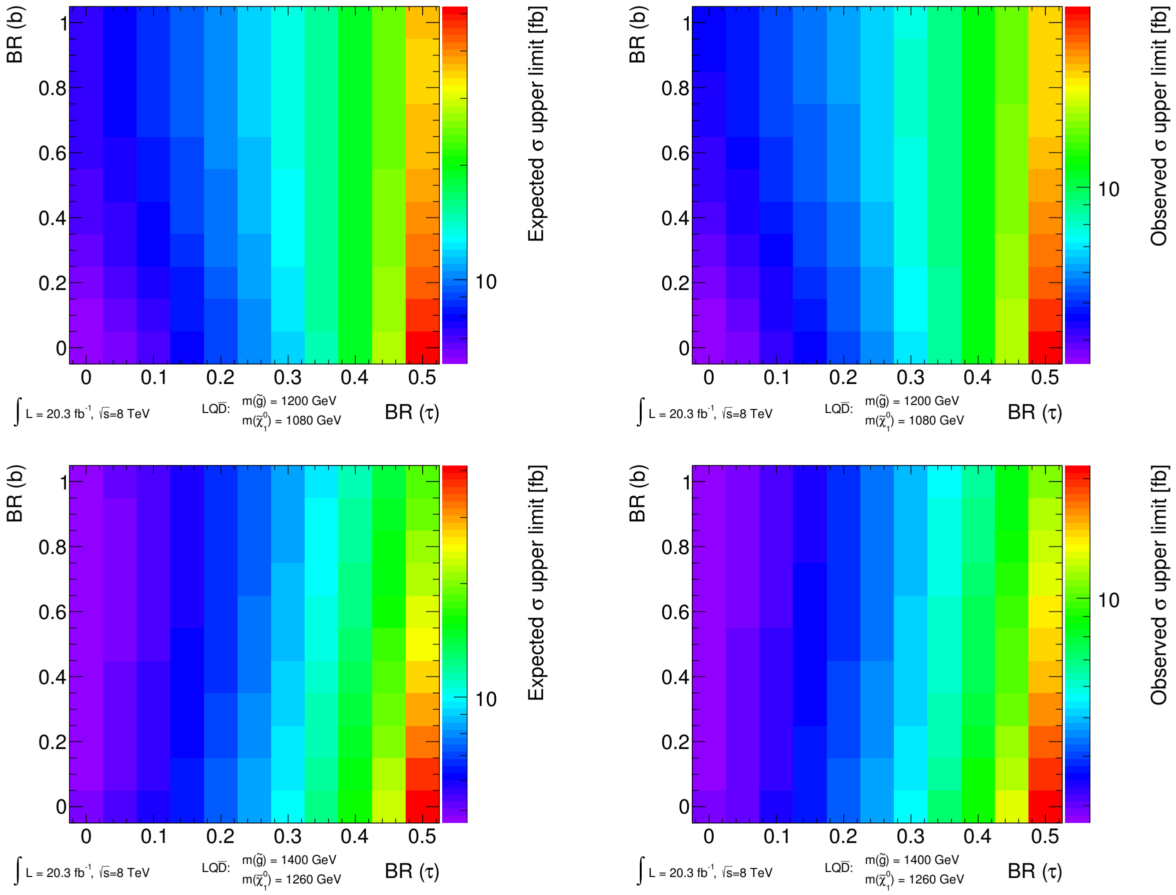

Figure F.11: Results of the reinterpretation of the 1L+jets+E_T^{miss} analysis in the context of the $LQ\bar{D}$ model with gluino production: Expected (left) and observed (right) cross-section limits for for $m(\tilde{g}) = 1200\,\mathrm{GeV}$, $m(\tilde{\chi}_1^0) = 1080\,\mathrm{GeV}$ (top) and $m(\tilde{g}) = 1400\,\mathrm{GeV}$, $m(\tilde{\chi}_1^0) = 1260\,\mathrm{GeV}$ (bottom).

Acknowledgments

After over three years of doctoral studies and 206 pages (or 3299 lines) of PhD thesis, it is time to express my thanks to many people without whom this achievement would not have been possible.

First, I especially want to thank the supervisor of my PhD thesis, Prof. Raimund Ströhmer, for his continuous support and his helpful discussions about all sorts of details of my research in particular and high energy physics in general. I am also very thankful for all his useful comments regarding my thesis and for offering me the opportunity of an extended research stay at CERN and many short-term visits in Geneva and of different workshops, conferences and schools.

My special thanks go to Prof. Werner Porod, speaker of the DFG Graduate School GRK 1147, for the assessment of this thesis. Furthermore, he always helped me with questions about the theoretical basis of SUSY and granted me the possibility for a very nice and productive research stay at IFIC, Valencia.

I also want to express my gratitude to Prof. Thomas Trefzger for all his help with the ATLAS administration and the financial support for various stays abroad.

My thanks extent to Anna Weisensel, Karin Kuhns and Brigitte Wehner for their administrative assistance especially concerning questions about reimbursement of travel expenses.

I want to thank Andreas for the direct supervision of my PhD thesis, for helping me to find the interesting topic, all his advice and not least for his helpful comments on the first draft of this thesis.

All PhD students in the PiD working group, especially Stefan, Verena, Jochen, Susan und Florian, always listened to my complaints about ATLAS software, about poor documentation or about untraceable bugs in my code. We had a lot of very nice chats both at and after work and I am really thankful to them that they made the last three years so enjoyable for me. I want to thank Lena, Jochen, Verena and Stefan for reading and commenting on my thesis. Thank you! also to all other members and students of the PiD group for the good atmosphere, in particular to all people with whom I was sharing the office in the last years.

The major part of my work would not have been possible without the enormous support from the Z+jets+E_T^{miss} analysis team, namely Emma T., Emma K., Zach, Elena, Alex and Naoko. They answered my countless questions, provided guidance and many ideas for my studies and helped me with all sorts of problems regarding software, talks, etc. It was a great pleasure for me to be part of this team! Emma T., Emma K. and Zach also read the draft of my thesis and sent me many useful comments for which I want to express my special thanks.

Last but not least, I want to thank Mike, Jeanette and Dominik for their support with the 1L+jets+E_T^{miss} reinterpretation. They provided very valuable inputs to the analysis and all I had to do was to put the pieces together. My special thanks got to Mike for the helpful comments on my thesis.